

DARK GAS, THE GAS OF THE GAPS IN THE COLD ISM

by

EMMANUEL DONATE PEREZ

(Under the Direction of Loris Magnani)

ABSTRACT

In this thesis we study the diffuse molecular gas in the high-latitude cloud MBM 53 and the Southern Galactic Hemisphere. In particular, we conduct searches for dark molecular gas using high-sensitivity, high-velocity resolution CO(1-0) measurements, the OH 18 cm main lines, and composite radio and infrared dust spectra in a portion of the diffuse molecular cloud MBM 53. The results of our sensitive CO(1-0) observations increase the amount of CO-detectable molecular gas in MBM 53 by a factor of two with 15 new detections along 88 lines of sight. Our OH measurements find dark gas in 11 of 44 lines of sight overlapping the CO-sampled region. The CO(1-0) detections have A_V threshold of 0.25 *mag* while the OH detection threshold in A_V is 0.35 *mag*. In the composite radio-infrared spectra we found no indications of changes in dust grain size distribution or composition for the lines of sight where we had CO or OH detections compared to nondetections. Overall, we find that CO detections provide better information as to the extent of the borders of MBM 53 but OH detections provide a greater dark gas mass estimate.

Finally, we examine the molecular content of a ~ 2200 square degree region in Pegasus-Pisces with an estimated dark molecular gas fraction of 59%. Using data from the CO(1-0) Southern Galactic hemisphere, high-latitude survey by Magnani et al. (2000) we re-examined

the CO-detectable mass estimates for the region. By averaging all the CO spectra in subsections of varying sizes we decreased the rms of the averaged CO spectra by factors of 3-10, trading spatial resolution for sensitivity. With the new spectra we are able to make mass estimates as a function of sensitivity. Using the optimal estimate, the CO-detectable mass increases from 2200 to 4000 M_{\odot} , thereby decreasing the dark molecular gas fraction in the region to 0.24. In summary, sensitive CO(1-0) and OH 18 cm observations can detect significantly more molecular gas than is revealed by conventional molecular mapping. Thus the dark gas content of molecular clouds is critically dependent on the sensitivity and velocity resolution of the corresponding CO and OH maps.

INDEX WORDS: ISM: clouds — ISM: molecules — radio lines: ISM

DARK GAS, THE GAS OF THE GAPS IN THE COLD ISM

by

EMMANUEL DONATE PEREZ

B.S., University of Puerto Rico Recinto de Rio Piedras (2005)

J.D. Mercer University (2010)

A Dissertation Submitted to the Graduate Faculty
of The University of Georgia in Partial Fulfillment

of the

Requirements for the Degree

DOCTORATE OF PHILOSOPHY

ATHENS, GEORGIA

2019

© 2019

Emmanuel Donate Perez

All Rights Reserved

DARK GAS, THE GAS OF THE GAPS IN THE COLD ISM

by

EMMANUEL DONATE PEREZ

Approved:

Major Professor: Loris Magnani

Committee: Jean-Pierre Caillault
Phillip Stancil

Electronic Version Approved:

Suzanne Barbour
Dean of the Graduate School
The University of Georgia
August 2019

DEDICATION

I began this project with Loris Magnani primarily because I wanted to use the Arecibo Observatory in Puerto Rico. I remember going to the observatory with my father some years prior. As it happens I was born in Arecibo and I am one of very few Puerto Ricans who have used the observatory for research purposes. Being able to use the facility has been one of the greatest privileges of my life. I couldn't be more thankful to all the people that helped me along the way.

To Loris Magnani my best friend and thesis advisor who put up with all my idiosyncracies and never doubted my capacity to complete this project. His attention was always genuine and he didn't once let me doubt his appreciation for me as a student. Loris has given so much to see me succeed that I simply cannot put into words how much love and gratitude I have for him. Thank you for everything.

To Hector Arce for inviting me to his research group at Yale while I was visiting Connecticut. I was given the opportunity to present my research and to take classes as if I was a Yale student, I even had a desk space. I learned so much from my time there. Being able to see someone like me, who had come from where I came from, performing at the highest levels of astronomy was inspirational. I was always honored to be around him and I truly appreciate all the time he put into helping me learn about our Galaxy.

To my parents and sisters, without my incredible childhood I wouldn't be the adult I am today. This thesis is as much theirs as it is mine. My mother and father have always supported my goals, even the ones they didn't understand or think were necessary. My sisters have believed in me every step of the way and were a constant source of some very necessary reality checks. In the last seven years I have re-learned that there is nothing more valuable than having a supportive family.

ACKNOWLEDGMENTS

We acknowledge the use of the Legacy Archive for Microwave Background Data Analysis (LAMBDA), part of the High Energy Astrophysics Science Archive Center (HEASARC). HEASARC/LAMBDA is a service of the Astrophysics Science Division at the NASA Goddard Space Flight Center. Several of the images in this thesis were made with the Skyview Virtual Observatory which was developed with generous support from the NASA AISR and ADP programs (P.I. Thomas A. McGlynn) under the auspices of the High Energy Astrophysics Science Archive Research Center (HEASARC) at the NASA/GSFC Astrophysics Science Division.

TABLE OF CONTENTS

	Page
ACKNOWLEDGMENTS	v
LIST OF FIGURES	ix
LIST OF TABLES	xviii
CHAPTER	
1 GAS, DUST, STARS, AND GALAXIES	1
1.1 STARS AND GALAXIES	1
1.2 GAS IN THE INTERSTELLAR MEDIUM	4
1.3 DUST, MAGNETIC FIELDS, AND COSMIC RAYS	7
1.4 HEATING AND COOLING	8
1.5 THE STAR-GAS CYCLE	10
1.6 MOLECULAR CLOUDS	10
1.7 OUTLINE OF THE THESIS	14
2 OBSERVING MOLECULAR CLOUDS	15
2.1 MOLECULAR SPECTROSCOPY	15
2.2 INFRARED EMISSION	18
2.3 PHOTO DISSOCIATION REGION'S (PDRs)	19
2.4 DARK MOLECULAR GAS	21
3 REVIEW OF THE LITERATURE ON DARK GAS	28
3.1 TRACING DIFFUSE MOLECULAR GAS	28
3.2 CO IN DIFFUSE CLOUDS	29

3.3	OBSERVATIONS OF OH AND CH IN LOW EXTINCTION REGIONS . . .	30
3.4	MBM 53	31
3.5	AFTER 2005	32
4	SENSITIVE CO(1-0) SURVEY IN PEGASUS-PISCES REDUCES CO-DARK GAS INVENTORY BY FACTOR OF TWO	35
4.1	ABSTRACT	35
4.2	INTRODUCTION	35
4.3	THE SGH HIGH-LATITUDE SURVEY IN PEGASUS-PISCES	38
4.4	OBSERVATIONS	39
4.5	RESULTS AND IMPLICATIONS	44
4.6	DISCUSSION	46
5	OH AND CO AS TRACERS OF MOLECULAR GAS IN MBM 53	57
5.1	ABSTRACT	57
5.2	INTRODUCTION	57
5.3	THE EFFICACY OF THE OH 18 CM LINES FOR TRACING DIFFUSE MOLECULAR GAS	59
5.4	OBSERVATIONAL SETUP AND STRATEGY	60
5.5	RESULTS	62
5.6	DISCUSSION	67
5.7	SUMMARY	71
6	DARK MOLECULAR GAS IN PEGASUS-PISCES	85
6.1	ABSTRACT	85
6.2	INTRODUCTION	86
6.3	PREVIOUS CO DETECTIONS IN PEGASUS-PISCES	90
6.4	THE H ₂ MASS IN PEGASUS-PISCES FROM THE SGH-HL SURVEY	93

6.5	AVERAGING THE SPECTRA TO INCREASE THE SENSITIVITY OF THE SURVEY	95
6.6	CO-DETECTABLE VS. CO-DARK GAS	98
6.7	SUMMARY	98
7	RADIO AND INFRARED CONTINUUM SPECTRA OF MBM 53	113
7.1	DUST SPECTRA	113
8	SUMMARY AND FUTURE WORK	165
8.1	SUMMARY	165
8.2	ASSUMPTIONS AND PROBLEMS	167
8.3	FUTURE WORK	168

LIST OF FIGURES

2.1	Three-color IRIS (recalibrated infrared data from the Infrared Astronomy Satellite) composite map of the infrared sky at 25 (blue), 60 (green), and 100 (red) microns. The high-latitude cirrus are the easily noticeable low-brightness wisps above and below the bright Galactic plane. Image credit: NASA via the Legacy Archive for Microwave Background Data Analysis (LAMBDA). . . .	24
2.2	Dust map in Galactic coordinates of a $14^\circ \times 6^\circ$ centered on MBM 53. The quantity on a logarithmic color scale ranging from 0.03 to 0.45 magnitudes is $E(B-V)$, a measure of the dust column density, from the Schlegel, Finkbeiner, and Davis (1999) database. The bright structure at the bottom of the figure is MBM 54 The image was made with the Skyview Virtual Observatory. . . .	25
2.3	Same region as in Figure 2.2, but using the <i>Planck</i> 353 GHz channel which traces primarily thermal dust emission. The scale is linear and ranges from 3.17×10^{-4} to 6.44×10^{-3} K. The image was made with the Skyview Virtual Observatory.	26
2.4	Basic model of a photodissociation region (PDR) taken from Wolfire, Hollenbach, and McKee (2010). The model shows how the carbon transitions from C^+ to C to CO as one moves from the outer to the inner regions of a PDR. The inner two regions can be considered as the molecular cloud. Reproduced by permission of the AAS.	27
3.1	Histogram of the MBM clouds as a function of visual extinction in magnitudes. The extinction is for the most opaque 6region in the cloud based on the Schlegel, Finkbeiner, and Davis (1999) database.	34

- 4.1 The Southern Galactic Hemisphere - High Latitude (SGH-HL) CO(1-0) survey. The 4982 grid points which were observed by Magnani et al. (2000) are depicted as the small black dots. Detections from the survey are the round dots color coded in velocity (see top right corner). Other detections from Magnani, Hartmann, and Speck (1996) that were missed by the SGH-HL sampling grid are denoted by diamonds (the green diamond has no velocity information in the literature). The black box denotes the boundary of the region in Pegasus-Pisces included in the GCT dark gas calculations (see text). 49
- 4.2 Contour map of the northern portion of MBM 53 in E(B-V) from Schlegel, Finkbeiner, and Davis (1999) in linear scale from 0.10 to 0.51 mag in steps of 0.17 mag. The diamonds indicate the 88 positions that were observed in CO(1-0) for this paper. Each position corresponds to an observation from the SGH-HL survey (see §2). The five CO(1-0) detections from that survey at the T_{mb} level of 0.1 K (listed in Table 1) are denoted by squares with a plus sign in them. The 15 new detections are denoted by squares. Parameters for all the detections are in Table 2. 50
- 4.3 Comparison between the beam of the Harvard Smithsonian – Center for Astrophysics 1.2 m mm-wave telescope (beam size $8.4'$ at 115 GHz) with the 13-point beam pattern from the 12-m Arizona Radio Observatory telescope used to sample the larger beam. The sampling pattern is for one of the 88 observed positions (see Figure 2) and is representative of how each of those positions were observed in CO, with the final spectrum for that position produced by averaging the 13 individual spectra. The beam size of the 12-m at 115 GHz is $55''$ 51
- 4.4 CO(1-0) spectrum from position $(\ell, b) = (95.7^\circ, -34.0^\circ)$. The y-axis is antenna temperature in K in the form T_R^* and the x-axis denotes v_{LSR} in km s^{-1} . The velocity resolution and rms per channel are 0.06 km s^{-1} and 39 mK, respectively. 52

- 4.5 CO(1-0) spectrum from position $(\ell, b) = (92.4^\circ, -32.0^\circ)$. The x- and y-axes are as in Figure 5a. The rms is 34 mK per channel. The narrow pip at $v_{LSR} \approx 0 \text{ km s}^{-1}$ is RFI from the system electronics. 53
- 4.6 CO(1-0) spectrum from position $(\ell, b) = (92.4^\circ, -32.0^\circ)$ *Correction in Thesis: position should be 96.8, -34.0*. The The x- and y-axes are as in Figure 5a. The rms is 37 mK per channel. 54
- 4.7 CO(1-0) spectrum from the SGH-HL survey. The spectrum was made using on-off mode with the on position at $(\ell, b) = (90.2^\circ, -32.0^\circ)$ and the off position at $(\ell, b) = (90.2^\circ, -33.0^\circ)$. See Hartmann, Magnani, and Thaddeus (1998) for details. With this observing technique, if a CO(1-0) emission line were to be present in the off position, it would appear as an absorption line in the spectrum. The y-axis is antenna temperature in K in the form T_R^* . The velocity resolution is 0.65 km s^{-1} 55
- 4.8 CO(1-0) spectrum from position $(\ell, b) = (92.4^\circ, -33.0^\circ)$ *Correction in Thesis: position should be 90.2, -33.0*. The FWHM of the line from Gaussian fitting is 0.60 km s^{-1} . The downward going spike at 0 km s^{-1} is interference. The y-axis is antenna temperature in K in the form T_R^* and the x-axis is v_{LSR} in km s^{-1} . The velocity resolution is 0.06 km s^{-1} and the rms is 25 mK. 56

5.1	E(B-V) contour map of the northern portion of MBM 53 from the Schlegel, Finkebeiner, and Davis (1998) database in linear scale from 0.10 to 0.51 mag in steps of 0.13 mag. The diamonds indicate the 44 positions that were observed in the OH 18 cm lines for this paper. Each position corresponds to an observation from the CO (1-0) SGH-HL survey (see §3) and the deeper survey by Donate & Magnani (2017). The 20 CO(1-0) detections from Donate & Magnani (2017) are denoted by plus signs. Detections of at least the 1667 MHz line are denoted by squares with Gaussian-fit parameters for all the detections listed in Table 2. A complete CO(1-0) map of the region encompassing MBM 53-55 is given by Yamamoto et al. (2003).	73
5.2	Comparison between the beam of the Harvard Smithsonian – Center for Astrophysics 1.2 m mm-wave telescope (beam size 8.4' at 115 GHz) with the 5-point beam pattern from the 305-m Arecibo radio telescope used to sample the larger beam. The sampling pattern in RA and Dec is for one of the 44 observed positions (central point at $\ell = 94.6^\circ, b = -34.0^\circ$) and is representative of how each of those positions were observed in OH, with the final spectrum for that position produced by averaging the five individual spectra. The beam size of the 305-m at 1.6 GHz is $2.6' \times 3.1'$ elongated in azimuth, but is here represented by a 2.85' radius circle.	74
5.3	Spectrum of the OH 1667 MHz line for the line of sight G92.4–31.0 (see Table 1). The spike at $v_{LSR} = 0.0 \text{ km s}^{-1}$ is internal interference.	75
5.4	Spectrum of the OH 1667 MHz line for the line of sight G92.4–33.0 (see Table 1).	76
5.5	Spectrum of the OH 1667 MHz line for the line of sight G94.6–34.0 (see Table 1). The spike at $v_{LSR} = 0.0 \text{ km s}^{-1}$ is internal interference.	77

- 5.6 Comparison between the CO(1-0) spectrum (top) for position G95.7–32.0 and the equivalent OH 1667 MHz spectrum (bottom). The spike at $v= 0.0 \text{ km s}^{-1}$ in both spectra is due to internal interference. The scale of the CO spectrum has been reduced by a factor of ten. The OH feature at -12 km s^{-1} is only tentatively detected but, if real, it has no counterpart in the CO spectrum. 78
- 5.7 Comparison between the CO(1-0) spectrum (top) for position G96.8–30.0 and the equivalent OH 1667 MHz spectrum (bottom). The spike at $v= 0.0 \text{ km s}^{-1}$ in both spectra is due to internal interference. The scale of the CO spectrum has been reduced by a factor of ten. The OH feature at -9 km s^{-1} is only tentatively detected but, if real, it has no clear counterpart in the CO spectrum. 79
- 5.8 The relationship between the velocity-integrated CO(1-0) main beam antenna temperature at 115 GHz, $W(\text{CO})$, and the velocity-integrated OH 1667 MHz brightness temperature, $W(\text{OH})$. The CO data are from Donate & Magnani (2017). The dashed line represents the best fit line to the detections (see text). Representative error bars are shown for one of the detections. Gray arrows represent 2σ upper limits for $W(\text{OH})$ and $W(\text{CO})$ nondetections. 80
- 5.9 The relationship between the velocity-integrated CO(1-0) main beam antenna temperature, $W(\text{CO})$, from Donate & Magnani (2017), and the visual extinction, A_V , from Schlafly & Finkbeiner(2011). The dashed line represents the best fit line for detections only (see text). One-sigma uncertainties for $W(\text{CO})$ are shown for the detections. The grey points without error bars represent 2σ upper limits in $W(\text{CO})$ for non-detections. The uncertainty in A_V is $\approx 16\%$ 81

5.10	The relationship between the velocity-integrated OH 1667 MHz brightness temperature, $W(\text{OH})$, and the visual extinction, A_V , from Schafly and Finkbeiner (2011). The dashed line represents the best fit line for detections only (see text). One-sigma uncertainties, $W(\text{OH})$, are shown for the detections. The grey points without error bars represent 2σ upper limits in $W(\text{OH})$ for the non-detections. The uncertainty in A_V is $\approx 16\%$	82
5.11	Detection rate of the CO(1-0) line (black line) and the OH 1667 MHz line (gray line) as a function of visual extinction in magnitudes. <i>Correction in Thesis: x-axis values should be divided by 10</i>	83
5.12	Same as Figure 7 but for the OH detections in this paper (black exes) and similar data for the L1642 translucent molecular cloud (gray circles) from Sandell et al. (1981). The black line represents the best fit line for our OH detections and the gray line for the Sandell et al. (1981) detections (see text).	84
6.1	CO(1-0) spectrum from the SGH-HL survey made by averaging all the spectra in a $5^\circ \times 5^\circ$ region centered on $(\ell, b) = (67^\circ, -52.^\circ)$. The parameters of the detection are listed in Table 1. The absorption-like feature from $v_{LSR} = -10$ to $+10$ km s $^{-1}$ is negative because of the position-switching scheme used in the SGH-HL survey (see §4 and Hartmann, Magnani, & Thaddeus (1986)). A negative signal indicates that there is more emission in the off-position than the on-position (see Magnani et al. 2000, for details). The feature at ~ 25 km s $^{-1}$ km does not meet our 6σ threshold for detections.	104
6.2	Same as Figure 2a for the $5^\circ \times 5^\circ$ region centered on $(\ell, b) = (87.4^\circ, -38.0^\circ)$.	105
6.3	Same as Figure 2a for the $5^\circ \times 5^\circ$ region centered on $(\ell, b) = (87.4^\circ, -44.0^\circ)$. A positive signal indicates that there is more emission in the on-position than the off-position (see Magnani et al. 2000, for details).	106
6.4	Same as Figure 2a for the $5^\circ \times 5^\circ$ region centered on $(\ell, b) = (92.5^\circ, -32.0^\circ)$. The feature at ~ 15 km s $^{-1}$ km does not meet our 6σ threshold for detections.	107

6.5	Same as Figure 2a for the $5^\circ \times 5^\circ$ region centered on $(\ell, b) = (102.7^\circ, -32.0^\circ)$.	108
6.6	Same as Figure 2a for the $5^\circ \times 5^\circ$ region centered on $(\ell, b) = (112.9^\circ, -38.0^\circ)$.	109
6.7	Same as Figure 2a for the $5^\circ \times 5^\circ$ region centered on $(\ell, b) = (128.2^\circ, -44.0^\circ)$.	110
6.8	Same as Figure 2a for the $5^\circ \times 5^\circ$ region centered on $(\ell, b) = (133.4^\circ, -44.0^\circ)$.	111
6.9	The product of the detection rate times the average W_{CO} for a given sized region as a function of the region size in square degrees (smaller black dots and dashed-dotted line), and the detection rate as a function of area (larger gray dots and dashed line).	112
7.1	Gas to dust comparison for the MBM 53-55 complex. The image on the left is the CO(1-0) map from Yamamoto et al. (2003) with the points observed in CO and OH in Chapters 4 and 5 shown as the blue diamonds (image courtesy of Amanda Stricklan (2019)). On the right is the same region as on the left but in E(B-V) from the Schlegel, Finkbeiner, and Davis (1999) database. The similarity between the images is clear on the large scales but breaks down on small scales.	118
7.2	Millimeter-submillimeter-far infrared spectrum of the line of sight $(\ell, b) = (82.5^\circ, -34.0^\circ)$, based on <i>Planck</i> and IRAS data (see text).	119
7.3	Same as figure 7.1 at position $(\ell, b) = (83.6^\circ, -34.0^\circ)$	120
7.4	Same as figure 7.1 at position $(\ell, b) = (84.7^\circ, -34.0^\circ)$	121
7.5	Same as figure 7.1 at position $(\ell, b) = (85.8^\circ, -34.0^\circ)$	122
7.6	Same as figure 7.1 at position $(\ell, b) = (86.9^\circ, -34.0^\circ)$	123
7.7	Same as figure 7.1 at position $(\ell, b) = (88.0^\circ, -34.0^\circ)$	124
7.8	Same as figure 7.1 at position $(\ell, b) = (89.1^\circ, -34.0^\circ)$	125
7.9	Same as figure 7.1 at position $(\ell, b) = (90.2^\circ, -34.0^\circ)$	126
7.10	Same as figure 7.1 at position $(\ell, b) = (91.3^\circ, -34.0^\circ)$	127
7.11	Same as figure 7.1 at position $(\ell, b) = (92.4^\circ, -30.0^\circ)$	128
7.12	Same as figure 7.1 at position $(\ell, b) = (92.4^\circ, -31.0^\circ)$	129

7.13	Same as figure 7.1 at position $(\ell, b) = (92.4^\circ, -32.0^\circ)$	130
7.14	Same as figure 7.1 at position $(\ell, b) = (92.4^\circ, -33.0^\circ)$	131
7.15	Same as figure 7.1 at position $(\ell, b) = (92.4^\circ, -34.0^\circ)$	132
7.16	Same as figure 7.1 at position $(\ell, b) = (93.5^\circ, -30.0^\circ)$	133
7.17	Same as figure 7.1 at position $(\ell, b) = (93.5^\circ, -31.0^\circ)$	134
7.18	Same as figure 7.1 at position $(\ell, b) = (93.5^\circ, -32.0^\circ)$	135
7.19	Same as figure 7.1 at position $(\ell, b) = (93.5^\circ, -33.0^\circ)$	136
7.20	Same as figure 7.1 at position $(\ell, b) = (93.5^\circ, -34.0^\circ)$	137
7.21	Same as figure 7.1 at position $(\ell, b) = (94.6^\circ, -30.0^\circ)$	138
7.22	Same as figure 7.1 at position $(\ell, b) = (94.6^\circ, -31.0^\circ)$	139
7.23	Same as figure 7.1 at position $(\ell, b) = (94.6^\circ, -32.0^\circ)$	140
7.24	Same as figure 7.1 at position $(\ell, b) = (94.6^\circ, -33.0^\circ)$	141
7.25	Same as figure 7.1 at position $(\ell, b) = (94.6^\circ, -34.0^\circ)$	142
7.26	Same as figure 7.1 at position $(\ell, b) = (95.7^\circ, -30.0^\circ)$	143
7.27	Same as figure 7.1 at position $(\ell, b) = (95.7^\circ, -31.0^\circ)$	144
7.28	Same as figure 7.1 at position $(\ell, b) = (95.7^\circ, -32.0^\circ)$	145
7.29	Same as figure 7.1 at position $(\ell, b) = (95.7^\circ, -33.0^\circ)$	146
7.30	Same as figure 7.1 at position $(\ell, b) = (95.7^\circ, -34.0^\circ)$	147
7.31	Same as figure 7.1 at position $(\ell, b) = (96.8^\circ, -30.0^\circ)$	148
7.32	Same as figure 7.1 at position $(\ell, b) = (96.8^\circ, -31.0^\circ)$	149
7.33	Same as figure 7.1 at position $(\ell, b) = (96.8^\circ, -32.0^\circ)$	150
7.34	Same as figure 7.1 at position $(\ell, b) = (96.8^\circ, -33.0^\circ)$	151
7.35	Same as figure 7.1 at position $(\ell, b) = (96.8^\circ, -34.0^\circ)$	152
7.36	Same as figure 7.1 at position $(\ell, b) = (97.9^\circ, -30.0^\circ)$	153
7.37	Same as figure 7.1 at position $(\ell, b) = (97.9^\circ, -31.0^\circ)$	154
7.38	Same as figure 7.1 at position $(\ell, b) = (97.9^\circ, -32.0^\circ)$	155
7.39	Same as figure 7.1 at position $(\ell, b) = (97.9^\circ, -33.0^\circ)$	156

7.40	Same as figure 7.1 at position $(\ell, b) = (97.9^\circ, -34.0^\circ)$	157
7.41	Same as figure 7.1 at position $(\ell, b) = (99.0^\circ, -30.0^\circ)$	158
7.42	Same as figure 7.1 at position $(\ell, b) = (99.0^\circ, -31.0^\circ)$	159
7.43	Same as figure 7.1 at position $(\ell, b) = (99.0^\circ, -32.0^\circ)$	160
7.44	Same as figure 7.1 at position $(\ell, b) = (99.0^\circ, -33.0^\circ)$	161
7.45	Same as figure 7.1 at position $(\ell, b) = (99.0^\circ, -34.0^\circ)$	162
7.46	The spectrum for position $(\ell, b) = (92.4^\circ, -34.1^\circ)$ shown above with a scaled blackbody spectrum with $T = 14$ K superposed on the data.	163
7.47	Combined dust spectra for all 44 sightlines observed in OH. The blue spectra are for lines of sight with molecular detections of OH and/or CO and the red spectra are for lines of sight with non-detections.	164

LIST OF TABLES

4.1	W_{CO} for the five positions in common between the SGH-HL and the current survey.	41
4.2	Gaussian-fit parameters and W_{CO} for CO(1-0) detections in our survey.	42
4.3	Total W_{CO} from the three surveys.	45
5.1	Gaussian-fit parameters and W_{OH} for OH 1667 MHz detections in our survey.	62
5.2	OH column densities for four possible excitation temperatures.	68
5.3	OH and CO masses for MBM 53.	68
6.1	Results of $5^\circ \times 5^\circ$ co-added regions.	101
6.2	Results of $5^\circ \times 5^\circ$ co-added regions, continued	102
6.3	Results of $5^\circ \times 5^\circ$ co-added regions, continued	103
6.4	Results from summing over regions of varying size.	103
7.1	Summary information for the radio and infrared data.	117

CHAPTER 1

GAS, DUST, STARS, AND GALAXIES

1.1 STARS AND GALAXIES

In the early 1900's most astronomers believed that our Galaxy¹, the Milky Way, was a single island universe of stars that contained all of the cosmos. In 1923 Edwin Hubble observed stars in the Andromeda nebula, also known as M31, previously identified as a faint, fuzzy patch of light. Other nebulae like it had been observed and it was unclear whether these patches were part of our Galaxy or far away galaxies unto themselves. Hubble observed a kind of star called a Cepheid variable within the Andromeda nebulosity. These stars change their brightness in regular, measurable periods and have a period-luminosity relation. The longer the period, the higher the absolute brightness of the Cepheid. If the absolute brightness of a star is known, measuring the apparent brightness yields the distance via the famous relation: $m - M = 5 \log d + 5$. In this manner Hubble determined that the Andromeda nebula was 900,000 light years away, much farther than anything that could be part of our Milky Way. Astronomers now place Andromeda at about 2.5 million light years or 780,000 parsecs. Hubble also saw many faint stars within Andromeda and determined with finality that the Andromeda nebula was actually the Andromeda galaxy. In a little more than 100 years astronomers have determined that there are billions of galaxies each containing billions of stars with these systems ranging between ten and a hundred thousand light years across.

Astronomers have observed four different basic shapes for galaxies: spiral, elliptical, peculiar, and irregular. The Milky Way is a spiral galaxy, which typically consist of broad, thin, flat, rotating disks of stars, gas, and dust (we will ignore dark matter for the moment).

¹When referring to the Milky Way galaxy we will capitalize the word "galaxy".

Spiral galaxies have bulges of varying size in their centers and can sometimes contain an elongated bar feature in their central regions where stars and interstellar matter are highly concentrated. Categories of galaxies contain subcategories and, in the case of spiral galaxies, various types of spiral features can be seen. These galaxies' spiral arms come in many different forms such as short and tight arms or grand spirals whose arms extend much further out. Ellipticals are the most common form of galaxy ranging in size from small (e.g. the satellite galaxies of Andromeda) to larger than the largest spirals. Finally, the peculiar and larger irregulars seem to be galaxies that have undergone collisions and are in the process of reforming themselves, likely into ellipticals. Some irregular galaxies may be too small to gravitationally form themselves into anything more than a strange shape.

Galaxies can also be classified by their energetic output in addition to their morphology, size, and mass. In 1959 a point-like object named 3C273 was observed giving off incredible amounts of energy in the radio part of the electromagnetic spectrum. 3C273 was determined to be an active galaxy approximately 2 billion light years away. The prodigious energy output was due to a central, super massive black hole with an active accretion disk funneling gas into the black hole. At the time it was the most luminous object ever to be observed as it was emitting 4 trillion times the energy of the Sun. It was dubbed a quasar, for quasi-stellar radio source (sometimes referred to as QSO), since, with the optical telescopes of the time, it resembled a high energy point source similar to a distant star with strange spectral lines and sometimes varying luminosity. Many more were found by astronomers as observations continued. When astronomers started detecting x-rays and gamma rays with space-based observatories they found even more of these QSO's, since some of them do not emit strongly in the radio spectrum, but do so in the x-ray region.

To emit x-rays and gamma rays a QSO must be enormously energetic, and a mechanism for emitting so much energy had to be found. By the 1980's astronomers established that these massive and energetic QSO's are powered by massive black holes at their centers with at least millions of times more mass than our Sun and some were found to have central

black holes with masses in the $10^9 M_{\odot}$ range². The gas surrounding the black hole is in a dense, hot accretion disc, and undergoing a lot of frictional heating (the source of x-rays and gamma-rays). The surrounding disc is called an accretion disc because it funnels gas into the black hole thereby converting gravitational potential energy into heat and luminosity. Thus, the accretion disc is the source of the high-energy emission observed in the gamma ray, x-ray, and sometimes radio portions of the spectrum.

Galaxies cluster into groups and the Milky Way galaxy is part of what is known as The Local Group. The three largest galaxies in the Local Group are the Milky Way, Andromeda, and the Triangulum galaxy (M33) and they are all spirals. There are a few dozen smaller galaxies in The Local Group as well. The Milky Way and Andromeda are apparently set to collide in the next 4 billion years, and it is possible that through these collisions the black holes at their centers will collide, merge, and feed off the dust and gas surrounding them creating an active galactic nucleus that produces the high energy x-rays and gamma rays mentioned above.

Galaxies clump into galaxy clusters tens of millions of light years across that can contain as many as thousands of galaxies; as opposed to the dozens in a smaller group like our Local Group. To date, thousands of galaxy clusters have been observed. Galaxy clusters also cluster and these much larger groupings are known as superclusters. These can contain some few dozen clusters and are found to be millions of light years across. Our Local Group is part of the Virgo cluster and the Virgo supercluster. Using the Hubble deep field telescope astronomers estimate there could be up to or more than 100 billion galaxies in the observable universe.

The above is but a brief primer on galaxies on the large scale and their interactions with each other. Internally, galaxies have their own structures, kinematics, and dynamics. A large spiral galaxy like the Milky Way is dominated by stars and dark matter. The former produce enormous amounts of energy and the latter dominates the gravitational potential

²One solar mass is denoted as $1 M_{\odot}$.

of a galaxy. In this thesis we will ignore dark matter (thought to be an exotic, hitherto unidentified particle or particles with no electromagnetic interaction but a sizeable mass per particle) because, at the scales we are concerned with, ~ 10 pc, the gravitational potential produced by dark matter behaves like a constant background with no dynamic or kinematic effects on the objects themselves. We also mostly ignore stars, choosing instead to focus on the gas and dust.

1.2 GAS IN THE INTERSTELLAR MEDIUM

After dark matter and stars, the next most massive component of a spiral galaxy is the gas that permeates the disk and halo of the system. In a typical large spiral like the Milky Way, the total gas content is about two orders of magnitude lower than the stellar content, and the total dust mass is another two orders of magnitude lower than the gas mass. At first, given their low overall masses with respect to the stellar and dark matter components, it would seem somewhat foolish to spend much time on their study. However, the gas and stars are linked inextricably through the star-gas cycle where, in overly simplistic terms, the gas gives rise to the stars, and the stars recycle a portion of their mass into the gas. The dust, although an even lesser mass component, plays an outsize role because it absorbs starlight and re-radiates it in the infrared. With the advent of infrared telescopes, the dust is now as easy to trace as stars.

On average, away from the Galactic Center, there are a few light years between stars in the Milky Way. However, the space between them is not empty. Instead it is filled with tenuous gas and dust known as the interstellar medium or the ISM. In the Milky Way, the ISM has an average density of one particle per cubic centimeter but can range between 10^{-4} to 10^6 particles per cubic centimeter (and even larger values in star-forming cores). Temperatures in the ISM range from as low as 10 K to as high as 10^7 K. The ISM organizes itself into phases, stable configurations each defined by the density and temperature of the

hydrogen. In theory, the phases are in pressure equilibrium, so that the hotter the phase the less dense the hydrogen, (see review by Kulkarni and Heiles 1987).

The phases that contain neutral atomic hydrogen, or HI, are the Cold and Warm Neutral Mediums; CNM and WNM, respectively. The temperatures in the CNM and WNM vary between 100-10,000 K. These phases of the ISM were identified in the 1950's and 60's through the HI 21 cm line. The 21 cm line emission of atomic hydrogen is a hyperfine transition produced by the energy difference between the spin states of the proton and electron in a hydrogen atom. As the spins for the proton and electron are parallel with each other the atom has more energy than when the spins are antiparallel. When the excited state decays, the spin flips between these states and the atom emits a photon with a wavelength of 21 cm (or 1420 MHz) and this line is the strongest, non-masing, spectral line in the ISM. The prediction that the line could be observable in the ISM in emission was made in 1944 by the Dutch astronomer H.C. van de Hulst, and the 21 cm line was first observed by Harold Ewen and Edward Purcell in 1951. Observation of the 21 cm line revolutionized ISM astronomy and marked the beginning of spectral-line radio astronomy. Since then, the atomic hydrogen distribution in our galaxy, specifically in the CNM and WNM, has been mapped by the observation of this transition (see, e.g., Hartmann and Burton 1997).

Ionized hydrogen, or HII, is hydrogen whose electron has been stripped off by the radiation emitted by very hot stars. When a hydrogen atom absorbs radiation above 13.6 eV the electron in the hydrogen atom can be stripped off, leaving a single proton. The phases associated with ionized hydrogen are the Warm Ionized Medium (WIM) also known as the Diffuse Ionized Gas (DIG) or the Reynolds Layer, and the Hot Ionized Medium (HIM) or Coronal Gas. HII regions are considered separately from the WIM because they are substantially denser and thus not in pressure equilibrium with their surroundings. While the WIM and HII regions can reach temperatures up to 10,000 K the HIM can reach up to several million degrees. Since the HIM is so hot, its particle density is only a few thousandths per cubic centimeter, where the WIM has a density of a few tenths per cubic centimeter. The

gas in the HIM is thought to originate primarily from supernova explosions which form large cavities in the disk which can vent the hot gas into the halo. The HIM thus dominates the gas content of the halo. It is difficult to ascertain just how much mass there is in the HIM, and it has been suggested there is as much gas mass in this form in the Galactic halo as there is in the main disk (Cox 2006). As mentioned above, HII regions are associated with zones around early-type stars and tend to be significantly denser than either the WIM or HIM at around 100-10,000 particles per cubic centimeter. In addition, HII regions are localized while the WIM is widely distributed.

At the other extremes, the coldest and densest regions of the ISM are where the molecular hydrogen, H_2 , resides. These regions are very cold with temperatures near 10 K and average densities in the 100-1000 cm^{-3} range. This phase is concentrated in cloud-like structures and most of the molecular gas in the Galaxy is found in the disk in discrete entities known as Giant Molecular Clouds, or GMC's. Since the denser component is colder, it is primarily detectable in the radio part of the spectrum. Radio wavelengths are significantly longer than infrared radiation and can make it through the earth's atmosphere so that radio astronomers have been probing molecular clouds and the cold ISM with ground-based radio telescopes since the 1960s. Unfortunately, H_2 is very difficult to observe from the Earth's surface for several reasons. Principally, the low moment of inertia of the molecule means that the rotational transitions are widely separated in energy and occur in the infrared part of the spectrum. Thus, the lowest rotational transition ($J=2-0$) has an energy equivalent to 2000 K, so in interstellar clouds the upper state is not very populated. To make matters more difficult, the Earth's atmosphere is very opaque in the mid and far infrared region of the spectrum where the lowest H_2 rotational lines are found. Finally, H_2 is homonuclear, so it does not have dipole but, rather, quadrupole transitions which are weaker than dipole transitions. Because of these factors, astronomers studying molecular clouds must resort to other molecules to estimate the molecular hydrogen column through conversion factors or radiative transfer and

astrochemistry models that estimate the molecular hydrogen content given the abundance of another molecule or ion.

The second most abundant molecule in the ISM is carbon monoxide or CO and its lowest rotational transitions have traditionally been the primary molecular gas tracers of the ISM. The workhorse tracer for many decades was the lowest rotational transition ($J=1-0$) at 115.271 GHz or 2.6 mm first detected in the ISM by Wilson, Jefferts, and Penzias (1970). For most of the first half century of these observations, a CO(1-0) map of the ISM was considered to be equivalent to an H₂ map and CO surveys of the Milky Way were used to reveal its molecular distribution (Dame, Hartmann, and Thaddeus 2001; see Heyer and Dame 2015 for a review). However, in 2005 Grenier, Cassandjian, and Terrier found that CO(1-0) line might not be able to trace all or even most of the molecular gas in the Galaxy and since that time a spirited debate has arisen over the best way to trace the molecular hydrogen content of the ISM, especially at low densities. Transitions of other molecules have been proposed as tracers of H₂ (especially CH and OH), and a strong case has been made even for an ion, C⁺.

1.3 DUST, MAGNETIC FIELDS, AND COSMIC RAYS

Aside from all the different phases of hydrogen a few other important particles and phenomena pervade the ISM. The most notable is interstellar dust which permeates the Galaxy and is easy to detect by thermal emission in the infrared. Dust in the ISM is often less than a micron in size and generally acts like tiny dirt particles in that it is opaque and interacts readily with light of visible and ultraviolet wavelengths. The interactions consist of scattering or absorption with the dust strongly absorbing optical and ultraviolet light, then radiating it in the infrared where it can be readily detected by infrared cameras. Light of a wavelength larger than a micron does not interact readily with the dust and so the extinction in the infrared is quite low. However, most infrared light is blocked by Earth's atmosphere and so infrared telescopes must be put on satellites into orbit outside of the

earth's atmosphere. The first large scale infrared surveys of the Galaxy were made with the Infrared Astronomy Satellite (IRAS) in the early 1980's (Neugebauer et al. 1984). Since then it has become clear that the dust content can be traced by infrared detectors and missions such as Herschel and Spitzer have continued the infrared study of the sky (see Chapter of 5 of Magnani and Shore 2017).

In addition to dust, magnetic fields and cosmic rays pervade the ISM. The typical magnetic field in the ISM ranges between 5 and 6 microgauss and gets stronger in molecular clouds. This has the effect of aligning the dust grains in the ISM and thence polarizing the starlight that passes through the clouds which are denser and thus have more dust than the ambient medium. Polarization studies have shown the structure of the magnetic fields of the Galaxy and other techniques (Faraday rotation, the Zeeman effect) can reveal the strength of the field in molecular clouds (see Magnani and Shore 2017 for details). Although magnetic fields are critical for understanding the structure and dynamics of molecular clouds, such considerations are not the focus of this thesis and thus we will not discuss them further.

Cosmic rays are protons, electrons, and heavier nuclei that travel at relativistic speeds. The word ray is an artifact of prior ignorance, since astronomers initially believed that these energetic particles were electromagnetic radiation. These highly-accelerated particles are very energetic, generally close to about 0.3 GeV with some cosmic rays reaching 3×10^{20} eV. Their interaction with hydrogen nucleons which produces gamma-rays is discussed in section 2.4. For a review of other ways they affect the ISM see Magnani and Shore (2017).

1.4 HEATING AND COOLING

The temperature of the cosmic microwave background is about 2.7 K yet the different phases of the ISM exist at temperatures that are hotter. In order for the phases to reach the temperatures they do there have to be mechanisms for heating and cooling the gas in the ISM. In the diffuse ISM the dust pervading the hydrogen absorbs ultraviolet photons and ejects electrons which then heat the hydrogen gas collisionally. This mechanism known

as photoelectric heating is the primary driver for heating the atomic and diffuse molecular portions of the ISM. The ionized gas in the WIM is also heated by starlight but in this case the radiation that is heating the gas is the ionizing radiation that comes from early-type stars which somehow percolates throughout the ISM to produce a widespread WIM. Naively, one would expect these photons to be immediately soaked up by the pervasive atomic hydrogen in the ISM, but somehow these photons are distributed throughout the disk. The porous, turbulent structure of the neutral gas is the likely mechanism that allows this (Miller and Cox 1993) Mechanical heating by supernovae or the concerted action of stellar winds also plays a role in the heating of the HIM and both mechanisms blow large, long-lived cavities in the ISM. While the general picture of the heating of the ISM is fairly well established, the details regarding filling factors and morphology are still being debated and a review by Cox (2006) describes the current views and areas of active research.

The cooling of the ISM proceeds primarily by collisions between the hydrogen and key coolants which then radiate energy by spontaneous emission. The WIM and WNM cooling is dominated by H-alpha emission while the CNM is cooled primarily by the forbidden line of C^+ at 158 micron. Details on the heating and cooling of the various phases of the ISM are given by Kulkarni and Heiles (1987) and Magnani and Shore (2017).

Although molecular clouds are not part of the phases of the ISM (because the great majority are not in pressure equilibrium with their surroundings), they are also heated by photoelectric heating and cool primarily by the lowest CO rotational transitions. It is clear from the above considerations that a strong source of UV photons will directly affect the heating and thus the structure of the ISM in its vicinity. Different phases are likely to be present as one travels farther from the source. This idea has been developed in a model known as a photodissociation region and is discussed in Chapter 2.

1.5 THE STAR-GAS CYCLE

When galaxies are forming, much of the gas that is accreted by the galaxy goes into forming stars. The leftover gas residing in the ISM after the galaxy's initial stars have formed then proceeds to form new generations of high and low mass stars mostly in GMCs. Smaller clouds known as dark molecular clouds form only low-mass stars. Some of the gas that goes into making stars is continuously replenished by being slowly accreted onto our Galaxy from the surrounding intergalactic medium. Once stars form, they then evolve depending on their initial mass. As old massive stars (with mass greater than 8 solar masses) burn through their fuel and die, their contents are explosively ejected into the ISM in Type II supernova explosions that replenish the gas mass and feed the turbulence in the ISM. Low mass stars at the end of their evolution eject their envelopes more gently as planetary nebulae. These expanding shells also replenish the gas inventory of the ISM. The dynamical action of these end stages of stellar evolution, especially of supernovae, results in changing the temperatures, densities, and intermixing of the different ISM phases. Whether through supernovae or planetary nebulae, the hot gas that has been recycled into the ISM eventually cools and becomes part of the warm or cold neutral media. Under the action of outside mechanical triggers, (e.g., shocks driven by stellar winds or supernovae) a portion of the CNM becomes molecular, and the cycle closes. This cycle of star formation, evolution, and death is clearly the primary driver of galactic evolution. The gas plays a key role in the formation of stars and is recycled into the ionized, neutral, and molecular stages, but the focus of this thesis is molecular clouds and we turn to this topic next.

1.6 MOLECULAR CLOUDS

Molecular clouds are broadly defined as the component of the ISM that is coldest and densest. However the definition of what constitutes a molecular cloud or the molecular component of the ISM has varied over time as well as over the research interests of particular

astronomers. In 1937 the first molecule was detected in interstellar space. Dunham (1937) and Dunham and Adams (1939) found CH absorption lines along lines of sight to stars behind molecular clouds (though the concept was unknown at the time). CH^+ and CN were also found soon after in the early 1940s in the spectra of stars. In the optical, molecules could only be detected in absorption towards early type stars. Thus, only relatively few lines of sight could be observed so that the concept of a molecular “cloud” could not be realized. However, World War II led to the rise of radar technology and this gave birth to radio astronomy (see Sullivan 2009). In 1963 the hydroxyl molecule (OH) was found in emission (Weinreb et al. 1963) at 18 cm and other molecules soon began to be found: five years later ammonia was detected (Cheung, et al. 1968), and in 1969 the organic molecule formaldehyde was even seen in absorption by Snyder et al. (1969). When Wilson, Jefferts, and Penzias first discovered the CO(1-0) emission line at 115.271 GHz in 1970, it was soon realized that CO(1-0) was the strongest non-masing molecular line and the early molecular hydrogen studies were done using this line as a tracer of H_2 . The first of these studies were made between 1970 and 1980 but were focused on the Galactic plane at low latitudes (e.g., Stark 1979; Burton and Gordon 1978; Dame 1984; Sanders, Solomon, and Scoville 1984; and references therein). The principal, most complete, survey was started by Pat Thaddeus and Tom Dame at Columbia University in the early 1970s, then continued at the Harvard-Smithsonian Center for Astrophysics in the 1980s and continues to this day. There are now more than 270,000 scans in the survey comprising the CO(1-0) map of the Milky Way and the most recent summary of the results was published by Dame, Hartmann, and Thaddeus (2001).

The basic distribution of the CO emission from the Galaxy is as follows: There is a strong concentration of molecular gas in the Galactic Center followed by a rapid drop off in the first two kiloparsecs. In the Inner Galaxy, CO emission peaks between 3-6 kpc and from 1-8 kpc molecular gas dominates the atomic gas. Beyond 8 kpc atomic gas dominates but one can still find many GMC’s as far out as 11 kpc. At that point the molecular gas

significantly decreases although some GMCs have even been found out to 20 kpc (Wouterloot and Brand 1989; Digel, de Geus, and Thaddeus 1994). Beyond 16 kpc the molecular mass surface density drops to about 0.095 solar masses per pc^{-2} compared to 0.50 per pc^{-2} between 1-8 kpc. For a complete picture of the molecular gas one can see the images from the *Planck* satellite that are the most complete whole-sky distribution of molecular gas at 2.6 mm (Planck Collaboration 2013). Although not as complete in sky coverage, the Dame, Hartmann, and Thaddeus (2001) survey shows conclusively that molecular clouds are mostly distributed along the plane and have a more restricted distribution than the CNM. Analyses of these data indicate that most of the gas detected by this survey and similar Galactic plane surveys is contained in GMCs (Scoville & Sanders 1987). It is important to note that the Dame, Hartmann, and Thaddeus (2001) survey is a spectral survey, i.e., the CO(1-0) line provides velocity information, whereas the *Planck* survey is based on imaging data with one of the bands centered on the CO(1-0) line at 115 GHz. In addition to the CO(1-0) line, the *Planck* band contains the $^{13}\text{CO}(1-0)$ isotopic line, thermal emission from dust in the Galaxy and the Cosmic Microwave Background, and non-thermal components. All these backgrounds have to be subtracted to give an image of the CO(1-0) distribution (with no velocity information).

GMCs contain thousands to millions of solar masses of molecular gas, but there are also smaller molecular entities ranging from a few to a few thousand solar masses. These smaller objects can be subdivided into three categories: dark, translucent, and diffuse clouds (van Dishoeck and Black 1988). The distinction was made in terms of the extinction by dust within the cloud, so that dark clouds have extinctions above 5 mag, translucent between 1 and 5 mag, and diffuse have less than 1 mag extinction. One can think of the dark clouds as dense, condensed entities with a few dense clumps within them. They obscure a great deal of background light and have been seen to form low mass stars. The dark clouds are found primarily in the Galactic plane where molecular gas abounds and these objects can contain a few tens to hundreds of solar masses, (see review by Heyer and Dame 2015).

Where GMCs and dark clouds contain multiple dense clumps, and are dominated by gravity, the translucent and diffuse clouds form a separate category in that they are not massive or dense enough to be gravitationally bound, and hence are tenuous and dominated by turbulence and, likely, magnetic fields. The distinction between the translucent and diffuse clouds, aside from their extinction values, is hazy. Neither diffuse nor translucent clouds, form stars with the exception of one object (see Magnani and Shore 2017). Although translucent clouds can extend into the few hundred solar mass range individual diffuse clouds are much smaller. Ironically, an extended complex of many diffuse clouds can form a related structure that can reach a few thousand solar masses (e.g. the MBM 53-55 complex, see Yamamoto et al. 2003 and Chapter 4 of this thesis), larger than most dark molecular clouds. In addition to individual diffuse clouds, translucent cores will be surrounded by extended diffuse region making it even more difficult to distinguish between them. In reality these distinctions between molecular clouds are taxonomic exercises to facilitate research and investigation. Translucent and diffuse clouds are ever evolving due to their turbulent natures, and Magnani, Blitz, and Mundy (1985) established that their lifetimes are relatively short, on the order of 10^6 years.

GMCs and dark clouds also have translucent and diffuse envelopes surrounding them that sometimes occupy a greater volume than the cold dense regions within the more opaque cloud so that the study of diffuse and translucent gas is important for understanding all molecular clouds (Magnani and Shore 2017). Another commonality is that isolated translucent and diffuse clouds are often embedded in extended atomic filaments, and GMCs and dark clouds have atomic hydrogen envelopes so that a transition from the CNM to the molecular cloud is an important aspect of all molecular astrophysics and will be discussed in Chapter 2.

Despite the vast variety in the molecular cloud zoo, this thesis focuses on the smaller, more diffuse molecular clouds, in particular the techniques necessary to study the most diffuse molecular portions of these clouds. We will elaborate on some of these techniques in subsequent chapters, but first we outline the topics covered in this thesis.

1.7 OUTLINE OF THE THESIS

In this chapter I have discussed galaxies and galactic astronomy with an emphasis on the interstellar medium and molecular clouds. It serves as a general introduction for the specifics that come in the later parts of the thesis. Chapter 2 begins with introducing the methods and models that we use to study the molecular clouds in the ISM. In addition it covers the origin of the dark gas region³ of molecular clouds that is the focus of my research. Chapter 3 goes over the history of the dark gas idea in astronomy and leaves us positioned at the edge of what was known regarding dark gas at the time I began this study. Chapters 4, 5 and 6 are all of my publications regarding CO and OH as tracers of regular and dark gas. Specifically, Chapter 4 covers sensitive CO measurements in the diffuse high-latitude cloud MBM 53, published on August 21, 2017 in Monthly Notices of the Royal Astronomical Society (MNRAS). Chapter 5 compares OH and CO against each other in MBM 53 and was accepted for publication in MNRAS on April 20, 2019. Chapter 6 examines statistics behind what happens when we trade resolution for sensitivity in the Galactic Southern Hemisphere High-Latitude CO(1-0) survey (Magnani et al. 2000). This chapter was accepted for publication in MNRAS on April 10, 2019. In Chapter 7 we examine radio and infrared spectra in the regions where we observed CO and OH in an attempt to look for a relationship between the dust properties and the molecular emission. We conclude in Chapter 8 with a summary and possible directions for future research.

³“Dark gas” has nothing to do with dark molecular cloud or dark matter.

CHAPTER 2

OBSERVING MOLECULAR CLOUDS

2.1 MOLECULAR SPECTROSCOPY

Earth's atmosphere only permits certain wavelengths of light to reach the surface. On Earth there are two regions of the electromagnetic spectrum that the atmosphere does not mostly or totally block: the optical and the radio. For optical light the window goes from about 350 nm to about 800 nm in wavelength and then continues to about 1100 nm in the near infrared. For radio it goes from about 1 cm to 11 m. Molecular clouds are cold and dark, hence they cannot be observed directly through the optical window although some are illuminated by reflected starlight and show up as bright nebulae (Lynds 1965). Perhaps more compellingly the dust in the clouds dims the optical light from background stars and thus a dust-rich, nearby cloud can be seen in silhouette against a background star field (Lynds 1962). The dimming of star light because of intervening dust is known as interstellar extinction and the greater the column of dust the more the light is extinguished, and background stars can even become invisible. Studying the cloud optically thus becomes difficult, so the best way for ground-based astronomers to study molecular clouds is through the radio wavelengths. With the advent of radio molecular spectroscopy in the 1960's, molecular cloud studies became an established area of astrophysical research.

The strength of a molecular line is related to how asymmetric the molecule is and the energy required to change the rotational state of a molecule depends on how massive the molecule is. Since molecular hydrogen is perfectly symmetric and is the lightest of all molecules the rotational levels are significantly separated so that temperatures greater than 500 K are required to provide the energy to significantly populate the lower rotational levels.

The temperatures inside a molecular cloud on average are about 10 K - 20 K hence cold clouds are not going to be strong H₂ emitters. To make matters worse, the atmosphere is opaque in the relevant wavelength ranges (the infrared).

Fortunately, more than 200 other molecules have been detected in the interstellar medium¹. Among those is the carbon monoxide molecule (CO), the most abundant species in molecular clouds after molecular hydrogen with an abundance with respect to H in dark clouds and GMCs in the $10^{-5} - 10^{-4}$ range. The CO molecule is asymmetric and is 14 times more massive than the hydrogen molecule. As such the energy required to excite the CO molecule from its rotational ground state to its first excited state is equivalent to a temperature of 5 K, hence the lowest CO rotational levels are easily excited within the confines of a molecular cloud. The excitation of the lower CO rotational states is driven by collisions with molecular hydrogen. The lowest rotational transition, known as the CO(J=1-0) or, more simply, the CO(1-0) line, emits at 115.273 GHz which corresponds to a wavelength of 2.6 mm making it easily visible in the radio window of Earth's atmosphere on clear, dry days. The Arizona Radio Observatory, a part of the University of Arizona's Steward Observatory, operates a 12 meter millimeter wave dish that is suited for studying the 0.6 mm - 4.6 mm radio window of the electromagnetic spectrum and can be used to observe the CO(1-0) line. This is the instrument we used for the observations described in Chapter 4.

The principal problem with observations of the CO(1-0) line is that the transition is optically thick and so a mass determination of the cloud based on CO(1-0) observations should not, in principle, be possible. However, empirical results over the years have shown that there is a relationship between the intensity of the CO(1-0) line and N(H₂) (see, e.g. Solomon et al. 1987). The reasons for this empirical relationship have been attributed to the clouds being in virial equilibrium (Solomon et al. 1987; Scoville et al. 1987), to an empirical size-linewidth relation in the absence of virial equilibrium (Maloney 1990), or turbulent flow effects (Shore et al. 2006). Regardless of the mechanism(s) an empirical factor defined as

¹The website https://en.wikipedia.org/wiki/List_of_interstellar_and_circumstellar_molecules has a list of all known interstellar molecules.

$N(\text{H}_2)/W_{\text{CO}}$, where W_{CO} is the velocity-integrated CO(1-0) main beam temperature, can be defined and seems to be successful in allowing CO(1-0) observations to determine $N(\text{H}_2)$ and hence cloud masses (see review by Bolatto, Wolfire, and Leroy 2013). This factor is sometimes known as the X-factor or X_{CO} and typically has values in the $2\text{-}4 \times 10^{20} \text{ cm}^{-2} [\text{K km s}^{-1}]^{-1}$.

Another molecule, hydroxyl or OH, is also present within molecular clouds and under normal conditions it is the third most abundant molecule after H_2 and CO with abundances in the $10^{-8} - 10^{-6}$ range. The energy level structure in the radio part of the spectrum for OH is much more complicated than the simple rotational ladder for CO. The odd number of electrons means that one is unpaired and its spin $1/2$ angular momentum can couple in several ways with the other angular momenta. Thus, its spin angular momentum, \vec{S} , couples with its orbital angular momentum, \vec{N} , to give $\vec{J} = \vec{N} + \vec{S}$. For rotational quantum numbers ($N = 1, 2, 3, \dots$) we get two rotational ladders with two ground states for each ladder: $J = 1/2$ and $J = 3/2$ with the latter being lower in energy (for OH) so that the rotational ground state for OH is ${}^2\Pi_{J=3/2}$ for $N = 1$. The unpaired electron's spin also couples with the overall angular momentum of the electrons to split each rotational level. This is called lambda doubling. Each lambda-doubled state again doubled by the interaction of the angular momentum of the nucleus with that of the unpaired electron. This hyperfine interaction splits each rotational level into a total of four levels. The OH ground state is thus ${}^2\Pi_{3/2}$, $J = 3/2$, with four hyperfine lines : $F = 2-2, 2-1, 1-2, 1-1$ at 1667, 1720, 1612, and 1665 MHz respectively. They are known collectively as the OH 18 cm lines. Of these, the strongest two under thermal excitation conditions are the so called main lines at 1667 MHz and 1665 MHz corresponding to wavelengths of 17.98 and 18.01 cm, hence visible in Earth's radio window. The Arecibo Observatory located in Puerto Rico is capable of receiving electromagnetic radiation of 3 cm - 1 m wavelengths and can be used to observe the OH hyperfine transitions. This is the instrument we used for the observations in chapter 5.

2.2 INFRARED EMISSION

Interstellar dust absorbs starlight and re-radiates it in infrared. Typical dust temperatures range from 15-40 K and if we consider dust particles as blackbodies, their emission dominates the infrared at $\lambda > 30$ microns. The first all sky survey was by the Infrared Astronomy Satellite (IRAS) (see Neugebauer et al. 1984). It surveyed the sky at 12, 25, 60, and 100 microns detecting widespread emission (see Figure 2.1). But emission at 12 and 25 microns is tricky to interpret because of heavy contamination from the zodiacal dust in the Solar System. Thus, 60 and 100 micron data are generally used to trace the interstellar dust. One of the big initial discoveries from IRAS was the existence of the infrared cirrus (Low et al. 1984), which consists of low level emission from extended structures at high galactic latitudes (see Figure 2.1). These were thought to be diffuse atomic clouds (the CNM) close to the Sun, but because the IRAS satellite primarily an imaging instrument and did not provide velocity information in the 60 and 100 micron bands, Low et al. (1984) could not rule out the Solar System or extragalactic dust as possible sources.

This dilemma was resolved by Weiland et al. (1986) who established that 1) the denser parts of the cirrus are associated with molecular clouds at high Galactic latitudes, thus 2) the infrared cirrus are local structures because high latitude clouds are local. A typical dense cirrus cloud that we study in this thesis is the high-latitude molecular cloud, MBM 53, and Figure 2.2 is an IRAS 100 micron map of the region centered on MBM 53. The *Planck satellite* launched May 2009 was a big step forward in dust studies because it had similar resolution to IRAS but better sensitivity at 9 bands from 30 - 857 GHz (thus, it is more of a submillimeter- and millimeter-wave instrument). The dust emission shows up best at 353 GHz (see Figure 2.3). We can combine IRAS and *Planck* data to create millimeter, submillimeter, and infrared spectra for our region of interest. This will be done in Chapter 7.

2.3 PHOTO DISSOCIATION REGION'S (PDRs)

Most of the mass in the ISM is in the giant molecular clouds and the cold neutral medium. We saw above how starlight affects the dust in these regions, but it also affects the chemistry and structure of the gas. The term photodissociation region (PDR)² is applied to the colder, compact structures in the ISM as they are profoundly affected by starlight, in particular far-ultraviolet radiation that is below the 13.6 eV required to ionize hydrogen and above 6 eV. Any molecular or neutral region illuminated by ultraviolet light is a candidate for study using PDR models. Their study allows for understanding or at least framing many questions: How does molecular gas evolve? How is the chemistry affected or driven by far-UV starlight? How does this affect star formation? And, specifically, to this thesis, does far-UV radiation affect our ability to detect the tracer molecules we use to find low-density molecular gas in the first place?

Astrophysicists sometimes measure depth into clouds by using the amount of visual extinction as one moves into the cloud. The greater the extinction the more opaque the cloud is with $\tau = 1.086 A_V$ (see Carroll and Ostlie, 2016) where τ is the opacity³. It is generally assumed that the gas-dust ratio of the clouds is constant (Spitzer 1978), therefore we can in principle calculate the molecular gas content of a cloud once we know how opaque the cloud is, as measured by A_V . In general, an $A_V \approx 1$ mag corresponds to a hydrogen nucleon column density $\approx 2 \times 10^{21} \text{ cm}^{-2}$ (van Dishoeck and Black 1988) for a standard interstellar radiation field.

Figure 2.4 shows a schematic diagram of a PDR from Wolfire, Hollenbach, and McKee (2010). At the interface of the radiation field with the cloud, molecules are not generally present in any appreciable quantity. However, molecules begin to form as the radiation field is depleted as the dust absorbs the far-UV radiation and H_2 molecules absorb UV photons by dissociating (see below). In general, a PDR begins with a layer of atomic hydrogen,

²PDRs are sometimes known as Photon-Dominated Regions if hot massive stars are nearby.

³Opacity measures the absorptivity of the medium: $I_\nu = I_o e^{-\tau}$, where I is the intensity

an interface where atomic hydrogen cools and is far enough from the ultraviolet radiation sources to start forming molecules, and then a thicker layer of primarily molecular hydrogen.

H_2 forms on dust grains so the more opaque the cloud, the more nucleation sites for molecule formation. In addition, H_2 photodissociates by line rather than continuum radiation so that once the particular photons involved in the photodissociation process are used up, the H_2 column density behind this sacrificial layer can increase markedly. This is known as self-shielding because the sacrificial layer of H_2 shields the molecules behind it.

A simplified model of a PDR can be thought of as a series of regions where different atoms and molecules become prevalent. In the outermost region H is in the form of neutral hydrogen and C is in the form of C^+ . Then comes a region where H_2 formation begins but C remains the form of C^+ . Then, molecules such as OH and CH begin forming and C transitions from C^+ to C^0 . The next region has the C transitioning primarily to CO. In the 1980's and 90s, the "molecular cloud" was thought to begin here. At this point the PDR region ends but the molecular cloud continues to denser, more opaque regions where complex molecules and star formation can be found.

Molecules such as CO and OH dominate different regions depending on where they form and/or dissociate as a function of distance into the PDR further from the ionizing radiation. The locations of these interfaces as a function of A_V change as the radiation field intensity changes. The more radiation a PDR is exposed to, the more opaque has to be the region at which these molecules form. The gas density also plays a role with increasing density having the opposite effect compared to increasing radiation.

Of primary interest for us in this thesis is the detection of molecules within these last two regions, specifically where OH and then CO dominate. Recall that molecular hydrogen is virtually undetectable from the ground and so the principal question in this thesis is, are there places within molecular clouds where significant H_2 is present but OH and/or CO detections in emission are not possible? Is it possible to see all or even most of the molecular gas in a diffuse cloud in the presence of a typical interstellar ultraviolet-field? At what A_V

are the clouds so affected by typical interstellar radiation fields so that the molecules we use to detect molecular gas are no longer present in sufficient column density for us to detect in emission? PDR models predict that there are such places where molecular hydrogen is present but OH and CO are not present in sufficient quantities so as to be detectable by ground-based radio observations (Hollenbach and Tielens (1997) and references therein). The real question is, how much of the molecular inventory is detectable in emission by OH and CO observations and how much is not.

2.4 DARK MOLECULAR GAS

The term “dark gas” was introduced into the literature when Grenier, Casandijan and Terrier (2005), hereafter GCT, published their study of gamma ray and infrared emission from gas emitted by matter in the Milky Way. GCT inventoried the gamma ray emission from various sources in the sky: atomic hydrogen, molecular hydrogen, compact objects, dust, inverse Compton scattering, and an extragalactic background likely due to quasars and active galaxies.

Inverse Compton scattering produces gamma rays by having cosmic rays boost the energy of photons from the interstellar radiation field or the Cosmic Microwave Background (CMB). When cosmic rays interact with the low energy electromagnetic radiation in the galaxy, such as the CMB, starlight, or infrared emission from dust, the cosmic rays impart some of their momentum to the otherwise low energy electromagnetic radiation. The massive cosmic ray particles are slowed down and, as a result of the lost energy, the emitted photons from the interactions are now gamma ray photons. The interaction that produces gamma rays from hydrogen nucleons also involves cosmic ray interactions. The collisions between the two particles produce a cascade of elementary particles including neutral pions which decay into gamma rays. Once point sources, both Galactic and extragalactic, are removed and once the inverse Compton contribution is also removed, the resulting gamma-ray map is a linear combination of the ionized, atomic and molecular hydrogen distribution in the Galaxy.

GCT removed the various gamma ray backgrounds and linearly correlated the atomic and molecular gas content of the Milky Way with the remaining gamma ray emission. After removing the contribution from atomic hydrogen (using HI maps) and molecular hydrogen (using CO maps and an X-factor), there was a substantial residual of gamma-ray emission. When GCT checked this gamma ray emission against the maps of dust and gas for the Galaxy they found that it correlated with cold dust typically found in molecular clouds but unaccounted for by the CO maps. GCT attributed this residual to a molecular component (because it was cold) that was not traced by the CO(1-0) emission maps.

Grenier and her colleagues named this new gap in the molecular gas inventory “dark gas”, as in gas that could not be seen spectroscopically. The name is somewhat unfortunate in that it is similar to dark matter, although the two are clearly completely different things. Dark gas is basically molecular hydrogen whereas dark matter is an exotic particle without electromagnetic interaction. Perhaps more confusing, we have referred previously to dark clouds in the sense of dense dust clouds that are opaque in the visual part of the spectrum. These objects have very strong CO(1-0) lines and were among the first objects detected when detectors for the CO(1-0) line were built. In contrast, dark gas is difficult or impossible to detect with the CO(1-0) line. In this thesis, we will distinguish between dark gas and dark clouds in the sense that the latter will only refer to opaque, dense, dust clouds with $A_V > 5$ mag and strong CO(1-0) emission.

As it happens radio astronomers had already seen traces of what GCT call dark gas spectroscopically in other tracers besides CO (see Chapter 3), but there will always be some region that contains H_2 but cannot be detected in CO (see PDR discussion). However, the literature has evolved since 2005 and the term dark gas has morphed to mean molecular gas that is untraceable by conventional CO mapping and thus researchers began discussing CO-rich and CO-poor gas with the latter representing the dark gas. Dark gas regions have been added to the PDR models and a number of studies have been done to find just how far out dark gas regions extend, how much molecular gas is contained in them, and what are the

best ways to detect this gas mass (e.g. Wolfire, Hollenbach, and McKee. 2010). We discuss the literature associated with dark gas in Chapter 3. The goal of this thesis to determine whether we could shed some CO and OH light on this dark gas to find out how dark these gaps in the molecular gas inventory of the Galaxy are.

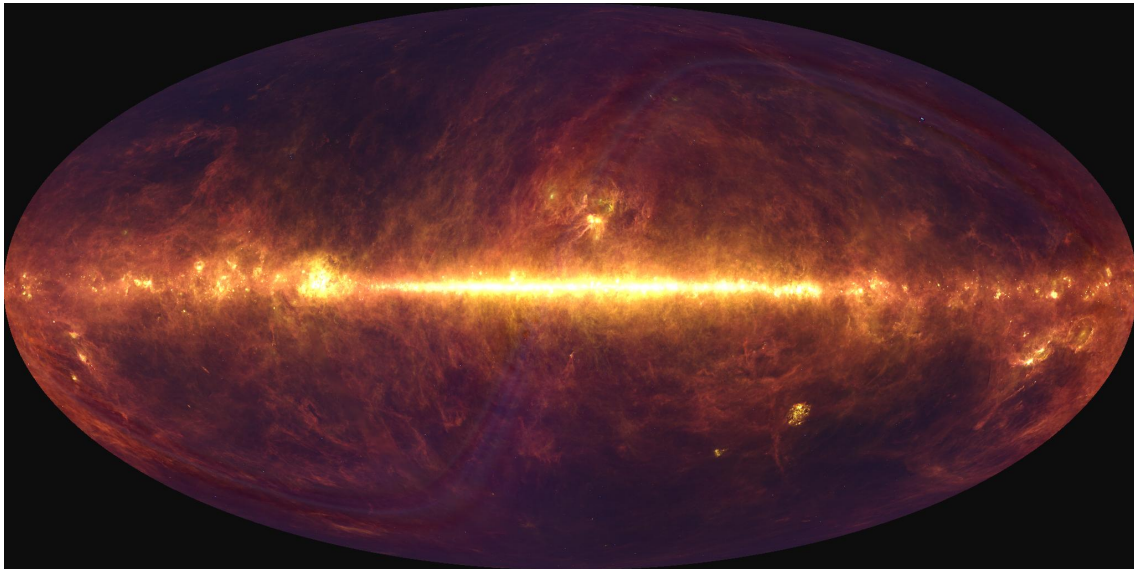


Figure 2.1 Three-color IRIS (recalibrated infrared data from the Infrared Astronomy Satellite) composite map of the infrared sky at 25 (blue), 60 (green), and 100 (red) microns. The high-latitude cirrus are the easily noticeable low-brightness wisps above and below the bright Galactic plane. Image credit: NASA via the Legacy Archive for Microwave Background Data Analysis (LAMBDA).

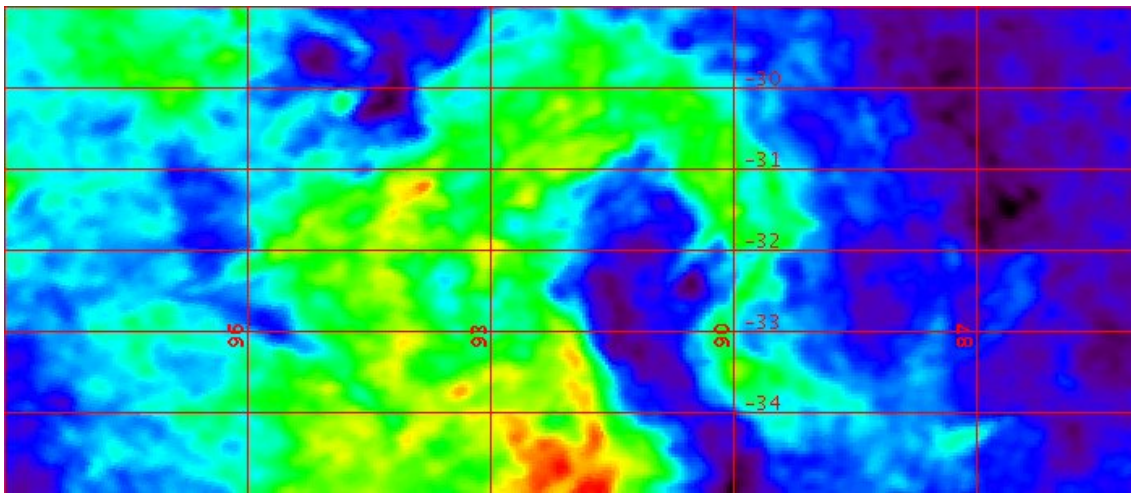


Figure 2.2 Dust map in Galactic coordinates of a $14^\circ \times 6^\circ$ centered on MBM 53. The quantity on a logarithmic color scale ranging from 0.03 to 0.45 magnitudes is $E(B-V)$, a measure of the dust column density, from the Schlegel, Finkbeiner, and Davis (1999) database. The bright structure at the bottom of the figure is MBM 54. The image was made with the Skyview Virtual Observatory.

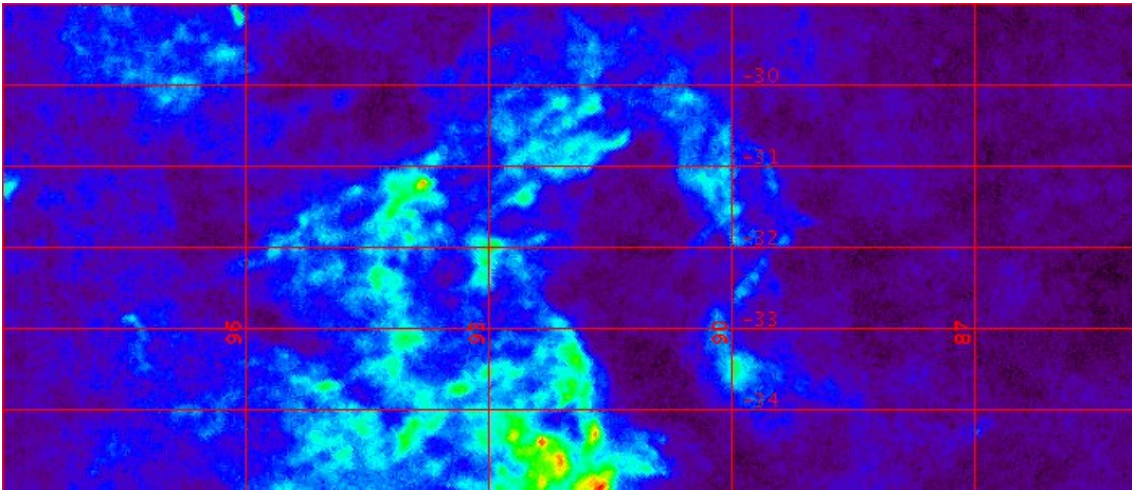


Figure 2.3 Same region as in Figure 2.2, but using the *Planck* 353 GHz channel which traces primarily thermal dust emission. The scale is linear and ranges from 3.17×10^{-4} to 6.44×10^{-3} K. The image was made with the Skyview Virtual Observatory.

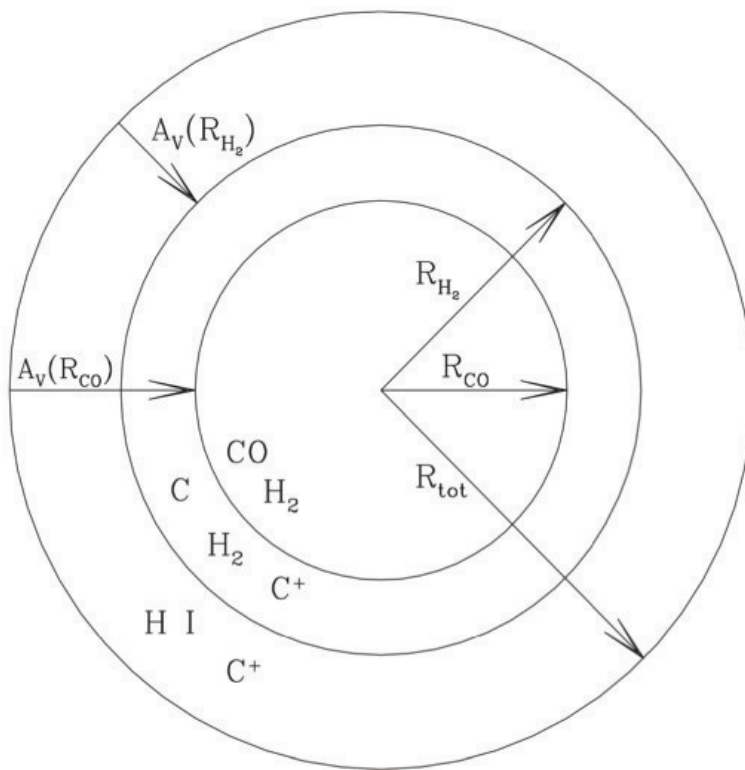


Figure 2.4 Basic model of a photodissociation region (PDR) taken from Wolfire, Hollenbach, and McKee (2010). The model shows how the carbon transitions from C⁺ to C to CO as one moves from the outer to the inner regions of a PDR. The inner two regions can be considered as the molecular cloud. Reproduced by permission of the AAS.

CHAPTER 3

REVIEW OF THE LITERATURE ON DARK GAS

3.1 TRACING DIFFUSE MOLECULAR GAS

Historically, molecular surveys of the Galaxy in CO(1-0) have traced GMCs and dark clouds. The most complete spectral survey is by Dame, Hartmann, and Thaddeus (2001) and is still ongoing under the direction of Dr. Tom Dame at the Harvard-Smithsonian Center for Astrophysics. Prior to 1983 diffuse molecular lines of sight were studied almost exclusively by optical absorption techniques (see discussion in Chapter 1). In 1983, Loris Magnani, Leo Blitz, and Lee Mundy searched for molecular gas at high Galactic latitudes and catalogued 57 clouds at $|b| \geq 30^\circ$ (Magnani, Blitz, and Mundy (1985)). Nearly all of the clouds were diffuse or translucent. Figure 3.1 shows the histogram of the so-called MBM clouds as a function of extinction. The MBM high latitude cloud catalog was, at the time, the largest compendium of diffuse and translucent clouds. Since then, the study of low-extinction clouds and cloud edges has become more prevalent especially with the advent of high-sensitivity, high resolution space missions like FUSE, Herschel, Spitzer, Planck and WISE (see Magnani and Shore 2017).

This thesis focuses on the detection of molecular gas using molecular radio spectroscopy at the lowest extinctions for which lines can be seen in emission. The work of Grenier, Casandjian, and Terrier (2005) spurred new interest in molecular gas in low extinction regions but there is a rich history of such studies before 2005. In this chapter we review the theoretical and observational contributions to this topic.

3.2 CO IN DIFFUSE CLOUDS

CO(1-0) detections of diffuse clouds were made as early as 1976 by Knapp and Jura, who observed lines of sight previously studied by optical absorption lines. A similar study was made by Dickman et al. (1983) but there was relatively little interest in studying these objects using the CO(1-0) line because most of the observations of this line were reserved for GMCs and star-forming regions. The discovery of the high-latitude molecular clouds by Blitz, Magnani, and Mundy (1984), Magnani, Blitz, and Mundy (1985), and Keto and Myers (1986) renewed some interest in studying low extinction molecular regions, but, at the time, it was not clear exactly what type of object the high-latitude clouds were. Magnani and Blitz referred to them during that period as dense diffuse clouds (Magnani, private communication), as it was not clear that these objects were diffuse molecular clouds given the relatively strong CO(1-0) emission.

In an important work, van Dishoeck and Black (1988) studied the production and destruction of CO in PDRs. For a standard interstellar radiation field (e.g., Draine 1978), van Dishoeck and Black show a rapid rise in both $N(\text{CO})$ and the CO/H_2 ratio at $N(\text{H}_2) \approx 1 \times 10^{21} \text{cm}^{-2}$, equivalent to $E(\text{B-V}) \approx 0.3$ mag or $A_V \approx 1$ mag. In this regime from $A_V \approx 1$ mag to 5 mag the CO/H_2 abundance rises from $< 10^{-6}$ to $\sim 10^{-4}$. Although the exact extinction range over which this transition takes place depends on the interstellar radiation field and gas density, van Dishoeck and Black realized that in this transition regime the molecular clouds were neither diffuse nor dark, and thus they coined a new term: translucent molecular clouds. In addition to extinction, there is also an astrochemistry difference between these regions. Diffuse cloud chemistry proceeds primarily by photoprocesses, dark molecular clouds by collisional processes, and in translucent clouds both are important. With this terminology, a new paradigm developed. Dark molecular clouds had $A_V > 5$ mag, were gravitationally bound, and were the sites of low mass star formation. Diffuse clouds had $A_V < 1$ and were best studied by optical and UV techniques, and, in between were translucent clouds with high latitude molecular clouds being this type of object.

The paradigm changed again based primarily on the work by Dr. Harvey Liszt. Liszt, Pety and Lucas (2010) attributed significant CO luminosity to the diffuse and partially molecular ISM, in particular, when C^+ is the dominant form of gas-phase carbon. They observed Galactic lines of sight in HI, HCO^+ and CO where the latter was present with column densities below $2 \times 10^{16} \text{ cm}^{-2}$. The conclusion from their work was that the CO(1-0) emission from diffuse molecular clouds was similar in intensity to that of the dark clouds. So similar that they suggested that there was a possibility that much of the CO(1-0) emission from the traditional CO survey actually arose from diffuse clouds, thus changing the traditional interpretation of what CO(1-0) mapping of the Galaxy indicated. In their words, a CO(1-0) map reveals more about the CO chemistry and abundance rather than the molecular mass. These results suggested that even in the diffuse regions where dark gas is expected to be dominant there may be ways of observing the gas using sensitive measurements in CO.

3.3 OBSERVATIONS OF OH AND CH IN LOW EXTINCTION REGIONS

Although the CO(1-0) line was the workhorse tracer of H_2 throughout the 1980's and 1990's, there are indications that other molecules like OH and CH might be able to trace H_2 when CO(1-0) emission is not easily detectable. Wannier et al. (1993) used the OH lines at 18 cm to survey the outer regions of several Lynds dark clouds and determined that the 1665 and 1667 MHz main lines could be detected further out in the cloud envelope than the CO(1-0) line. These results were confirmed by Cotten et al. (2012) and Barriault et al. (2010a, 2010b). Earlier OH studies at 18 cm in diffuse molecular regions include the surveys by Dickey, Crovisier, and Kazés (1981) and Liszt and Lucas (1986) although these were absorption line studies toward extragalactic continuum sources. Magnani and Siskind (1990) conducted a survey of high-latitude clouds at Arecibo detecting the 1665 and 1667 MHz emission lines along many diffuse sightlines.

Even before the OH observations by Magnani and Siskind and Wannier et al., Lars E.B. Johansson (1979) had made a survey of the CH 3335 MHz line along the Galactic plane. The

CH 3335 MHz line is the main line hyperfine transition similar to the OH hyperfine lines (see Section 2.1). However, for CH, the other rotational ladder ($J=1/2$) has the ground state and so the hyperfine structure involves $F=1,1$, $F=1,0$, and $F=0,1$ transitions with the $F=0,0$ transition forbidden. Thus there is only one main line (3335 MHz) instead of two as in the case of OH (1665 and 1667 MHz). Johansson's survey, when compared to the available CO surveys, showed much more CH (and, thus, H_2) beyond the molecular ring at 5-6 kpc than indicated by CO. The CH distribution was in between that of CO and HI, possibly indicating that the CO surveys were not picking up low-level molecular emission. This contention was supported by Magnani and Onello (1993) who studied a high latitude cloud, MBM 16, using the CH 3335 MHz line. In their study they found broad wings in three of their CH spectra. These broad CH wings were not seen in CO and thus revealed diffuse molecular gas that was untraced in the CO(1-0) line along those lines of sight. The idea that CH might trace low-density molecular gas that is not seen in emission in other molecular tracers has been attributed to the peculiar excitation of the $^2\Pi_{1/2}$ ($J=1/2$) ground state (Bertojo, Chung, and Townes, 1976) which may overpopulate the upper lambda-doubled state of the transition and thus make the 3335 MHz line a weak maser. Despite these interesting properties, CH 3335 MHz observations of the ISM are relatively rare. The reason this transition has not been studied as extensively as those of CO and OH has to do with the dearth of upper S-band receivers at radio observatories. Other notable studies of CH in low extinction regions include observations of the 3335 MHz line by Federman and Wilson (1982), Sandell, Stevens, and Heiles (1987), and Magnani et al. (1989).

3.4 MBM 53

GCT studied regions mostly along the Galactic plane. However, one of their regions, named Pegasus, was at high latitudes ranging from $[50^\circ \text{ to } 140^\circ]$ - $[-60^\circ \text{ to } -26^\circ]$ in Galactic longitude and latitude. Contained within the region were several high latitude molecular clouds, including MBM 53-55 the largest such complex in the Southern Galactic Hemisphere.

Yamamoto et al. (2003) mapped the MBM 53-55 cloud complex in CO(1-0) to an rms of 0.4 K. GCT assumed that this was the extent of the known molecular mass in the Pegasus region but the Southern Galactic Hemisphere High-Latitude CO(1-0) survey by Magnani et al. (2000) reveals the existence of more molecular clouds in this region (see discussion in Chapter 6). Although the Magnani et al. (2000) survey is more sensitive than the Yamamoto et al. (2003) survey (rms ≈ 0.1 K vs 0.4K), it is very poorly sampled so it also provides an incomplete molecular picture. GCT used the Yamamoto results to calculate the molecular mass in the Pegasus region leading to their conclusions that dark molecular gas was a significant component of the ISM. Given the Magnani et al. (2000), Yamamoto et al. (2003), and GCT estimates for the mass in the region makes MBM 53-55 prime targets to test the efficacy of CO and OH as tracers of the molecular mass in the diffuse regions and thus determine how much, if any, of the gas is dark gas.

3.5 AFTER 2005

After the original GCT paper, little work was done on dark gas for several years. Interest picked up in 2010 when Wolfire, Hollenbach, and McKee (2010) theoretically modeled PDRs using basic astrochemical networks and varying interstellar radiation fields and cloud densities. Their work was designed specifically to address dark molecular gas and showed that the outermost layers of PDRs contain more OH than CO and that the dark molecular gas fraction should be about 30% of the overall molecular inventory. Observations of OH in diffuse and translucent clouds came soon afterwards and a number of observers began searching for dark gas using OH. Barriault et al. (2010a) confirmed OH traced dark gas when they observed a correlation between infrared intensity and the OH column density in two diffuse clouds. Cotten et al. (2012) confirmed OH as a good tracer of dark gas in a diffuse high latitude cloud. In GMCs, one of the first proponents of OH as a surrogate tracer for CO were Allen et al. (2012) who found, along the Galactic plane, weak, widespread, OH similar in extent to the HI emission where less than 10 percent of the OH emission had a

CO counterpart. Allen et al (2015), Xu et al. (2016) and Nguyen et al. (2018), published results agreeing with these findings by again finding OH emission in molecular gas without corresponding CO emission. Similarly Tang et al. (2017) used OH 18 cm observations to find dark gas in regions where $0.05 < A_V < 2$ mag as did Li et al. (2018) when $A_V > 2.3$ mag.

In addition to OH, the presence of dark gas in the ISM has been confirmed by Planck studies (e.g. Planck Collaboration 2011b) and CH 3335 MHz observation are promising for detecting diffuse molecular gas (Xu et al. 2018). Finally, an ion, C^+ , associated with the outermost molecular part of PDRs (see Figure 2.4) has also been used to identify dark gas (Langer et al. 2010, 2014). With these indications that at least some dark gas can be spectroscopically detectable, we began our study of this subject. Our first effort was to make sensitive CO(1-0) observations in order to evaluate whether deeper than usual CO observations can reveal at least some of the dark gas component.

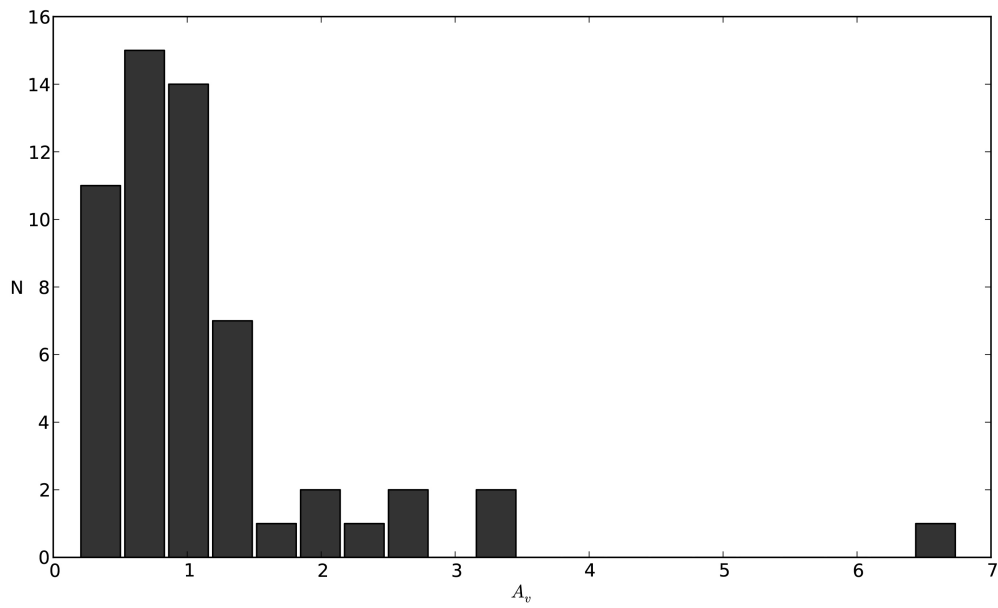


Figure 3.1 Histogram of the MBM clouds as a function of visual extinction in magnitudes. The extinction is for the most opaque 6 region in the cloud based on the Schlegel, Finkbeiner, and Davis (1999) database.

CHAPTER 4

SENSITIVE CO(1-0) SURVEY IN PEGASUS-PISCES REDUCES CO-DARK GAS
INVENTORY BY FACTOR OF TWO¹

by Emmanuel Donate² and Loris Magnani³

4.1 ABSTRACT

We conducted high-sensitivity, high-velocity resolution CO(1-0) observations in a region containing a portion of the diffuse molecular cloud MBM 53 to determine whether weak CO emission was present. The results of our observations increase the amount of CO-detectable molecular gas in the region by a factor of two. The increased molecular mass for the cloud, if applicable to the molecular clouds in the entire Pegasus-Pisces region, decreases the dark molecular gas content from 58% of the total H₂ mass to $\sim 30\%$. If the results for MBM53 are applicable to other diffuse clouds, then the fraction of dark gas directly detectable via sensitive CO(1-0) observations in diffuse molecular clouds is similar to that predicted by models for Giant Molecular Clouds.

4.2 INTRODUCTION

The idea that substantial molecular gas is present in the interstellar medium (ISM) but is not detectable by the CO(1-0) emission line has become fairly prevalent in the last decade. This component has become known as “dark gas”, a term first suggested in a paper describing

¹Published in Monthly Notices of the Royal Astronomical Society, **472**, 3169 (2017)

²Department of Physics and Astronomy, University of Georgia, Athens, GA 30602, USA

³Department of Physics and Astronomy, University of Georgia, Athens, GA 30602, USA

its properties and extent by Grenier, Casandjian and Terrier (2005; hereafter GCT)⁴. GCT used a combination of gamma-ray and infrared data to identify regions with cold dust. By comparing these with maps of CO and HI emission, they found that a significant fraction of the H₂ mass is not traced by the CO(1-0) observations. Their main conclusion is that the dark gas mass in the Milky Way is comparable to the molecular mass detected by CO(1-0) emission. More recent studies corroborate this (Abdo et al. 2010; Planck Collaboration, 2011b).

This phenomenon is predicted by models of photo-dissociation regions (PDRs) (e.g., Hollenbach & Tielens 1997). The depths into a PDR at which H₂ and CO form depend directly on the intensity of the interstellar radiation field and the volume density of hydrogen nucleons. It is convenient from the observational point of view to talk about depth into a PDR in terms of extinction or color excess. Liszt (2014) ascribes a break in slope in the N(HI) - E(B-V) relation at E(B-V) \sim 0.1 mag to the onset of H₂ formation. For a standard interstellar radiation field (e.g., Draine 1978), the models of van Dishoeck & Black (1988) show a significant rise in both N(CO) and the CO/H₂ ratio at N(H₂) \sim 1 x 10²¹ cm⁻², equivalent to E(B-V) \approx 0.3 mag or A_V \approx 1 mag. Thus, under normal conditions, CO-dark gas should be found in regions with 0.1 \lesssim E(B-V) \lesssim 0.3 mag.

van Dishoeck & Black defined *diffuse* molecular clouds as those with A_V \leq 1 mag. Before the development of sensitive millimeter-wave receivers, observations of diffuse molecular clouds were confined to optical and UV absorption lines. However, under certain conditions, CO(1-0) emission can trace diffuse molecular gas fairly easily (e.g., Liszt, Pety, and Lucas 2010), complicating the picture described above. But even by the late 1980s, CO(1-0) detections in regions with A_V < 1 mag were possible. For instance, many of the high-latitude clouds identified by Magnani, Blitz, and Mundy (1985) have A_V < 1 mag and yet are readily detectable by CO(1-0) emission. More recently, Chastain et al. (2006), Liszt and Pety (2012), and Cotten and Magnani (2013) detected CO(1-0) lines from regions with E(B-V) as low as

⁴Some of the dark gas may be in atomic form and not readily detectable by the 21 cm line because of opacity effects. In this paper we will focus on the *molecular* dark gas.

0.1 mag. Clearly, under certain conditions to be explained, CO(1-0) emission can trace gas in the dark molecular regime.

One of the fields studied by GCT includes 1888 square degrees centered on Pegasus-Pisces for which they obtain the ratios of CO-detectable molecular gas, to CO-dark gas, to atomic gas. We will abbreviate these ratios as H₂:DG:HI. The CO-detectable molecular gas was determined from estimates of the masses of some of the mapped high-latitude clouds in the region, and GCT derive H₂:DG:HI to be 0.7: 1.0: 3.4, with a total mass of $1.6 \times 10^4 M_{\odot}$. However, of the many molecular clouds in the region, GCT only included the MBM 53-55 complex and its environs as mapped by Yamamoto et al. (2003 - hereafter Y2003; 2006). Blair et al. (2017)⁵ examine the Magnani et al. (2000) high-latitude CO(1-0) survey and, by including all known molecular clouds in the region, revise the H₂:DG:HI ratios to 0.9: 1.0: 3.8. Even with this revision, the CO-dark gas fraction is still significant. But are the dark gas regions described by GCT really undetectable in CO(1-0)? A key factor is the sensitivity of the CO(1-0) observations. While the total mass in hydrogen nucleons for Pegasus-Pisces derived by GCT may be correct, the breakdown into H₂:DG:HI depends on the sensitivity of the CO observations of the molecular clouds in the region. If more sensitive observations of these clouds were available, the CO-detectable molecular mass might increase at the expense of the CO-dark gas fraction.

In this paper we examine whether sensitive CO(1-0) observations can reveal the presence of at least some of the dark gas in a high-latitude region containing a portion of a diffuse molecular cloud (MBM 53). In section 2, we discuss the Magnani et al. (2000) Southern Galactic Hemisphere high-latitude CO(1-0) survey (SGH-HL) and the region in Pegasus-Pisces that overlaps one of the GCT fields. We describe the observational set-up in section 3 and, in section 4, we compare our results with those from GCT. We then estimate the fraction of dark gas detectable by very sensitive CO(1-0) observations. A discussion and summary is presented in section 5.

⁵This paper was never published, but the work was completed by me and now forms Chapter 6 of this thesis.

4.3 THE SGH HIGH-LATITUDE SURVEY IN PEGASUS-PISCES

GCT derived their quantitative conclusions on the dark gas by examining seven nearby areas, one of which substantially overlaps a portion of the SGH-HL survey (see Figure 1). The area called Pegasus by GCT and Pegasus-Pisces in this paper is bounded by the black box. Of the 4982 grid points observed in the SGH by Magnani et al. (2000), 2080 points are located within the region that overlaps 84% of the GCT Pegasus field⁶. In that region, Magnani et al. (2000) recorded 48 CO detections with an rms in T_{mb} of 0.1 K for a detection rate of 0.023.

GCT quote values for the molecular mass in the Pegasus-Pisces region in CO-detectable H_2 and CO-dark H_2 of 2200 M_\odot and 3100 M_\odot , respectively. Their estimate of the CO-detectable H_2 in the region comes solely from the MBM 53-55 cloud complex as mapped by Y2003. We presume that the difference in the molecular mass estimate of the complex between GCT and the Y2003 value is due to GCT using a value of X_{CO} ⁷ = $1.74 \times 10^{20} \text{ cm}^{-2} [\text{K km s}^{-1}]^{-1}$ rather than the value of $1.0 \times 10^{20} \text{ cm}^{-2} [\text{K km s}^{-1}]^{-1}$ used by Y2003. Despite the presence of other clouds in the region (see Blair et al. 2017), we assume, for the moment, that the total mass in hydrogen nucleons detected by GCT is accurate, hence any increase in the CO-detected gas in the MBM 53-55 clouds must come at the expense of the dark gas mass.

As mentioned above, the key factor in determining the amount of CO-detected gas is the sensitivity of the CO(1-0) observations. More sensitive (lower rms) CO observations should yield new detections of molecular gas at cloud edges. For example, the high-latitude cloud MBM 40 was sampled over 103 lines of sight in the CO(1-0) line at sensitivities of 0.05 - 0.11 K (1σ rms in T_R^* , or 0.06 - 0.13 K in T_{mb}) by Cotten & Magnani (2013). Sampling was over the whole cloud, including the outermost parts of the cloud with $E(B-V) \lesssim 0.12$ mag. There,

⁶The GCT Pegasus region extends over $-60^\circ \leq b \leq -26^\circ$, but the SGH-HL CO survey begins at $b = -30^\circ$.

⁷ X_{CO} is the empirically derived conversion factor between $N(H_2)$ and the velocity-integrated CO(1-0) main beam antenna temperature.

weak CO emission was present in 13 out of 21 lines of sight. The antenna temperature, T_R^* , ranged from 0.11 - 2.29 K for the 13 detections with 7 of those ranging from 0.11 - 0.61 K. Many of these latter detections would have been missed by conventional mapping which typically has rms antenna temperature of a few tenths of a K. By including the molecular mass detected by the sensitive CO observations of the outermost region of MBM 40, the cloud mass estimate increased from 20 M_\odot (Chastain 2007) to 32 M_\odot .

To determine how much molecular gas could be detected by a more sensitive CO survey at high Galactic latitude, we re-observed a small region of the SGH-HL survey in Pegasus-Pisces. The SGH-HL survey has 2080 observed lines of sight within the black box in Figure 1 with $T_{mb} \approx 0.1$ K for the 1σ rms value. Since our goal was to improve this by at least a factor of 4-5, we had to choose a significantly smaller region to sample. We wanted an area containing at least a portion of a known molecular cloud (because GCT emphasized that dark gas regions “...surround all the nearby CO clouds and bridge the dense cores to broader atomic clouds...”). Moreover, the only cloud complex recognized by GCT in the Pegasus-Pisces region in Figure 1 is MBM 53-55, thus, by choosing a region containing at least part of this complex, we can directly compare how our mass estimates for a portion of this complex change with more sensitive observations. We settled on the region bounded by $80.3^\circ \leq \ell \leq 99.0^\circ$; $-34^\circ \leq b \leq -30.0^\circ$. This area includes five detections of MBM 53 from the SGH-HL survey. The location of the 88 points we observed is shown in Figure 2. The five CO(1-0) detections from the SGH-HL survey arising from the diffuse high-latitude cloud MBM 53 are noted in the figure.

4.4 OBSERVATIONS

The CO(1-0) observations were made at the 12 m mm-wave telescope of the Arizona Radio Observatory on Kitt Peak. We used the 3 mm ALMA Type Band 3 dual-polarization receiver with system temperatures on the sky typically less than 200 K (single sideband). The antenna temperature scale, T_A^* (see Kutner and Ulich 1981), is set by the chopper wheel

method and is given at the telescope as T_R^* , the antenna temperature corrected for spillover and scattering. Conversion to the main beam brightness temperature, T_{mb} is via T_R^*/η_{mb} , where η_{mb} is the main beam efficiency (at 115 GHz, $\eta_{mb} \approx 0.85$). We assume that the source fills the beam so that the beam filling factor is unity. The backend spectrometers were the Millimeter Autocorrelator (MAC) and the 250 kHz filter banks. The MAC was configured to have 200 MHz total bandwidth (150 MHz of usable bandwidth) over 6144 channels for a frequency resolution of 24.4 kHz per channel equivalent to 0.063 km s^{-1} . The 250 kHz filter banks were used as a backup for the MAC and have a velocity resolution per channel of 0.65 km s^{-1} . A fiducial position ($\ell = 92.4^\circ; b = -34.0^\circ$) with a strong CO line was monitored each day and a Gaussian fit to the line showed variations in peak T_R^* of less than 5% in clear weather.

The observations were made in on-off mode with an absolute off-position with the lowest reddening in the region [$E(B-V) = 0.03 \text{ mag}$ at (R.A., Dec) = ($22^h 37^m 37.6^s; 23^\circ 35' 20.2''$)] as given by the Schlegel, Finkbeiner, and Davis (1999) dust maps. At 115 GHz, the beam size of the 12-m telescope is $55''$. The SGH-HL survey was sampled every degree in Galactic longitude and latitude at a resolution of $8.4'$ for an under sampling of a factor of ~ 60 . A meaningful comparison between the CO observations from the two telescopes requires that we “map” the $8.4'$ beam with our ARO 12-m telescope observations. We thus sampled each of the 88 points in Figure 2 using the thirteen-point pattern shown in Figure 3. Although the areal ratio is approximately 0.155, the thirteen point sampling pattern was the best compromise between covering the $8.4'$ beam from the SGH-HL survey and achieving the factor of 5 improvement in sensitivity we desired. There could be even more CO emission in the region if isolated, small-scale structures exist in the periphery of the cloud. This issue will be addressed in a separate paper.

A comparison of the integrated antenna temperature for the five detected positions from SGH-HL with our thirteen-point pattern averaged to form a single spectrum for each position shows very good agreement (see Table 1 and discussion in §3.1). With two minutes on source

Table 4.1 W_{CO} for the five positions in common between the SGH-HL and the current survey.

Position	ℓ	b	W_{CO}^a (SGH-HL)	W_{CO}^a (this paper)
	deg	deg	K km s ⁻¹	K km s ⁻¹
G92.4–34	92.4	–34.0	4.09±0.39	4.41±0.19
G93.5–32	93.5	–32.0	0.57±0.39	0.50±0.06
G94.6–34	94.6	–34.0	1.44±0.40	1.49±0.24
G96.8–30	96.8	–30.0	0.46±0.50	0.86±0.10
G99.0–31	99.0	–31.0	1.00±0.39	1.27±0.18
Total	—	—	7.56±0.93	8.53±0.37

^a W_{CO} is defined as $\int T_{mb} dv$

and two minutes off, each summed spectrum consisted of 26 minutes on-source resulting in rms values per channel for the MAC of 11 - 45 mK.

The results of our observations are shown in Table 2. Fifteen new detections were made for a total of 20 out of 88 observed lines of sight detectable in the CO(1-0) line. Figure 2 shows the distribution of the new and previously known detections. Representative spectra of some of the new detections are shown in Figure 4*a-c*.

4.4.1 COMPARISON WITH EARLIER RESULTS

Five of the ARO detections had been previously detected with the Harvard-Smithsonian Center for Astrophysics 1.2 m telescope (Magnani et al. 2000). As can be seen from Table 1, the agreement between the two sets of observations is quite good. The SGH-HL observations were about a factor of five less sensitive in T_{mb} while the difference in W_{CO} 1σ uncertainties improves for the ARO observations by factors of about 2 to 6. For the ARO data, W_{CO} is calculated from the parameters of the Gaussian fit as $1.07[T_{mb}\Delta v(\text{FWHM})]$. The total W_{CO} for the five SGH-HL detections is 7.56 ± 0.93 K km s⁻¹ and, for the ARO observations, 8.53 ± 0.37 K km s⁻¹, so that estimates of the mass based on these results would be consistent.

Table 4.2 Gaussian-fit parameters and W_{CO} for CO(1-0) detections in our survey.

Position	ℓ deg	b deg	T_R^* K	Δv km s ⁻¹	v_{LSR} km s ⁻¹	W_{CO}^a K km s ⁻¹	Notes
G92.4-30	92.4	-30.0	0.14±0.04	1.85	-9.99	0.33±0.13	redshifted and blueshifted wings on profile ^c
G93.5-30	93.5	-30.0	0.36±0.04	2.12	-10.09	0.96±0.15	
G96.8-30	96.8	-30.0	0.62±0.05	1.10	-14.90	0.86±0.10	
			0.35±0.09 ^b	1.25	-14.66	0.46±0.50	Magnani et al. (2000)
G92.4-31	92.4	-31.0	0.25±0.03	1.11	-5.44	0.35±0.06	first component ^d
			0.14±0.03	0.73	-8.32	0.13±0.04	second component
G93.5-31	93.5	-31.0	0.65±0.05	0.92	-3.15	0.75±0.08	first component
			0.43±0.05	0.95	-4.72	0.51±0.08	second component
G97.9-31	97.9	-31.0	0.097±0.033	0.88	-11.61	0.11±0.05	
G99.0-31	99.0	-31.0	0.49±0.05	2.06	-8.18	1.27±0.18	blueshifted wing on profile
			0.27±0.07 ^b	3.41	-8.47	1.00±0.39	Magnani et al. (2000)
G92.4-32	92.4	-32.0	0.23±0.03	1.01	-2.33	0.29±0.05	first component - redshifted wing on profile
			0.11±0.03	0.91	-7.86	0.13±0.05	second component
G93.5-32	93.5	-32.0	0.43±0.03	0.63	-4.67	0.34±0.03	first component
			0.14±0.03	0.89	-3.95	0.16±0.05	second component
			0.37±0.07 ^b	1.46	-4.60	0.57±0.39	Magnani et al. (2000)
G94.6-32	94.6	-32.0	0.48±0.03	0.71	-2.91	0.43±0.04	
G95.7-32	95.7	-32.0	0.32±0.03	2.86	-6.40	1.15±0.15	
G99.0-32	99.0	-32.0	0.31±0.03	1.13	-6.71	0.44±0.06	
G90.2-33	90.2	-33.0	0.38±0.03	0.60	-0.56	0.28±0.03	
G92.4-33	92.4	-33.0	0.076±0.028	2.05	-5.22	0.20±0.10	first component
			0.077±0.028	1.20	-8.63	0.12±0.06	second component
G97.9-33	97.9	-33.0	0.31±0.04	0.98	-1.62	0.38±0.07	first component
			0.10±0.04	1.36	-3.58	0.17±0.09	second component
G92.4-34	92.4	-34.0	1.52±0.05	2.01	-7.48	3.85±0.18	first component
			0.54±0.05	0.83	-7.27	0.56±0.07	second component
			1.34±0.07 ^b	2.84	-7.47	4.09±0.39	Magnani et al. (2000)
G93.5-34	93.5	-34.0	0.61±0.03	1.46	-4.21	1.12±0.08	blueshifted wing centered at ~ -7 km s ⁻¹
G94.6-34	94.6	-34.0	0.51±0.06	1.81	-6.06	1.17±0.19	first component
			0.20±0.06	1.27	-2.92	0.32±0.14	second component
			0.49±0.07 ^b	2.77	-6.13	1.44±0.40	Magnani et al. (2000)
G95.7-34	95.7	-34.0	0.31±0.04	0.69	-4.89	0.27±0.05	
G96.8-34	96.8	-34.0	0.37±0.04	2.88	-12.58	1.34±0.21	first component
			0.21±0.04	1.66	-7.07	0.44±0.12	second component
							redshifted wing centered at ~ -4.5 km s ⁻¹

^a W_{CO} is defined as $\int T_{mb} dv$

^b T_{mb} from Magnani et al. (2000)

^c Some of the line profiles were not well-fit by one or two Gaussians and showed weak emission in either the blue or red (or both) wings of the profile. In these instances, the quoted value of W_{CO} is an underestimate since it is estimated based on the Gaussian fits.

^d Some of the line profiles showed two distinct components.

However, because of the limited sampling of the SGH-HL beam by our current observations we note that the ARO results are lower limits.

When looking at Table 2, some of the new ARO detections have W_{CO} values that should have been detected by the SGH-HL survey. An example of this is position G902-33, with $T_R^* \approx 0.4$ K, equivalent to $T_{mb} \approx 0.5$ K. The rms sensitivity of the SGH-HL survey was 0.1 K and should have resulted in a detection. However, the SGH-HL spectrum shown in top half of Figure 5 shows no evidence of the line. This issue can be understood by noting the narrowness of the line at this position (0.6 km s^{-1}) compared to the velocity resolution of the filter banks used in the SGH-HL survey: 0.65 km s^{-1} . The line, if it had been detected would have been in only 1-2 channels, making it more susceptible to noise fluctuations than if higher frequency resolution was employed. Figure 5 shows the non-detection from SGH-HL compared to the spectrum from the data presented in this paper. The surprise here is the importance of observing diffuse molecular cloud at high velocity resolution.

4.4.2 THE MASS OF MBM 53-55

Since we are re-observing a part of the MBM 53-55 region sampled in CO(1-0) by Magnani et al. (2000), any new detections will increase the mass of that cloud complex. Here we determine the mass of the complex from the original Magnani et al. (2000) data and compare our result to that of Y2003. The Pegasus-Pisces region (with northernmost boundary $b = -30^\circ$) shown in Figure 1 covers 0.5749 steradians. The SGH-HL survey covers this region with 2080 points. Of the 48 detections in this region, 23 are associated with the MBM 53-55 cloud complex (see Magnani et al. 2000) providing an estimate of the solid angle of the cloud. We can derive the mass of these clouds using the average W_{CO} value from SGH-HL (2.47 K km s^{-1}), the distance to the clouds (150 pc), a value for the mean molecular weight of 2.8, and $X_{CO} = 1.0 \times 10^{20} \text{ cm}^{-2} [\text{K km s}^{-1}]^{-1}$. The latter three values were chosen to be identical to those used by Y2003. In this fashion we obtain a mass of $790 M_\odot$ compared to $1200 M_\odot$ by Y2003. In comparing these results, we note that the region

surveyed by Y2003 is slightly larger than ours, extending to $b = -29^\circ$, but the clouds there are not very prominent and contribute little mass to the complex. The discrepancy in the mass estimate is also not due to sensitivity considerations since the SGH-HL survey has an rms of 0.1 K versus 0.5 for Y2003. The reasons are likely to be either the peculiar sampling method used by Magnani et al. (2000) where the off position for the spectra was chosen to be one degree south of the on scan (see discussion by Hartmann, Magnani, and Thaddeus 1998), beam dilution of small structures at the cloud edges, and/or non-detections of narrow lines because of the relatively poor velocity resolution of the SGH-HL survey (see discussion above). The SGH-HL survey has a beam of $8.4'$ and a velocity resolution of 0.65 km s^{-1} versus $2.6'$ and 0.1 km s^{-1} , respectively, for Y2003.

GCT increase the Y2003 mass estimate to $2200 M_\odot$ by using a larger value of X_{CO} . If we increase the SGH-HL result by the same factor, the mass of the clouds would then be $1450 M_\odot$. This is the result we will use for the CO-detected mass in the MBM 53-55 complex based on the SGH-HL survey.

4.5 RESULTS AND IMPLICATIONS

The 15 new detections from our ARO observations more than double the W_{CO} value from the SGH-HL survey (from 8.53 K km s^{-1} to $18.42 \text{ K km s}^{-1}$, see Tables 2 and 3). Since the cloud mass is directly proportional to W_{CO} , if our results are typical for the rest of the cloud complex, then the overall mass would increase by a factor of 2.16. Given the results of §3.2, this would mean that the mass of the MBM 53-55 complex would increase on the basis of our sensitive, high velocity resolution CO observations from $1450 M_\odot$ to $3130 M_\odot$.

GCT derive $\text{H}_2:\text{DG}:\text{HI}$ for the entire Pegasus-Pisces region to be 0.7: 1.0: 3.4. If the total mass from the gamma-ray data is $1.6 \times 10^4 M_\odot$, then the ratio $\text{H}_2:\text{DG}:\text{HI}$ in solar masses would be 2200: 3100: 10,700 M_\odot . Assuming the atomic hydrogen is well-determined (i.e., there are no opacity issues), *the increase of 930 M_\odot in CO-detectable gas (i.e., from GCT's value of 2200 M_\odot to our value of 3130 M_\odot) must come at the expense of the CO-dark gas.*

Table 4.3 Total W_{CO} from the three surveys.

Survey	W_{CO}^a K km s ⁻¹	rms K km s ⁻¹
SGHL-HL survey	7.56	0.93
This paper. SGH-HL detections	8.53	0.37
This paper, new detections	9.89	0.57

^a W_{CO} is defined as $\int T_{mb} dv$

This would reduce the CO-dark gas in the region from GCT’s estimate of 3100 M_{\odot} to 2170 M_{\odot} . The total molecular gas content (i.e., CO-detectable plus dark) remains the same, so the CO-dark gas contribution to the total molecular gas now decreases to about $\sim 40\%$.

These results are based on sampling 88 of the 2080 points observed in the SGH-HL survey for this region. Our observations focus on the northernmost portion of the MBM 53-55 complex which is the only molecular gas considered by GCT in the region. The locations of our new detections (see Figure 2) are, for the most part, in the outer regions of the cloud, where low-intensity CO-emitting gas should be located. Since the region chosen for our high-sensitivity observations was chosen randomly along the MBM 53-55 cloud, it seems reasonable to assume that this pattern holds throughout the cloud. A similar result was obtained for the diffuse molecular cloud, MBM 40, by Cotten & Magnani (2013) who derived a mass of 32 M_{\odot} from sensitive CO(1-0) observations (rms values 0.05 - 0.09 K). Conventional CO maps of this cloud (i.e., with rms values of 0.1 - 0.7 K in antenna temperature) yielded mass estimates in the 11-20 M_{\odot} range (Magnani, Hartmann, & Speck 1996; Chastain 2005).

If our results are applicable to other regions, then \sim one-third of the CO-dark gas is not “dark” as far as CO observations are concerned. Unfortunately, the long integration times necessary to detect much of the low-level CO emission reported in this paper, likely preclude any significant mapping of this portion of the dark gas.

The best spectroscopic tracer of dark gas is the [CII] line at $158 \mu\text{m}$ since the integration times are more reasonable (e.g., Langer et al. 2010; Langer et al. 2014). The other spectroscopic candidates for tracing dark gas are the OH 18 cm main lines and, in particular, the 1667 MHz line. Several studies [Barriault et al, 2010; Cotten et al. (2012); and Allen et al. (2015)] have indicated that OH observations may pick up molecular gas not detectable in CO - but these authors compared their results to conventional CO mapping with rms values ~ 0.1 K. We believe that sensitive CO(1-0) observations like the ones reported here would be as successful in detecting a portion of the dark gas as OH, and with comparable integration times.

Our results are based on the assumption that the low-level emission we detected during our survey can be analyzed in the same manner as the stronger emission from the SGH-HL survey (e.g., the same X_{CO} applies to both components). However, Liszt and Pety (2012) showed that the CO(1-0) line can be over luminous in diffuse molecular gas. If the newly-detected CO emission arises from this type of gas, then a lower value of X_{CO} would have to be used to determine its contribution to the molecular mass. However, Liszt and Pety (2012) state that in diffuse molecular clouds gas the lines of sight with $W_{CO} \geq 1.5 \text{ K km s}^{-1}$ are likely to be over luminous. None of the new detections described in this paper are over that threshold. Nevertheless, the issue of what X_{CO} value to use when converting CO(1-0) observations to $N(\text{H}_2)$ has always been thorny. Further observations, perhaps using the CH line at 3.3 GHz to determine independently $N(\text{H}_2)$ (e.g., Magnani and Onello 1995), could settle this question.

4.6 DISCUSSION

By making more sensitive, higher velocity resolution CO(1-0) observations of a region containing a portion of the high-latitude molecular cloud complex, MBM 53-55, we determine that the mass of molecular gas in that region detectable by the CO(1-0) line increases by about a factor of two. If that result is applicable to the entire cloud, then the increase in

molecular mass detectable by CO(1-0) observations increases significantly - at the expense of the dark gas estimate for that region. The increase in gas mass comes at the periphery of the cloud and consists of low-surface brightness CO emission. We stress that in addition to greater sensitivity, observations at high velocity resolution (at least 0.1 km s^{-1} per channel) are necessary to detect some of the weak CO emission in diffuse and translucent molecular gas.

Our results are reminiscent of those from mapping the Gemini OB1 molecular cloud complex by Carpenter, Snell, and Schloerb (1995) who find that up to 50% of the CO *intensity* map may be tied up in low surface brightness gas normally surrounding the dense cores of a GMC. Perhaps we are seeing this phenomenon at lower intensity levels given that we are observing a diffuse/translucent molecular cloud rather than a GMC. In a similar vein, Liszt, Pety, and Lucas (2010) and Goldsmith et al. (2008) have found that a large fraction of CO emission comes from warm (50 - 100 K), low-density ($100 - 500 \text{ cm}^{-3}$), weakly-shielded diffuse molecular gas, even though most of the carbon in these regions is in the form of C^+ .

Low intensity CO emission arising from more diffuse molecular gas than that traced by conventional surveys may be more commonplace in the Galaxy than is currently thought. Dame & Thaddeus (1994) detected a faint, thick molecular disk in the inner Galaxy, with a $^{12}\text{CO}/^{13}\text{CO}$ ratio more similar to that in diffuse and translucent clouds than in GMCs. A similar result has been found by Pety et al. (2013) in M51.

Our results are confined to a small area in the MBM 53-55 cloud complex, but there are other known molecular clouds in the region that were ignored by GCT but detected in the SGH-HL survey. Blair et al. (2017) estimate that these clouds contribute an additional $300 M_{\odot}$ of CO-detectable gas (at typical rms values of 0.1 K). This further reduces the dark gas inventory in the region from about 40% of the total molecular mass to about 35%. If we assume that sensitive CO observations would also double the mass of these clouds, then the dark gas inventory in the Pegasus Pisces region drops to 30%. This value is similar to what Wolfire, Hollenbach, & McKee (2010) determine on the basis of static PDR models of

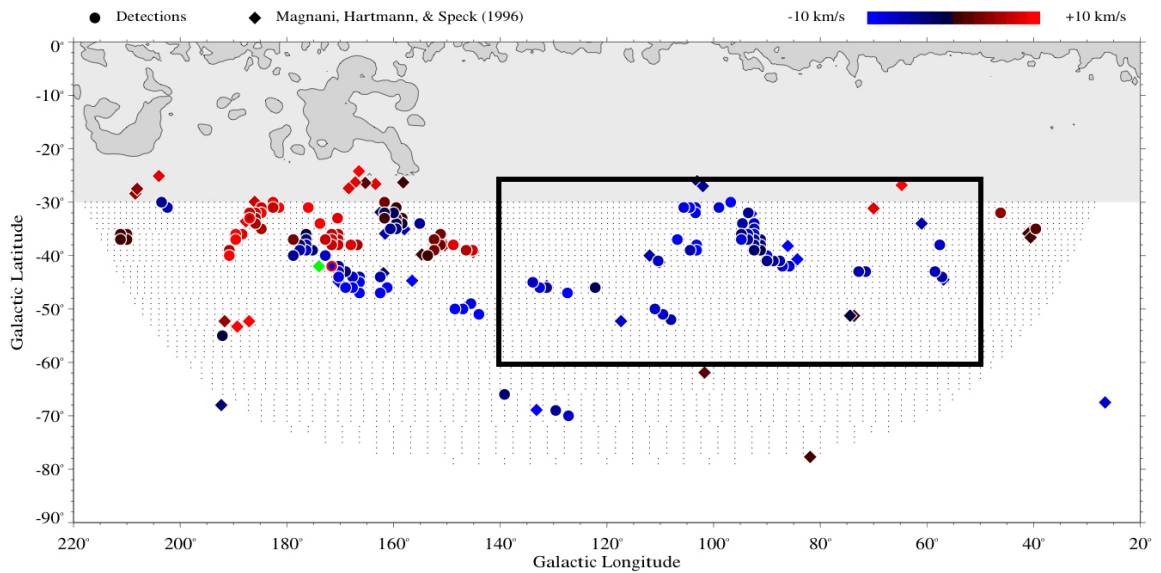
GMC envelopes. It would appear from our results, that the CO-dark gas fraction does not significantly increase in diffuse and translucent gas. We note that dynamical effects in PDR models could alter the dark gas fraction.

The detection of a significant fraction of CO-dark gas by sensitive CO(1-0) observations is important not just as a proof-of-concept. As mentioned above, spectral line detections also provide velocity information. Moreover, the systematics in using CO data are completely different than those from gamma-ray and infrared observations. CO(1-0) observations are not subject to variations in the gas-to-dust ratio, the uniformity of the cosmic ray environment, or their penetration depth.

We are not advocating that sensitive CO(1-0) observations are the best way to trace dark gas. It is clear that [CII] observations are the best way of spectroscopically tracing this component (see Langer et al. 2010; 2014). However, there have been many claims that as much molecular gas exists in dark as opposed to CO-detectable form (e.g., GCT; Abdo, et al. 2010; Planck Collaboration 2011b). In addition, several authors [Barriault et al. (2010); Allen et al. (2012; 2015)], claim the OH 18 cm main lines are better tracers of diffuse molecular gas than the CO(1-0) line. Our results show these claims are premature unless the regions in question have been observed in CO(1-0) both with adequate sensitivity *and* sufficient velocity resolution.

ACKNOWLEDGMENTS

We thank Professor Lucy Ziurys for generously allocating the observing time to complete this project. The Kitt Peak 12 meter radio telescope is operated by the Arizona Radio Observatory (ARO), Steward Observatory, University of Arizona. We also thank Professors Hector Arce and Steven Shore for comments which greatly improved this work. Finally, we thank the anonymous referee who raised several points which clarified and improved the manuscript.



sgh_fig1b 5-MAR-1999 20:19 dap hartmann

Figure 4.1 The Southern Galactic Hemisphere - High Latitude (SGH-HL) CO(1-0) survey. The 4982 grid points which were observed by Magnani et al. (2000) are depicted as the small black dots. Detections from the survey are the round dots color coded in velocity (see top right corner). Other detections from Magnani, Hartmann, and Speck (1996) that were missed by the SGH-HL sampling grid are denoted by diamonds (the green diamond has no velocity information in the literature). The black box denotes the boundary of the region in Pegasus-Pisces included in the GCT dark gas calculations (see text). (A color version of this figure is available in the online journal.)

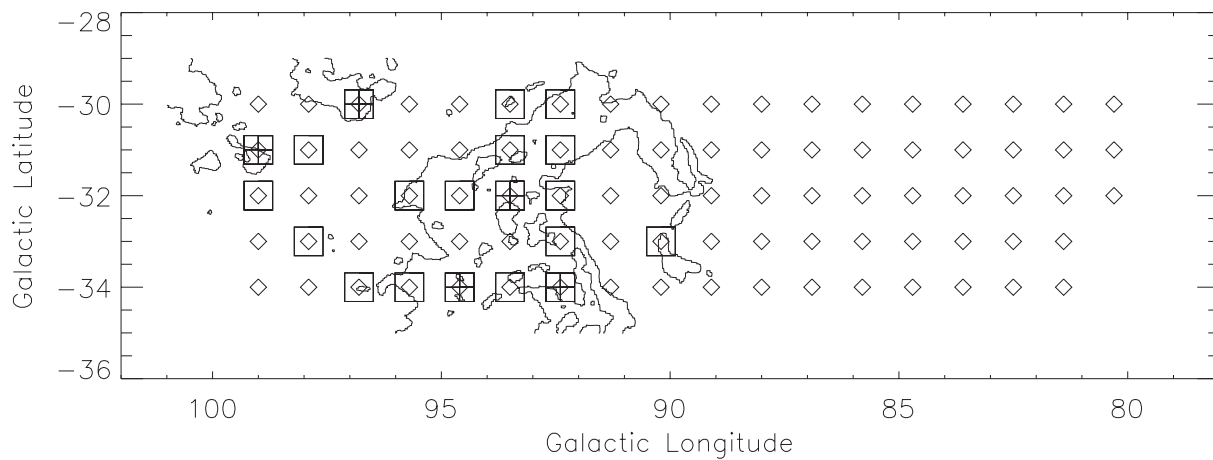


Figure 4.2 Contour map of the northern portion of MBM 53 in $E(B-V)$ from Schlegel, Finkbeiner, and Davis (1999) in linear scale from 0.10 to 0.51 mag in steps of 0.17 mag. The diamonds indicate the 88 positions that were observed in CO(1-0) for this paper. Each position corresponds to an observation from the SGH-HL survey (see §2). The five CO(1-0) detections from that survey at the T_{mb} level of 0.1 K (listed in Table 1) are denoted by squares with a plus sign in them. The 15 new detections are denoted by squares. Parameters for all the detections are in Table 2.

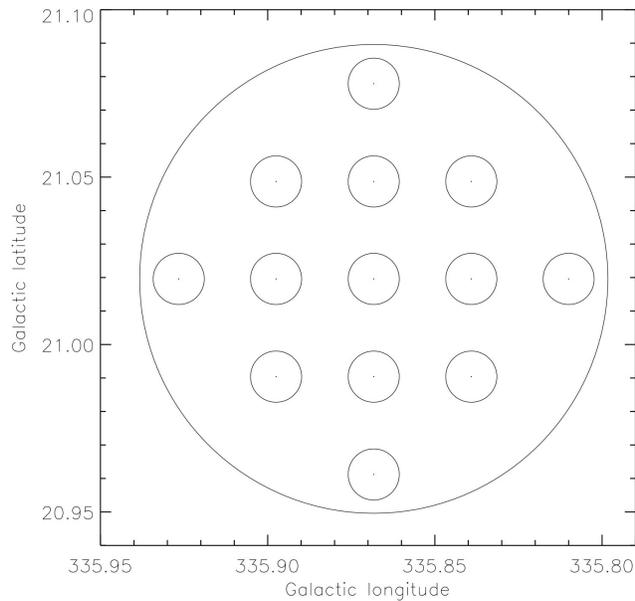


Figure 4.3 Comparison between the beam of the Harvard Smithsonian – Center for Astrophysics 1.2 m mm-wave telescope (beam size 8.4' at 115 GHz) with the 13-point beam pattern from the 12-m Arizona Radio Observatory telescope used to sample the larger beam. The sampling pattern is for one of the 88 observed positions (see Figure 2) and is representative of how each of those positions were observed in CO, with the final spectrum for that position produced by averaging the 13 individual spectra. The beam size of the 12-m at 115 GHz is 55".

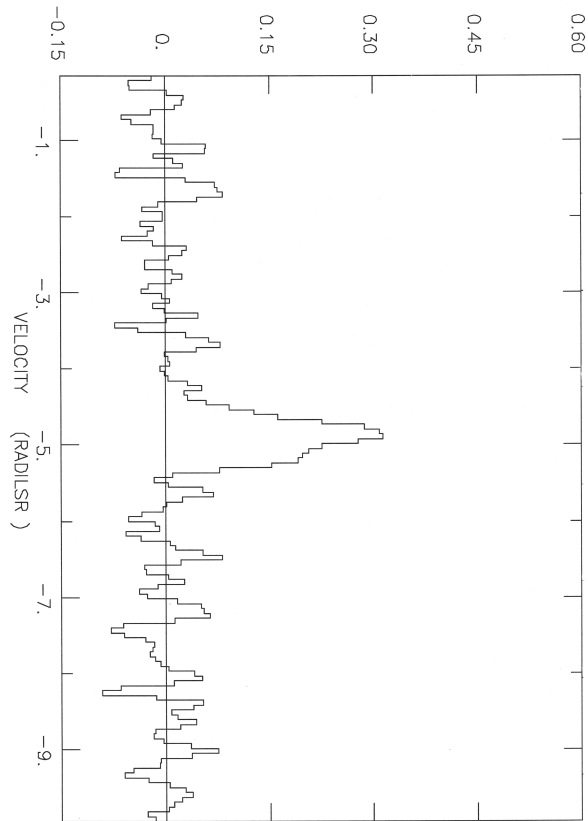


Figure 4.4 CO(1-0) spectrum from position $(\ell, b) = (95.7^\circ, -34.0^\circ)$. The y-axis is antenna temperature in K in the form T_R^* and the x-axis denotes v_{LSR} in km s^{-1} . The velocity resolution and rms per channel are 0.06 km s^{-1} and 39 mK , respectively.

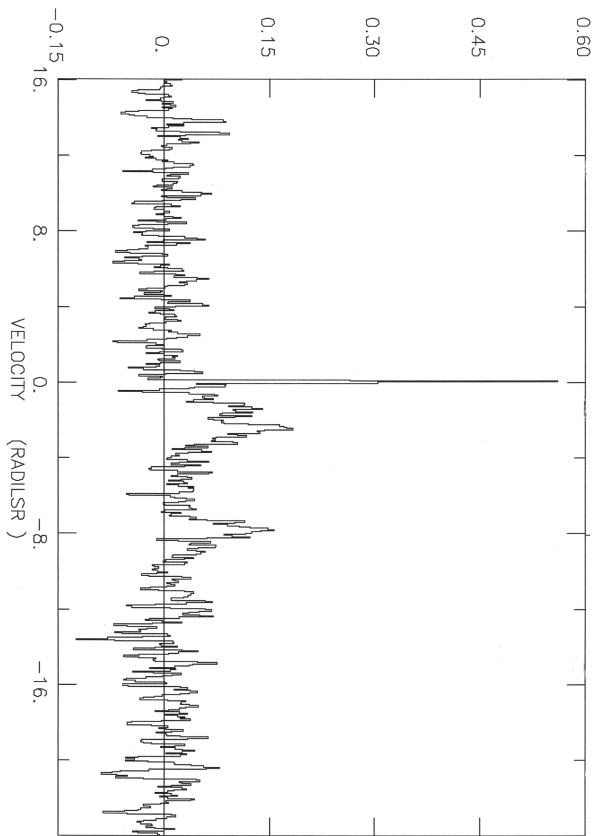


Figure 4.5 CO(1-0) spectrum from position $(\ell, b) = (92.4^\circ, -32.0^\circ)$. The x- and y-axes are as in Figure 5a. The rms is 34 mK per channel. The narrow pip at $v_{LSR} \approx 0 \text{ km s}^{-1}$ is RFI from the system electronics.

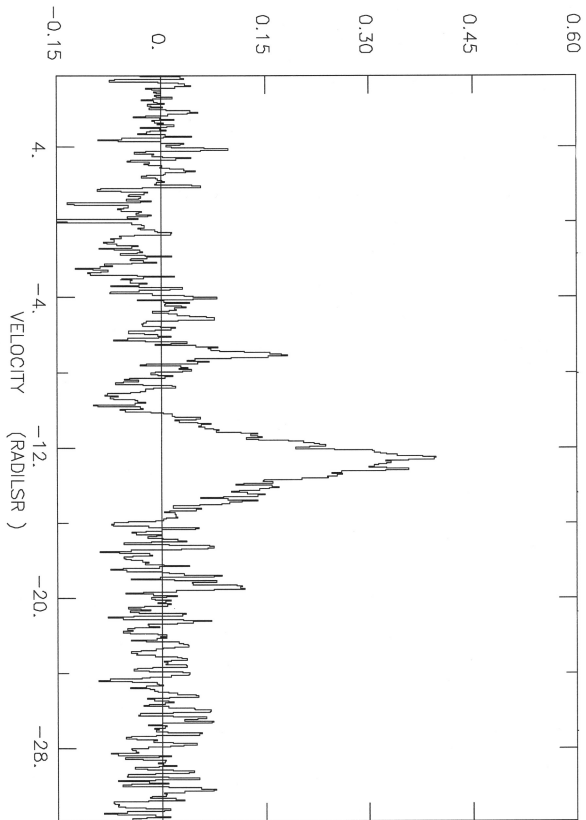


Figure 4.6 CO(1-0) spectrum from position $(\ell, b) = (92.4^\circ, -32.0^\circ)$ *Correction in Thesis: position should be 96.8, -34.0.* The x- and y-axes are as in Figure 5a. The rms is 37 mK per channel.

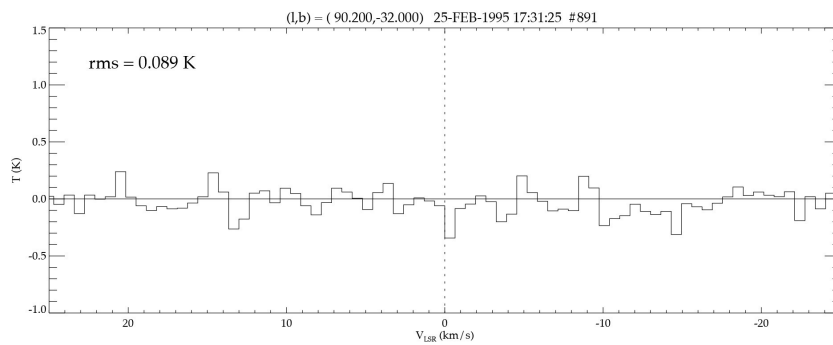


Figure 4.7 CO(1-0) spectrum from the SGH-HL survey. The spectrum was made using on-off mode with the on position at $(\ell, b) = (90.2^\circ, -32.0^\circ)$ and the off position at $(\ell, b) = (90.2^\circ, -33.0^\circ)$. See Hartmann, Magnani, and Thaddeus (1998) for details. With this observing technique, if a CO(1-0) emission line were to be present in the off position, it would appear as an absorption line in the spectrum. The y-axis is antenna temperature in K in the form T_R^* . The velocity resolution is 0.65 km s^{-1} .

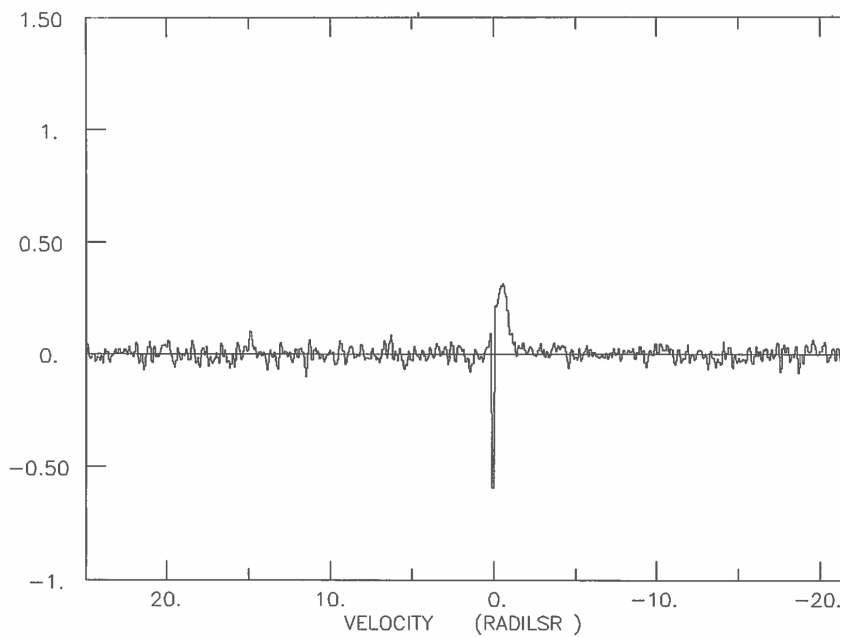


Figure 4.8 CO(1-0) spectrum from position $(\ell, b) = (92.4^\circ, -33.0^\circ)$ *Correction in Thesis: position should be 90.2, -33.0.* The FWHM of the line from Gaussian fitting is 0.60 km s^{-1} . The downward going spike at 0 km s^{-1} is interference. The y-axis is antenna temperature in K in the form T_R^* and the x-axis is v_{LSR} in km s^{-1} . The velocity resolution is 0.06 km s^{-1} and the rms is 25 mK.

CHAPTER 5

OH AND CO AS TRACERS OF MOLECULAR GAS IN MBM 53¹

by Emmanuel Donate², Josh White³, and Loris Magnani⁴

5.1 ABSTRACT

We observed the OH 18 cm lines in the northern portion of the high-latitude diffuse molecular cloud, MBM 53. The 1667 MHz line was detected in 11 of 44 lines of sight at rms levels of 7-10 mK. This region was previously observed in the CO(1-0) line at high sensitivity and spectral resolution. Donate & Magnani (2017) detected CO in 19 of the 44 lines of sight with an A_V threshold of 0.25 *mag* while the OH detection threshold in A_V is 0.35 *mag*. We see more of the cloud with the CO(1-0) line. However, using standard assumptions for converting the OH and CO observations to the molecular mass in the region leads to a three-times greater value in the OH-derived mass. This paradox can be resolved most directly by invoking a larger CO-H₂ conversion factor in the outer, low extinction regions of MBM 53.

5.2 INTRODUCTION

Radio astronomers have consistently used the CO(1-0) line as the primary tracer of molecular gas. The conventional wisdom for many years was that a CO(1-0) map was equivalent to a map of the distribution of H₂, and Heyer & Dame (2015) review the accomplishments of the last 20 years of CO observations of the Milky Way. However, Grenier, Casandjian,

¹Published in Monthly Notices of the Royal Astronomical Society, **486**, 4414

²Department of Physics and Astronomy, University of Georgia, Athens, GA 30602, USA

³Department of Physics and Astronomy, University of Georgia, Athens, GA 30602, USA

⁴Department of Physics and Astronomy, University of Georgia, Athens, GA 30602, USA

and Terrier (2005; hereafter GCT) used cosmic rays and infrared emission to trace molecular gas and, after accounting for the gas traced by CO, asserted that approximately 50% of the molecular mass could not be detected by the CO(1-0) line. GCT named this spectroscopically invisible component of the interstellar medium “dark gas”. Many studies since GCT have confirmed the presence of dark gas (e.g., Abdo et al. 2010; Planck Collaboration 2011b) so that it has become an established part of the molecular inventory of the interstellar medium. Since the original work by GCT spectral lines like the OH ground state hyperfine main lines at 1665 and 1667 MHz (Barriault et al, 2010; Cotten et al. 2012; Allen et al. 2012; 2015; Xu et al. 2016; Tang et al. 2017; Li et al, 2018) or the C⁺ forbidden line at 158 μm (Langer et al. 2010; 2014) have been used to trace some or most of the dark gas so that it is now often referred to as “CO-dark” gas.

A key, but neglected, consideration in these studies is the sensitivity of the CO observations against which the various molecular tracing techniques are compared. Clearly, more sensitive CO(1-0) observations will reveal more CO emission and thus molecular gas (see, e.g., Chastain et al. 2006). The issue then becomes to determine the ideal rms level that will produce a comprehensive view of that portion of the molecular gas traceable by CO in a reasonable amount of integration time. In our previous work (Donate & Magnani 2017) we observed in the CO(1-0) transition the northern portion of the diffuse high-latitude cloud, MBM 53, in Pegasus that overlapped a region GCT had studied. By using 30-minute integration times and rms values of 10-20 mK per point, we found that decreasing the rms by a factor of 5-10 from conventional CO surveys increased the CO-traceable molecular mass by a factor of two. However, there are limits to what even very sensitive CO surveys can do.

Models of Photodissociation Regions (PDRs) have long shown that the outermost regions of molecular clouds did not contain a high enough column density of CO to be detectable with existing mm-wave detection technology. (e.g., Hollenbach & Tielens 1997; and references therein). A recent model of molecular clouds and PDRs designed to address the issue of dark molecular gas suggests that about 28-30% of the molecular gas mass should be untrace-

able using CO(1-0) emission (Wolfire, Hollenbach, & McKee 2010). In a typical interstellar radiation field the CO abundance in a molecular cloud drops from 10^{-4} to less than 10^{-6} for A_V less than one magnitude (van Dishoeck & Black 1988), making $N(\text{CO})$ too low to be detectable in emission with the CO(1-0) line. But, can other molecular transitions trace this gas? Astrochemistry models (e.g., van Dishoeck & Black 1986) have OH as one of the precursor molecules necessary for the formation of CO. In addition, the models by Wolfire, Hollenbach, & McKee (2010) show that at $A_V \lesssim 0.3 \text{ mag}$ the OH abundance overtakes that of CO, giving some credence to the idea that OH could be a better molecular gas tracer for CO-dark gas in the outer envelopes of molecular clouds.

To address this issue we have re-observed a portion of the high latitude region in Pegasus-Pisces studied by Donate & Magnani (2017: $-30.0^\circ \geq b \geq -34.0^\circ$; $80.3^\circ \leq \ell \leq 99.0^\circ$) with the OH 1667 line. GCT report the total molecular gas mass in a larger region in Pegasus-Pisces as $2200 M_\odot$ in CO-detectable gas and $3100 M_\odot$ in CO-dark gas. If the more sensitive CO observations by Donate & Magnani (2017) would scale to the larger region studied by GCT, the CO-detectable mass of the whole region would increase to $3130 M_\odot$ while the CO-dark mass decreases to $2170 M_\odot$. The question we address in this paper is what do comparable observations (as far as integration times) using the OH 1667 MHz line reveal about the dark molecular gas content of this region?

We organize the paper as follows: §2 discusses previous observations of the OH 18 cm lines in tracing low-density, low-extinction molecular gas. The observational setup and strategy is described in §3 and our results are presented in §4. We analyze the results to determine an “OH-detectable” molecular mass and compare it to the CO-detectable mass in the studied region in §5. We close with a summary our results in §6.

5.3 THE EFFICACY OF THE OH 18 CM LINES FOR TRACING DIFFUSE MOLECULAR GAS

More than two decades ago, the case was made by Wannier et al. (1993) that molecular gas not detectable by the CO(1-0) transition could be seen with OH observations at 1665 and

1667 MHz. Later, Barriault et al. (2010) and Cotten et al. (2012) came to similar conclusions based on OH observations of high-latitude molecular clouds, as did Li et al. (2018) for gas in regions with $0.05 < A_V < 2 \text{ mag}$ and Tang et al. (2017) for $A_V > 2.3 \text{ mag}$. The predicted OH abundance in the Wolfire, Hollenbach, & McKee (2010) models for regions with $A_V \lesssim 0.3 \text{ mag}$ is $\sim 10^{-9}$, about one to two orders of magnitude lower than in the traditional CO-rich outer regions of a molecular cloud ($0.3 \lesssim A_V \lesssim 2 \text{ mag}$), but possibly still detectable with sensitive observations at 18 cm. Indeed, the previously mentioned papers all detect OH main line emission from regions with $A_V \lesssim 0.3 \text{ mag}$, so the associated molecular gas is “dark” only insofar as CO is concerned. Allen et al. (2012) sparsely mapped a $4^\circ \times 4^\circ$ region centered on $\ell \approx 108^\circ$ and $b \approx 5^\circ$ and found weak, but widespread, OH 1667 MHz emission ($T_A \approx 20 - 40 \text{ mK}$). The OH emission showed similar extent to the HI emission, but less than 10% of the OH emission had CO(1-0) counterparts. A subsequent paper by Allen et al. (2015) came to similar conclusions. Most recently, Tang et al. (2018), Li et al. (2018) and Nguyen et al. (2018) find that OH 18 cm observations can be used as reliable tracers of H₂ including at least some of the dark molecular gas. Since most of the studies of dark molecular gas compare the H₂ content of a region with CO observations, it is important to compare the efficacy of OH versus CO observations. We describe below our OH observations at 18 cm of a portion of the region sampled in the CO(1-0) line by Donate and Magnani (2017).

5.4 OBSERVATIONAL SETUP AND STRATEGY

5.4.1 FRONTEND AND BACKEND

The OH observations were made from January to July 2016 with the 305m radio telescope at the Arecibo Observatory⁵ in Puerto Rico using the *L*-band Wide receiver. The spectrometer was the Wideband Arecibo Pulsar Processor (WAPP) configured into 8 sub-correlator boards each with 1.5625 MHz bandwidth, 9-level sampling, and 2048 channels.

⁵During these observations the Arecibo Observatory was operated by SRI International under a cooperative agreement with the National Science Foundation (AST-1100968), and in alliance with Ana G. Méndez-Universidad Metropolitana, and the Universities Space Research Association

The boards were assigned to cover the two OH main lines (1665, 1667 MHz), the two satellite OH lines (1612, 1720 MHz), and the HI 21 cm line (which was in the bandpass of the L-band receiver). The remaining three boards provided redundant coverage of the OH main lines and the HI line. Each WAPP subcorrelator board registered both polarizations and resulted in a resolution of 0.14 km s^{-1} per channel over a bandwidth of 281 km s^{-1} for the 1667 MHz line. All boards were centered at $v_{\text{LSR}} = 0 \text{ km s}^{-1}$.

At 1667 MHz the *L*-band Wide receiver has beam size $2.6' \times 3.1'$ elongated in azimuth. System temperatures at 1.6 GHz were typically 25–32 K (including sky contribution) and a five minute scan resulted in rms noise levels per channel of $\sim 50 \text{ mK}$. Each scan consisted only of on source observations and a fifth-order baseline was removed from each spectrum.

5.4.2 OBSERVING STRATEGY

The location of all the observed positions are shown in Figure 1 (right) superposed on an $E(B - V)$ map from the Schlegel, Finkbeiner, and Davis (1999) database. These positions were chosen to match those of the Southern Galactic Hemisphere High-Latitude (SGH-HL) survey made by Magnani et al. (2000). In addition, the region in Figure 1 was more fully explored in CO(1-0) by Donate and Magnani (2017) who observed 88 lines of sight at 115 GHz with high sensitivity and spectral resolution. While we had originally planned to match all of their CO observations with equivalent OH 18 cm observations, we were only able to observe the 44 positions shown in Figure 1. The CO observations attempted to match the angular resolution of the SGH-HL survey ($8.4'$) by using a thirteen-point pattern shown in Figure 3 of the paper by Donate and Magnani (2017). Given the larger beam of our OH observations, we were to able to cover the $8.4'$ beam of the original SGH-HL survey with a five-point pattern shown in Figure 2. Thus, each position in Figure 1 was observed typically for 25-50 minutes on-source and resulting rms levels after baseline subtraction and smoothing were 7-10 mK. This sensitivity level was chosen on the basis of integrating each

Table 5.1 Gaussian-fit parameters and W_{OH} for OH 1667 MHz detections in our survey.

Position	ℓ deg	b deg	T_A mK	Δv km s ⁻¹	v_{LSR} km s ⁻¹	$W(OH)^a$ mK km s ⁻¹	$W(CO)^b$ K km s ⁻¹	A_V^c mag
G92.4-31 ^d	92.4	-31.0	38.4±9.3	1.73±0.42	-5.37	104.7±37.1	0.35±0.06	0.52
G92.4-31 ^e	92.4	-31.0	21.3±9.3	1.31±0.57	-8.26	43.9±27.3	0.13±0.04	—
G92.4-33 ^d	92.4	-33.0	16.9±7.2	2.35±0.40	-5.17	62.3±38.0	0.20±0.10	0.40
G92.4-33 ^e	92.4	-33.0	31.2±7.2	1.75±1.00	-8.27	85.8±29.0	0.12±0.06	—
G92.4-34	92.4	-34.0	49.0±10.0	3.28±0.67	-7.59	253.3±76.4	4.41±0.19 ^f	0.63
G93.5-30	93.5	-30.0	17.8±7.3	3.44±1.41	-10.17	96.4±56.6	0.96±0.15	0.36
G93.5-31	93.5	-31.0	22.8±7.8	1.81±0.62	-3.45	64.9±31.9	1.25±0.11 ^f	0.44
G93.5-32	93.5	-32.0	49.7±9.2	1.51±0.28	-4.60	117.8±32.6	0.50±0.06 ^f	0.46
G93.5-34	93.5	-34.0	52.7±9.8	3.61±0.67	-4.64	299.4±83.0	1.12±0.08	0.62
G94.6-34 ^d	94.6	-34.0	19.4±6.9	2.00±0.71	-2.55	61.1±31.1	0.32±0.14	0.57
G94.6-34 ^e	94.6	-34.0	23.8±6.9	2.62±0.76	-6.51	98.1±41.2	1.17±0.19	—
G95.7-32 ^d	95.7	-32.0	32.3±7.5	3.27±0.76	-6.38	166.1±56.5	1.15±0.15	0.52
G95.7-32 ^e	95.7	-32.0	[18.6±7.5]	[2.82±1.14]	[-11.77]	[82.5±47.6]	—	—
G96.8-30 ^d	96.8	-30.0	[10.8±6.8]	[2.24±1.40]	[-8.81]	38.2±34.1	—	0.51
G96.8-30 ^e	96.8	-30.0	18.0±6.8	2.20±0.83	-14.97	62.2±33.8	0.86±0.10	—
G99.0-31	99.0	-31.0	26.0±6.7	2.35±0.60	-9.04	96.1±36.0	1.27±0.18	0.35

Square brackets indicate the detection is tentative.

^a W_{OH} is defined as $\int T_B dv$ where $T_B = T_A/\eta_B$ - see text.

^b Donate & Magnani (2017)

^c Schlafly & Finkbeiner (2011)

^d first component

^e second component

^f two CO(1-0) components

line of sight for approximately the same amount of time as the CO(1-0) observations of Donate & Magnani (2017).

5.5 RESULTS

Using the technique we discussed above we observed 44 lines of sight (see Figure 1) and detected OH 1667 MHz emission from 11 of these. Five of the lines of sight showed two velocity components (also seen in CO(1-0) for some of the lines of sight by Donate and Magnani 2017). The results of Gaussian fits to the lines are shown in Table 1 and representative spectra are shown in Figures 3a-c.

5.5.1 COMPARISONS WITH CO

Magnani and Donate (2017) detected CO(1-0) emission from 20 out of 88 lines of sight in the region shown in Figure 1. Of those 20 detections, 19 are among the 44 lines of sight we observed in the OH 18 lines. The Gaussian-fit parameters of the 1667 MHz detections are shown in Table 1. The velocity of the molecular gas in this region is complex with at least four distinct components in CO (-3 , -7 , -11 , and -15 km s $^{-1}$). The wide extent of the OH emission is also observed in the lower portions of the cloud complex [MBM 55, more than 10° from the region examined in this paper - Magnani & Siskind (1990)]. The OH and CO emission profiles are mostly similar as far as velocity with five exceptions (over 16 components). Three lines of sight show two distinct velocity components in CO but only one in OH. In all three instances, the OH lines are significantly broader than either of the corresponding CO lines so the OH components are likely similar in intensity and blend together in velocity. More interestingly, two lines of sight show OH emission at two distinct velocities (although in each case the weaker OH emission line is only tentatively detected), but only one has corresponding CO emission. The comparison between the CO(1-0) and 1667 MHz OH spectra in these latter two cases is shown in Figures 4*a-b*.

For those components with similar velocities there is a linear relationship between the intensities of the CO and OH emission (see Figure 5). The best-fit line to those components detected in both transitions has a slope of 5.79, an intercept of 0.12, and an r value of 0.54. The correlation, though present, is not very tight. Similarly, Li et al. (2018) find that, when the CO line is detected along with OH absorption or emission, $N(\text{OH})$ and $N(\text{CO})$ are correlated.

The existence of this correlation depends on where the points are located in a PDR. In the outermost layer of the molecular portion of the PDR, where CO(1-0) emission begins to disappear (and the dark molecular gas begins to dominate), one does not expect CO and OH to correlate. From astrochemistry models, in the outermost layers of PDRs there should be more OH than CO (e.g., Wolfire, Hollenbach, & McKee (2010)). In the opposite regime

(i.e., the fully molecular, dense, opaque regions of molecular clouds) the OH should become depleted as it converts to CO and other species (e.g., Nguyen et al. 2018). Observationally, Barriault et al. (2010) mapped two translucent clouds in both CO and OH and see no correlation for regions with $A_V > 2 \text{ mag}$. A broader study by Tang et al. (2017) along the Galactic plane does not show a correlation between CO and OH but their sample covers what are likely GMCs with column density values $\log N(\text{OH}) > 14.25$.

In summary, it is only in the regions where A_V ranges from 0.3 - 2 mag (under normal interstellar radiation fields) where one expects CO and OH to correlate in both intensity and column density. In this regime, the studies which claim OH 1667 MHz detections without corresponding CO(1-0) emission (e.g., Allen et al. 2015) likely do not have sufficiently sensitive CO(1-0) observations to compare with the corresponding OH *emission* line data. Of course, absorption line studies (e.g., Li et al. 2018) are able trace a lower column density regime than can be detected in emission. Given the complexity of this situation, direct comparisons between CO and OH are difficult to interpret, but we can examine how both species correlate separately with dust at low extinctions in the same region to determine which of the two is a more successful tracer of the molecular content of the cloud.

5.5.2 COMPARISON WITH EXTINCTION

We present $W(\text{CO})$ and $W(\text{OH})$ as a function of A_V (from the Schlafly & Finkbeiner database) in Figures 6 and 7. It is clear that the sensitive CO(1-0) observations result in detections a full tenth of a magnitude lower than the OH 1667 emission line (integrated for a comparable time). Figure 8 shows the detection rate as a function of A_V . At all extinctions less than 0.6 mag, the CO(1-0) line is detected at a higher rate than the OH 1667 MHz line. At $A_V > 0.6 \text{ mag}$ for this region of the cloud, both lines were always detected. At least in the case of this diffuse molecular cloud (MBM 53), as far as emission lines are concerned, CO is better at delineating the molecular extent of the cloud.

The CO- A_V correlation can be expressed as $W(\text{CO}) = 2.76A_V - 0.57 \text{ K km s}^{-1}$ with an r value of 0.37. For OH, we obtain $W(\text{OH}) = 0.45A_V - 0.12 \text{ K km s}^{-1}$ (with an r of 0.63). If we compare our results to a previous study of W(OH)- A_V in a translucent cloud (L1642) by Sandell et al. (1981) we notice that our data are at significantly lower extinctions (see Figure 9). Although our slope is higher, the scatter in our W(OH) values may indicate that at cloud edges excitation and/or abundance variations may be more pronounced than in denser gas. As more OH data become available from regions at these extinctions, it would be worthwhile to examine the variations for $A_V \lesssim 2 \text{ mag}$.

We can convert the above relationship to $N(\text{OH})/A_V$ by using equation 1 (see below) and an excitation temperature, T_{ex} , for the 1667 MHz line of 5 K. The $N(\text{OH})/A_V$ slope then becomes $4.5 \times 10^{14} \text{ cm}^{-2} \text{ mag}^{-1}$ for our data over a restricted range of A_V . Previous studies find values for this slope ranging from 0.15 to $8.5 \times 10^{14} \text{ cm}^{-2} \text{ mag}^{-1}$ (Crutcher 1979; Toriseva & Mattila 1985; Grossman et al. 1990; Barriault et al. 2010). The wide range in slope probably reflects large variations in excitation and abundance in diffuse molecular regions.

5.5.3 OH COLUMN DENSITIES AND MASS

The molecular mass within the boundary shown in Figure 1 can be estimated using the OH data from this paper and the CO(1-0) data from Donate & Magnani (2017). In order to do this we first determine $N(\text{OH})$ for each detected position in the cloud. For the OH 1667 MHz line, in the optically thin approximation, $N(\text{OH})$ can be expressed as

$$N(\text{OH}) = \frac{C}{F\eta_B} \left[\frac{T_{ex}}{T_{ex} - T_{bg}} \right] \int T_A dv \quad \text{cm}^{-2}, \quad (5.1)$$

where C is a constant [$= 2.24 \times 10^{14} \text{ cm}^{-2} \text{ K}^{-1} \text{ km}^{-1} \text{ s}$ for the 1667 MHz line, e.g., Lucas & Liszt (1996)], and F is the filling factor of the molecular gas in the Arecibo beam which we will assume to be 1.0. The beam efficiency, η_B , can be measured at Arecibo by observing bright continuum sources. During the 2016 observing run η_B varied between 0.57 and 0.78 at 1415 MHz with an average of 0.69 ± 0.07 . The beam efficiency decreases with frequency so

we used 0.65 ± 0.07 in our calculations. The quantity $\int T_A dv / \eta_B$ is given as $W(\text{OH})$ in Table 1. The factor in brackets in equation 1 requires assuming a value for T_{ex} and the background radiation temperature, T_{bg} , at 1.6 GHz. T_{bg} is a combination of the Cosmic Microwave Background radiation, the Galactic synchrotron emission, and the non-thermal background from unresolved radio sources which result in a value ≈ 3.3 K (see, e.g., Grossmann et al. 1990). The value of the excitation temperature of the ${}^2\Pi_{3/2}$ ($J=3/2$), $F=1-1$ line at 1667 MHz has been measured in diffuse clouds by Lucas & Liszt (1996) towards a sample of extragalactic sources. They obtain values in the range 3.5 – 5.5 K. In Table 2 we tabulate $N(\text{OH})$ for our detections for three values of T_{ex} : 5, 10, and 20 K. The latter two values are probably valid in denser regions not found in MBM 53. Most studies of diffuse and translucent clouds give estimates of T_{ex} in the 3–8 K range (Dickey, Crovisier, & K       (1981); Wouterloot & Habing (1985); Lucas & Liszt (1996); Xu et al. 2016; Li et al. 2018)]. The last entry for each column is the average OH column density, $\overline{N(\text{OH})}$, determined by averaging over the 11 lines of sight rather than the 16 individual components.

We can use $\overline{N(\text{OH})}$ for a given T_{ex} to obtain $\overline{N(\text{H}_2)}$. This requires the OH/H₂ abundance which has been determined to be $2.5\text{--}5.0 \times 10^{-8}$ for diffuse clouds with extinction similar to the lines of sight we observed (Lucas and Liszt 1996), and $1.0 \pm 0.2 \times 10^{-7}$ for a sample of diffuse and dark lines of sight (Liszt and Lucas 2002). Most recently, Weselak et al. (2010) derive an OH/H₂ abundance of $1.05 \pm 0.14 \times 10^{-7}$ for 16 translucent lines of sight. Thus, for the remainder of the paper we will adopt an OH/H₂ abundance ratio of 1.0×10^{-7} . In this fashion, we can estimate the mass in our sampled region by using

$$M = \overline{N(\text{H}_2)}_i \Omega_i d^2 f_i \mu m_H \quad \text{cm}^{-2} \quad (5.2)$$

where the letter i represents the value of the given quantity for either CO or OH observations. Thus, $\overline{N(\text{H}_2)}_i$ is the average molecular column density from the CO or OH data, Ω_i is the area of the sampled region, d is the distance which is assumed to be 253 ± 11 pc (Schlafly et al. (2014)), f_i is the fraction of the sampled area containing molecular gas as detected by OH

or CO, μ is the molecular weight (assumed to be 2.3), and m_H is the mass of the proton. The value of f_{OH} can be estimated as $11/44 = 0.25$. The value of Ω for the portion of the region in Figure 1 bounded by $80.3^\circ \leq \ell \leq 99.0^\circ$; $-34^\circ \leq b \leq -30.0^\circ$ is 0.01961 steradians. For OH we use $\overline{N(H_2)}$ obtained from $\overline{N(OH)}$ with $T_{ex} = 5$ K. The value of Ω_{OH} is 0.009587 steradians, and with $f_{OH} = 0.25$ we obtain a value for the OH-observed mass of $2900 M_\odot$ (see Table 3). For CO, we use the average value of the integrated CO main beam temperature ($= 0.921$ K km s^{-1}) from Donate & Magnani (2017) and convert to $N(H_2)$ using a standard value for the CO- H_2 conversion factor ($2.0 \times 10^{20} \text{ cm}^{-2} [\text{K km s}^{-1}]^{-1}$; e.g., Magnani & Onello 1995). With $\Omega_{CO} = 0.019174$ and $f_{CO} = 0.23$, the CO-derived mass for the region in Figure 1 is $960 M_\odot$. This is tantamount to saying that most of the molecular gas in the region sampled by Donate & Magnani (2017) is actually at $92.4^\circ \leq \ell \leq 99.0^\circ$.

If we just consider the region where we made our OH observations, the area of the original CO-sampled region decreases by a factor of 2, but the fraction of detections rises by nearly that amount so that the mass derived with the CO data for the OH region is nearly the same, $940 M_\odot$. The values used in these calculations and the results are summarized in Table 3. If we compare the CO-derived mass in regions where $A_V > 0.35$ mag (i.e., those regions containing OH detections) the CO mass decreases only slightly. We now have 16 out of 18 lines of sight with CO emission instead of 20 out of 88. For the 16 points, the average W_{CO} is 1.08 K km s^{-1} which for a CO- H_2 conversion factor, also known as X_{CO} , value of $2 \times 10^{20} \text{ cm}^{-2} [\text{K km s}^{-1}]^{-1}$ (we will suppress the units in the remainder of the paper) gives a mass of $890 M_\odot$.

5.6 DISCUSSION

One of our goals in this project was to determine the OH-detectable molecular mass in a region where we had previously observed CO. After making the OH observations and comparing the gas mass estimates we find an initially counterintuitive result. Our OH observations reveal a significantly higher molecular mass than is derived from our CO measure-

Table 5.2 OH column densities for four possible excitation temperatures.

Position	$N(\text{OH})$ for $T_{\text{ex}} = 5$ K cm^{-2}	$N(\text{OH})$ for $T_{\text{ex}} = 10$ K cm^{-2}	$N(\text{OH})$ for $T_{\text{ex}} = 20$ K cm^{-2}
G92.4–31 ^a	$6.90 \pm 2.44 \times 10^{13}$	$3.50 \pm 1.24 \times 10^{13}$	$2.81 \pm 0.99 \times 10^{13}$
G92.4–31 ^b	$2.89 \pm 1.80 \times 10^{13}$	$1.47 \pm 0.91 \times 10^{13}$	$1.18 \pm 0.73 \times 10^{13}$
G92.4–33 ^a	$5.65 \pm 1.91 \times 10^{13}$	$2.87 \pm 0.97 \times 10^{13}$	$2.30 \pm 0.78 \times 10^{13}$
G92.4–33 ^b	$4.10 \pm 2.50 \times 10^{13}$	$2.08 \pm 1.27 \times 10^{13}$	$1.67 \pm 1.01 \times 10^{13}$
G92.4–34	$1.67 \pm 0.49 \times 10^{14}$	$8.47 \pm 2.55 \times 10^{13}$	$6.79 \pm 2.04 \times 10^{13}$
G93.5–30	$6.35 \pm 3.73 \times 10^{13}$	$3.22 \pm 1.89 \times 10^{13}$	$2.59 \pm 1.52 \times 10^{13}$
G93.5–31	$4.28 \pm 2.10 \times 10^{13}$	$2.17 \pm 1.07 \times 10^{13}$	$1.74 \pm 0.86 \times 10^{13}$
G93.5–32	$7.76 \pm 2.14 \times 10^{13}$	$3.94 \pm 1.09 \times 10^{13}$	$3.16 \pm 0.87 \times 10^{13}$
G93.5–34	$1.97 \pm 0.55 \times 10^{14}$	$1.00 \pm 0.28 \times 10^{14}$	$8.03 \pm 2.22 \times 10^{13}$
G94.6–34 ^a	$4.03 \pm 2.05 \times 10^{13}$	$2.04 \pm 1.04 \times 10^{13}$	$1.64 \pm 0.84 \times 10^{13}$
G94.6–34 ^b	$6.47 \pm 2.72 \times 10^{13}$	$3.28 \pm 1.38 \times 10^{13}$	$2.63 \pm 1.10 \times 10^{13}$
G95.7–32 ^a	$1.09 \pm 0.37 \times 10^{14}$	$5.55 \pm 1.89 \times 10^{13}$	$4.46 \pm 1.51 \times 10^{13}$
G95.7–32 ^b	$5.43 \pm 3.14 \times 10^{13}$	$2.76 \pm 1.59 \times 10^{13}$	$2.21 \pm 1.28 \times 10^{13}$
G96.8–30 ^a	$2.52 \pm 0.22 \times 10^{13}$	$1.28 \pm 1.14 \times 10^{13}$	$1.02 \pm 0.91 \times 10^{13}$
G96.8–30 ^b	$4.10 \pm 2.23 \times 10^{13}$	$2.08 \pm 1.13 \times 10^{13}$	$1.67 \pm 0.91 \times 10^{13}$
G99.0–31	$6.33 \pm 2.23 \times 10^{13}$	$3.21 \pm 1.20 \times 10^{13}$	$2.58 \pm 0.97 \times 10^{13}$
Average ^c	$1.04 \pm 0.53 \times 10^{14}$	$5.02 \pm 2.26 \times 10^{13}$	$4.23 \pm 1.80 \times 10^{13}$

^a first component^b second component^c Average is for the 11 lines of sight rather than the 16 individual components.

Table 5.3 OH and CO masses for MBM 53.

Species	Ω_i steradians	f_i	$N(\text{H}_2)_i$ cm^{-2}	Mass M_\odot
CO (entire region)	0.019174	0.23	1.84×10^{20} ^a	960
CO (OH region)	0.009587	0.43	1.91×10^{20} ^b	940
CO ($A_V > 0.35$ mag)	0.003922	0.89	2.16×10^{20}	890
OH	0.009587	0.25	1.04×10^{21} ^c	2900

^a H_2 column density derived from Donate & Magnani (2017) for 88 points^b excludes one CO detection from Donate & Magnani outside of OH-sampled region^c H_2 column density derived from average $W(\text{OH})$ value for $T_{\text{ex}} = 5$ K in Table 2.

ments; however, there are more detections in CO than in OH. More explicitly, the failure of the OH measurements to trace molecular gas in regions between $0.25 \text{ mag} < A_V < 0.35 \text{ mag}$ and the greater number of detections with CO rather than OH (19 detections versus 11) clearly indicates that we see more of the cloud in CO, at least for OH observations integrated for periods similar to the CO data. Thus, sensitive CO(1-0) observations are indeed more effective in tracing the *extent* of low-density molecular gas, but the standard assumptions about the value for X_{CO} versus excitation temperature and abundance for OH make the mass traced by the OH emission a factor of three greater than the CO-determined mass.

Thus, to reconcile the CO and OH mass estimates requires either increasing the CO mass by using a larger value for X_{CO} , or decreasing the OH mass by using either a higher T_{ex} or a lower OH abundance (or both). Several authors have estimated T_{ex} for the OH 1667 MHz line at $\approx 5 \text{ K}$ in low extinction regions (see §4.3). Similarly, recent abundance estimates for these regions cluster around 1×10^{-7} to a factor of two (see §4.3). However, Xu et al. (2016) derive an OH abundance of 8×10^{-7} in regions in Taurus with $A_V \approx 0.4 \text{ mag}$. Should such an abundance be valid for our low-extinction regions, the OH mass in Table 3 would increase by nearly an order of magnitude, exacerbating the discrepancy with CO and giving a cloud mass for the northern part of MBM 53 greater than the entire MBM 53-55 complex (see estimates in Donate and Magnani 2017). We can check the abundance in this region by using dust as a tracer of hydrogen nucleons. With the Bohlin, Savage, & Drake (1978) relation and an average value of $E(B-V)$ for the OH detections of 0.16 mag, the resulting $N(H)$ is $9.3 \times 10^{20} \text{ cm}^{-2}$. If we use the average value of $N(OH)$ for $T_{ex} = 5 \text{ K}$ shown in Table 2 the abundance is 1.1×10^{-7} , consistent with our assumed value.

Our results seem to contradict those of Tang et al. (2017) who surveyed lines of sight along the Galactic plane in CO and OH and concluded that OH seemed the better tracer of diffuse molecular regions. Part of the discrepancy may be due to differing definition of “diffuse”. While many of their lines of sight may be at the edges of GMCs, their lowest extinction is 2.3 mag ; our data are for A_V in the range 0.1 - 0.6 mag. Supporting this difference in

extinction regimes are the OH column densities. Their lowest values are $2 \times 10^{14} \text{ cm}^{-2}$ while ours are typically an order of magnitude lower. The lack of CO detections in gas with $A_V > 2.3 \text{ mag}$ is puzzling, but later attributed by Tang et al. (2018) to a population of “CO-poor” molecular clouds ($\text{CO}/\text{H}_2 \approx 10^{-6}$). In contrast, MBM 53 has lower extinction but has CO abundances typical of high-latitude clouds (10^{-5} - 10^{-4} ; Magnani, Blitz, & Wouterloot 1988). Another difference between the two studies is that Tang et al. (2017) see no correlation between OH and those lines of sight with CO emission, while we see a correlation at our lower extinctions (see Figure 5). Finally, the CO observations used by Tang et al. (2017) have neither the sensitivity nor the spectral resolution of those by Donate & Magnani (2017). It is doubtful they would have detected several of the lower intensity CO(1-0) lines noted by Donate & Magnani (2017) (see Table 1).

Historically, estimates of X_{CO} , in translucent and diffuse molecular regions have ranged from 0.5×10^{20} to $7 \times 10^{20} \text{ cm}^{-2}$ (e.g., de Vries, Heithausen, & Thaddeus 1987, Magnani & Onello 1995). Even within individual clouds, X_{CO} has been estimated to vary by factors of 11-14 (Magnani et al. 1998). If X_{CO} were to increase at cloud edges by a factor of 3 from the traditional value of 2×10^{20} , then the discrepancy in the CO and OH mass estimates could be alleviated. While there are few estimates of the value of X_{CO} at cloud edges, Cotten & Magnani (2013) do find evidence of an increase in X_{CO} at the edges of the diffuse cloud MBM 40. The increase is from 1 to $3 \times 10^{20} [\text{K km s}^{-1}]^{-1}$ with X_{CO} calibrated using the CH 3335 MHz line.

The greater aim of this project and our previous CO work was to make a clear determination between whether it was better to use OH or CO as a molecular gas tracer in low-extinction regions where dark molecular gas is thought to dominate the gas mass inventory. We see more of the cloud in the CO(1-0) line than with the OH 1667 MHz main line for comparable integration times. While our results indicate that sensitive CO(1-0) observations result in more outright molecular detections, the uncertainties in OH excitation temperature and abundance and in the CO- H_2 conversion factor make the question of which tracer is

best difficult to assess. The standard assumptions made when analyzing the OH 18 cm and CO 2.6 mm data lead to a greater mass estimate using the OH 1667 MHz line. It is thus easy to see why many researchers have turned to the OH 1667 MHz line for tracing the dark gas component. But sensitive CO observations should not be dismissed until a study of the variation of X_{CO} at low extinctions is made. When making these comparisons, it is critical to compare the OH data to *sensitive*, high-spectral resolution, CO(1-0) observations rather than typical CO mapping data.

5.7 SUMMARY

We observed the OH 18 cm lines in half of a region we had previously sampled in the CO(1-0) line (Donate & Magnani 2017). The CO study was more sensitive than typical CO mapping of molecular regions (11-40 mK vs. 100-200 mK) and showed emission in 20 out of 88 lines of sight. The OH observations showed 1667 MHz line emission for 11 out of 44 lines of sight and typical OH rms values were in the 7-10 mK range. Both the OH and CO observations for each position were made with comparable integration times. If we compare the CO data for the same 44 lines of sight as the OH observations, the detection rate was 19 out of 44. We see more of the cloud in the CO(1-0) line.

The CO(1-0) lines have an A_V threshold at 0.25 *mag* while the OH emission does not occur until the lines of sight are at 0.35 *mag*. The failure of OH 1667 MHz observations when compared to CO observations with similar integration times in tracing molecular gas below $A_V \approx 0.35$ *mag* contrasts recent work by Barriault et al. (2010), Allen (2012; 2015), and Tang et al. (2017) which indicate that OH emission line observations are more effective than CO(1-0) observations in tracing low-density molecular gas. Our results hold for observations made with integration times of 0.5 - 1 hour for each species. Higher sensitivity OH observations could produce more detections. For instance, the OH observations of Allen et al. (2015) achieved rms value of 3 - 3.5 mK, significantly better than ours. However, improving our sensitivity by a factor of two would require a fourfold increase in integration time.

Surprisingly, the CO-derived mass (using standard assumptions) from the 19 detections is $940 M_{\odot}$ while the OH-derived mass for typical excitation temperature and abundance is three times larger. This discrepancy could be due to excitation and/or abundance issues with OH or X_{CO} issues with CO. The OH excitation and abundances that we use are typical of those used by recent OH studies (see references in §1). Thus, the most likely explanation is that X_{CO} increases in low-extinction regions. There are indications that this might be the case in one other high-latitude cloud (see Cotten & Magnani 2013), but further observations are necessary to determine if this is a general characteristic of diffuse molecular clouds.

ACKNOWLEDGMENTS

We thank Dr. Chris Salter for help with setting up the OH observations and for helpful discussions. We also thank the referee for helpful comments. This research has made use of the NASA/IPAC Extragalactic Database (NED), which is operated by the Jet Propulsion Laboratory, California Institute of Technology, under contract with the National Aeronautics and Space Administration.

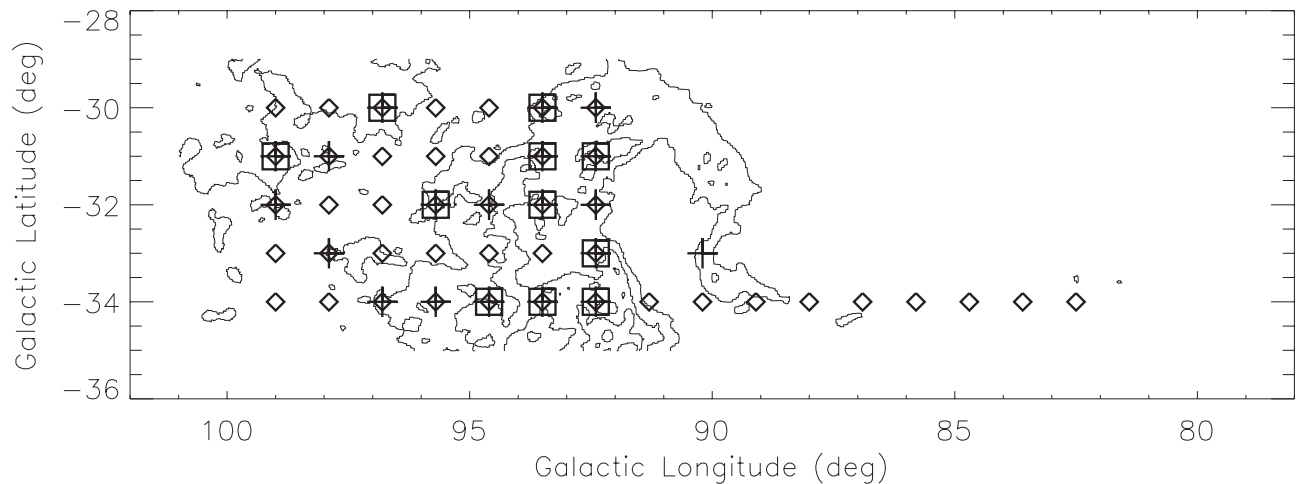


Figure 5.1 E(B-V) contour map of the northern portion of MBM 53 from the Schlegel, Finkebeiner, and Davis (1998) database in linear scale from 0.10 to 0.51 mag in steps of 0.13 mag. The diamonds indicate the 44 positions that were observed in the OH 18 cm lines for this paper. Each position corresponds to an observation from the CO (1-0) SGH-HL survey (see §3) and the deeper survey by Donate & Magnani (2017). The 20 CO(1-0) detections from Donate & Magnani (2017) are denoted by plus signs. Detections of at least the 1667 MHz line are denoted by squares with Gaussian-fit parameters for all the detections listed in Table 2. A complete CO(1-0) map of the region encompassing MBM 53-55 is given by Yamamoto et al. (2003).

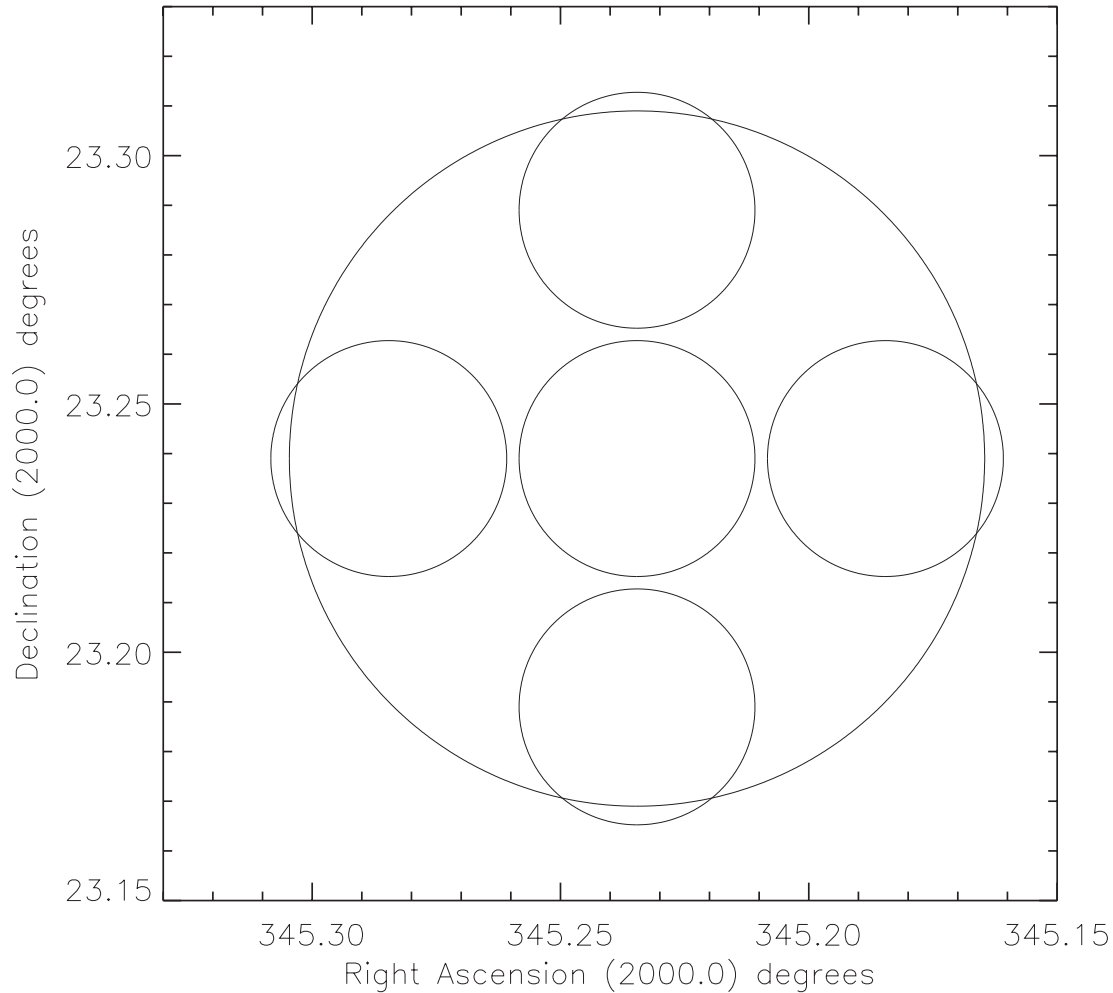


Figure 5.2 Comparison between the beam of the Harvard Smithsonian – Center for Astrophysics 1.2 m mm-wave telescope (beam size $8.4'$ at 115 GHz) with the 5-point beam pattern from the 305-m Arecibo radio telescope used to sample the larger beam. The sampling pattern in RA and Dec is for one of the 44 observed positions (central point at $\ell = 94.6^\circ$, $b = -34.0^\circ$) and is representative of how each of those positions were observed in OH, with the final spectrum for that position produced by averaging the five individual spectra. The beam size of the 305-m at 1.6 GHz is $2.6' \times 3.1'$ elongated in azimuth, but is here represented by a $2.85'$ radius circle.

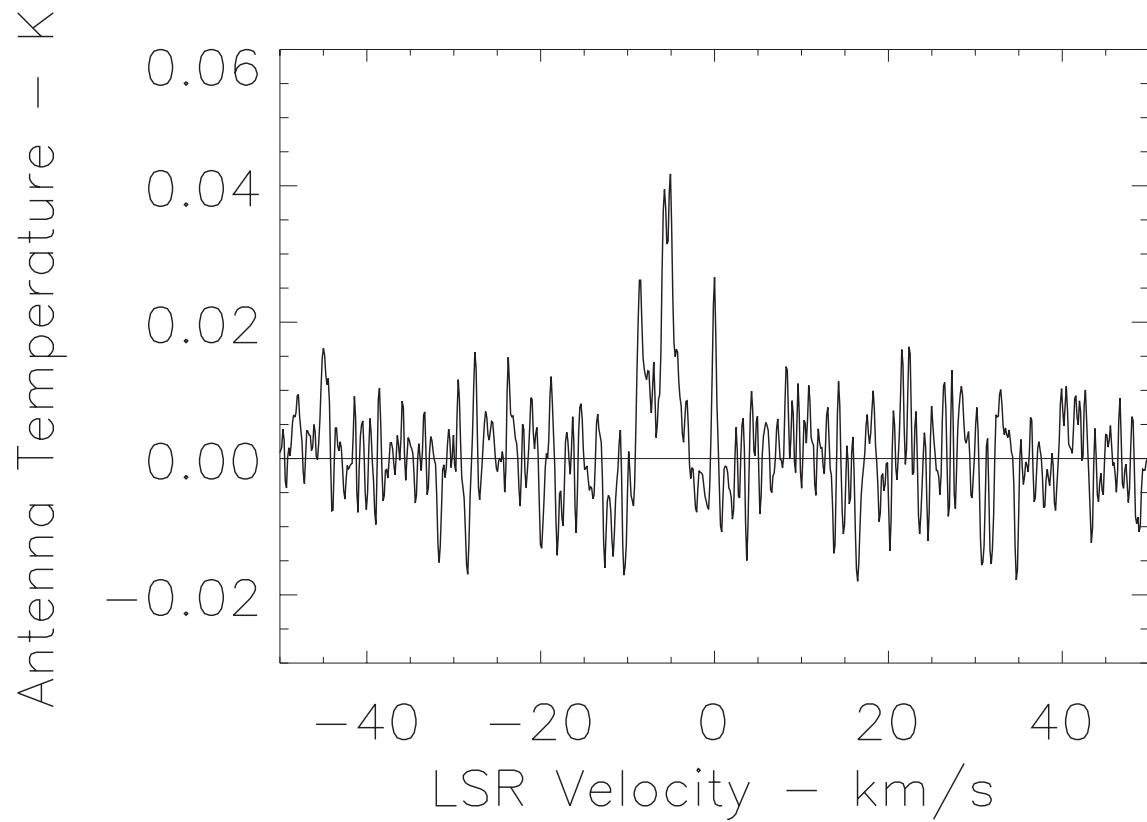


Figure 5.3 Spectrum of the OH 1667 MHz line for the line of sight G92.4–31.0 (see Table 1). The spike at $v_{LSR} = 0.0 \text{ km s}^{-1}$ is internal interference.

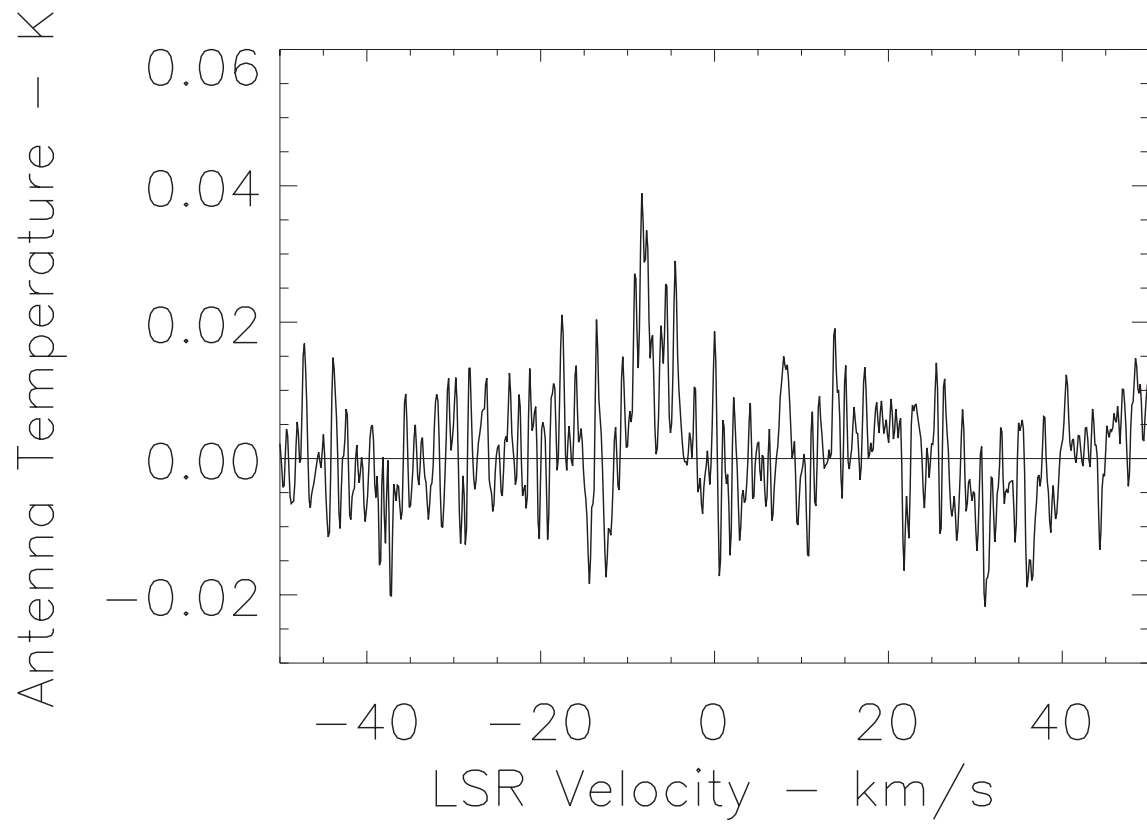


Figure 5.4 Spectrum of the OH 1667 MHz line for the line of sight G92.4–33.0 (see Table 1).

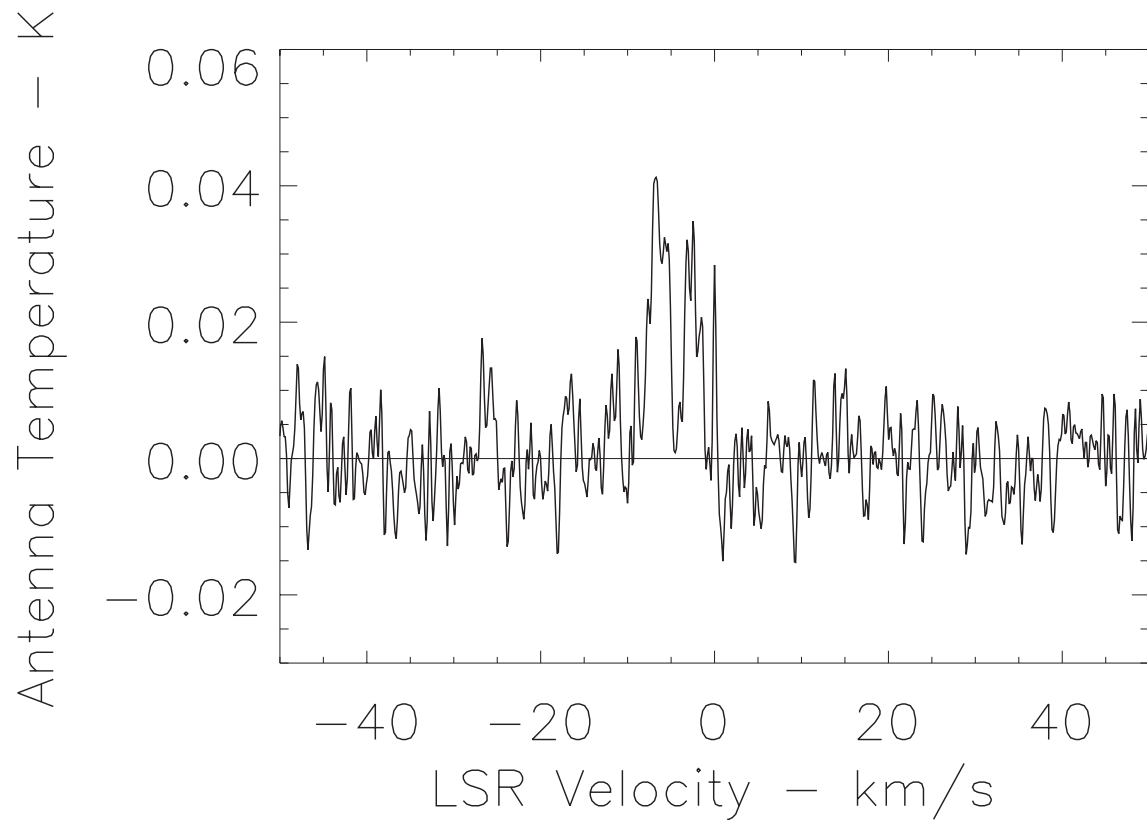


Figure 5.5 Spectrum of the OH 1667 MHz line for the line of sight G94.6–34.0 (see Table 1). The spike at $v_{LSR} = 0.0 \text{ km s}^{-1}$ is internal interference.

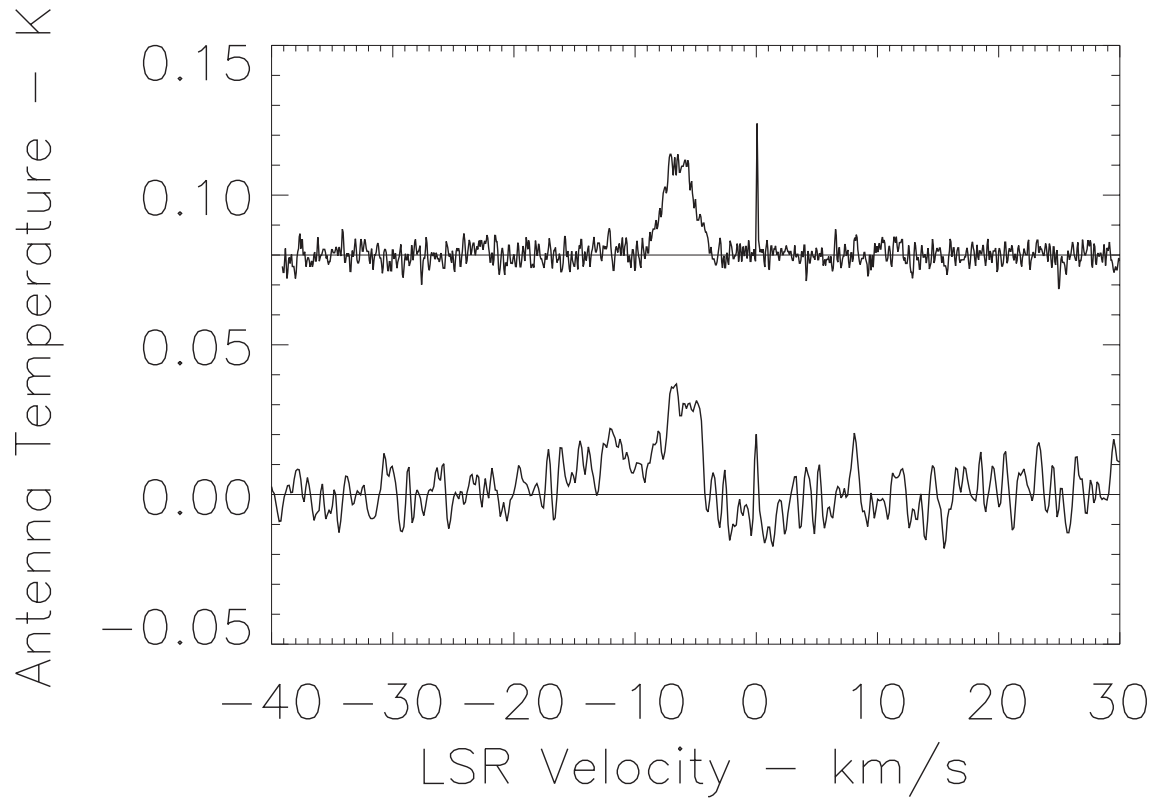


Figure 5.6 Comparison between the CO(1-0) spectrum (top) for position G95.7–32.0 and the equivalent OH 1667 MHz spectrum (bottom). The spike at $v = 0.0 \text{ km s}^{-1}$ in both spectra is due to internal interference. The scale of the CO spectrum has been reduced by a factor of ten. The OH feature at -12 km s^{-1} is only tentatively detected but, if real, it has no counterpart in the CO spectrum.

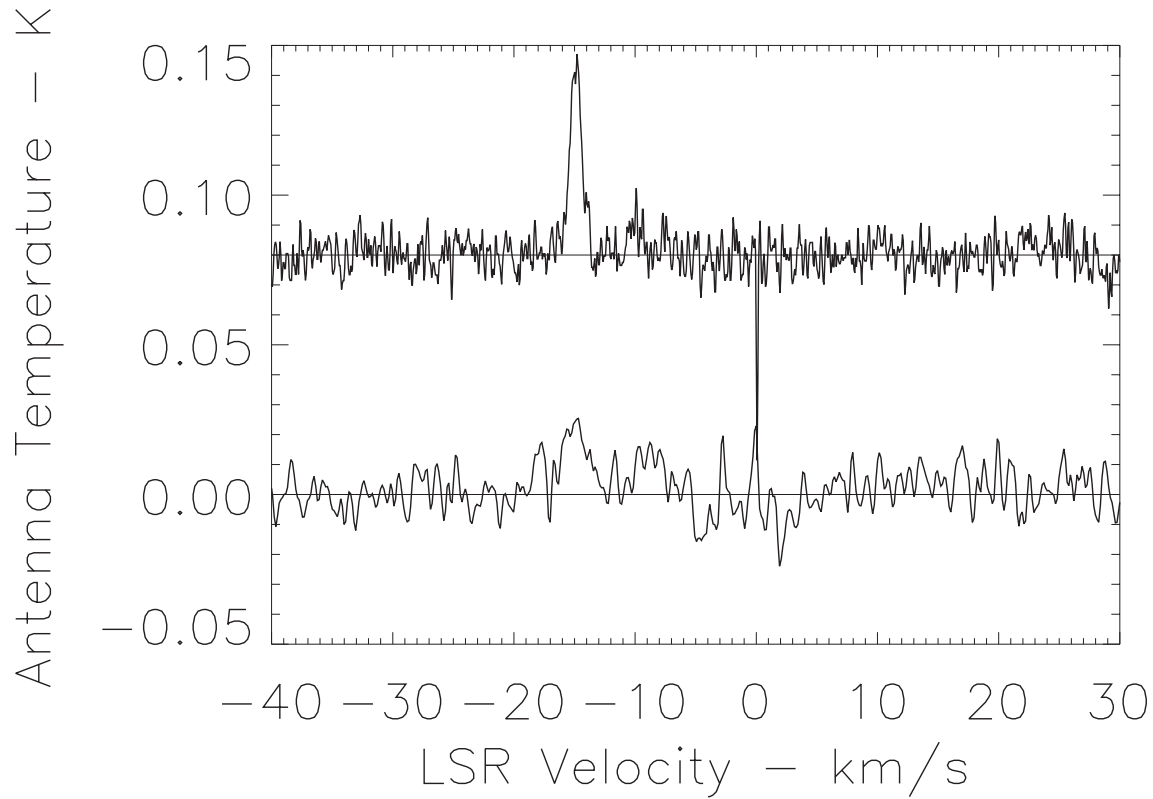


Figure 5.7 Comparison between the CO(1-0) spectrum (top) for position G96.8–30.0 and the equivalent OH 1667 MHz spectrum (bottom). The spike at $v = 0.0 \text{ km s}^{-1}$ in both spectra is due to internal interference. The scale of the CO spectrum has been reduced by a factor of ten. The OH feature at -9 km s^{-1} is only tentatively detected but, if real, it has no clear counterpart in the CO spectrum.

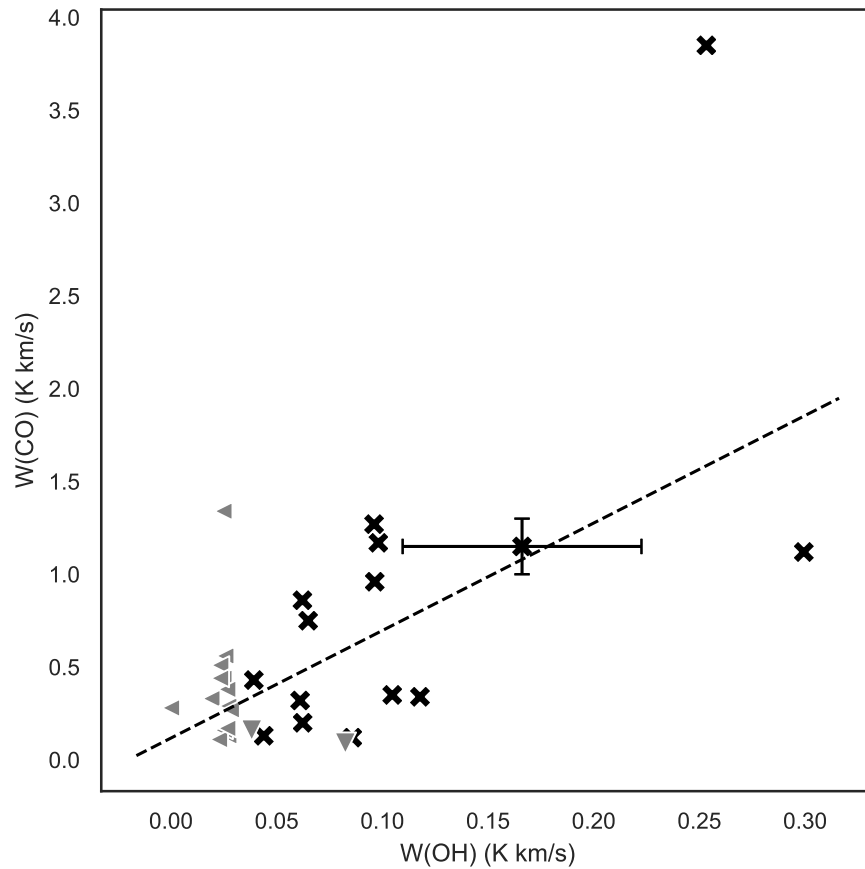


Figure 5.8 The relationship between the velocity-integrated CO(1-0) main beam antenna temperature at 115 GHz, $W(\text{CO})$, and the velocity-integrated OH 1667 MHz brightness temperature, $W(\text{OH})$. The CO data are from Donate & Magnani (2017). The dashed line represents the best fit line to the detections (see text). Representative error bars are shown for one of the detections. Gray arrows represent 2σ upper limits for $W(\text{OH})$ and $W(\text{CO})$ nondetections.

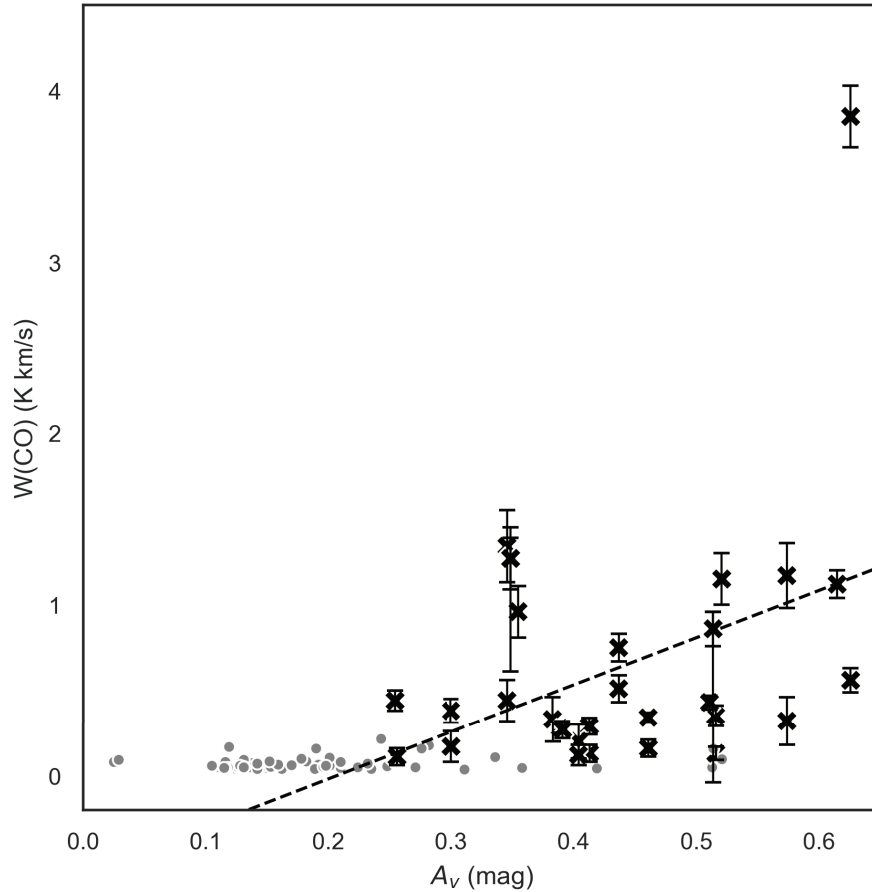


Figure 5.9 The relationship between the velocity-integrated CO(1-0) main beam antenna temperature, $W(\text{CO})$, from Donate & Magnani (2017), and the visual extinction, A_V , from Schlafly & Finkbeiner(2011). The dashed line represents the best fit line for detections only (see text). One-sigma uncertainties for $W(\text{CO})$ are shown for the detections. The grey points without error bars represent 2σ upper limits in $W(\text{CO})$ for non-detections. The uncertainty in A_V is $\approx 16\%$.

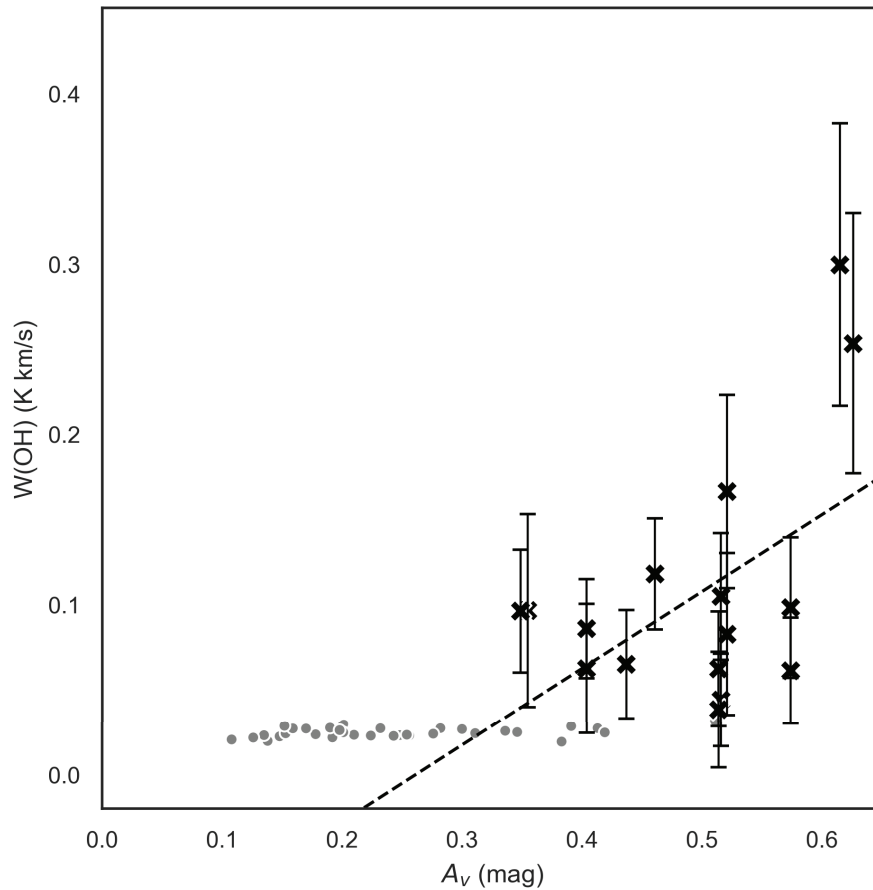


Figure 5.10 The relationship between the velocity-integrated OH 1667 MHz brightness temperature, $W(\text{OH})$, and the visual extinction, A_V , from Schafly and Finkbeiner (2011). The dashed line represents the best fit line for detections only (see text). One-sigma uncertainties, $W(\text{OH})$, are shown for the detections. The grey points without error bars represent 2σ upper limits in $W(\text{OH})$ for the non-detections. The uncertainty in A_V is $\approx 16\%$.

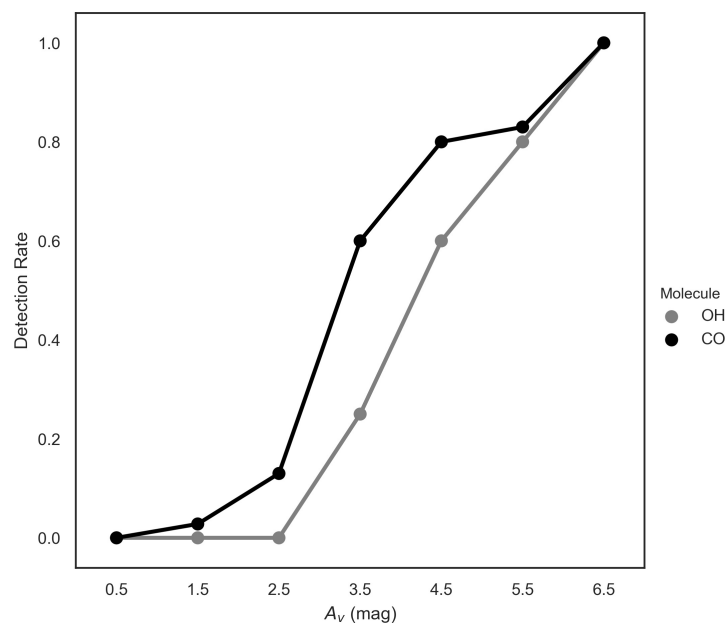


Figure 5.11 Detection rate of the CO(1-0) line (black line) and the OH 1667 MHz line (gray line) as a function of visual extinction in magnitudes. *Correction in Thesis: x-axis values should be divided by 10*

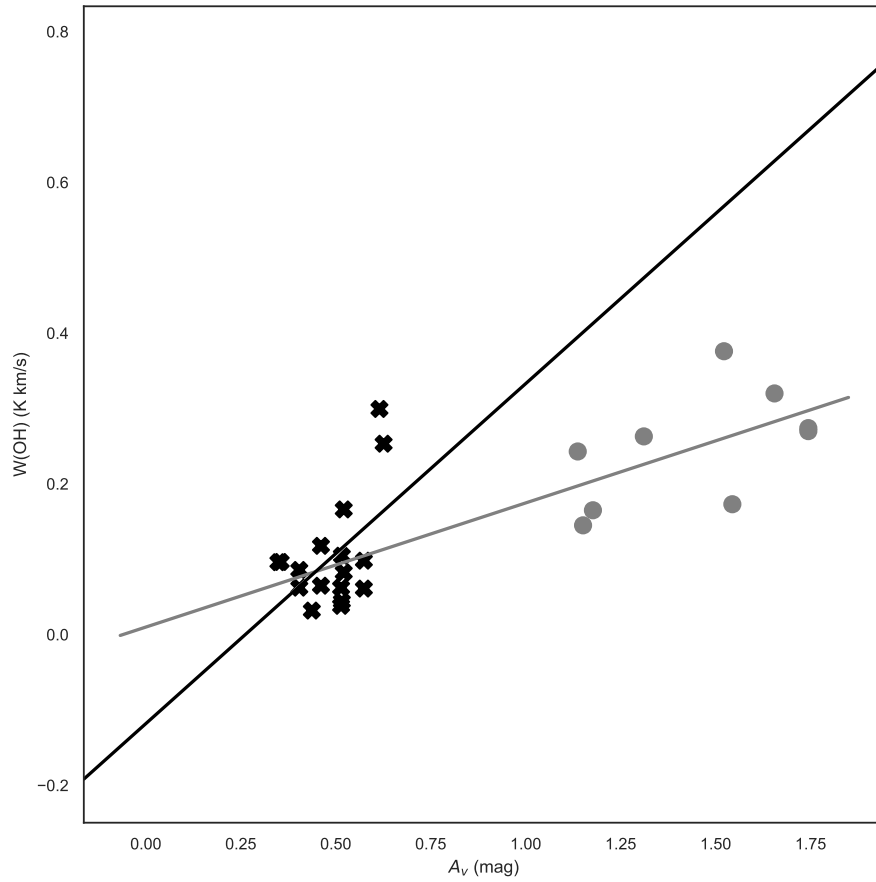


Figure 5.12 Same as Figure 7 but for the OH detections in this paper (black exes) and similar data for the L1642 translucent molecular cloud (gray circles) from Sandell et al. (1981). The black line represents the best fit line for our OH detections and the gray line for the Sandell et al. (1981) detections (see text).

CHAPTER 6

DARK MOLECULAR GAS IN PEGASUS-PISCES¹

by Emmanuel Donate², Samantha Blair³, Zachary Chilton⁴, Codie Gladney⁵, Jeremy W. Gordon⁶, Micah C. Goulart⁷, and Loris Magnani⁸

6.1 ABSTRACT

We examine the molecular content of a large region (~ 2200 square degrees) in Pegasus-Pisces with an estimated dark molecular gas fraction of 59%. Using the extensive CO(1-0) Southern Galactic hemisphere, high-latitude survey by Magnani et al. (2000) we re-examined the CO-detectable mass estimates for the region. By averaging all the CO spectra in subsections ranging in size from $3^\circ \times 3^\circ$ to $15^\circ \times 15^\circ$ we decreased the rms of the averaged CO spectra by factors of 3-10, effectively trading spatial resolution for sensitivity. With the new spectra we are able to make estimates of the CO-detectable mass as a function of sensitivity. Using the optimal estimate, the CO-detectable mass increases from 2200 to 4000 M_\odot , thereby decreasing the dark molecular gas fraction in the region to 0.24. CO(1-0) observations with rms values in the 20-30 mK range can nearly double the molecular mass in regions with diffuse and translucent molecular clouds.

¹Published in Monthly Notices of the Royal Astronomical Society, **486**, 2281 (2019)

²Department of Physics and Astronomy, University of Georgia, Athens, GA 30602, USA

³Department of Natural Sciences, Dalton State College, Dalton, GA 30720, USA

⁴Department of Physics and Astronomy, University of Georgia, Athens, GA 30602, USA

⁵Department of Physics and Astronomy, University of Georgia, Athens, GA 30602, USA

⁶Department of Physics and Astronomy, University of Georgia, Athens, GA 30602, USA

⁷Department of Natural Sciences, Dalton State College, Dalton, GA 30720, USA

⁸Department of Physics and Astronomy, University of Georgia, Athens, GA 30602, USA

6.2 INTRODUCTION

The possible existence of substantial molecular gas in the interstellar medium (ISM) that is not spectroscopically detectable via the CO(1-0) transition at 115.271 GHz was originally proposed by Grenier, Casandjian, & Terrier (2005; hereafter GCT). They use a combination of color-corrected dust maps (Schlegel, Finkbeiner, & Davis 1998; hereafter SFD), gamma-ray data from EGRET (Strong & Mattox 1996), and N(HI) and CO(1-0) emission maps (Dickey & Lockman 1990; Dame, Hartmann, & Thaddeus 2001) to identify regions with substantial gas column density not traced by the HI and CO(1-0) data. These regions appear to form large halos surrounding local molecular clouds and are believed to represent a molecular component dubbed “dark gas” which was supposed to be “invisible in HI, CO, and free-free emission.” The most surprising conclusion of the GCT study is that the mass in the dark gas is comparable to the known molecular mass from CO observations (i.e., a few times $10^9 M_{\odot}$).

The idea of a molecular component not traceable by CO(1-0) emission is not new. Standard models of Photo-Dissociation Regions (PDRs - see Hollenbach & Tielens 1997 and references therein) envision H₂ forming at substantial column densities (10^{19} cm^{-2}) in regions where the carbon is primarily locked up in C⁺ and C⁰. Consequently, the CO abundance is too low for detecting the CO(1-0) emission line at 115.271 GHz. Subsequent work by van Dishoeck & Black (1988) expanded on this by calculating models with the CO/H₂ ratio and N(CO) as a function of N(H₂) - effectively, the radial depth into the PDR. In this work they identify the region where the CO abundance rises precipitously from less than 10^{-6} to nearly 10^{-4} as constituting *translucent* molecular gas. For typical interstellar radiation fields, this regime occurs in regions with visual extinctions in the 1-5 mag range. Molecular gas in lower extinction regions is termed *diffuse* and regions with $A_V \geq 5$ mag constitute the traditional dark molecular clouds (not to be confused with GCT’s dark molecular gas) and the denser regions of Giant Molecular Clouds (GMCs) that have been the object of radio spectroscopic observations since the late 1960s.

A recent theoretical study of dark gas is by Wolfire, Hollenbach, & McKee (2010 – hereafter WHM) who examine the importance of dark gas in a spherical PDR using elaborate models to determine the dark gas fraction as a function of various parameters. They define the dark gas fraction as

$$f_{DG} = [M(R_{H_2}) - M(R_{CO})]/M(R_{H_2}) \quad , \quad (6.1)$$

where $M(R_{H_2})$ is the total molecular mass within the radius of their spherical model cloud in which the hydrogen is molecular, and $M(R_{CO})$ is the total molecular mass in the CO-dominated portion of the cloud. From an observational point of view, the region within R_{CO} would be where CO can be detected via the CO(1-0) line and the region between R_{CO} and R_{H_2} is where the dark gas resides. For GMCs with $M(R_{CO}) = 1 \times 10^6 M_\odot$ and a radiation field $10G_\odot$, WHM find $f_{DG} = 0.28 - 0.31$ for thermal gas pressures of $10^5 - 10^6 \text{ K cm}^{-3}$. This theoretical result compares favorably with what GCT determined for their 4 most massive clouds ($f_{DG} \sim 0.3$). A key finding from WHM is that f_{DG} should increase in regions with lower extinctions since the dark gas portion of the PDR is larger.

The WHM definition of dark gas ignores atomic hydrogen, in most cases the major repository of hydrogen nucleons in the diffuse ISM. A different approach was taken by Reach, Heiles, and Bernard (2015 - hereafter RHB) who used high-resolution HI observations and Planck 353 GHz data to study the gas-to-dust ratio in the diffuse ISM. By defining the fraction of dark gas as the column density of hydrogen nucleons based on the dust content of the region in question divided by the HI column density,

$$f_{dark} = N(H_{tot})/N(HI) \quad , \quad (6.2)$$

they could identify regions where the ratio increased from unity. If $f_{dark} > 1$, then these regions would contain gas not traced by optically thin HI. The reasons for $f_{dark} > 1$ could be ascribed to three scenarios acting singly or in concert: Molecular gas could be present; $N(HI)$ could underestimate the neutral atomic gas content because some portion of the 21 cm

emission is optically thick; Dust grain properties could vary over small spatial scales making the derivation of reliable $N(H_{tot})$ estimates difficult. With this definition, RHB identified 11 isolated interstellar clouds ($\sim 1^\circ$ in angular size), 5 of which are within our region of interest (see §2). When discussing the amount of dark gas in this region we will use both definitions with f_{DG} referring to the WHM definition and f_{dark} to the RHB definition.

The theoretical work on PDRs established that regimes where H_2 was present but CO was too under abundant to be observed had to exist. However, observational evidence of this region is difficult to establish. Part of the reason is that most astronomers focus on the fully molecular part of clouds because of an interest in star formation. Despite that, from the observational point of view, there are several indications that molecular regions without detectable CO emission are observable. Johansson (1979) claimed that the $CH^2\Pi_{1/2}$, $J=1/2$, lambda-doubled, hyperfine, main line transition at 3335 MHz traces more molecular gas along the Galactic plane than noted from the CO Galactic plane surveys. On a smaller scale, Magnani & Onello (1993; and reference therein) find evidence of CH emission without corresponding CO(1-0) emission. Reach, Koo, & Heiles (1994) note more infrared emission from a high-latitude molecular cloud than can be accounted for via HI and CO observations. More recently, Barriault et al. (2010*a, b*) reach the same conclusion for a region near the NCP rich in molecular gas by using excess far-infrared emission from dust and the OH 18 cm main lines as surrogates for H_2 . Moreover, observations by the Planck satellite (Planck Collaboration 2011b) show that there is a dust component traced by its mm and sub-mm continuum emission that does not have associated CO or HI. Locally, this dark gas has a mass that corresponds to 28% of what is estimated from the HI data and a staggering 118% of the CO-traceable molecular gas mass. All these results seem to confirm the GCT assertion that dark gas is present in substantial amounts in the ISM and that the CO(1-0) transition is blind to its presence.

It is important to note, however, that the observationally defined size of such regions will depend on the sensitivity of the CO(1-0) observations. For example, the high-latitude cloud

MBM 40 was sampled over 103 lines of sight in the CO(1-0) line at sensitivities of 50 - 110 mK (1σ rms in antenna temperature, T_R^*) by Cotten & Magnani (2013). They divided the cloud into three regions based on E(B-V) values from SFD. The two inner regions with $E(B-V) \geq 0.12$ and 0.17 mag, respectively, comprise the usual CO extent of the cloud as originally mapped by Magnani, Blitz, & Mundy (1985) or de Vries (1988). The outermost part with $E(B-V) \leq 0.12$ mag had not been observed in CO prior to Cotten & Magnani, but relatively deep integrations (50-80 mK rms) revealed weak CO emission in 13 out of 21 lines of sight with antenna temperatures, T_R^* , as low as 0.11 K. Almost all CO(1-0) Galactic observations in the literature would miss signals at this level, but the higher sensitivity observations only increased the cloud mass by about a third. A similar result was found using the OH 1667 MHz main line by Cotten et al. (2012). It is likely that this additional mass would be considered dark gas using GCT detection criteria in the absence of very sensitive CO or OH (or, possibly, CH) observations.

One of the fields studied by GCT includes a high-latitude region centered on Pegasus-Pisces for which they obtain the ratios of CO-detectable molecular gas, to dark gas, to atomic gas. We will abbreviate these ratios as $H_2:DG:HI$. They call this region “Pegasus”, but we will refer to it as Pegasus-Pisces. The amount of CO-detectable molecular gas in Pegasus-Pisces is determined from estimates of the masses of some of the mapped high-latitude clouds in the region (MBM 53 - 55). From their analysis, the masses of *some* of these clouds from the literature, and available HI surveys, GCT determine $H_2:DG:HI$ for this region to be 0.7: 1.0: 3.4 ($f_{DG} = 0.59$; $f_{dark} = 1.5$), with a total mass of $1.6 \times 10^4 M_\odot$. While the total mass for the region may be correct, the breakdown into $H_2:DG:HI$ depends on the sensitivity of the CO observations of the molecular clouds in the region. For example, Donate and Magnani (2017) made very sensitive observations of a small region in and around the high-latitude molecular cloud MBM 53 and found that the velocity-integrated, main beam, CO(1-0) antenna temperature increased by more than a factor of two compared to earlier, less sensitive observations. This, in turn, led to a higher estimate of the molecular

mass which, if extended throughout the Pegasus-Pisces region studied by GCT, changes the $\text{H}_2:\text{DG}:\text{HI}$ ratio there to 1.4: 1.0: 4.9 ($f_{DG} = 0.42$; $f_{dark} = 1.5$).

We can check the results of GCT for the Pegasus-Pisces region using the unbiased CO(1-0) survey of the high-latitude Southern Galactic Hemisphere (SGH) made by Magnani et al. (2000). This survey was made to determine the distribution of molecular gas at high Galactic latitudes, with nearly one-half of the southern Galactic hemisphere at $b \leq -30^\circ$ surveyed in the CO (1-0) transition at 115 GHz. The sampling was done on a locally Cartesian grid with 1° (true angle) spacing in Galactic longitude and latitude. Of the 11,478 possible points in the grid, the 4982 that rise above an elevation of 30° from Cambridge, Massachusetts, the site of the Harvard-Smithsonian Center for Astrophysics 1.2 m millimeter-wave telescope used for the survey, were observed to an rms of $T_A^* \sim 0.1$ K. A portion of this CO(1-0) survey covers 86% of the Pegasus-Pisces region from GCT.

In this paper we use the CO data from the SGH high-latitude survey (hereafter SGH-HL) to check the $\text{H}_2:\text{DG}:\text{HI}$ ratios obtained by GCT, and we examine how increasing the sensitivity of the SGH-HL changes the ratios. The paper is organized as follows: We describe in §2 the results of the SGH-HL survey for Pegasus-Pisces and describe the previously mapped molecular clouds in this region in an effort to determine the overall molecular mass from these earlier observations. From the CO data in the SGH-HL survey we derive a molecular mass in Pegasus-Pisces in §3. In §4 we increase the sensitivity of the SGH-HL survey by averaging spectra over larger regions, and see how the detection rate changes with more sensitive CO observations. In §5 we discuss how the ratio of CO-detectable vs. CO-non-detectable molecular gas (which we call “CO-dark” gas) changes as a function of sensitivity in the CO(1-0) observations, and we summarize our results in §6.

6.3 PREVIOUS CO DETECTIONS IN PEGASUS-PISCES

The area covered by the SGH-HL survey is shown in Figure 1 of Donate and Magnani (2017) with the black box denoting GCT’s Pegasus region. However, the SGH-HL survey

begins at $b = -30^\circ$ while the GCT Pegasus region begins at $b = -26^\circ$. There is thus 1.17 times more area there than what is covered by the SGH-HL survey. We will account for the possible mass in this missing area in §3. Of the 4982 grid points which were observed in the SGH by Magnani et al. (2000), 2080 are located within the region that overlaps the GCT Pegasus field. There were 48 CO detections in this region for a detection rate of 0.0231.

Within the region there are several well-known high-latitude molecular clouds including the MBM 53 - 55 complex, which was fully mapped in CO by Yamamoto et al. (2003) who derive a total mass for the complex (which also includes the high-latitude cloud HLCG 92-35) of $1200 M_\odot$. To the east and southeast of the MBM 53 - 55 region are 8 detections from SGH-HL which are part of a large shell of molecular and atomic gas studied by Yamamoto et al. (2006) and Chastain et al. (2006). Yamamoto et al. detected 78 small clouds in the region using observations of the CO(1-0) line with 1σ rms noise sensitivity of ~ 0.35 K. They used a mapping grid that was three times the beam size of their telescope with better sampling if CO was detected in a particular region, and estimated that the total mass contained in the 78 clouds is $64 M_\odot$.

Chastain et al. (2006) took a different approach by using the SFD E(B-V) dust maps as a guide to where CO emission might be detectable. They observed 106 positions in the dust shell identified as G107-45 in the Kiss, Moór, & Tóth (2004) infrared loop catalog and detected CO(1-0) or CO(2-1) emission in 65 of them. The 1σ rms sensitivity of these observations was significantly better than the one used by Yamamoto et al. (2006): 0.05 K vs. 0.35 K. Because Chastain et al. did not map the shell, they estimated its mass by assuming that all locations in the shell region with $E(B-V) \geq 0.15$ mag could potentially be detected in CO. They then used the detection rate from their observations (61%) to estimate the fraction of the dust-selected regions that might actually contain CO if the whole region had been mapped down to a sensitivity of 0.05 K rms. Using a mean CO integrated antenna temperature, a CO/H₂ conversion factor of $1.8 \times 10^{20} [\text{K km s}^{-1}]^{-1} \text{ cm}^{-2}$, and a distance to the shell of 150 pc, they estimate the molecular mass in the shell to be 1200 - 1300 M_\odot ,

nearly a factor of 20 greater than the estimate by Yamamoto et al. (2006) based on the number of small clouds found by their less sensitive survey.

East of the shell at $\ell \sim 130^\circ$, $b \sim -45^\circ$ are the high-latitude molecular clouds MBM 3 and MBM 4. The main portion of MBM 3 has been mapped in CO(1-0) by Shore et al. (2006) with a mass estimate of $54 M_\odot$. There is likely more molecular gas in the environs of the cloud but no complete maps exist in the literature, as is the case for all of MBM 4.

West of the MBM 53 - 55 complex, there are four detections from the SGH-HL survey three of which correspond to previously-known features, and one which was a new detection at the time of the survey. Two of the detections correspond to the molecular cloud associated with the well-studied line of sight to HD 210121 (de Vries & van Dishoeck 1988). This cloud was mapped in CO(1-0) by Gredel et al. (1992) with an estimated mass of $334 M_\odot$. The other previously-identified feature is DIR071-43, a region of excess infrared emission identified by Reach, Wall, & Odegard (1998) but never mapped in CO to our knowledge.

There are other known molecular clouds in the region which were not picked up by the SGH-HL survey because they are likely to be smaller than the grid spacing of the survey (1°). These clouds are MBM 49 - 52, and G61-34 (the latter object was found during the high-latitude “blind” CO survey by Magnani, Lada, & Blitz 1986). These are all small objects and the only ones with mass estimates are MBM 49 and MBM 51 with $7 M_\odot$ and $1 M_\odot$, respectively (see Magnani, Hartmann, & Speck 1996).

Thus, previous CO maps of some of the clouds in the Pegasus-Pisces region produce estimates of the molecular mass contained in these clouds ranging from $1700 - 2900 M_\odot$. This range represents a lower limit in that there are known clouds in this region that have not been mapped in CO fully or at all. These mass estimates are important because GCT quote values of the molecular mass in the Pegasus-Pisces region in normal H_2 and dark H_2 of $2200 M_\odot$ and $3100 M_\odot$, respectively. If the already-detected molecular mass is greater than $2200 M_\odot$, then any mass above that limit must come from the balance of dark gas, thereby reducing its estimate. GCT seem to imply that their estimate of the normal H_2 in the region

comes solely from the MBM 53 - 55 clouds as mapped by Yamamoto et al. (2003). Those authors quote $1200 M_{\odot}$ and not $2200 M_{\odot}$ because of differences in the adopted X_{CO} value (see discussion in Donate & Magnani 2017).

In summary, the GCT value ($2200 M_{\odot}$) for Pegasus-Pisces for the CO-detectable molecular mass is a lower limit and, by including all known clouds in the region, with the mass estimates provided by the original observers, we could have a value as high as $\sim 2900 M_{\odot}$ (or as low as $1700 M_{\odot}$ – demonstrating how large the uncertainties can be in determining the mass of molecular clouds using CO data). Unfortunately, each set of independently studied clouds were observed and analyzed differently, with different sensitivities, sampling, and values of the CO-H₂ conversion factor (defined as $X_{CO} = N(\text{H}_2)/W_{CO}$ where W_{CO} is the velocity-integrated main-beam antenna temperature). This makes adding all the separate mass values into a total CO-detectable molecular mass in the region problematic. In the next section, we will estimate the mass of H₂ in the region solely from the results of the SGH-HL survey.

6.4 THE H₂ MASS IN PEGASUS-PISCES FROM THE SGH-HL SURVEY

We use the SGH-HL survey's 48 detections in the Pegasus-Pisces region to determine the mass of H₂ and directly compare that number to the GCT estimate and the range of masses from previous observations. We can characterize the mass in a given region as

$$M_{H_2} = \overline{N}(\text{H}_2) A_{H_2} \mu m_H \quad (6.3)$$

where $\overline{N}(\text{H}_2)$ is the average column density in the region, A_{H_2} is the physical area in the region that contains CO-detectable molecular gas, μ is the molecular weight (which we take to be 2.0 for the remainder of this paper since we do not want to include the helium contribution to the H₂ mass), and m_H is the mass of the hydrogen atom.

The quantity $\overline{N}(\text{H}_2)$ can be estimated from the average velocity-integrated CO(1-0) antenna temperature (defined as $W_{CO} = \int T_{mb} dv$) of the 48 detections, and a value for

X_{CO} . The physical area can be related to the observed angular area by $A_{H_2} = \Omega d^2$, where Ω is the solid angle subtended by the region and d is the distance. Normally, estimating the distance to the various clouds in the region would be difficult, but GCT use a distance of 150 pc for all the molecular gas in this region so we will do the same. We are ignoring some of the recent distance estimates to the clouds in this region from the Schlafly et al. (2014) because we wish to compare our mass estimate with that of GCT. Of course, the SGH-HL survey is nowhere near fully sampled so we define the area with molecular emission as the region from the survey that overlaps the GCT Pegasus region (Ω_{PP}) times the detection rate (which we will define as D). We are assuming that the detection rate is derived from enough points to be well-sampled and representative of the amount of molecular gas in the region detectable using the CO(1-0) line.

Finally, we must correct for the extra area that GCT included in their calculations, i.e., the strip from $-30^\circ \leq b \leq -26^\circ$. The GCT-defined region covers 0.6717 steradians while the overlapping region from the SGH-HL survey covers 0.5749 steradians. If we assume that the detection rate in the extra area is the same as in the region $-60^\circ \leq b \leq -30^\circ$, then a multiplicative factor of 1.17 will account for the missing region. Thus, equation 2 becomes

$$M_{H_2} = 1.17[\overline{W}_{CO} X_{CO} \Omega_{PP} D d^2 \mu m_H] \quad (6.4)$$

For the 48 detections in Ω_{PP} , \overline{W}_{CO} is 1.96 K km s⁻¹ from Table 1 of Magnani et al. (2000). We choose a value for X_{CO} of 1.8×10^{20} [K km s⁻¹]⁻¹ cm⁻² (same as GCT), Ω_{PP} is 0.5749 steradians, and D is 0.0231. We are using this value of X_{CO} not because we believe it is the correct value for the clouds in this region, but only because this is the value used by GCT obtaining their CO(1-0) mass estimate and we wish to compare our results directly with theirs. For diffuse and translucent clouds it is not clear from a theoretical point of view that a single X_{CO} should apply to these objects since they are not in virial equilibrium. A value of X_{CO} can be applied to high-latitude clouds (most of which are diffuse) but it has to be calibrated separately for each cloud and large variations from cloud to cloud are common

(see discussion in Magnani & Onello 1995). In keeping with GCT we also choose $d=150$ pc as the distance of the clouds in the region and thus obtain a molecular mass of $1980 M_{\odot}$. This represents the H_2 mass as determined from the CO(1-0) observations from the SGH-HL survey which has a 1σ rms sensitivity of 0.1 K in T_{mb} . The equivalent $H_2:DG:HI$ ratio would be 0.6: 1.0: 3.2. This estimate is consistent with both the quoted GCT value and the lower mass limit derived in §2 by adding the masses of the mapped known clouds in the region. But the issue that this paper deals with is how does the detection rate change if we had more sensitive CO(1-0) observations? We cannot re-observe the SGH-HL positions at a better sensitivity, but we can average the spectra over given regions in effect trading resolution for sensitivity. In the next section we will examine how D and \overline{W}_{CO} change with sensitivity.

6.5 AVERAGING THE SPECTRA TO INCREASE THE SENSITIVITY OF THE SURVEY

The SGH-HL survey was carried out using a unique position-switching technique (see Hartmann, Magnani, and Thaddeus (1998) for details). Basically, the off-position for any given on-position was exactly one degree south of the on-position in Galactic latitude. Thus a CO source located exclusively in the off-position would result in a “negative” emission line and the possibility that emission at the same intensity and velocity in both the on and the off positions would cancel completely. Hartmann, Magnani, & Dame (1998) argue that this technique is effective for searching for high-latitude molecular clouds and the complete cancellation scenario for any given spectrum is extremely unlikely. In summary, the observing technique used for the SGH-HL survey leads to a single spectrum for two positions (each pair separated by one degree in Galactic latitude).

We cannot re-survey the SGH at higher sensitivity. However, by averaging together the spectra over a given region, we can effectively trade angular resolution for sensitivity. Our average spectra are made for regions of varying sizes ranging from $3^{\circ} \times 3^{\circ}$ to $15^{\circ} \times 15^{\circ}$. These sizes are not the true sizes on the sky, but, rather, $\Delta\ell$ and Δb . Thus, when averaging spectra

we did not correct for the variation of $\cos(b)$ over a given region. However, the SGH-HL survey begins at $b = -30^\circ$ and ends at $b = -60^\circ$, so that the changes in $\cos(b)$ over the ranges of Δb are not a serious problem.

6.5.1 SYSTEMATIC AVERAGING

We systematically averaged the spectra in areas of varying size: $3^\circ \times 3^\circ$, $5^\circ \times 5^\circ$, $6^\circ \times 6^\circ$, $10^\circ \times 10^\circ$, $15^\circ \times 15^\circ$, and we also averaged all of the spectra within the entire Pegasus-Pisces region. We illustrate the technique with the $5^\circ \times 5^\circ$ co-added regions as an example in Table 1. The first two entries designate the boundaries of the square region within which all spectra were averaged. The number of spectra which were added together is shown in column 3 with the resulting 1σ rms in column 4. The number of spectra varies widely from region to region because of the SGH-HL sampling pattern. Moreover, because the survey was made with a one-degree true-angle spacing, the number of spectra in a given area decreases with more negative latitudes and, thus, the noise level increases with $|b|$.

Column 5 lists the quality of the detection in terms of the rms value and columns 6 and 7 tabulate W_{CO} and the range in velocity over which W_{CO} is measured. We considered signals over 6σ to constitute a detection. The eight detections from the $5^\circ \times 5^\circ$ regions are shown in Figure 1. Since our averaged spectra over the $5^\circ \times 5^\circ$ regions are sums of the spectra in the SGH-HL survey, it is possible to have negative CO(1-0) lines because of the preponderance of spectra in a given region with CO emission in the off position (e.g., Fig. 1a), or a combination of positive and negative signals (e.g., Fig. 1h). If any kind of signal, positive, negative, or combination of both appeared in the final averaged spectrum for a region at the $\geq 6\sigma$ level, then that region was considered to have a detection and the parameters of that detection are listed in columns 5-7. Figures 1a-h show all of the averaged spectra that were considered detections for the $5^\circ \times 5^\circ$ regions.

6.5.2 THE DETECTION RATE AND \overline{W}_{CO} AS FUNCTIONS OF SENSITIVITY

The factor that changes in equation 3 as one averages over regions of different sizes is the product of D and \overline{W}_{CO} . Donate and Magnani (2017) show that higher sensitivity CO(1-0) observations result in more detections and higher values of W_{CO} in the environs of single a diffuse molecular cloud. Thus, as our averaged regions produce composite spectra with lower rms values, the detection rate, D , should increase. A look at Table 2 shows this to be the case for the $3^\circ \times 3^\circ$ and $5^\circ \times 5^\circ$ regions, but the trend reverses for the $6^\circ \times 6^\circ$ regions, then picks up again for the $10^\circ \times 10^\circ$ regions before dropping to zero for the $15^\circ \times 15^\circ$ (and larger ones had we produced them). This is expected because molecular gas detected via the CO(1-0) emission line is not ubiquitous in the ISM. Molecular clouds may be more extended than conventional CO mapping reveals, but they do have edges where the CO abundance drops sufficiently that CO(1-0) detection is impossible in emission and they can be deemed to terminate there - as far as CO-traceable regions. The surrounding region contains CO molecules and even substantial H_2 , but these dark molecular regions must be detected by other means [e.g., gamma-ray and dust emission (GCT), C^+ (Langer et al. (2010), Langer et al. (2014), and, possibly, OH (Allen et al. 2012; 2015)].

Figure 2 shows how \overline{W}_{CO} and the product $D\overline{W}_{CO}$ and the detection rate change with the area of the averaged regions. The average W_{CO} value for each of the summed regions drops steadily, as expected, and the product of $D\overline{W}_{CO}$ first rises and then drops to zero. The peak occurs for regions of size $5^\circ \times 5^\circ$. This is likely some sort of convolution of the size of typical clouds and the ideal sensitivity level for revealing the most CO-detectable molecular gas. The clear increase in $D\overline{W}_{CO}$ for the $3^\circ \times 3^\circ$ and $5^\circ \times 5^\circ$ regions - compared to the other regions - indicates that the trade-off between increased sensitivity (27-36 mK vs. ~ 100 mK) and decreased spatial sampling is optimized in this range.

6.6 CO-DETECTABLE VS. CO-DARK GAS

If we assume that the results from the $3^\circ \times 3^\circ$ and $5^\circ \times 5^\circ$ averaging are optimal as far as rms and sampling, the ratio of $D\overline{W}_{CO}$ doubles compared to that of the original survey. This indicates the increase in mass in the region had the SGH-HL survey been conducted with more sensitivity would also double. Applying the new $D\overline{W}_{CO}$ factor to the mass estimate from §3 yields the mass estimate likely to result from more sensitive CO(1-0) observations: $\approx 4000 M_\odot$. We note again that this result is based on assuming an X_{CO} of $1.8 \times 10^{20} [\text{K km s}^{-1}]^{-1} \text{ cm}^{-2}$ which may not be the correct value for all the clouds. But what choosing this value allows us to do is to compare our results to those of GCT.

If we take this to be the true CO-detectable mass in Pegasus-Pisces, then the increase in CO-detectable mass decreases the mass in CO-dark gas to $1300 M_\odot$ and the dark gas inventory would have decreased by a factor of two to three. This is similar to the result obtained by Donate and Magnani (2017). These results indicate that the $\text{H}_2:\text{DG}:\text{HI}$ ratio would now be 3.1: 1.0: 8.2 ($f_{DG} = 0.24$; $f_{dark} = 1.5$). CO-dark gas does exist in the Pegasus-Pisces region, but the bulk of molecular gas (76%) there can be traced by sensitive CO(1-0) observations. Because the Pegasus-Pisces region contains only diffuse and translucent molecular clouds, it is not clear whether our results can be extended to regions dominated by GMCs. Nevertheless, in diffuse and translucent environments sensitive CO(1-0) observations appear to trace most of the molecular gas in the region.

6.7 SUMMARY

We used the SGH-HL survey to examine a region studied by GCT in order to determine its dark gas inventory. They used gamma-ray, infrared and HI data to determine that the total gas mass, $1.6 \times 10^4 M_\odot$, could be divided into CO-detectable, CO-dark, and atomic components, with a $\text{H}_2:\text{DG}:\text{HI}$ ratio of 0.7: 1.0: 3.4. The region, in Pegasus-Pisces, is sampled by the SGH-HL survey with 2080 CO(1-0) pointings. By inventorying all the molecular mass

in the region we determined the H₂:DG:HI ratios of 0.6: 1.0: 3.2 is similar to the GCT values. The data used to determine the CO-detectable molecular mass in the region was based on the SGH-HL survey data with 1σ rms values of ~ 0.1 K. More sensitive CO observations should reveal the presence of more molecular gas and thus further decrease the dark molecular gas inventory. We achieved this by averaging over larger and larger regions of the SGH-HL survey, effectively trading angular resolution for sensitivity. As expected, we found that, initially, as the area of the averaged spectra increased, so did the detection rate. Once the area was greater than 225 square degrees, the detection rate then decreased to zero. The average W_{CO} of the detections in a given area decreases steadily from the original survey and so the product of the two, the relevant quantity for determining the molecular mass in the region, increases to a maximum for the areas with 25 square degrees, to then rapidly reach zero (see Figure 2).

The above behavior allows us to consider the sensitivity of the 16-25 square degree regions ($\sim 27 - 36$ mK) to be optimal for detecting CO(1-0) emission. The product of the accompanying detection rate and the average W_{CO} then leads to an increase in the molecular mass in Pegasus-Pisces from 2000 M_{\odot} to 4000 M_{\odot} . Because the increase in CO-detectable gas must come at the expense of CO-dark gas, the revised values for Pegasus-Pisces based on the GCT data are 4000, 1300, 10700 M_{\odot} , for the CO-detectable, CO-dark, and HI components, respectively. In terms of the H₂:DG:HI ratio employed by GCT this is 3.1: 1.0: 8.2 ($f_{DG} = 0.24$; $f_{dark} = 1.5$). The dark gas content of the region has decreased by a factor of two to three by significantly lowering the rms of the observations (from ≈ 100 mK to 20-30 mK). These results are consistent with those made by Donate and Magnani (2017) based on a much smaller region in Pegasus-Pisces centered on the high-latitude cloud MBM 53. The CO(1-0) emission line, when integrated to rms values in the 20-30 mK range, can detect significantly more molecular gas than is seen by conventional CO surveys.

ACKNOWLEDGMENTS

We thank the referee, Dr. Bill Reach, for comments which greatly clarified the discussion of the CO mass estimates in our studied region. We also acknowledge Dr. Tom Dame who provided several spectra from the Harvard-Smithsonian 1.2 m millimeter-wave telescope as we were testing the averaging procedure described in §4. This research has made use of the NASA/IPAC Extragalactic Database (NED) which is operated by the Jet Propulsion Laboratory, California Institute of Technology, under contract with the National Aeronautics and Space Administration.

Table 6.1 Results of $5^\circ \times 5^\circ$ co-added regions.

region boundary ℓ, b in deg	region boundary ℓ, b in deg	number of spectra	rms mK	detection quality	W_{CO} K km s $^{-1}$	vel. range km s $^{-1}$
49.2, -34	54.2, -30	15	24			
49.2, -40	54.2, -36	15	29			
49.2, -46	54.2, -42	10	30			
49.2, -52	54.2, -48	12	27			
49.2, -58	54.2, -54	9	30			
54.3, -34	59.3, -30	12	26			
54.3, -40	59.3, -36	12	29			
54.3, -46	59.3, -42	15	28			
54.3, -52	59.3, -48	8	33			
54.3, -58	59.3, -54	9	35			
59.4, -34	64.4, -30	15	25			
59.4, -40	64.4, -36	12	28			
59.4, -46	64.4, -42	12	28			
59.4, -52	64.4, -48	4	49			
59.4, -58	64.4, -54	9	34			
64.5, -34	69.5, -30	15	22			
64.5, -40	69.5, -36	12	25			
64.5, -46	69.5, -42	12	27			
64.5, -52	69.5, -48	11	24	11σ	1.69 ± 0.16	$-10 \rightarrow 10$
64.5, -58	69.5, -54	9	28			
69.6, -34	74.6, -30	12	27			
69.6, -40	74.6, -36	15	24			
69.6, -46	74.6, -42	14	29			
69.6, -52	74.6, -48	9	32			
69.6, -58	74.6, -54	8	32			
74.7, -34	79.7, -30	15	26			
74.7, -40	79.7, -36	12	26			
74.7, -46	79.7, -42	12	26			
74.7, -52	79.7, -48	12	29			
74.7, -58	79.7, -54	9	30			
79.8, -34	84.8, -30	15	26			
79.8, -40	84.8, -36	12	28			
79.8, -46	84.8, -42	12	26			
79.8, -52	84.8, -48	9	36			
79.8, -58	84.8, -54	9	32			
84.9, -34	89.9, -30	12	25			
84.9, -40	89.9, -36	12	27	7σ	0.81 ± 0.11	$-9 \rightarrow -2$
84.9, -46	89.9, -42	14	25	11σ	1.23 ± 0.11	$-13 \rightarrow -5$

Table 6.2 Results of $5^\circ \times 5^\circ$ co-added regions, continued

region boundary ℓ, b in deg	region boundary ℓ, b in deg	number of spectra	rms mK	detection quality	W_{CO} K km s $^{-1}$	vel. range km s $^{-1}$
84.9, -52	89.9, -48	9	33			
84.9, -58	89.9, -54	9	32			
90.0, -34	95.0, -30	15	23	9σ	0.83 ± 0.09	$-11 \rightarrow -4$
90.0, -40	95.0, -36	15	26			
90.0, -46	95.0, -42	13	24			
90.0, -52	95.0, -48	12	32			
90.0, -58	95.0, -54	9	36			
95.1, -34	100.1, -30	15	24			
95.1, -40	100.1, -36	14	25			
95.1, -46	100.1, -42	12	29			
95.1, -52	100.1, -48	9	33			
95.1, -58	100.1, -54	9	32			
100.2, -34	105.2, -30	12	25	6σ	0.38 ± 0.06	$-10 \rightarrow -8$
100.2, -40	105.2, -36	12	26			
100.2, -46	105.2, -42	9	30			
100.2, -52	105.2, -48	12	26			
100.2, -58	105.2, -54	9	36			
105.3, -34	110.3, -30	15	24			
105.3, -40	110.3, -36	12	26			
105.3, -46	110.3, -42	12	28			
105.3, -52	110.3, -48	9	31			
105.3, -58	110.3, -54	8	32			
110.4, -34	115.4, -30	12	26			
110.4, -40	115.4, -36	15	25	6σ	0.46 ± 0.08	$-8 \rightarrow -4$
110.4, -46	115.4, -42	12	27			
110.4, -52	115.4, -48	9	32			
110.4, -58	115.4, -54	9	31			
115.5, -34	120.5, -30	15	24			
115.5, -40	120.5, -36	18	23			
115.5, -46	120.5, -42	14	25			
115.5, -52	120.5, -48	17	22			
115.5, -58	120.5, -54	9	34			
120.6, -34	125.6, -30	15	24			
120.6, -40	125.6, -36	12	27			
120.6, -46	125.6, -42	12	28			
120.6, -52	125.6, -48	12	28			
120.6, -58	125.6, -54	9	32			
125.7, -34	130.7, -30	12	28			

Table 6.3 Results of $5^\circ \times 5^\circ$ co-added regions, continued

region boundary ℓ, b in deg	region boundary ℓ, b in deg	number of spectra	rms mK	detection quality	W_{CO} K km s $^{-1}$	vel. range km s $^{-1}$
125.7, -40	130.7, -36	12	27			
125.7, -46	130.7, -42	12	29	6σ	0.75 ± 0.12	$-13 \rightarrow -6$
125.7, -52	130.7, -48	12	28			
125.7, -58	130.7, -54	9	35			
130.8, -34	135.8, -30	15	25			
130.8, -40	135.8, -36	15	24			
130.8, -46	135.8, -42	12	28	14σ	1.50 ± 0.11	$-10 \rightarrow -0$
				6σ	0.61 ± 0.10	$+30 \rightarrow +39$
130.8, -52	135.8, -48	9	33			
130.8, -58	135.8, -54	10	32			
135.9, -34	140.9, -30	15	25			
135.9, -40	140.9, -36	12	26			
135.9, -46	140.9, -42	17	23			
135.9, -52	140.9, -48	12	31			
135.9, -58	140.9, -54	9	36			

Table 6.4 Results from summing over regions of varying size.

region size	sampling elements	average rms in mK	number of detections ^a	detection rate (D)	\overline{W}_{CO} K km s $^{-1}$	$D\overline{W}_{CO}$ K km s $^{-1}$
survey	2080	~ 100	48	0.023	1.96	0.045
$3^\circ \times 3^\circ$	176	36	8	0.045	1.79	0.081
$5^\circ \times 5^\circ$	90	27	8	0.089	1.08	0.096
$6^\circ \times 6^\circ$	75	24	3	0.040	0.78	0.031
$10^\circ \times 10^\circ$	27	16	2	0.074	0.40	0.030
$15^\circ \times 15^\circ$	12	10	0	0.0	0.0	0.0
entire region	1	4	0	0.0	0.0	0.0

^a Detections are regions with W_{CO} at 6σ or higher levels.

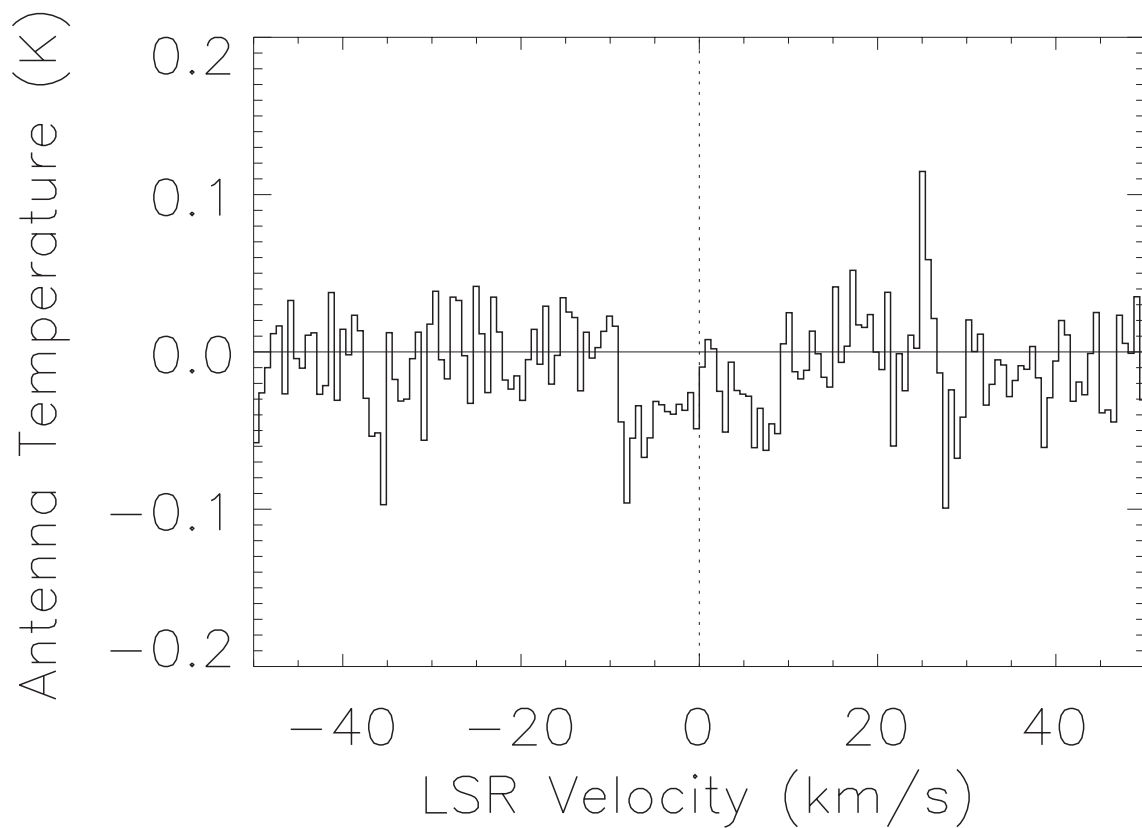


Figure 6.1 CO(1-0) spectrum from the SGH-HL survey made by averaging all the spectra in a $5^\circ \times 5^\circ$ region centered on $(\ell, b) = (67^\circ, -52^\circ)$. The parameters of the detection are listed in Table 1. The absorption-like feature from $v_{LSR} = -10$ to $+10$ km s $^{-1}$ is negative because of the position-switching scheme used in the SGH-HL survey (see §4 and Hartmann, Magnani, & Thaddeus (1986)). A negative signal indicates that there is more emission in the off-position than the on-position (see Magnani et al. 2000, for details). The feature at ~ 25 km s $^{-1}$ km does not meet our 6σ threshold for detections.

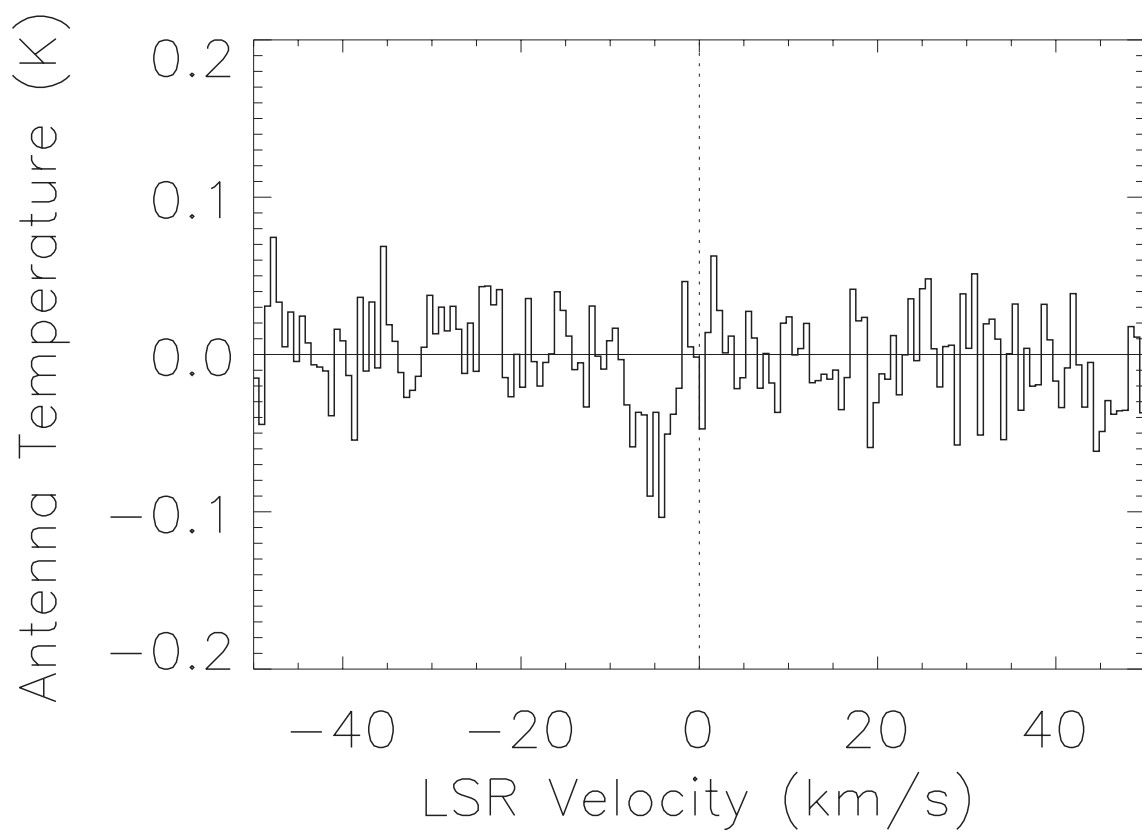


Figure 6.2 Same as Figure 2a for the $5^\circ \times 5^\circ$ region centered on $(\ell, b) = (87.4^\circ, -38.0^\circ)$.

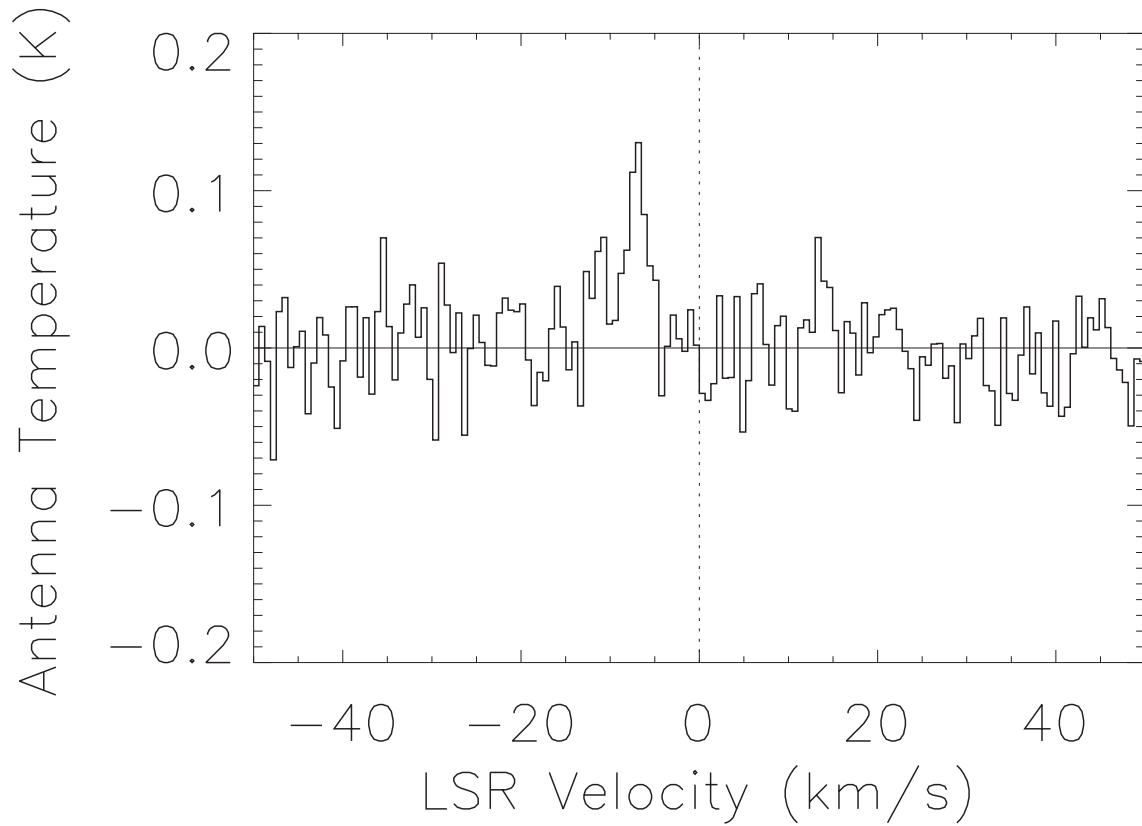


Figure 6.3 Same as Figure 2a for the $5^\circ \times 5^\circ$ region centered on $(\ell, b) = (87.4^\circ, -44.0^\circ)$. A positive signal indicates that there is more emission in the on-position than the off-position (see Magnani et al. 2000, for details).

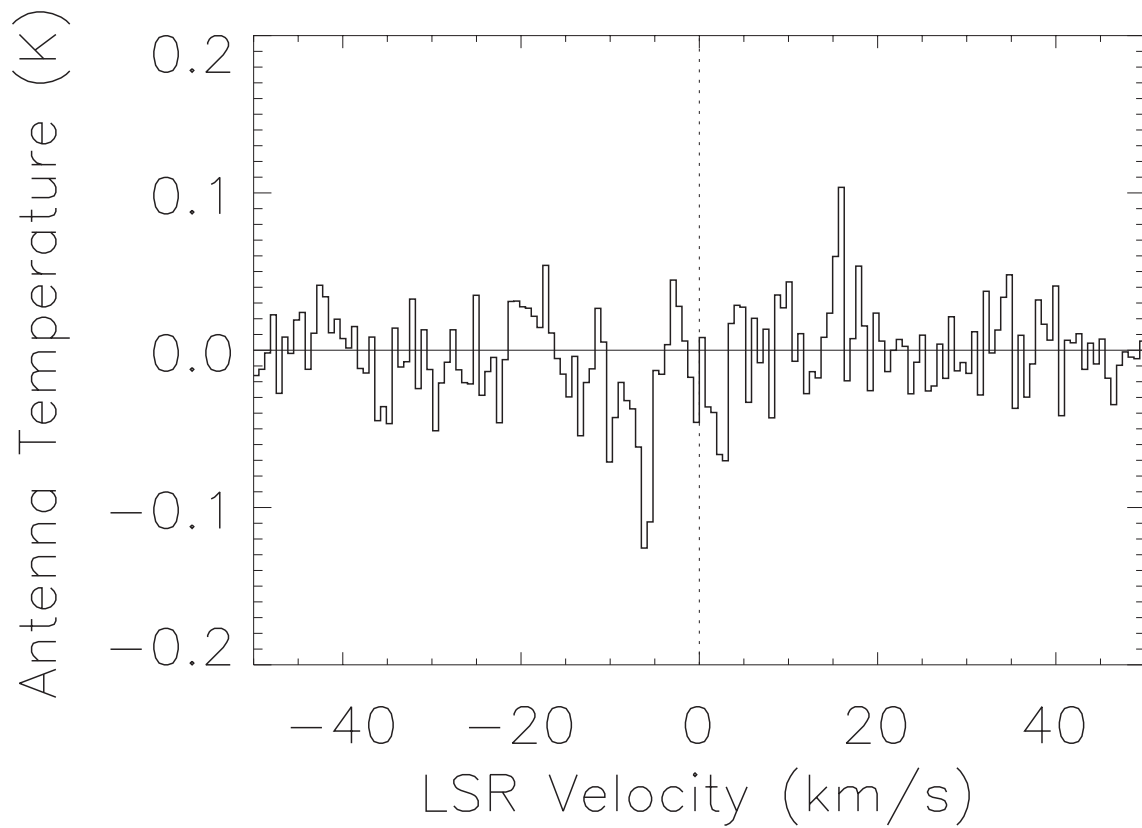


Figure 6.4 Same as Figure 2a for the $5^\circ \times 5^\circ$ region centered on $(\ell, b) = (92.5^\circ, -32.0^\circ)$. The feature at $\sim 15 \text{ km s}^{-1}$ does not meet our 6σ threshold for detections.

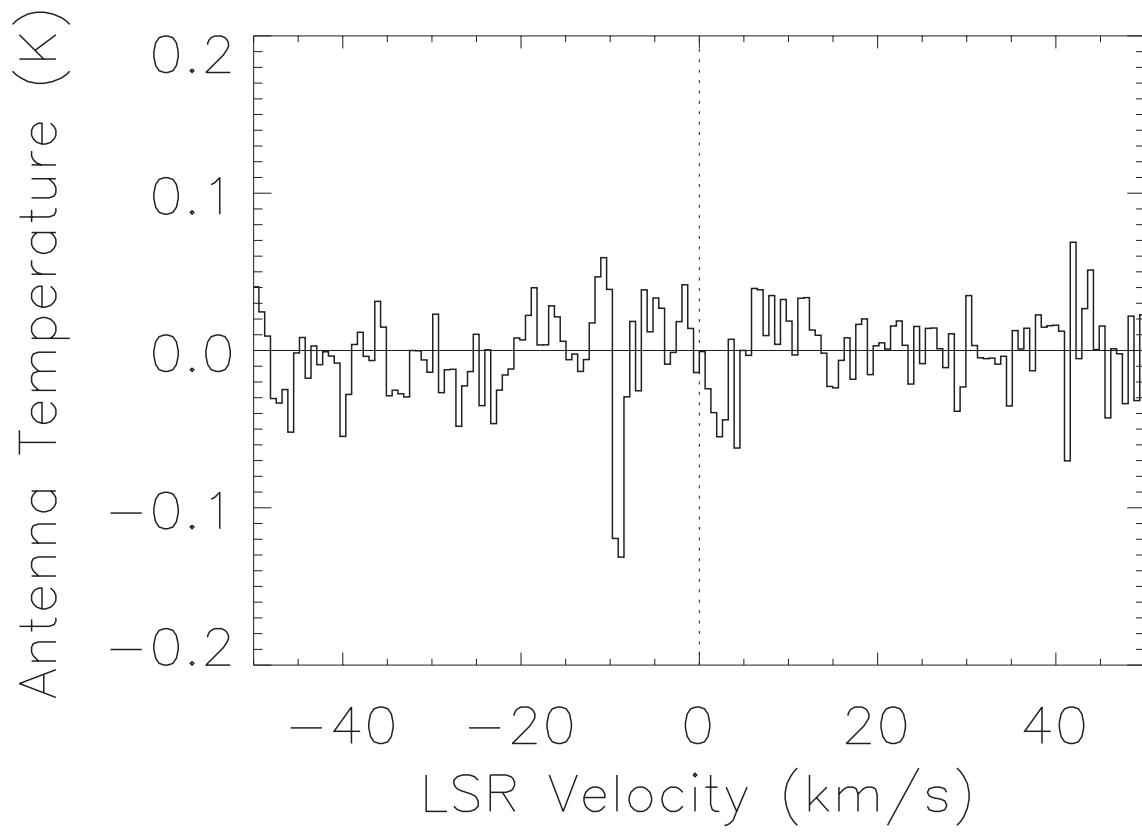


Figure 6.5 Same as Figure 2a for the $5^\circ \times 5^\circ$ region centered on $(\ell, b) = (102.7^\circ, -32.0^\circ)$.

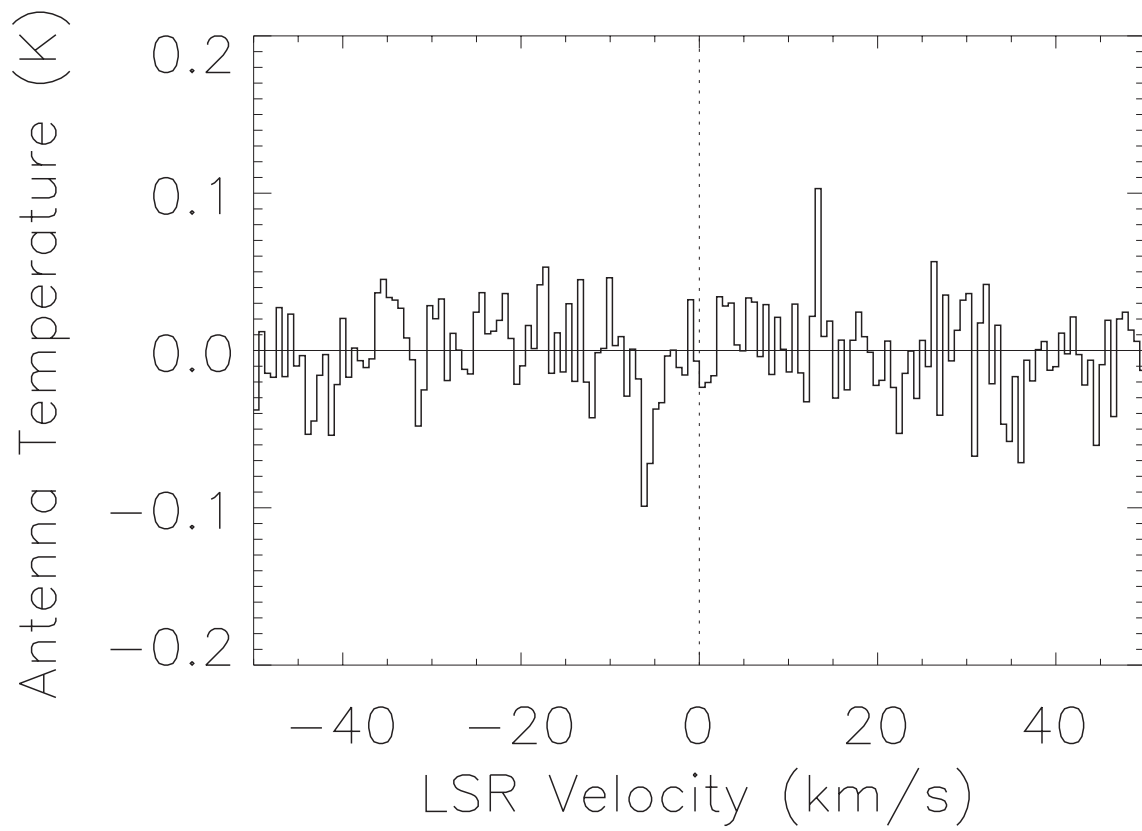


Figure 6.6 Same as Figure 2a for the $5^\circ \times 5^\circ$ region centered on $(\ell, b) = (112.9^\circ, -38.0^\circ)$.

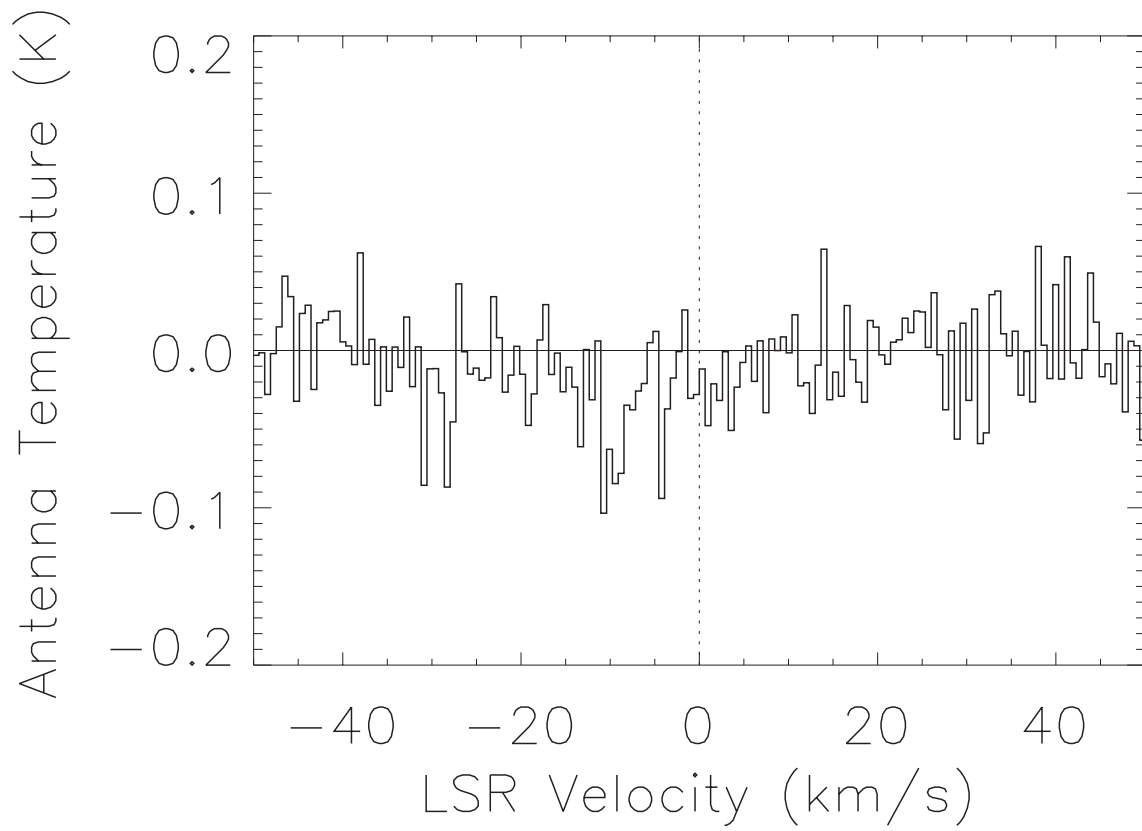


Figure 6.7 Same as Figure 2a for the $5^\circ \times 5^\circ$ region centered on $(\ell, b) = (128.2^\circ, -44.0^\circ)$.

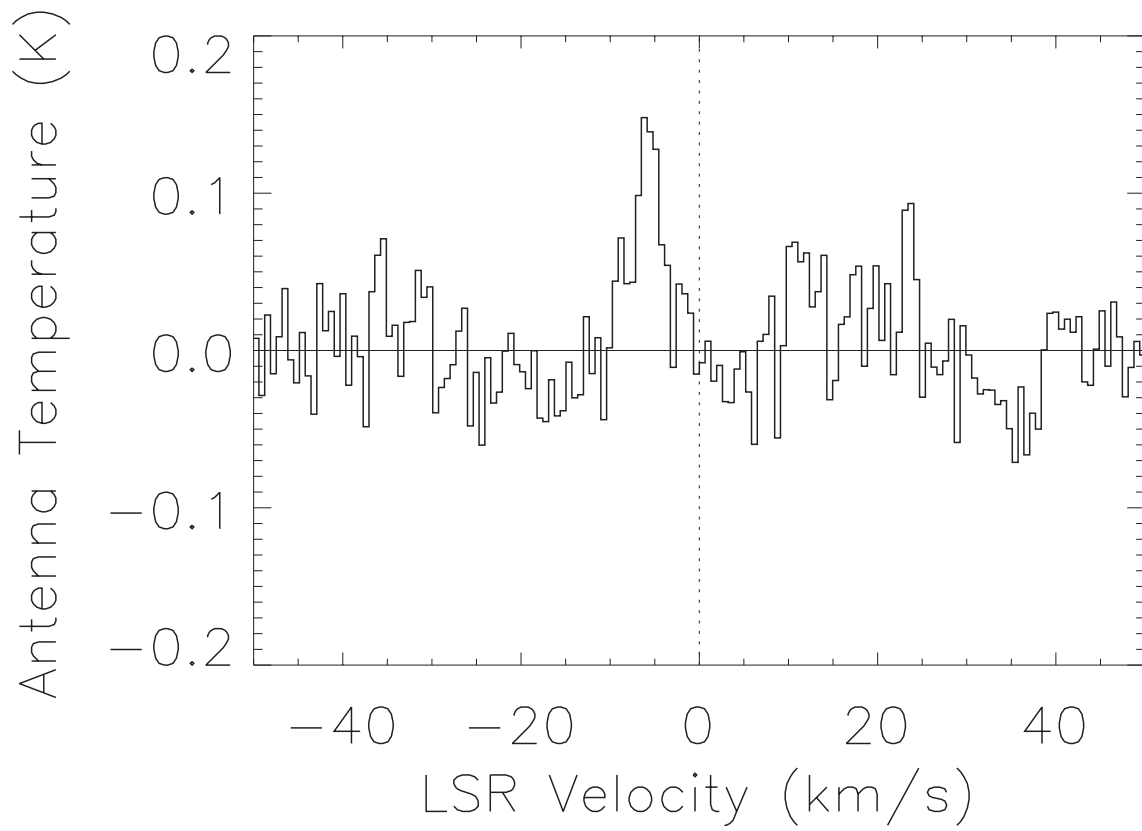


Figure 6.8 Same as Figure 2a for the $5^\circ \times 5^\circ$ region centered on $(\ell, b) = (133.4^\circ, -44.0^\circ)$.

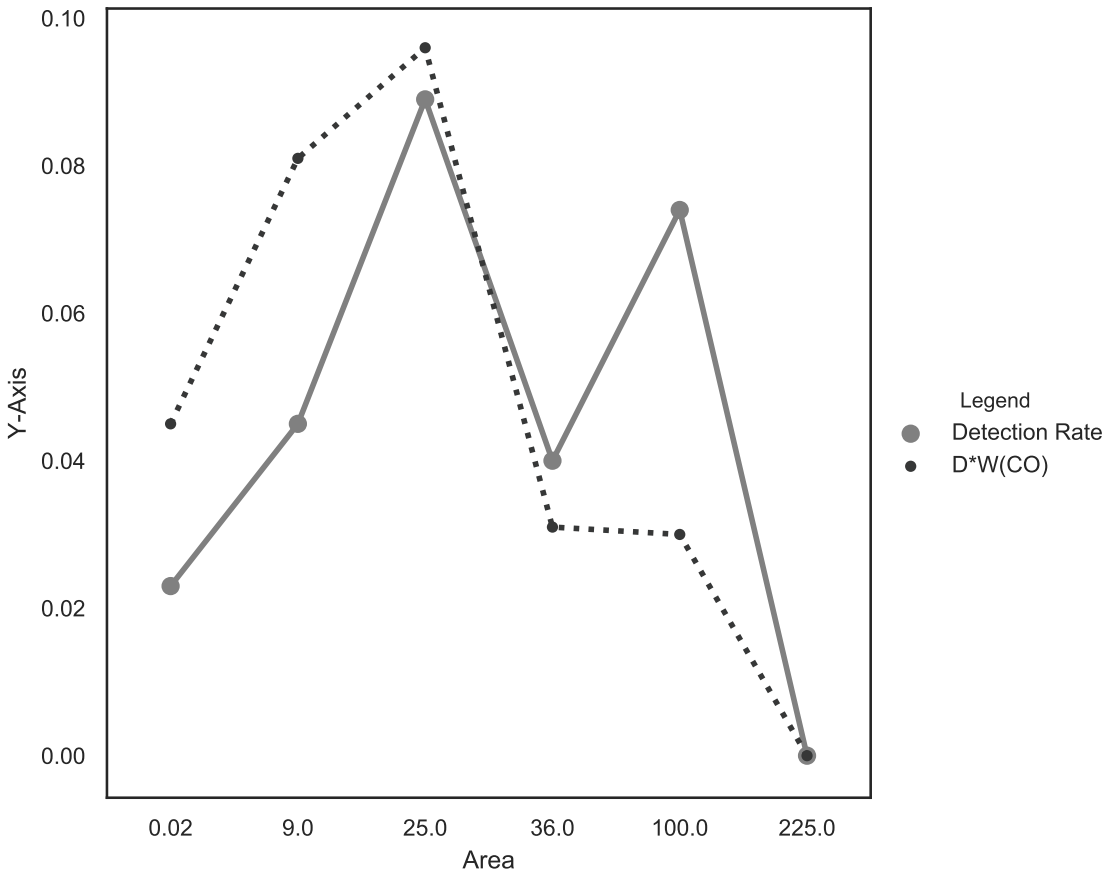


Figure 6.9 The product of the detection rate times the average W_{CO} for a given sized region as a function of the region size in square degrees (smaller black dots and dashed-dotted line), and the detection rate as a function of area (larger gray dots and dashed line).

CHAPTER 7

RADIO AND INFRARED CONTINUUM SPECTRA OF MBM 53

7.1 DUST SPECTRA

Gas and dust are tightly correlated in the ISM (e.g., Spitzer 1978) and the numerous infrared databases produced in the last three decades allow us to study the dust component of the Galaxy far more easily than the gas. As an example, Figure 7.1 shows the Yamamoto et al. (2003) CO(1-0) map of the MBM 53-55 complex compared to a dust map of the same region from the Schlegel, Finkbeiner, and Davis (1999) dust maps. The large scale correlation between the two maps is clear, but on small scales the correlation breaks down. Cotten (2011) showed that at low extinctions there is no absolute cutoff in extinction between lines of sight with or without CO emission. Instead, there is a gradual increase in the detection rate from 0.1 - 0.6 mag. If extinction can't be used to decide whether a line of sight has detectable CO emission, perhaps the continuum spectral profile from the far infrared to the centimeter part of the spectrum may hold the key. Thus, we decided to investigate whether radio and infrared emission from dust associated with the diffuse molecular cloud MBM 53 could provide clues as to why we detect molecular emission from some regions but not from others that have similar extinction. It could be possible that in regions containing CO or OH we might find a different distribution of dust sizes, or perhaps the amount of dust with respect to gas changes. We decided to use the infrared, submillimeter, and millimeter databases available online to determine whether spectra show a distinct feature for regions with molecular detections as opposed to those without.

Databases for producing the dust spectra were collected through the *Planck* and IRAS satellite missions (see mission descriptions in Chapter 5 of Magnani and Shore (2017))

allowing us to make spectra from 30 GHz to 5000 GHz (see Table 7.1). *Planck* was a European Space Agency satellite launched in 2009 with the purpose of surveying the sky in continuum and spectral line radiation at a number of different frequencies between 30-857 GHz with angular resolution from 33' to 5' (Tauber et al. 2010). The IRAS satellite was launched in 1983 and was the first satellite to produce infrared maps of the whole sky in four bands centered at wavelengths of 12, 25, 60 and 100 μm (Neugebauer et al. 1984).

We analyzed the region where we observed CO and OH (see Chapters 4 and 5) in Pegasus-Pisces $[\Delta\ell, \Delta b] = [82.5^\circ \text{ to } -99.0^\circ], [-26^\circ \text{ to } -32^\circ]$ with the 30, 44, 70, 100, 143, 217, 353, 545, and 857 GHz Planck bands, and the 3000 and 5000 GHz IRAS bands (100 and 60 μm , respectively). Each of these bands was observed at a different beam size (see Table 7.1) and, by using the Skyview Virtual Observatory¹ to average each band to 30 arc minutes, our composite radio and infrared spectrum would be at the same spatial resolution for each frequency. We wanted to plot flux against frequency for each position we observed in CO and OH to create the composite spectra. We describe below how we converted the raw data to flux.

For the first seven *Planck* bands, the data are presented in K rather than MegaJanskys per steradian (MJy/ster). Thus, to calculate flux we had two different procedures, because for bands 30 - 353 we had to convert from temperature to MJy/ster while the two highest frequency Planck bands and the two IRAS bands the data are already in MJy/ster. The conversion value for each band is unique and was provided from the *Planck* Observatory's documentation² and these values are presented here in Table 7.1. In this way, all of our data are in MJy/ster which has units of $1 \times 10^6 \text{ J s}^{-1} \text{ m}^{-2} \text{ Hz}^{-1} \text{ ster}^{-1}$, an intensity. To produce a flux we first get rid of the ster^{-1} by multiplying by $7.614 \times 10^{-5} \text{ ster}$ because that is the size of a $30' \times 30'$ square, our resolution element. We now have data in units of $\text{J s}^{-1} \text{ m}^{-2} \text{ Hz}^{-1}$. To get a flux from that, we multiply by the bandwidth for each of the bands to get $\text{J s}^{-1} \text{ m}^{-2}$ (see Table 7.1). This is the flux value we plot against frequency for all the spectra presented

¹<https://skyview.gsfc.nasa.gov/current/cgi/titlepage.pl>

²https://wiki.cosmos.esa.int/planck-legacy-archive/index.php/Effective_Beams

in Figures 7-2 to 7-45. Each spectrum corresponds to one of the positions for which we have OH data (see Chapter 5).

The spectra share clear dust peaks at 353 GHz, and peaks due to warmer dust in the far infrared between 60-100 microns. If we assume the dust particles emit as blackbodies, the 353 GHz peak corresponds to a dust temperature of 3.4 K, implying that the Cosmic Microwave Background radiation contributes strongly to this band. Ignoring the peak and fitting a blackbody curve to the spectrum shows a good fit for $T = 14$ K (see Figure 7.46). The peaks in the 60-100 micron range would be due to a warmer dust component ($T \sim 30$ K for peak at $97 \mu\text{m}$) but a background level would need to be subtracted for a true fit (see discussion below).

There are two basic differences in the spectra, the ones that present discontinuities in the radio and those that are continuous. The discontinuities are in the millimeter sub-millimeter range. There are 11 spectra that are continuous in the submillimeter range but among those only five correspond to points in which there were CO detections, there were six others that did not have corresponding CO detections. Thus the presence of those discontinuities cannot be used to discriminate between the presence and absence of molecular emission. When plotting all the spectra together (see Figure 7.47) one distinguishing feature is that the continuum spectra for lines of sight with detections on average show higher fluxes than those of non-detections. This is not surprising and may just be due to a constant gas to dust ratio: Molecular regions will have more gas, and thus more dust.

The main problem with our approach above is that we should be subtracting out the background radiation contributions. The continuum emission from the Galaxy in the bands used above involve, in addition to any continuum emission from the cloud itself, emission from the following sources: (1) thermal emission from dust along the line of sight not associated with the cloud, (2) thermal emission from the CMB, (3) non-thermal emission from synchrotron radiation, (4) non-thermal emission from bremsstrahlung radiation, (5) non-thermal emission from spinning dust. Subtracting the Galactic background radiation in the

Planck spectra is difficult as it varies across the sky and requires sophisticated modeling (see, e.g., Planck Collaboration 2011c, 2011d). However, the far infrared spectral shape looks the same for all of the spectra and subtracting the background does not appear as though it would resolve the problem or help in finding a pattern in the continuum spectra that would relate to whether we can find molecular gas along a line of sight or not.

Our basic assumption in attempting this project was that the various backgrounds would be fairly constant over the relatively small region we are studying and that their only effect would be to add DC offsets to all the bands. We are looking for differences in the spectra between our detections and nondetections rather than outright calibrated spectra for the dust continuum emission in MBM 53. Unfortunately, the morphologies of the spectral shapes were not clearly segregated between lines of sight with/without CO and/or OH emission so it is unclear if our assumption was valid or not. Our idea, that perhaps a signature of lines of sight with detectable molecular emission have a different dust continuum spectral signature than those without molecular emission may still be worth pursuing, but, if so, then the various backgrounds need to be removed. Alternatively, this method may still work but, instead of the far infrared/radio part of the spectrum, a better approach may lie in the near infrared. In this part of the electromagnetic spectrum are lines of polycyclic aromatic hydrocarbons (PAHs) and the diffuse infrared bands (see e.g. Verter et al. 2000) which may lead to unique signatures. In summary, our study of the continuum spectra of dust in the radio/far-infrared shows a clear trend only in that the lines of sight with molecular detections from Ch. 4 and Ch. 5 have slightly higher fluxes than those without. So, on large scales, the dust and gas are correlated but on the small scales the relationship is more complex.

Table 7.1 Summary information for the radio and infrared data.

Band Name	Satellite	Center Frequency	Bandwidth	Wavelength	K_{RJ} to MJy/ster	Beamsize
GHz		GHz	GHz	cm		arcminutes
30	<i>Planck</i>	28.5	6	0.999	24.845597	32.65
44	<i>Planck</i>	44.1	8.8	0.681	59.666236	27.00
70	<i>Planck</i>	70.3	14	0.428	151.73238	13.01
100	<i>Planck</i>	100	33.3	0.300	306.81118	9.94
143	<i>Planck</i>	143	47.2	0.210	627.39818	7.04
217	<i>Planck</i>	217	71.6	0.138	1444.7432	4.66
353	<i>Planck</i>	353	116.5	0.0859	3823.1434	4.41
545	<i>Planck</i>	545	179.85	0.0550	1 ^a	4.47
857	<i>Planck</i>	857	282.8	0.0350	1 ^a	4.23
3000	IRAS	3000	1080	0.0100	1 ^a	1.5 × 4.7
5000	IRAS	5000	3350	0.0060	1 ^a	2.0 × 5.0

^a Values are provided in MJy/ster and need no conversion.

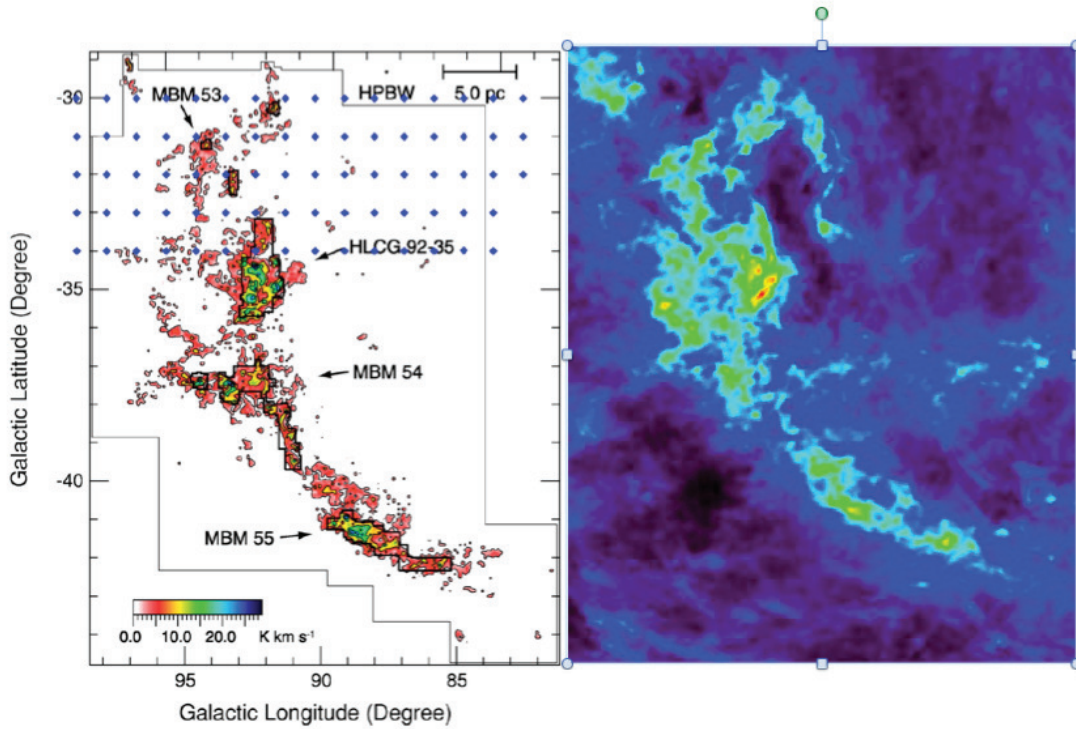


Figure 7.1 Gas to dust comparison for the MBM 53-55 complex. The image on the left is the CO(1-0) map from Yamamoto et al. (2003) with the points observed in CO and OH in Chapters 4 and 5 shown as the blue diamonds (image courtesy of Amanda Stricklan (2019)). On the right is the same region as on the left but in E(B-V) from the Schlegel, Finkbeiner, and Davis (1999) database. The similarity between the images is clear on the large scales but breaks down on small scales.

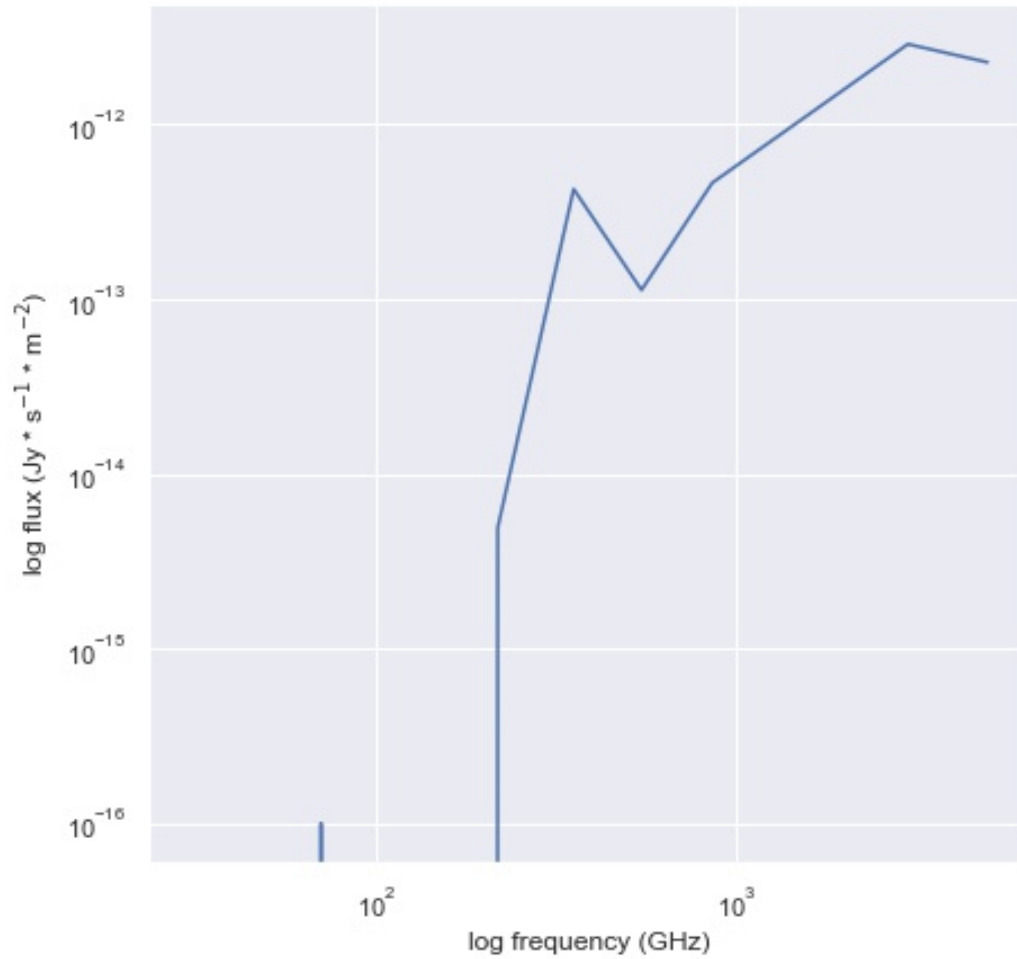


Figure 7.2 Millimeter-submillimeter-far infrared spectrum of the line of sight $(\ell, b) = (82.5^\circ, -34.0^\circ)$, based on *Planck* and IRAS data (see text).

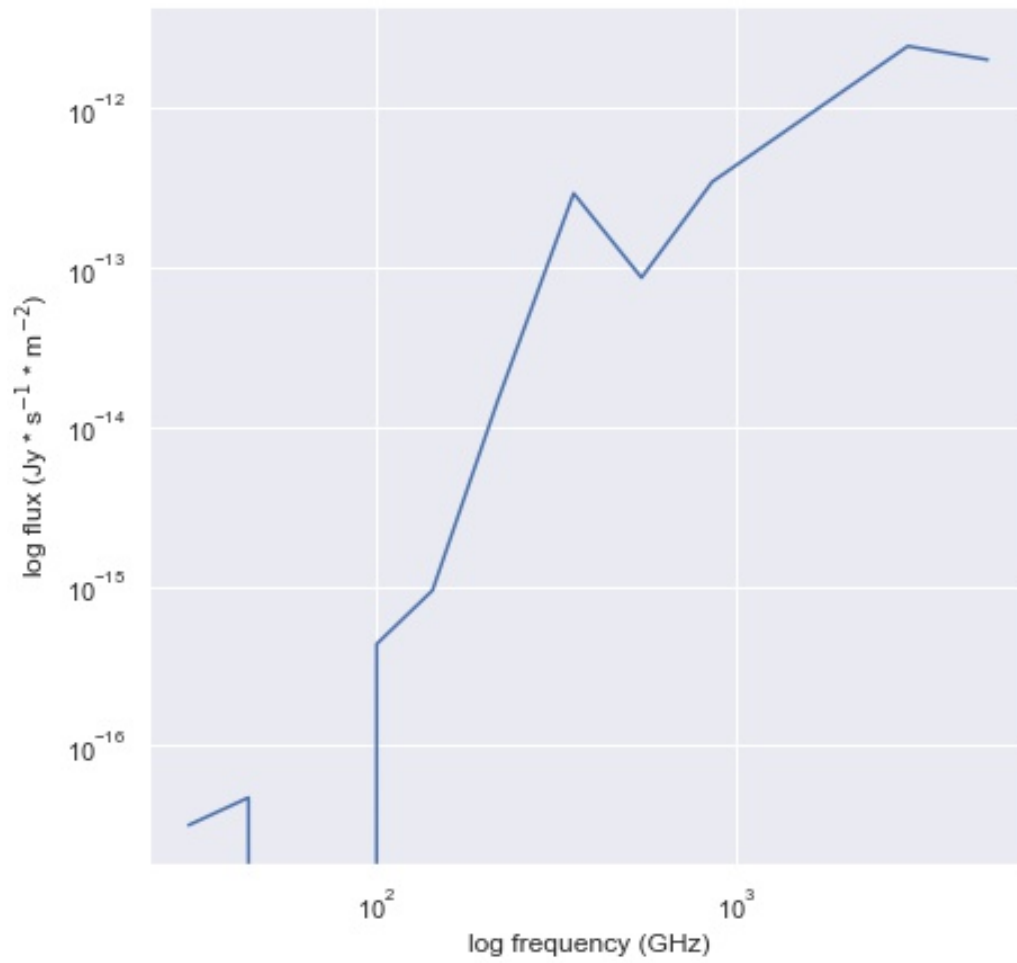


Figure 7.3 Same as figure 7.1 at position $(\ell, b) = (83.6^\circ, -34.0^\circ)$

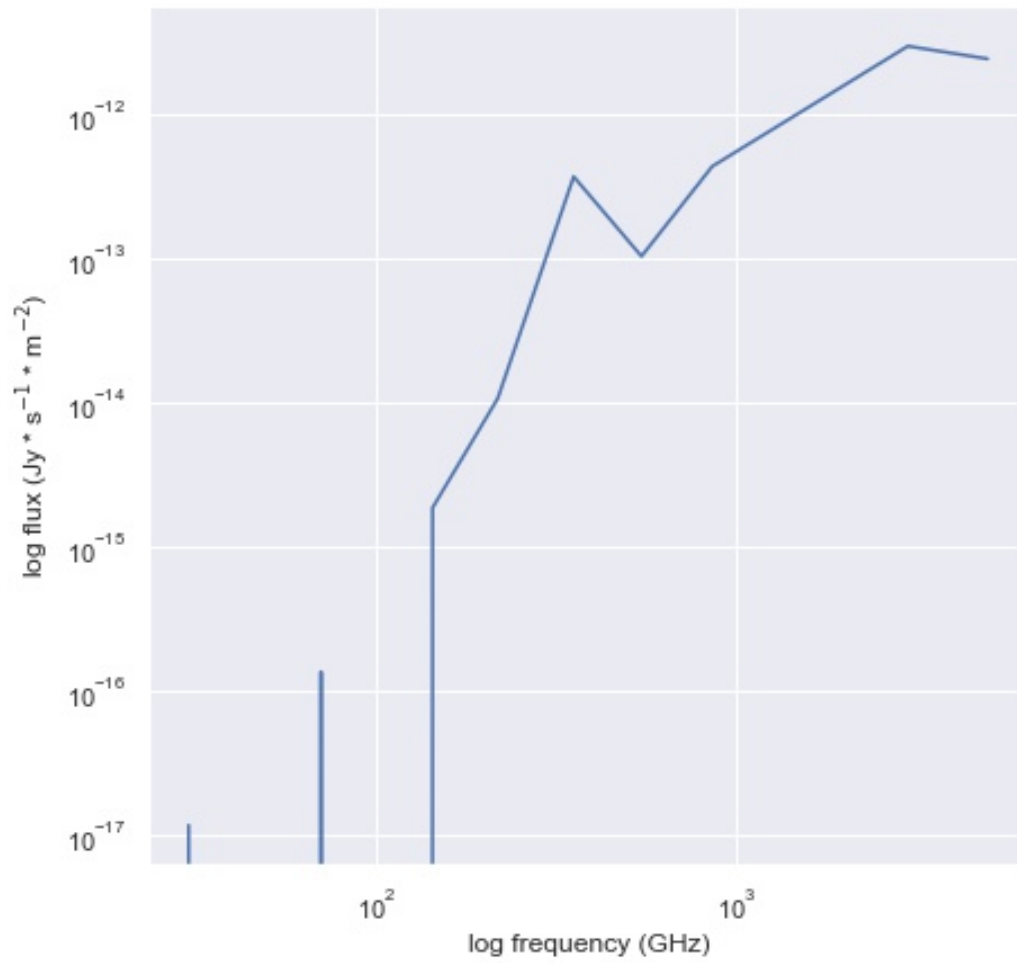


Figure 7.4 Same as figure 7.1 at position $(\ell, b) = (84.7^\circ, -34.0^\circ)$

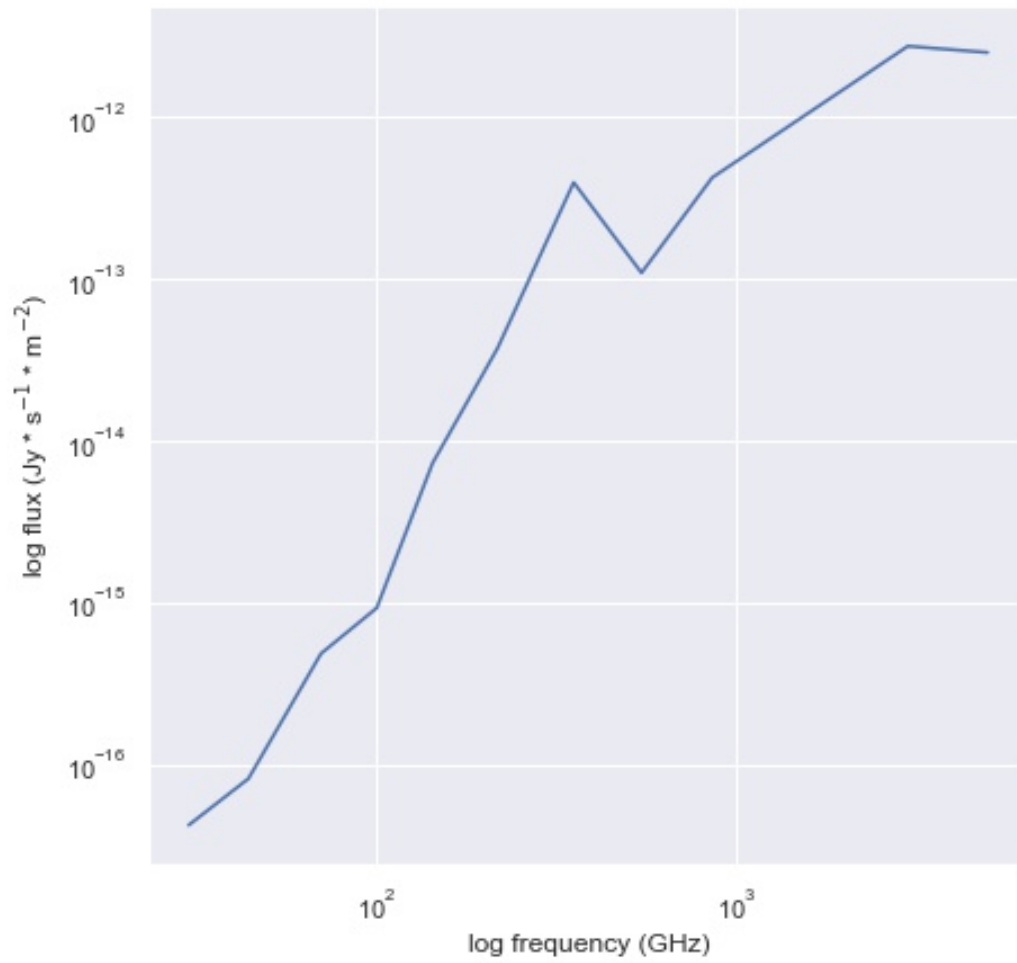


Figure 7.5 Same as figure 7.1 at position $(\ell, b) = (85.8^\circ, -34.0^\circ)$

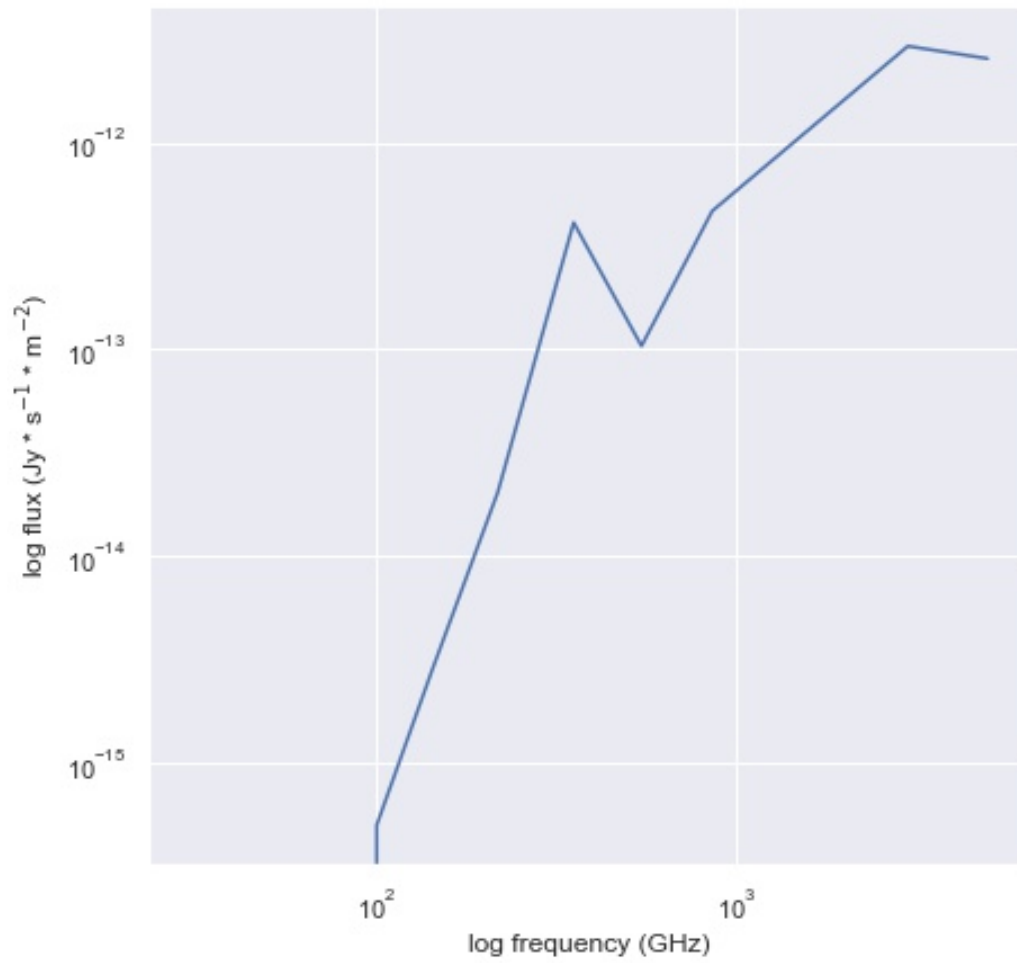


Figure 7.6 Same as figure 7.1 at position $(\ell, b) = (86.9^\circ, -34.0^\circ)$

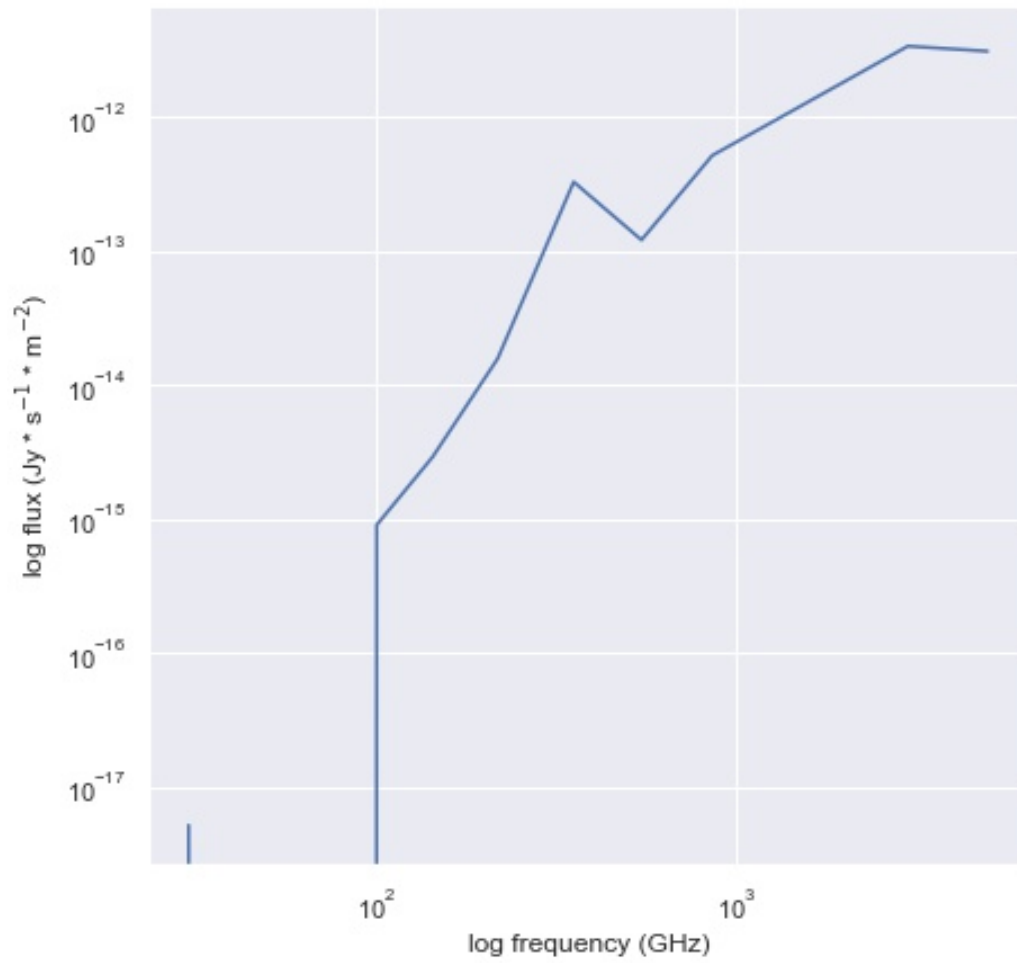


Figure 7.7 Same as figure 7.1 at position $(\ell, b) = (88.0^\circ, -34.0^\circ)$

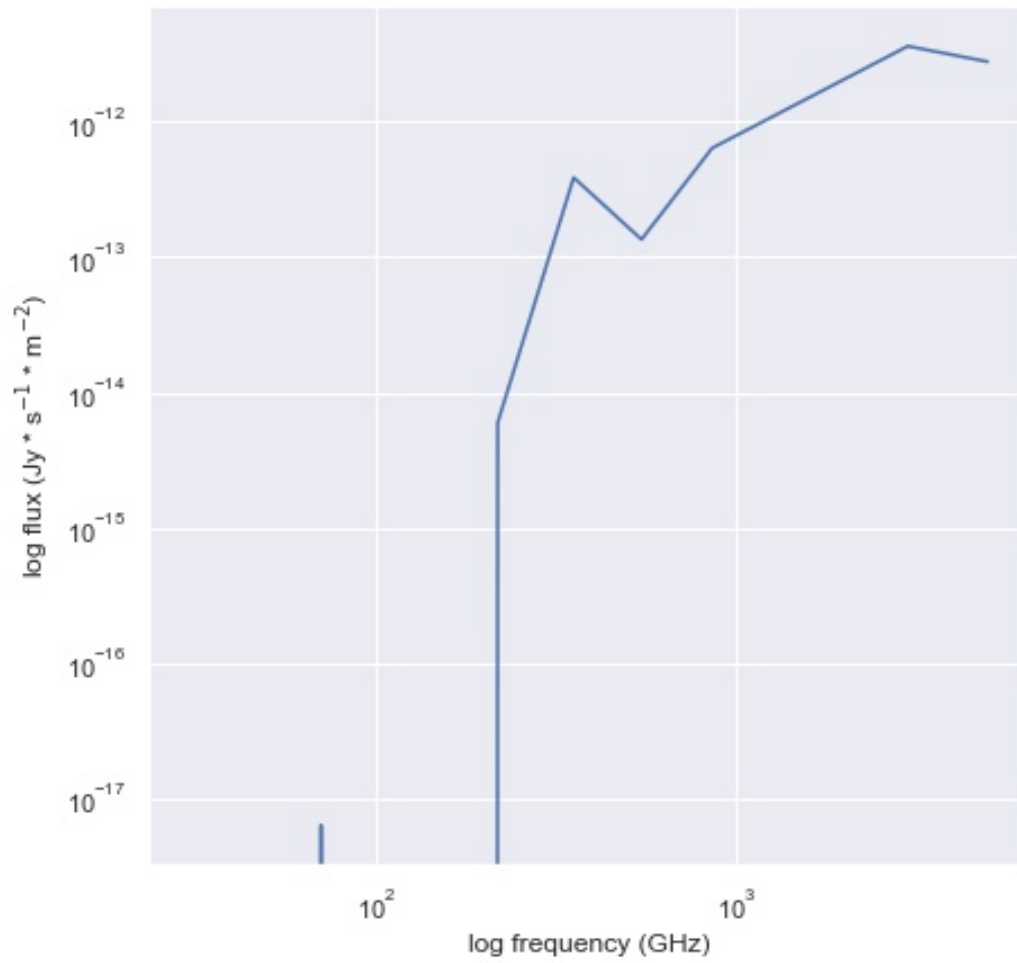


Figure 7.8 Same as figure 7.1 at position $(\ell, b) = (89.1^\circ, -34.0^\circ)$

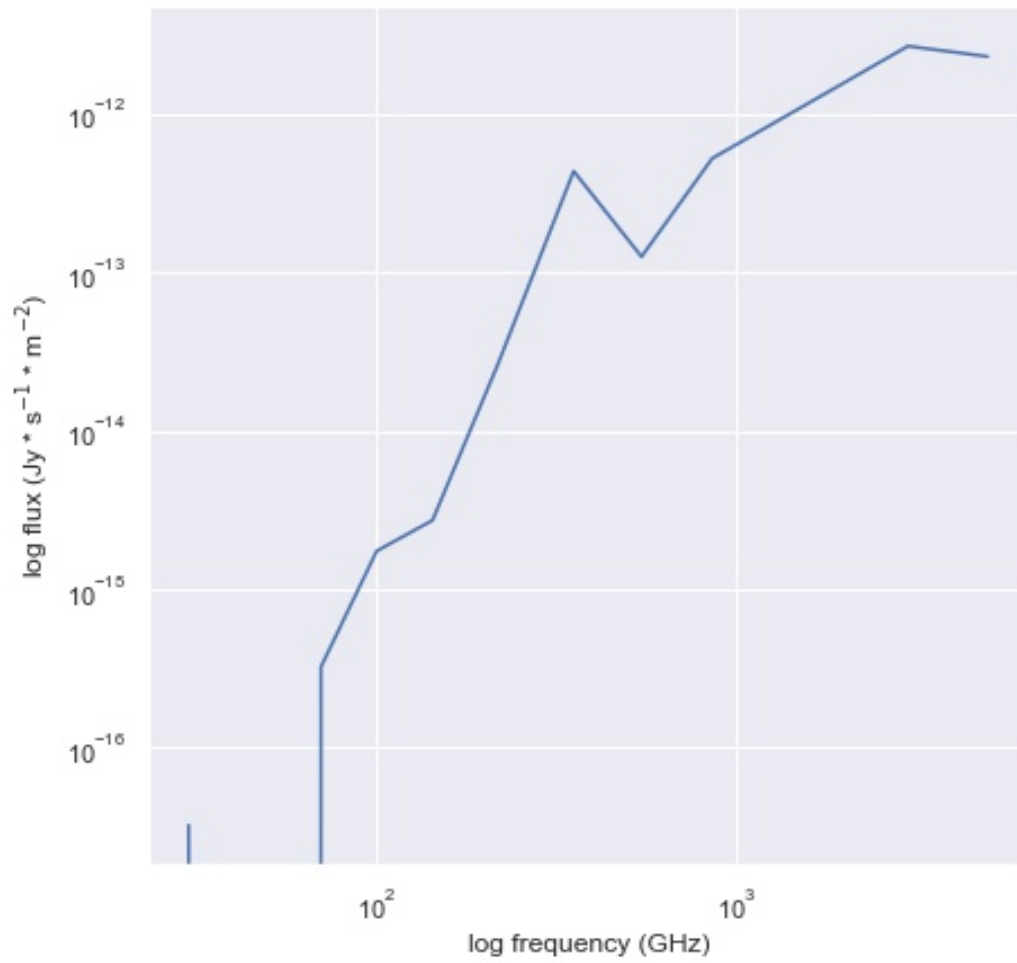


Figure 7.9 Same as figure 7.1 at position $(\ell, b) = (90.2^\circ, -34.0^\circ)$

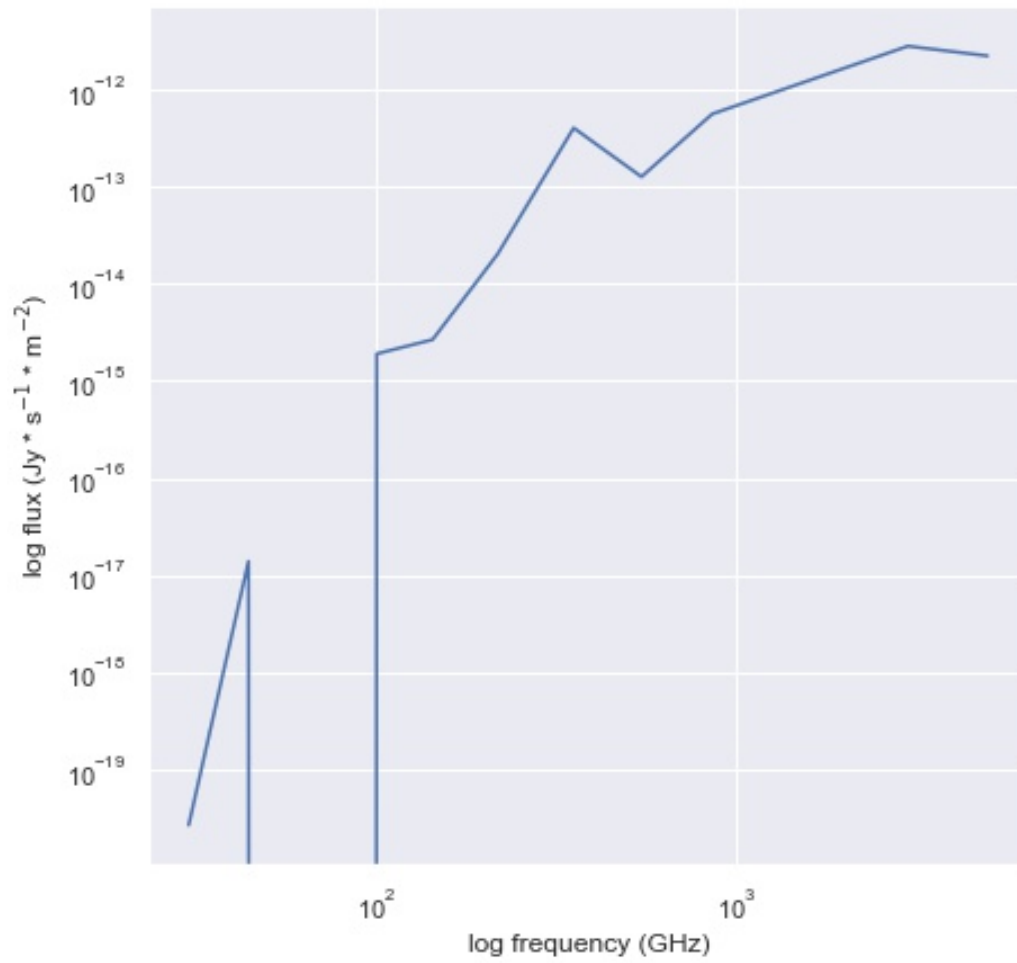


Figure 7.10 Same as figure 7.1 at position $(\ell, b) = (91.3^\circ, -34.0^\circ)$

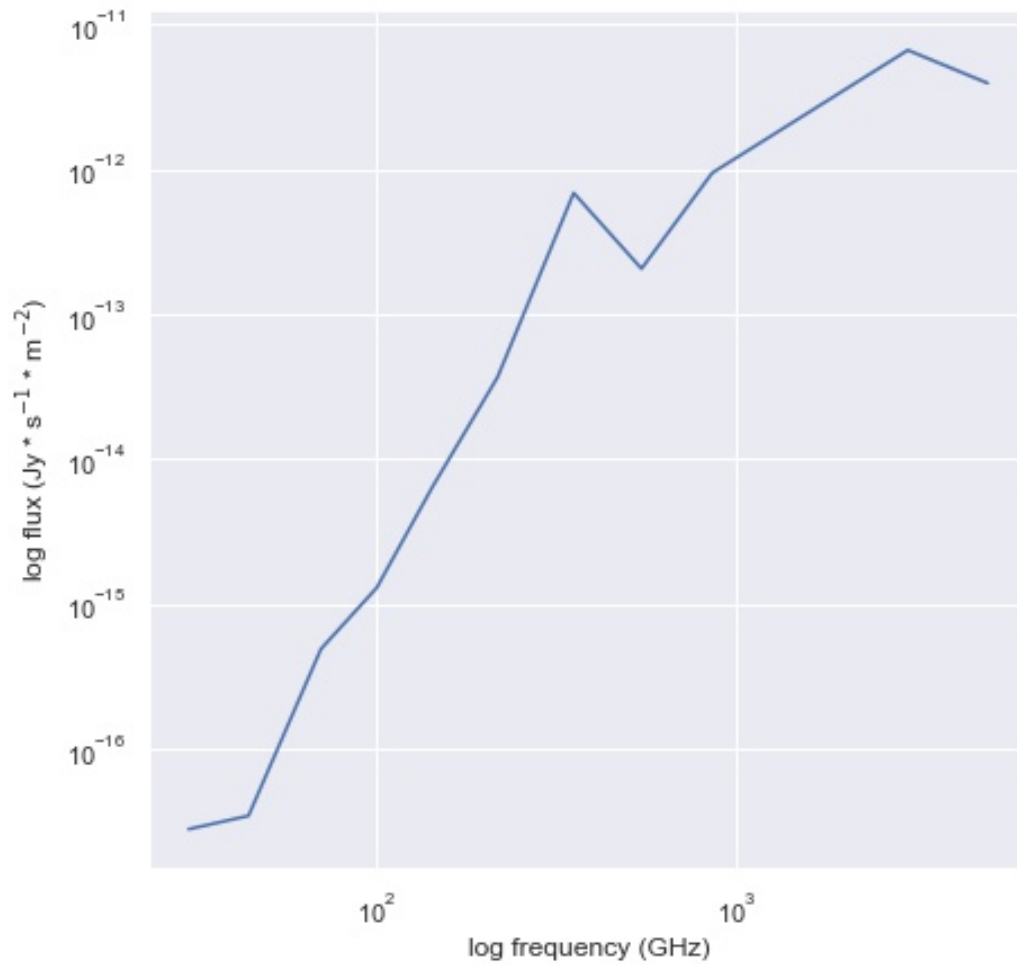


Figure 7.11 Same as figure 7.1 at position $(\ell, b) = (92.4^\circ, -30.0^\circ)$

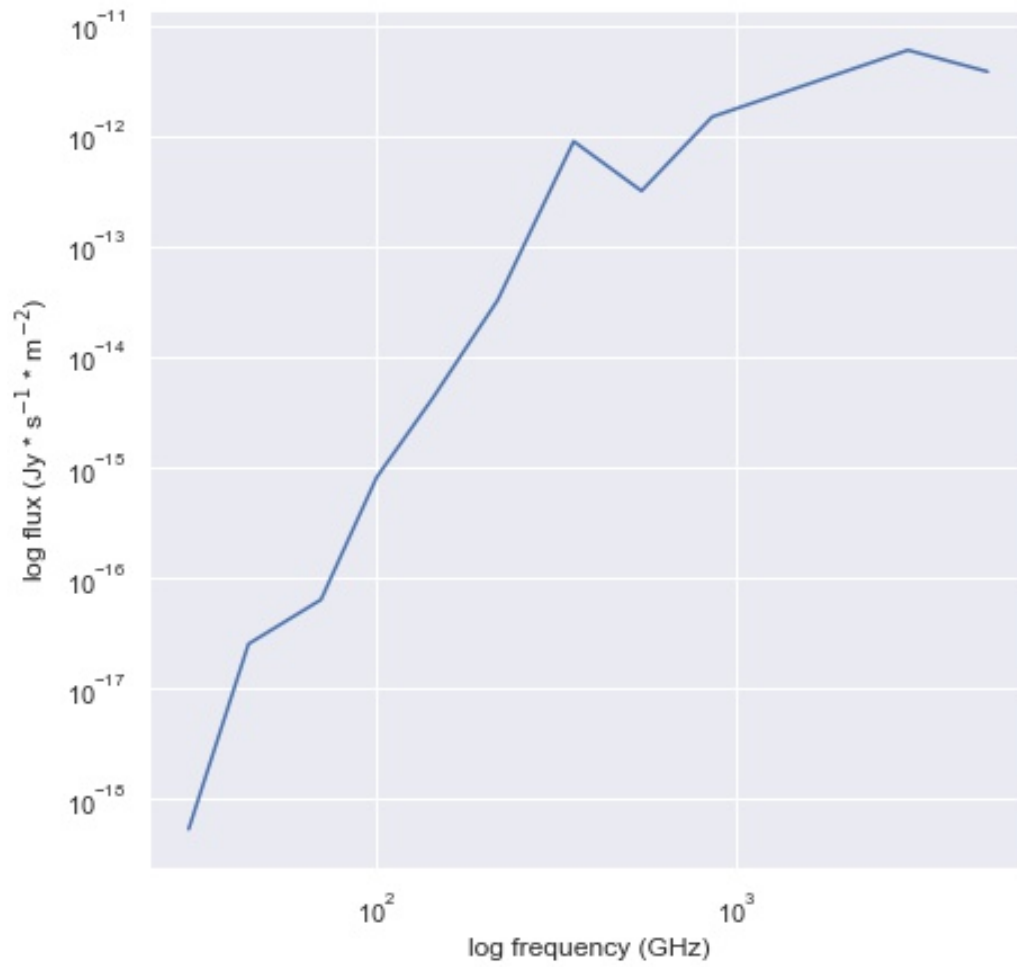


Figure 7.12 Same as figure 7.1 at position $(\ell, b) = (92.4^\circ, -31.0^\circ)$

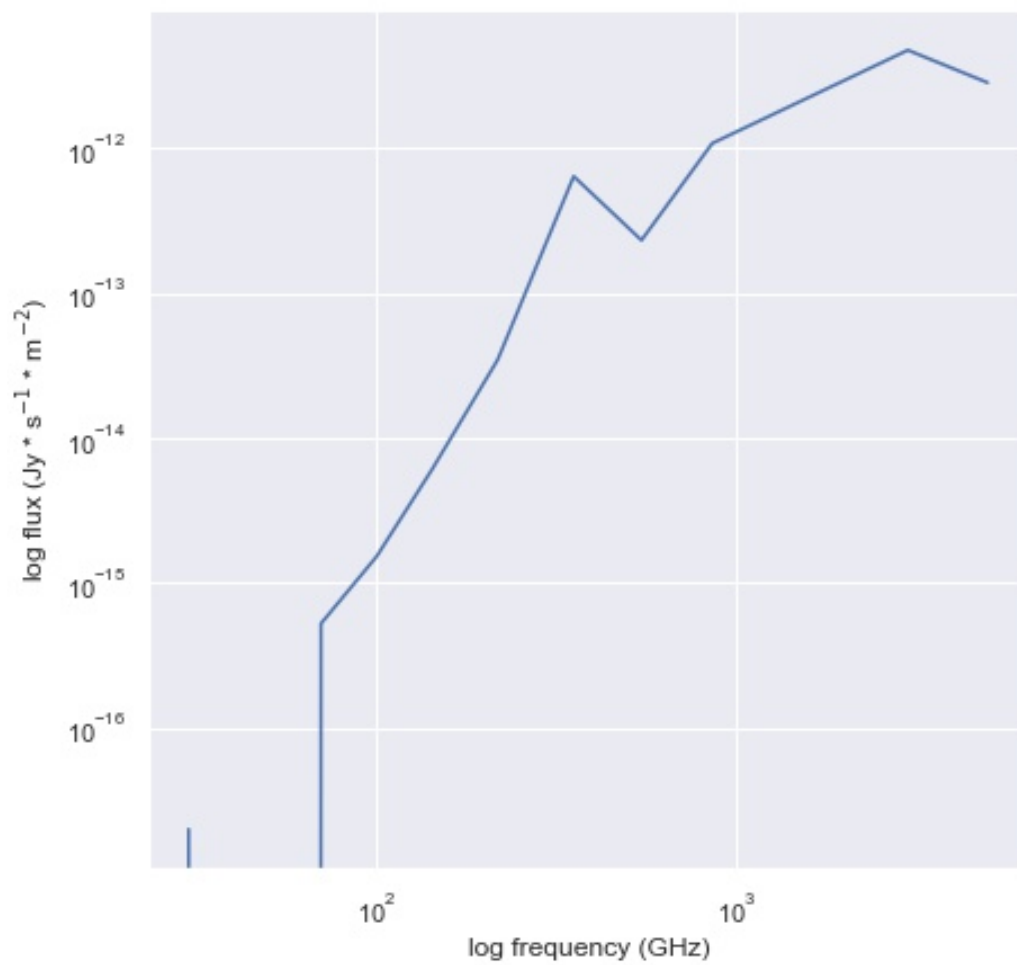


Figure 7.13 Same as figure 7.1 at position $(\ell, b) = (92.4^\circ, -32.0^\circ)$

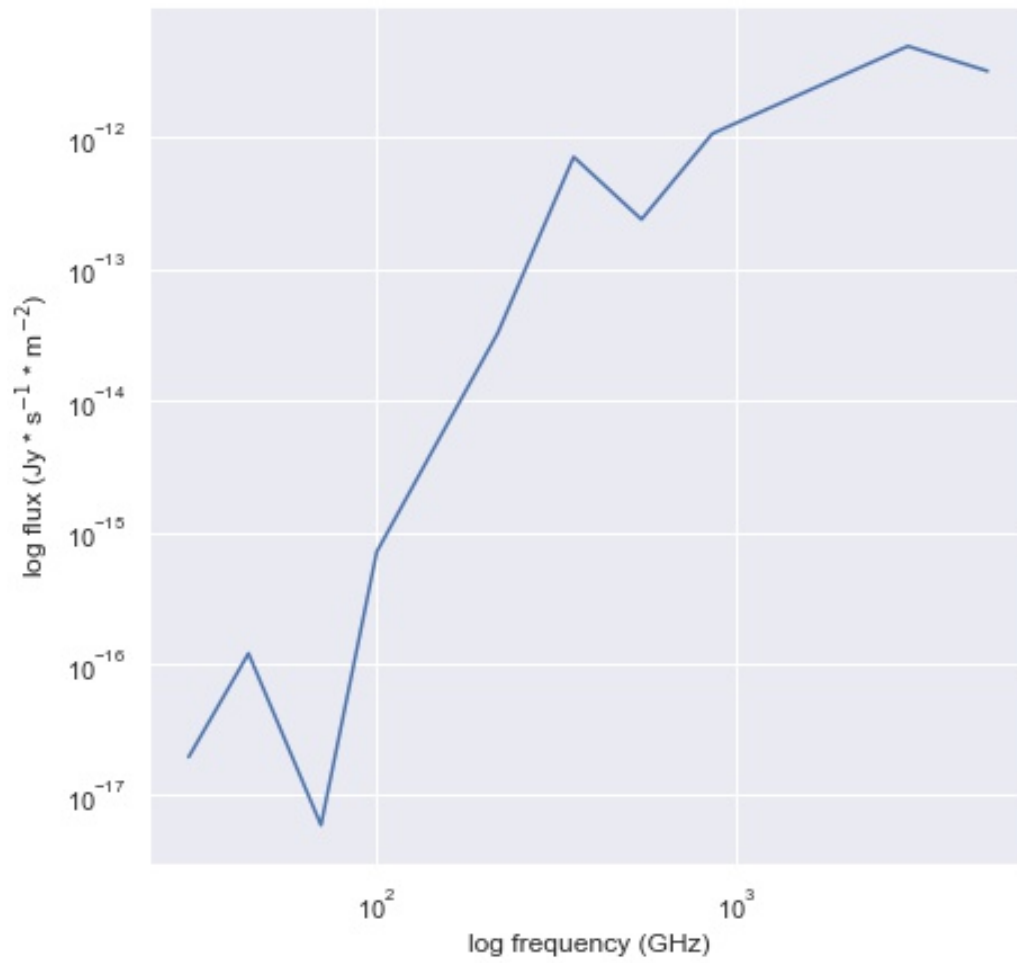


Figure 7.14 Same as figure 7.1 at position $(\ell, b) = (92.4^\circ, -33.0^\circ)$

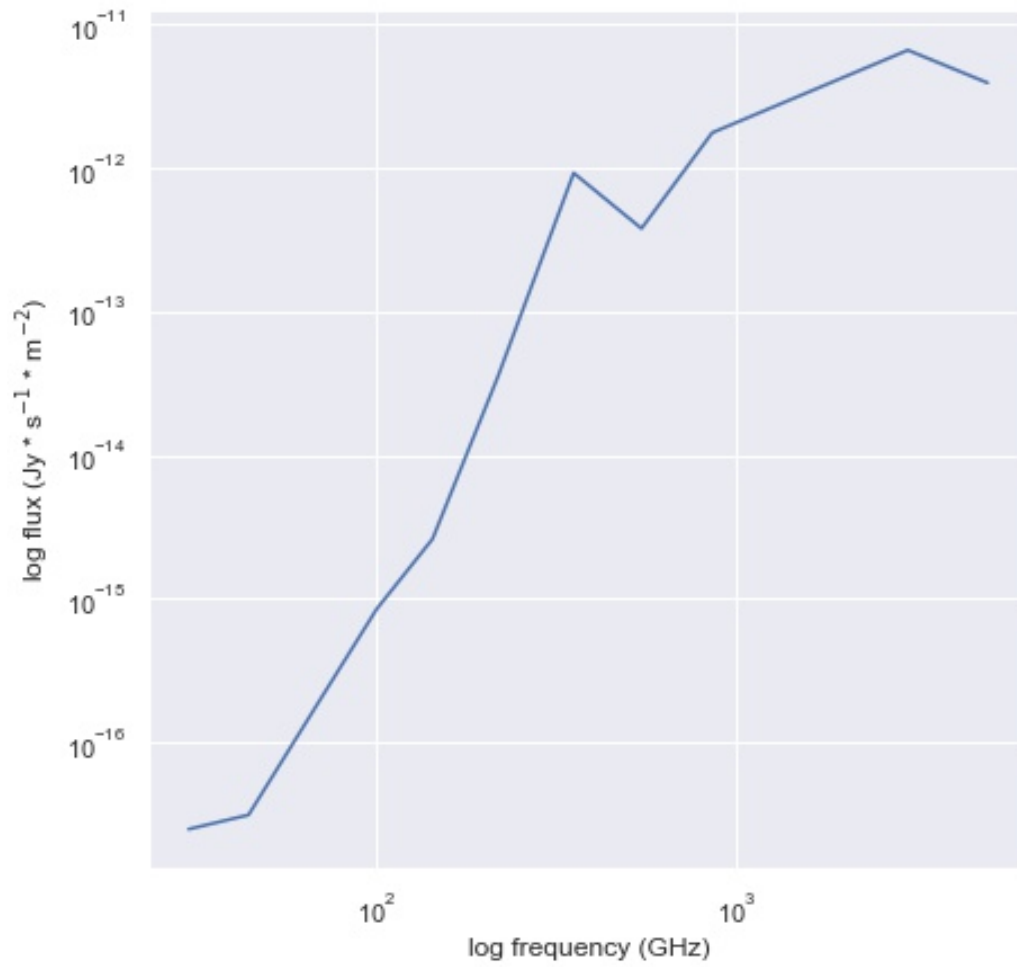


Figure 7.15 Same as figure 7.1 at position $(\ell, b) = (92.4^\circ, -34.0^\circ)$

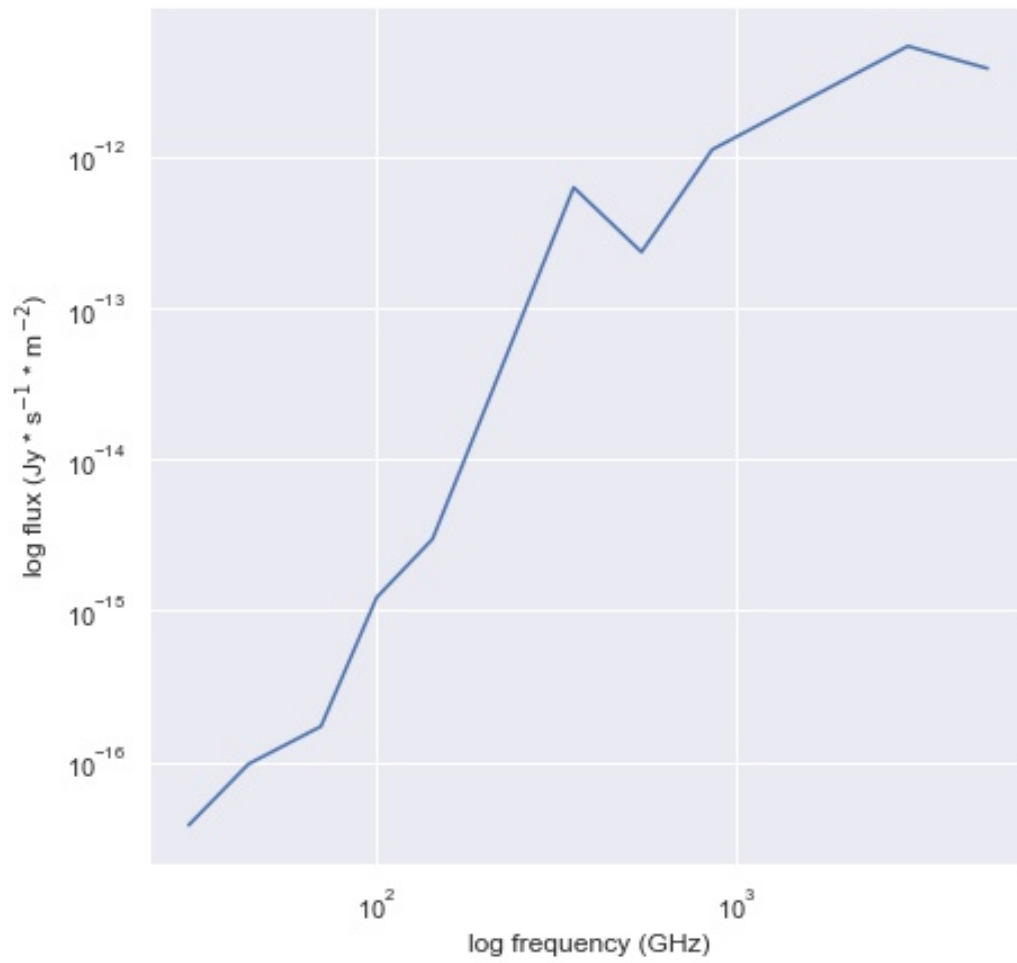


Figure 7.16 Same as figure 7.1 at position $(\ell, b) = (93.5^\circ, -30.0^\circ)$

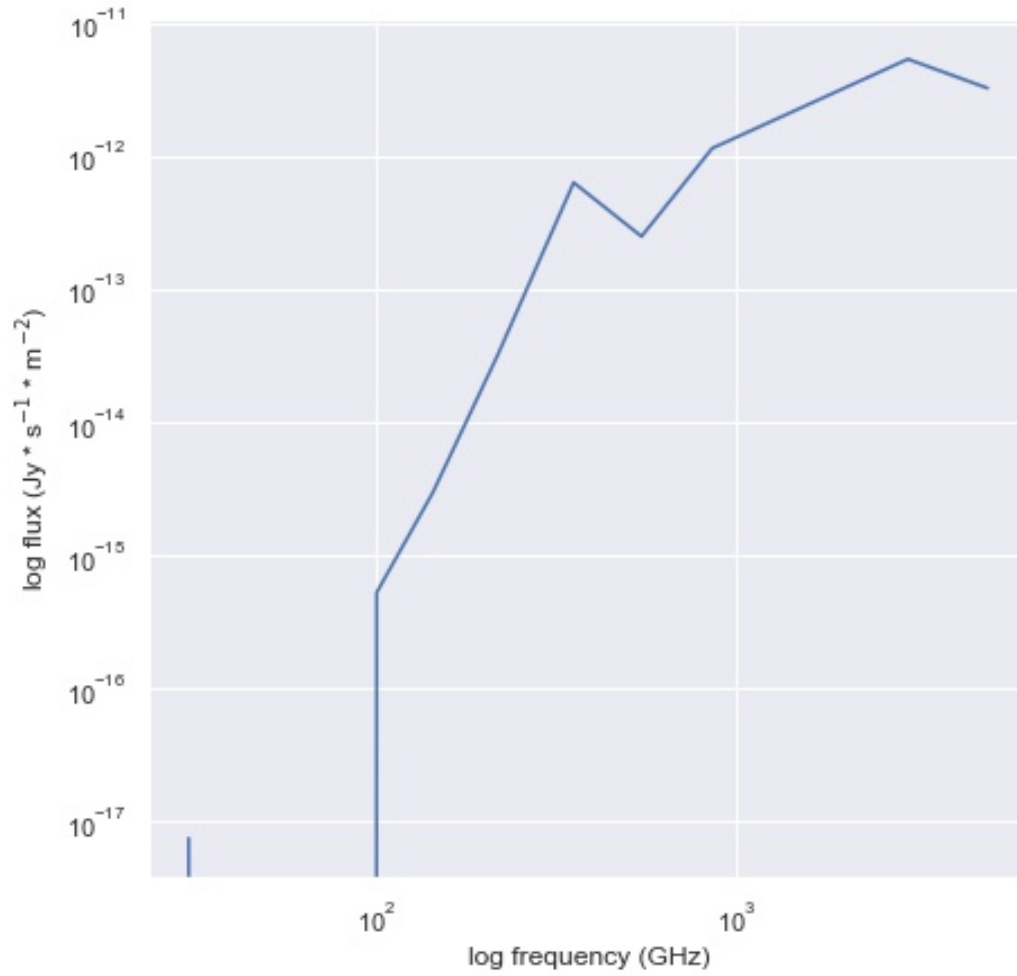


Figure 7.17 Same as figure 7.1 at position $(\ell, b) = (93.5^\circ, -31.0^\circ)$

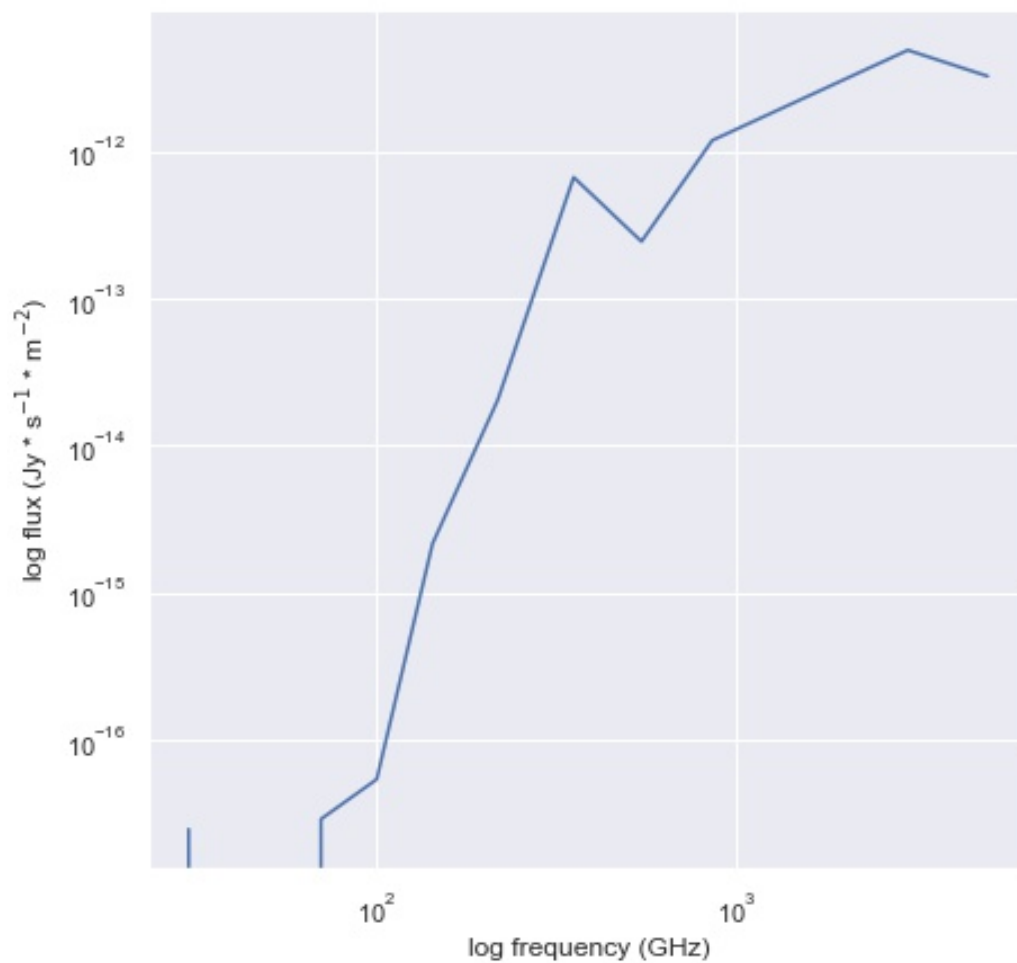


Figure 7.18 Same as figure 7.1 at position $(\ell, b) = (93.5^\circ, -32.0^\circ)$

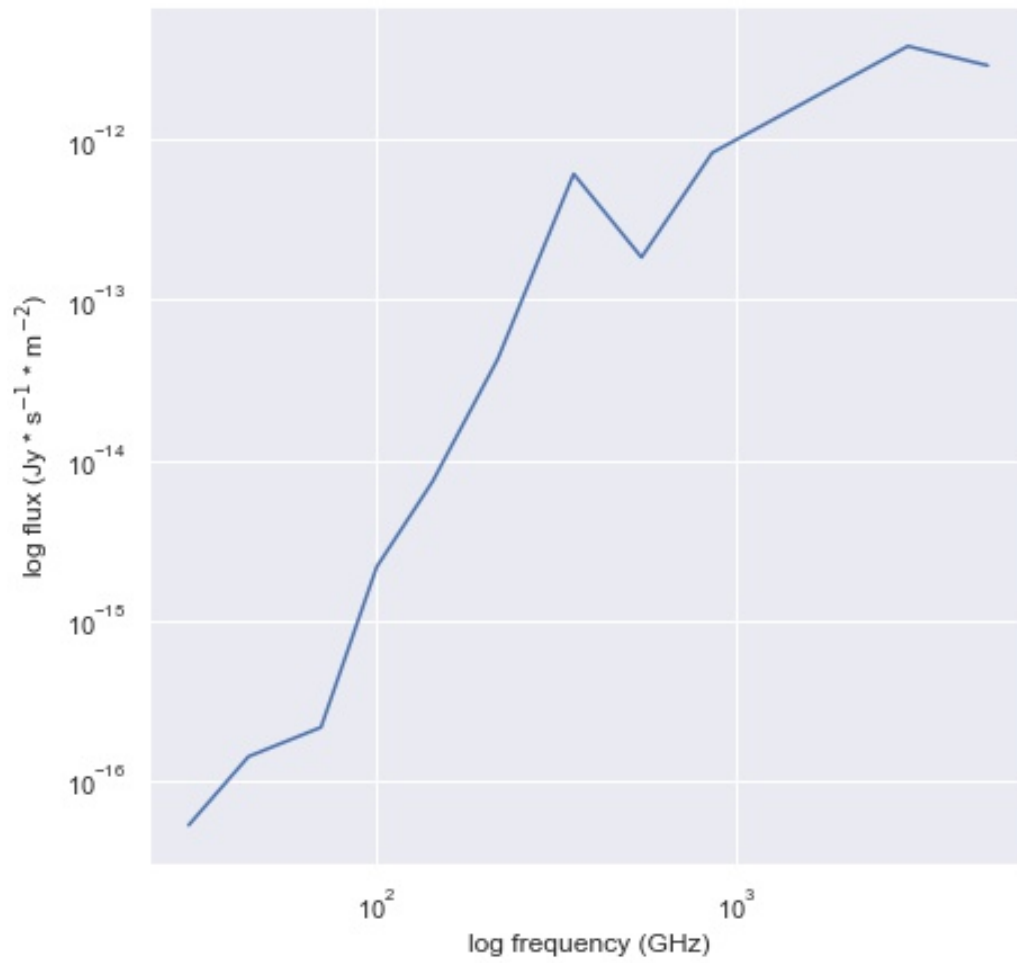


Figure 7.19 Same as figure 7.1 at position $(\ell, b) = (93.5^\circ, -33.0^\circ)$

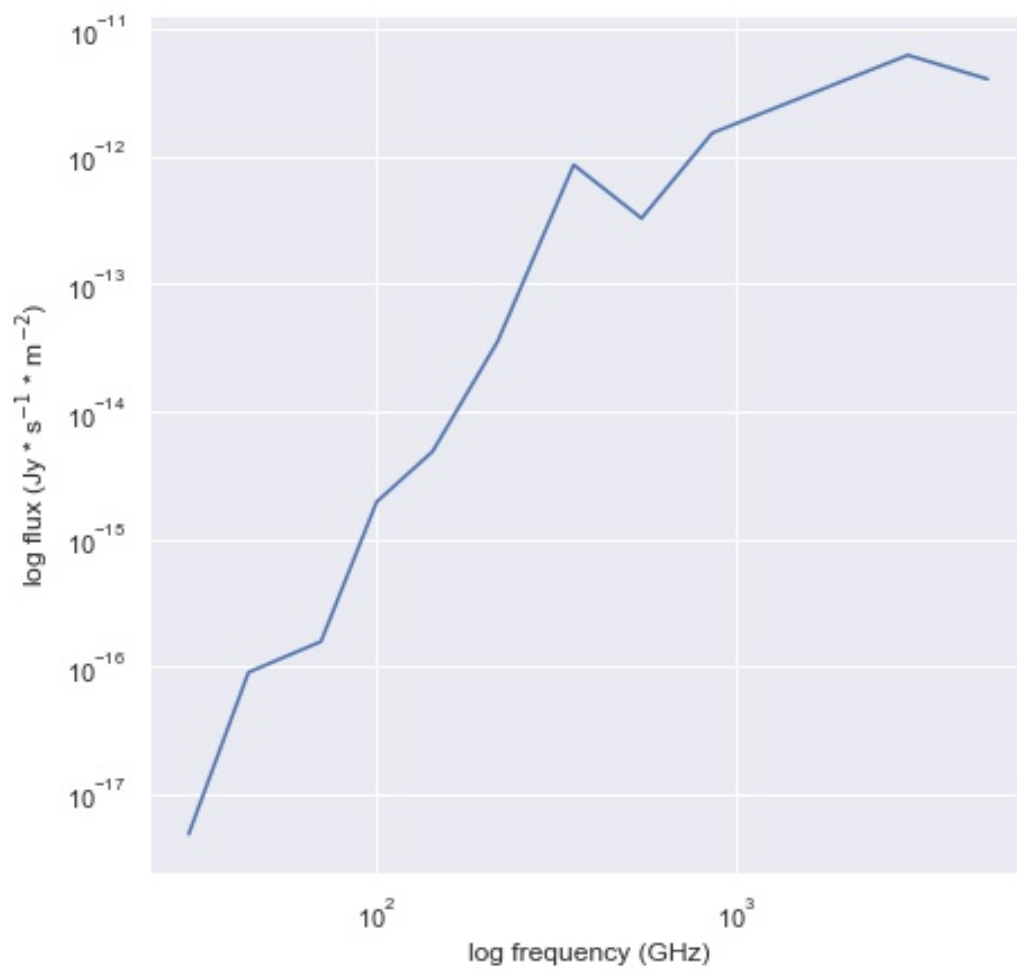


Figure 7.20 Same as figure 7.1 at position $(\ell, b) = (93.5^\circ, -34.0^\circ)$

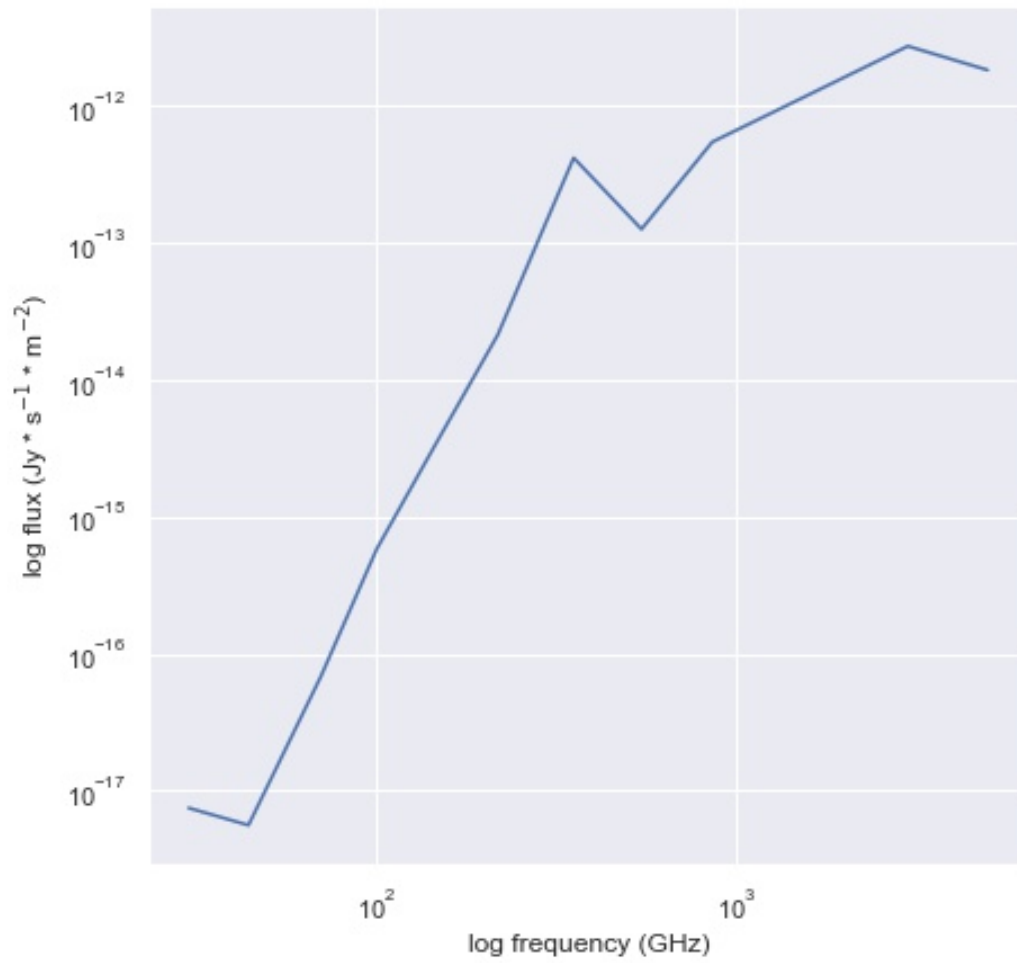


Figure 7.21 Same as figure 7.1 at position $(\ell, b) = (94.6^\circ, -30.0^\circ)$

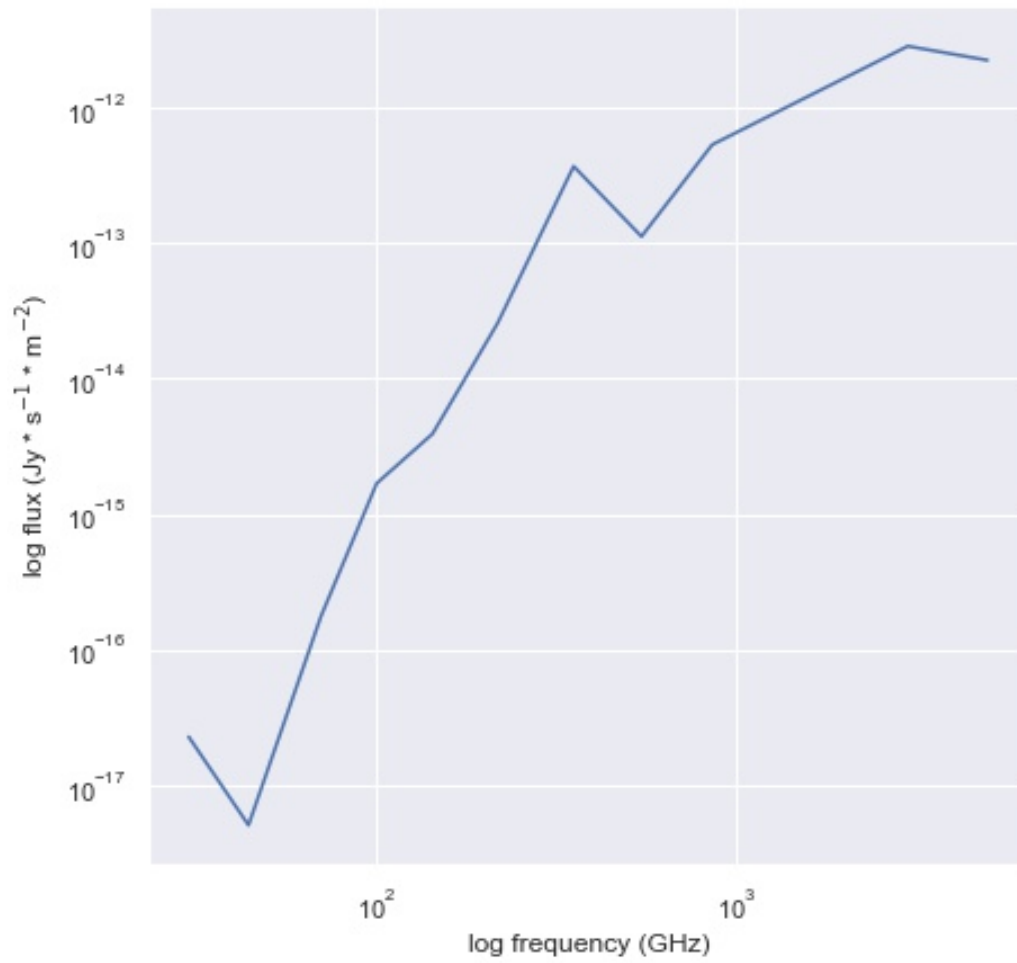


Figure 7.22 Same as figure 7.1 at position $(\ell, b) = (94.6^\circ, -31.0^\circ)$

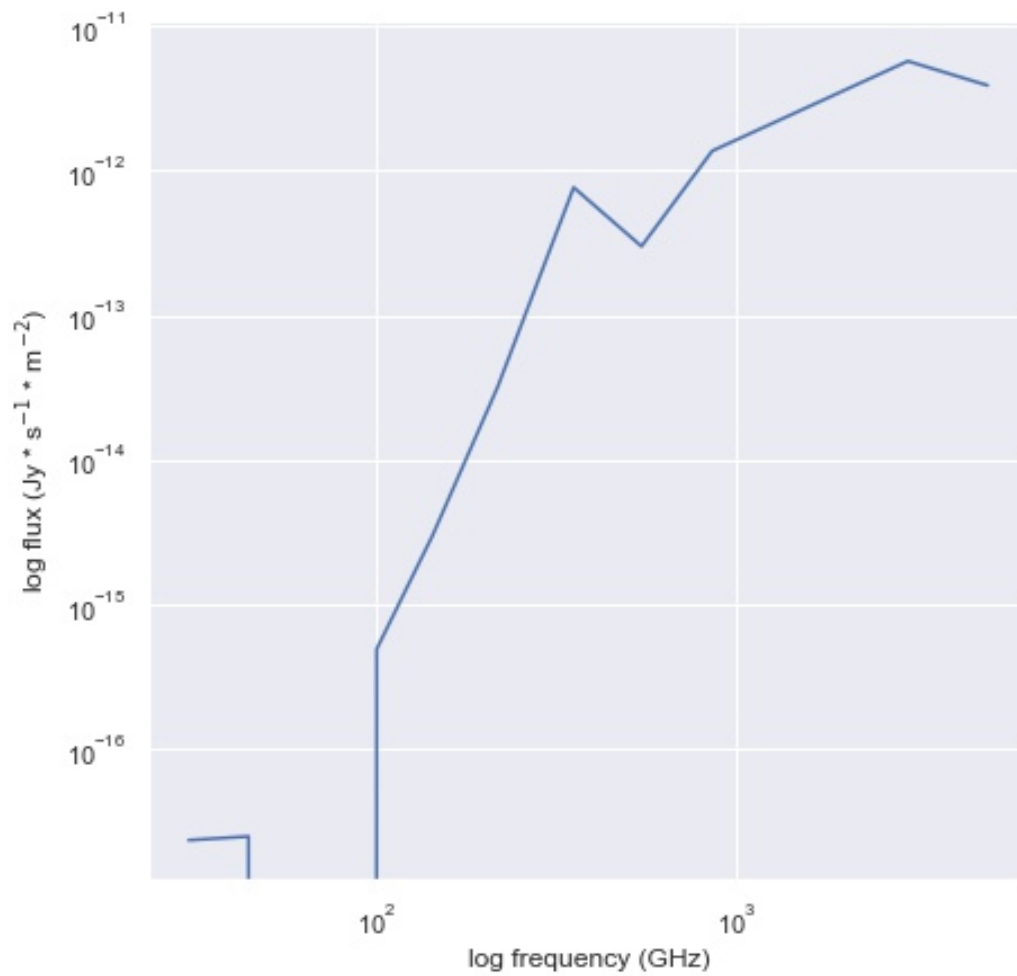


Figure 7.23 Same as figure 7.1 at position $(\ell, b) = (94.6^\circ, -32.0^\circ)$

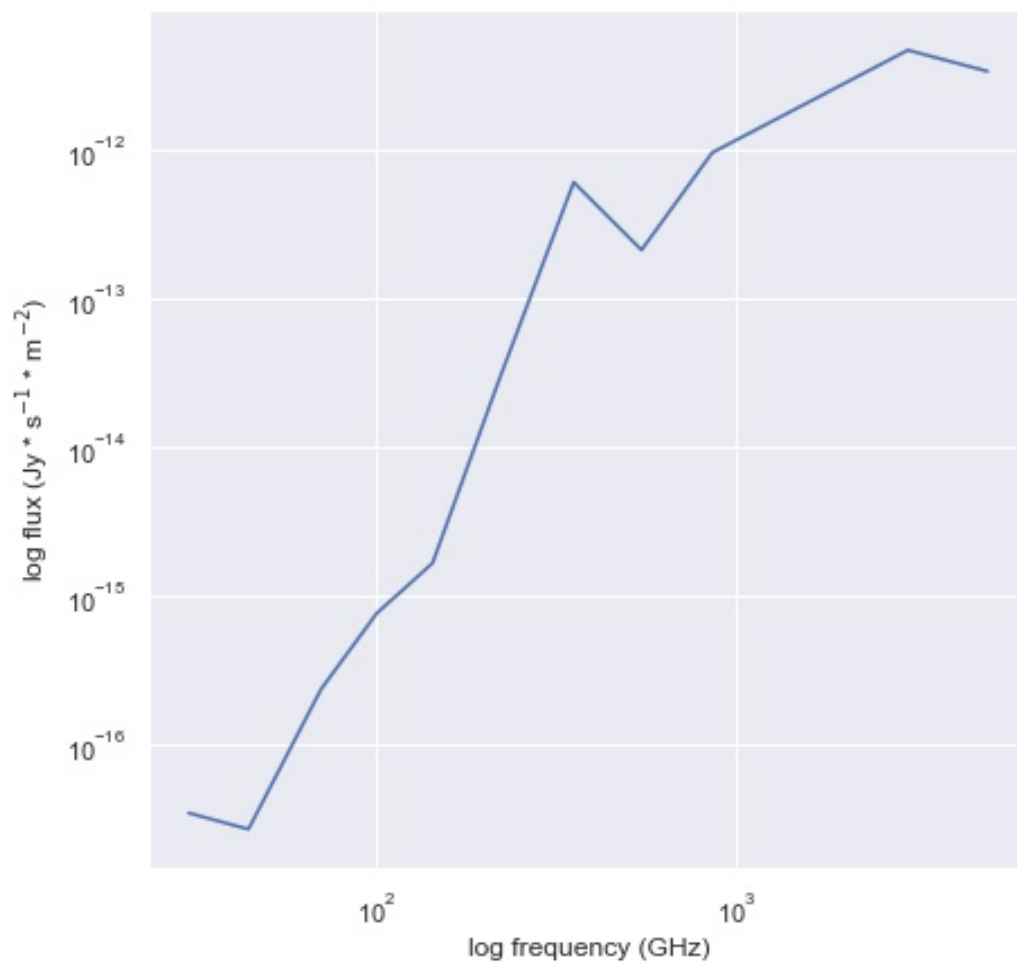


Figure 7.24 Same as figure 7.1 at position $(\ell, b) = (94.6^\circ, -33.0^\circ)$

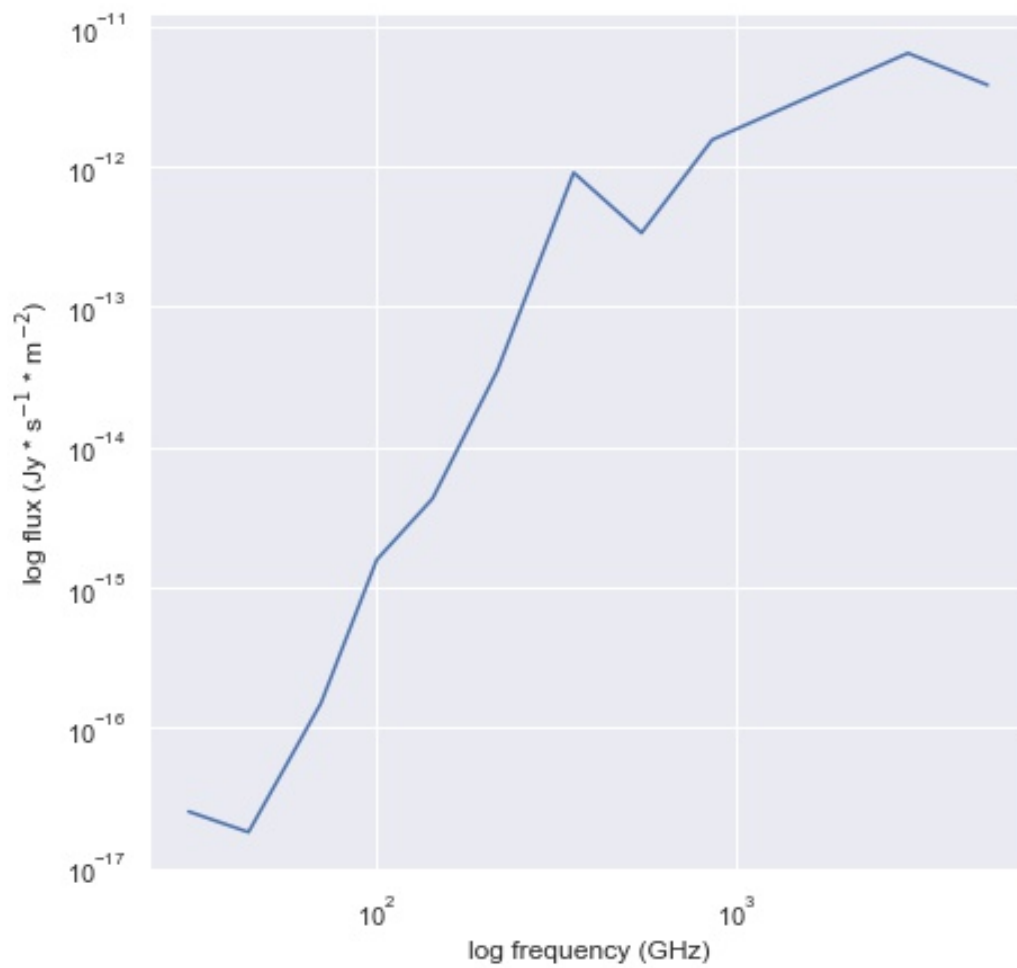


Figure 7.25 Same as figure 7.1 at position $(\ell, b) = (94.6^\circ, -34.0^\circ)$

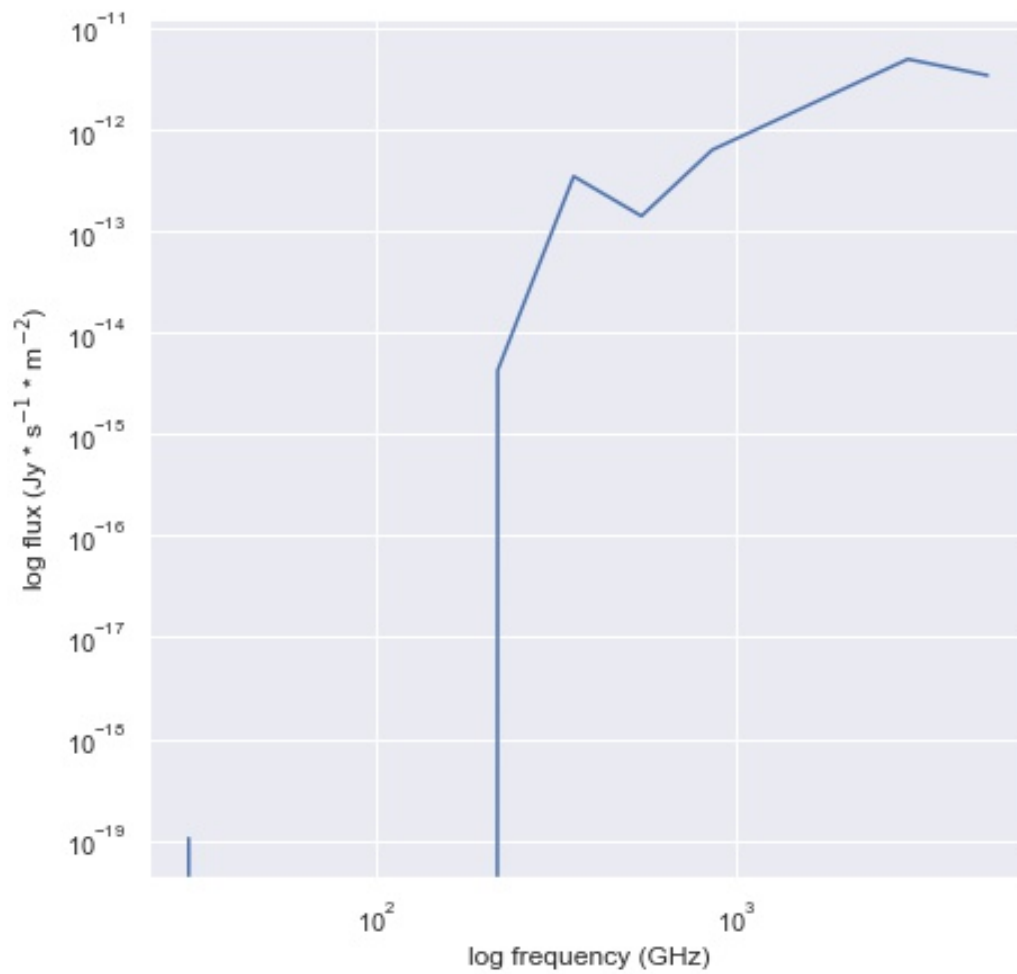


Figure 7.26 Same as figure 7.1 at position $(\ell, b) = (95.7^\circ, -30.0^\circ)$

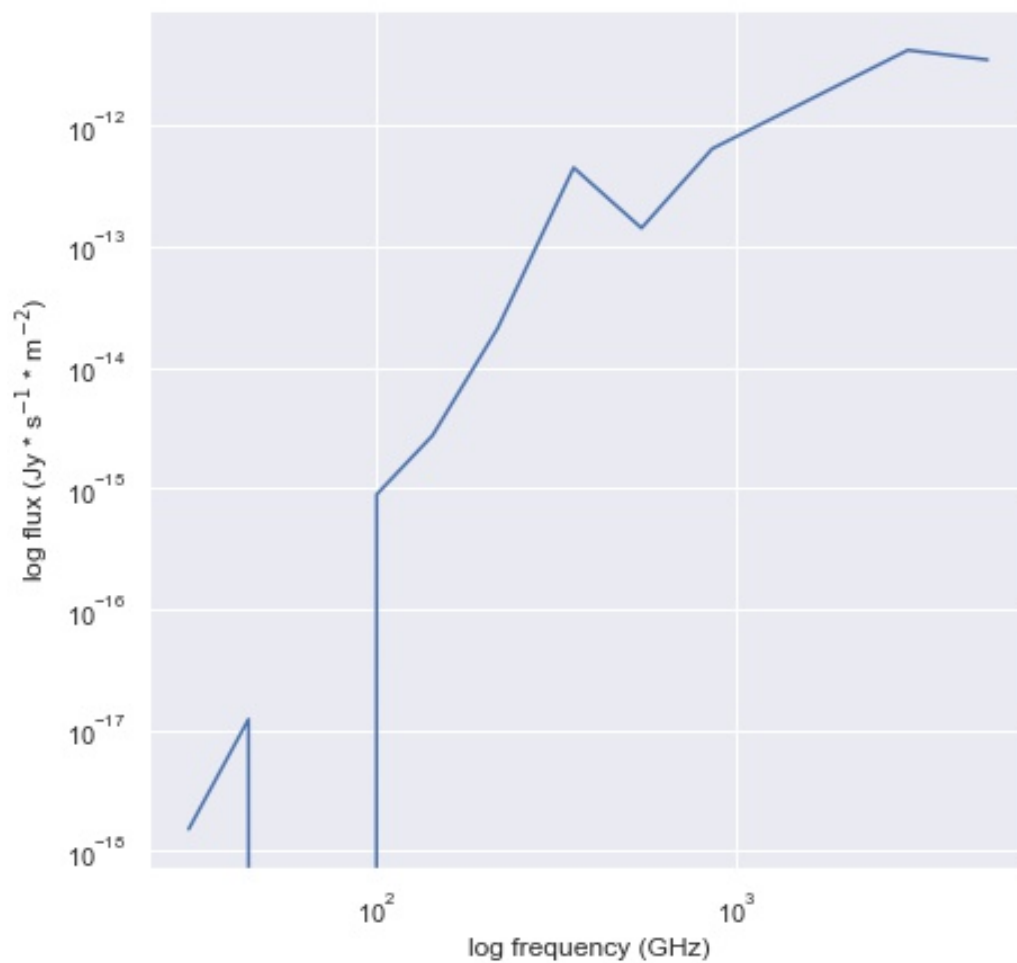


Figure 7.27 Same as figure 7.1 at position $(\ell, b) = (95.7^\circ, -31.0^\circ)$

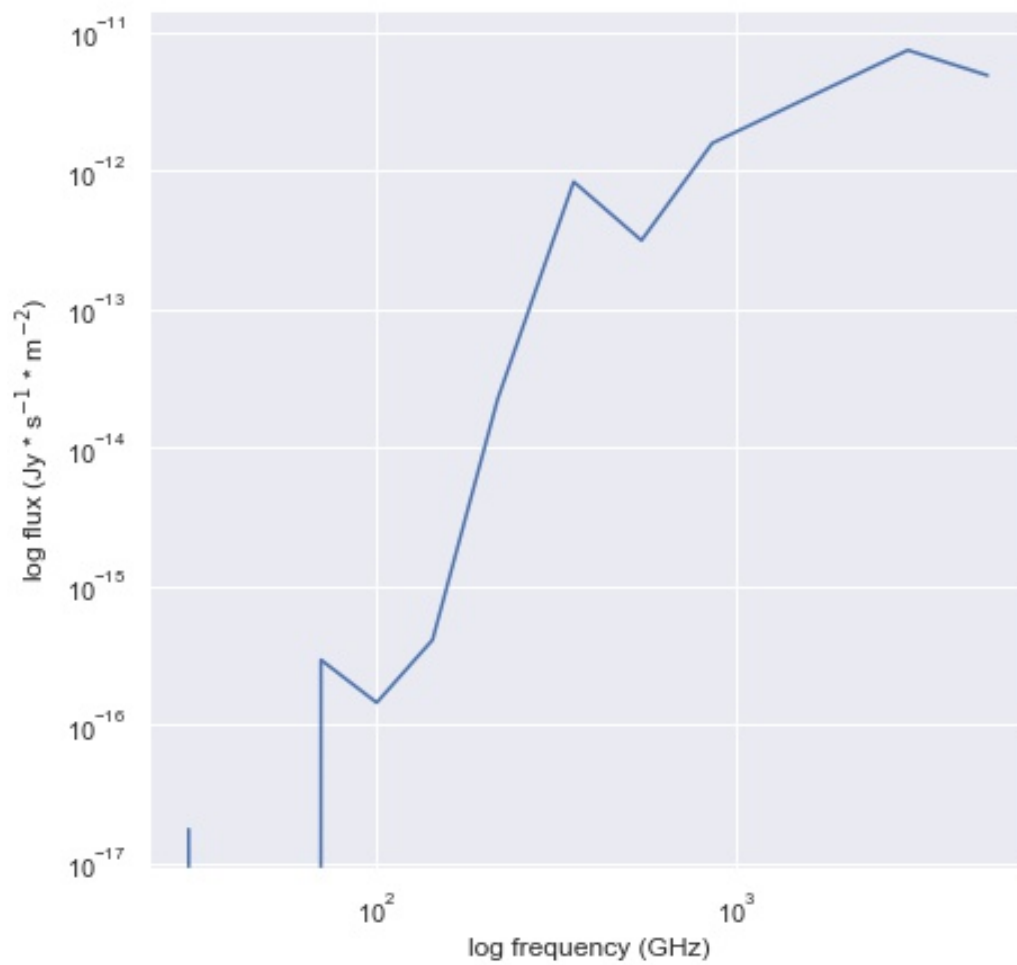


Figure 7.28 Same as figure 7.1 at position $(\ell, b) = (95.7^\circ, -32.0^\circ)$

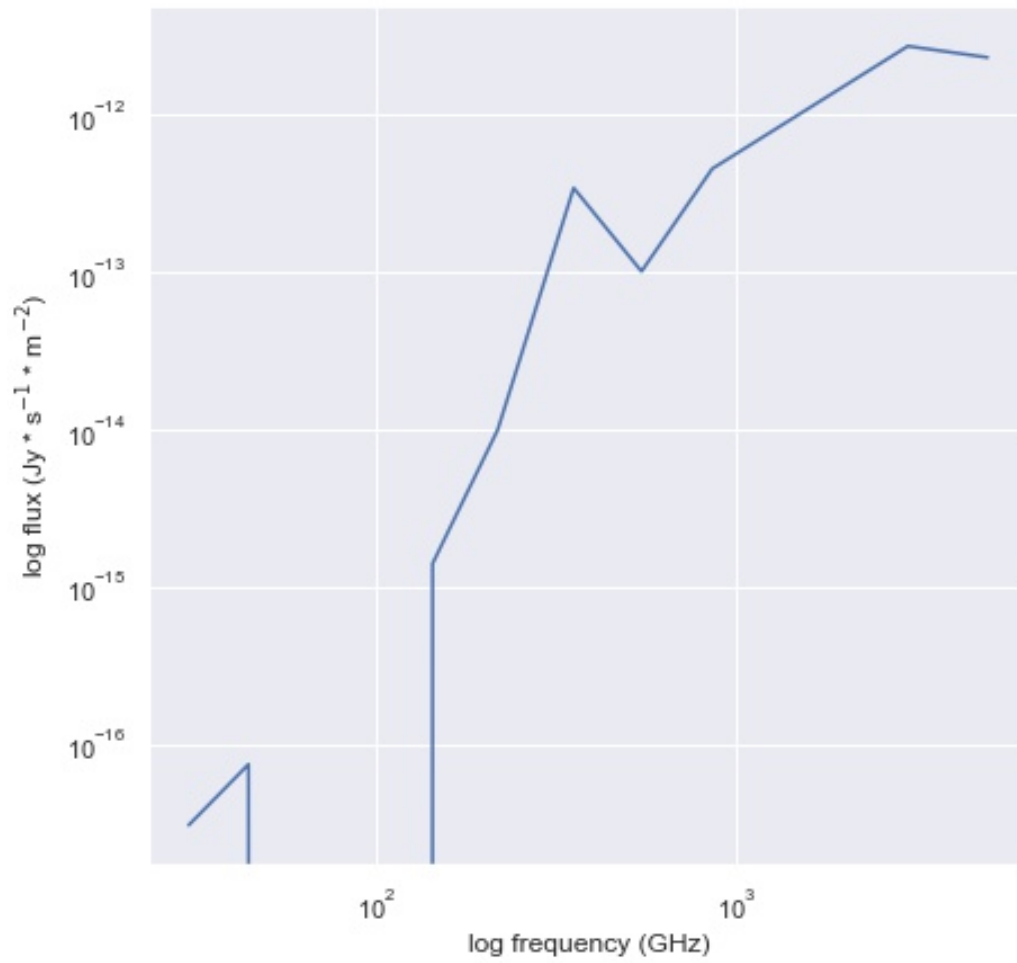


Figure 7.29 Same as figure 7.1 at position $(\ell, b) = (95.7^\circ, -33.0^\circ)$

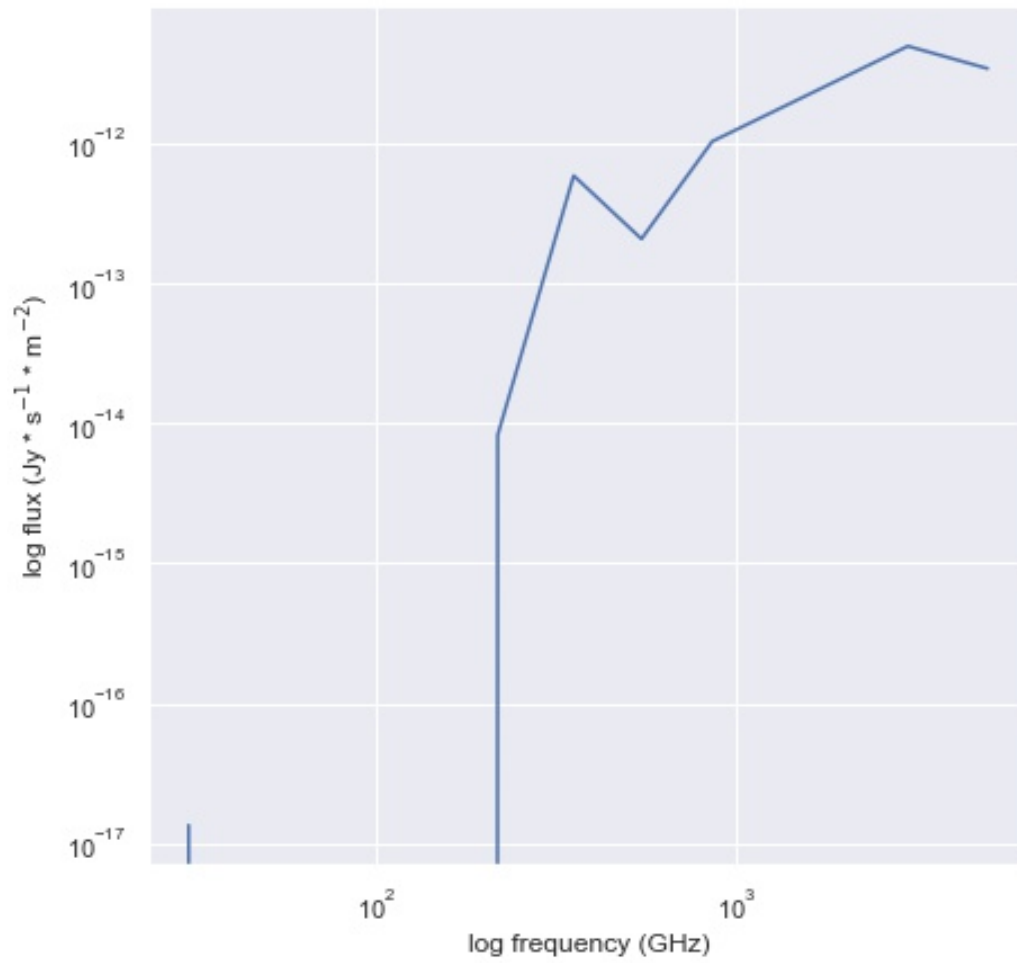


Figure 7.30 Same as figure 7.1 at position $(\ell, b) = (95.7^\circ, -34.0^\circ)$

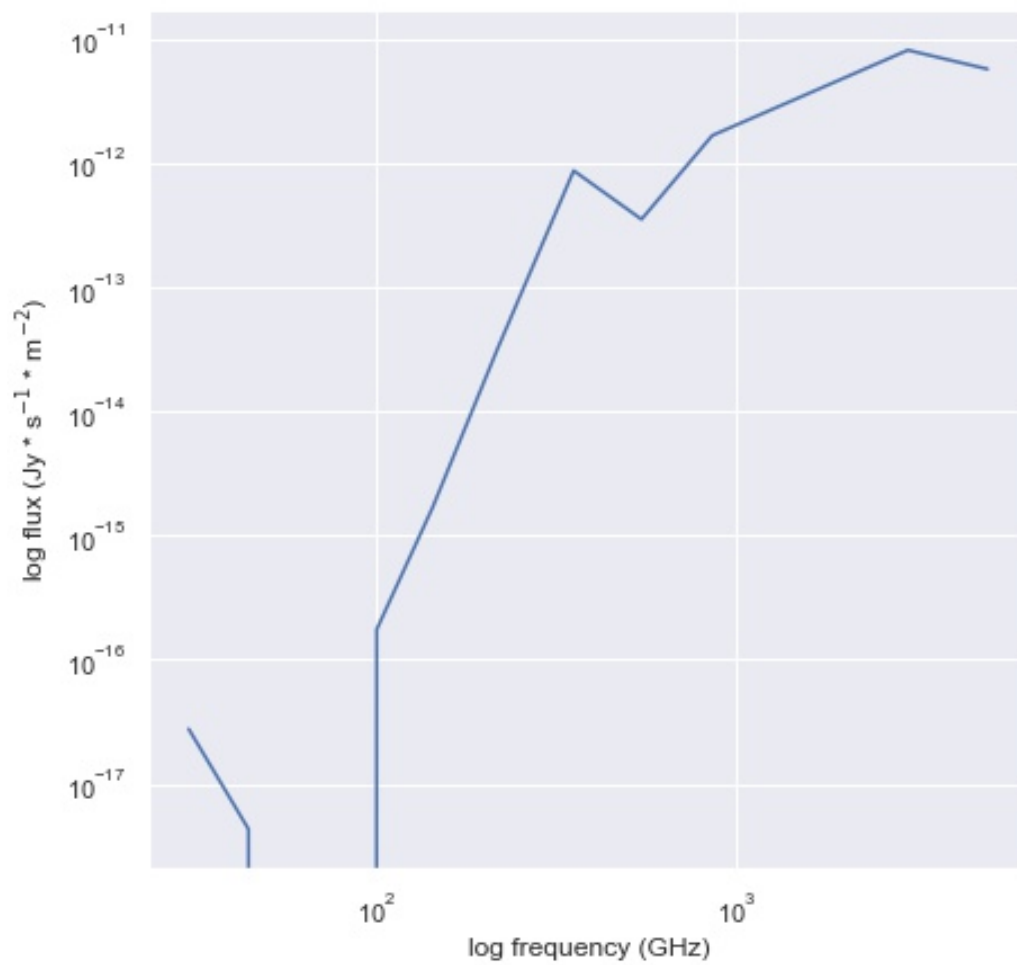


Figure 7.31 Same as figure 7.1 at position $(\ell, b) = (96.8^\circ, -30.0^\circ)$

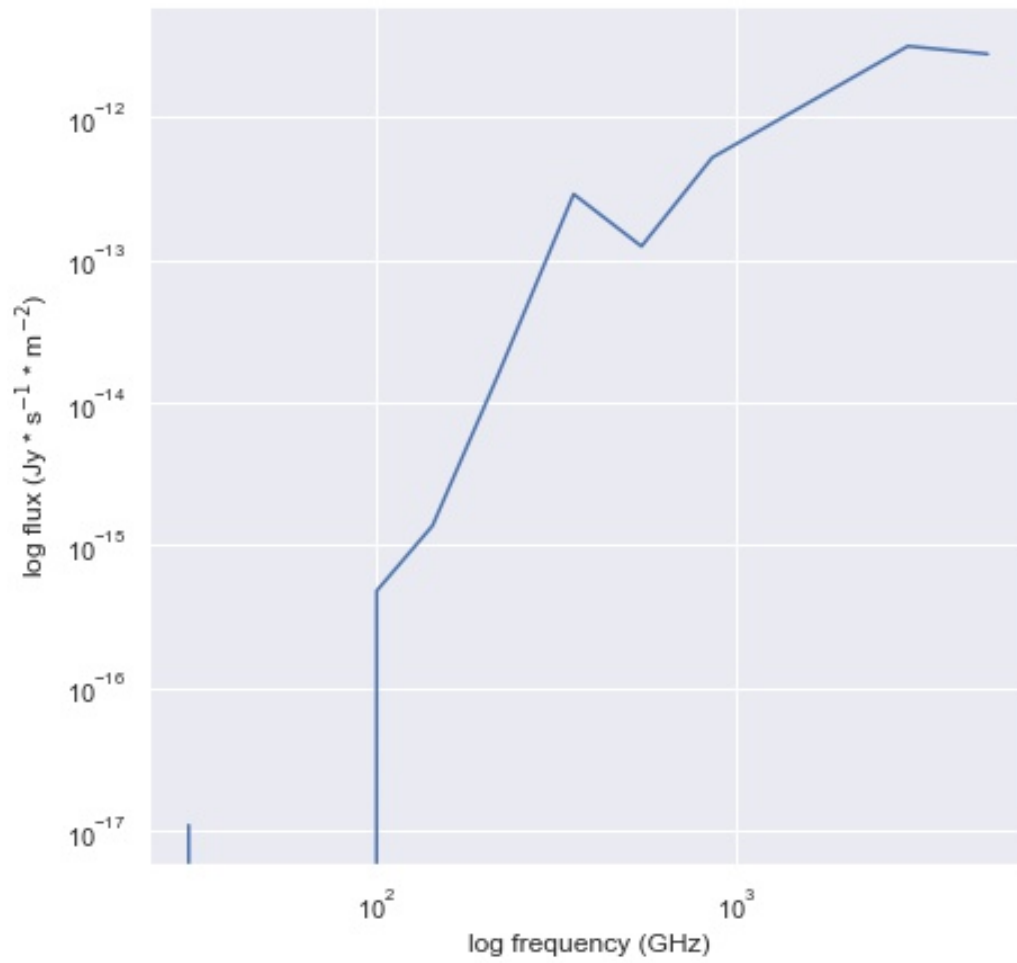


Figure 7.32 Same as figure 7.1 at position $(\ell, b) = (96.8^\circ, -31.0^\circ)$

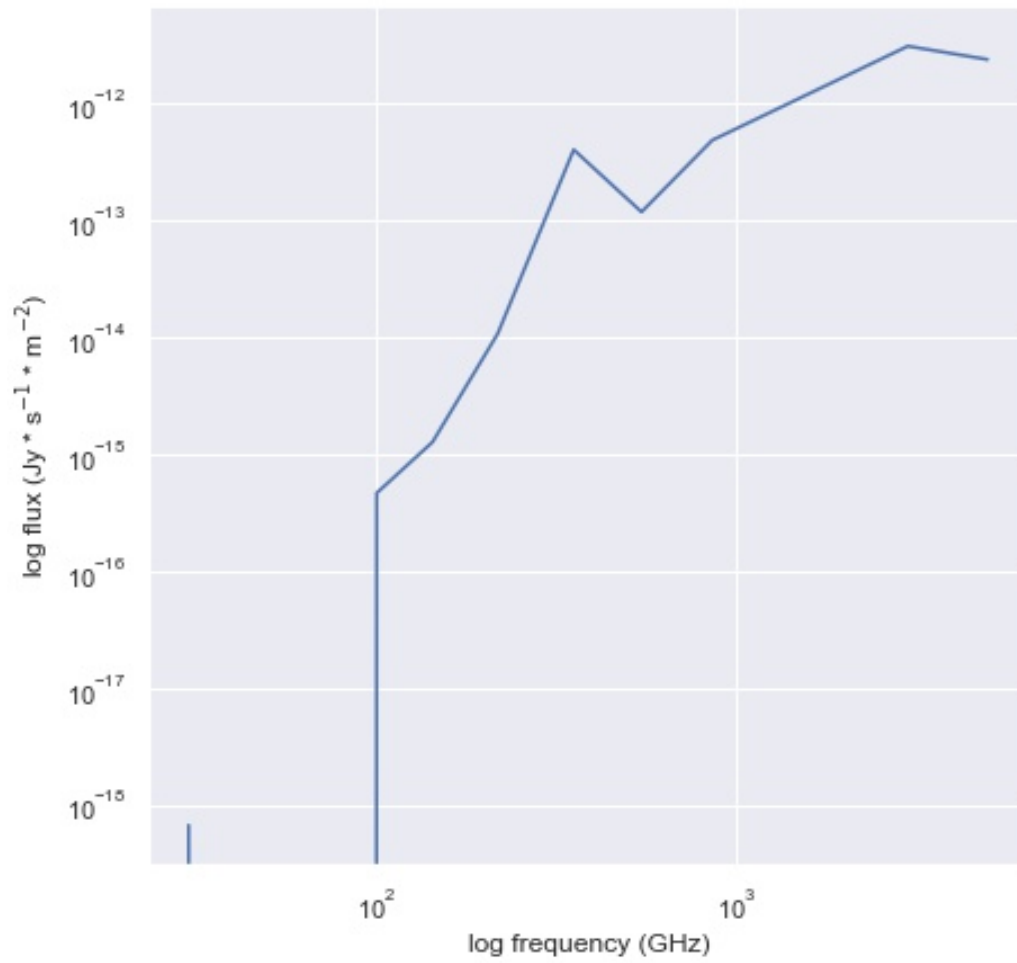


Figure 7.33 Same as figure 7.1 at position $(\ell, b) = (96.8^\circ, -32.0^\circ)$

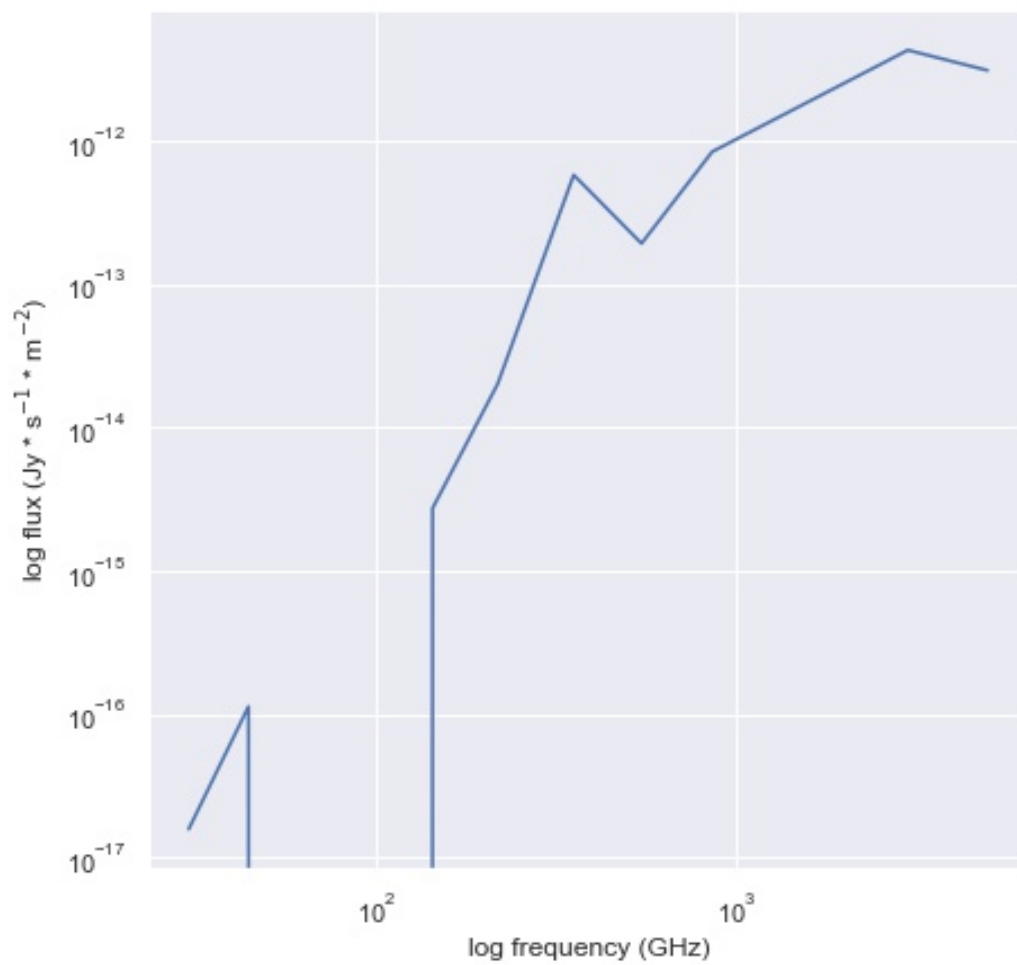


Figure 7.34 Same as figure 7.1 at position $(\ell, b) = (96.8^\circ, -33.0^\circ)$

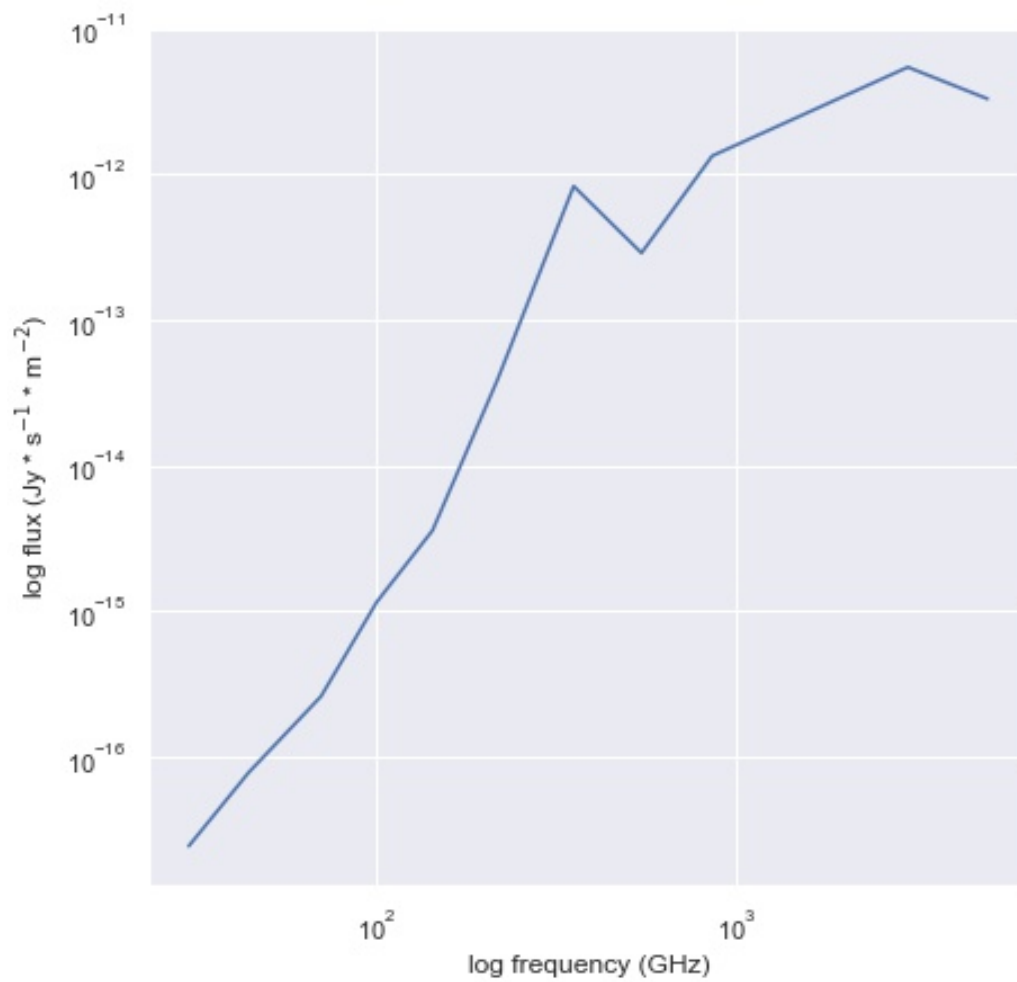


Figure 7.35 Same as figure 7.1 at position $(\ell, b) = (96.8^\circ, -34.0^\circ)$

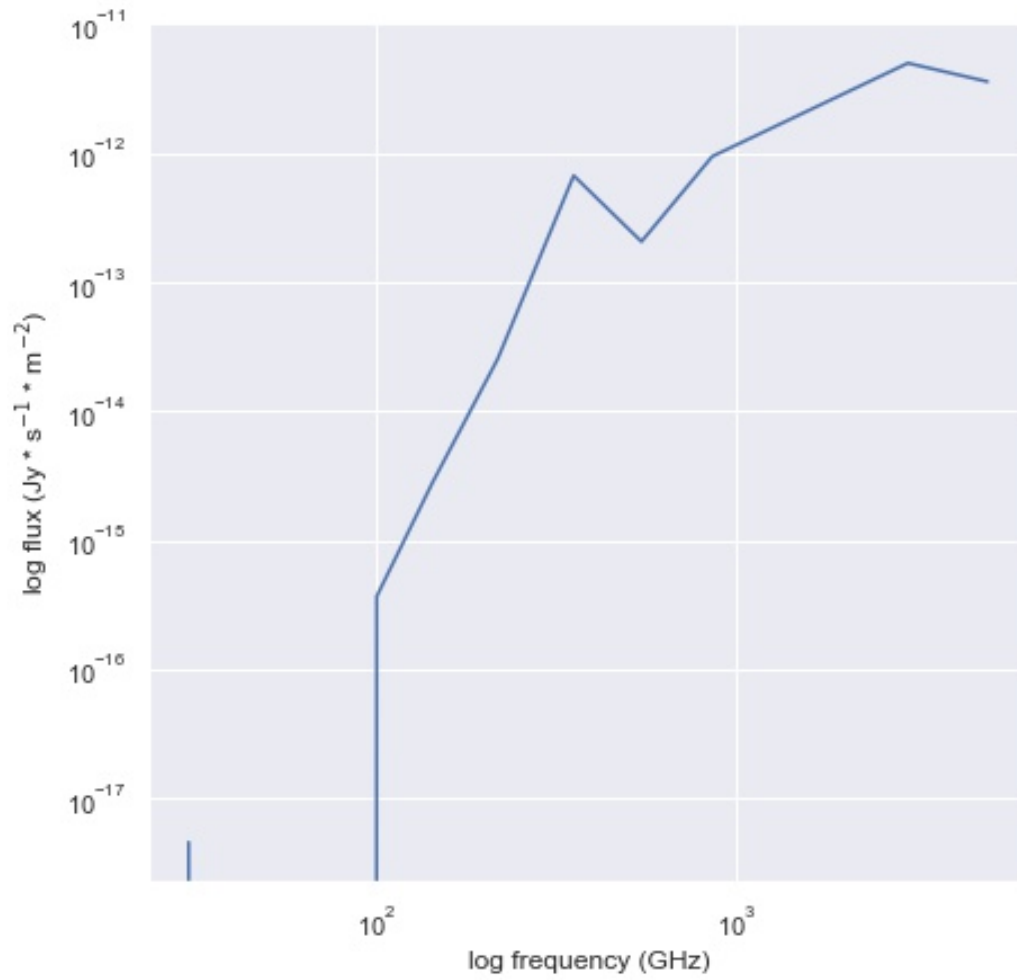


Figure 7.36 Same as figure 7.1 at position $(\ell, b) = (97.9^\circ, -30.0^\circ)$

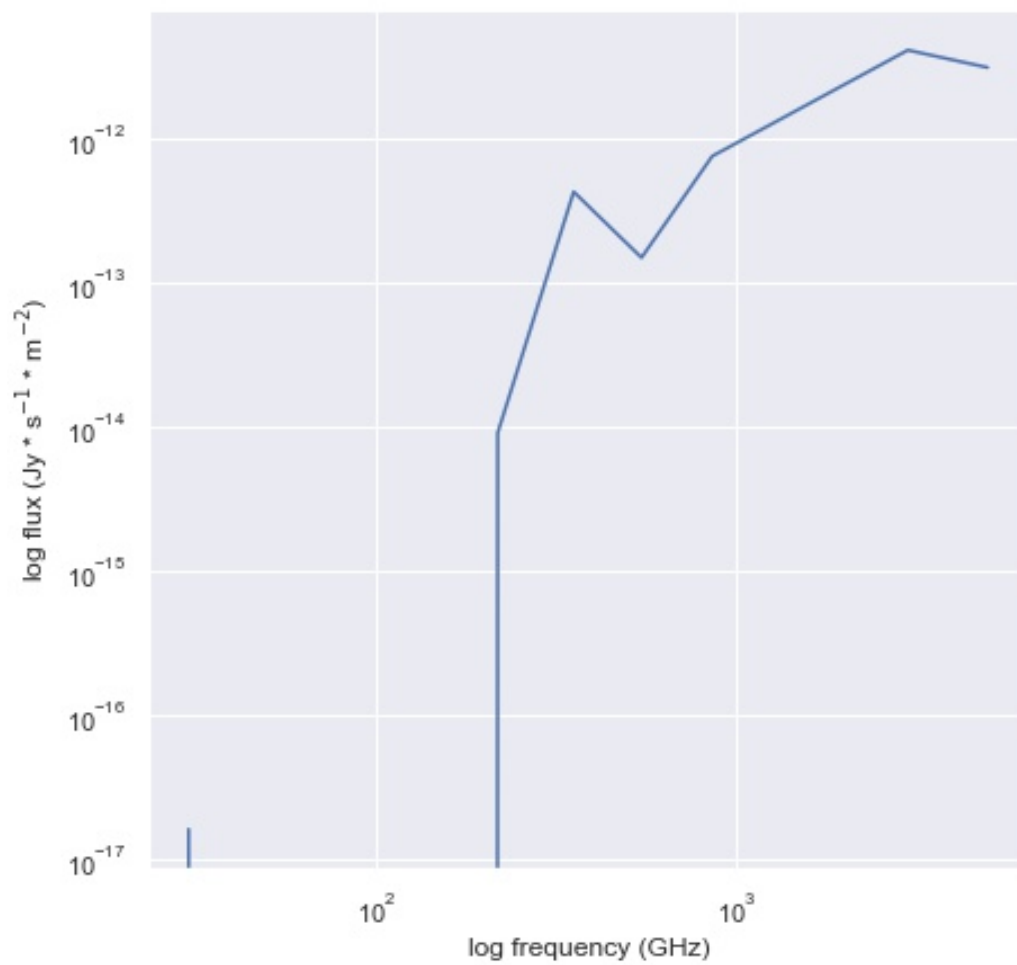


Figure 7.37 Same as figure 7.1 at position $(\ell, b) = (97.9^\circ, -31.0^\circ)$

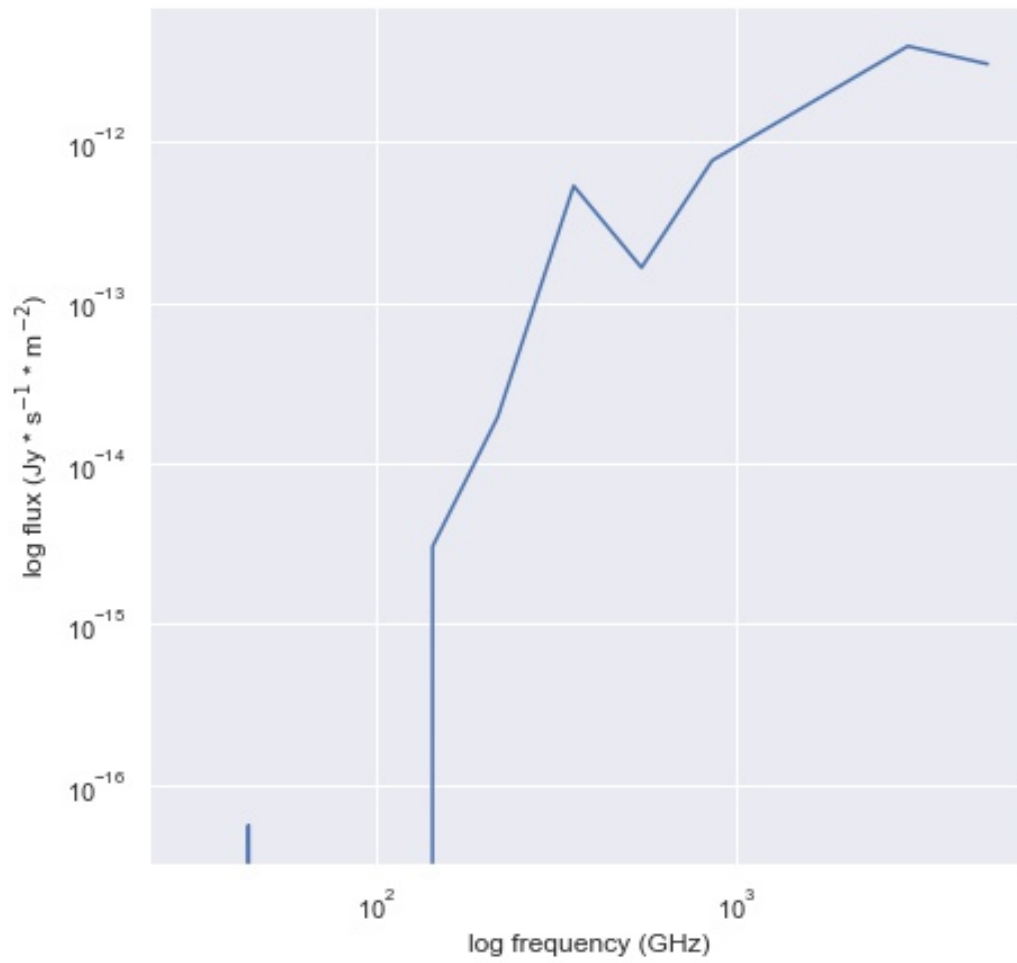


Figure 7.38 Same as figure 7.1 at position $(\ell, b) = (97.9^\circ, -32.0^\circ)$

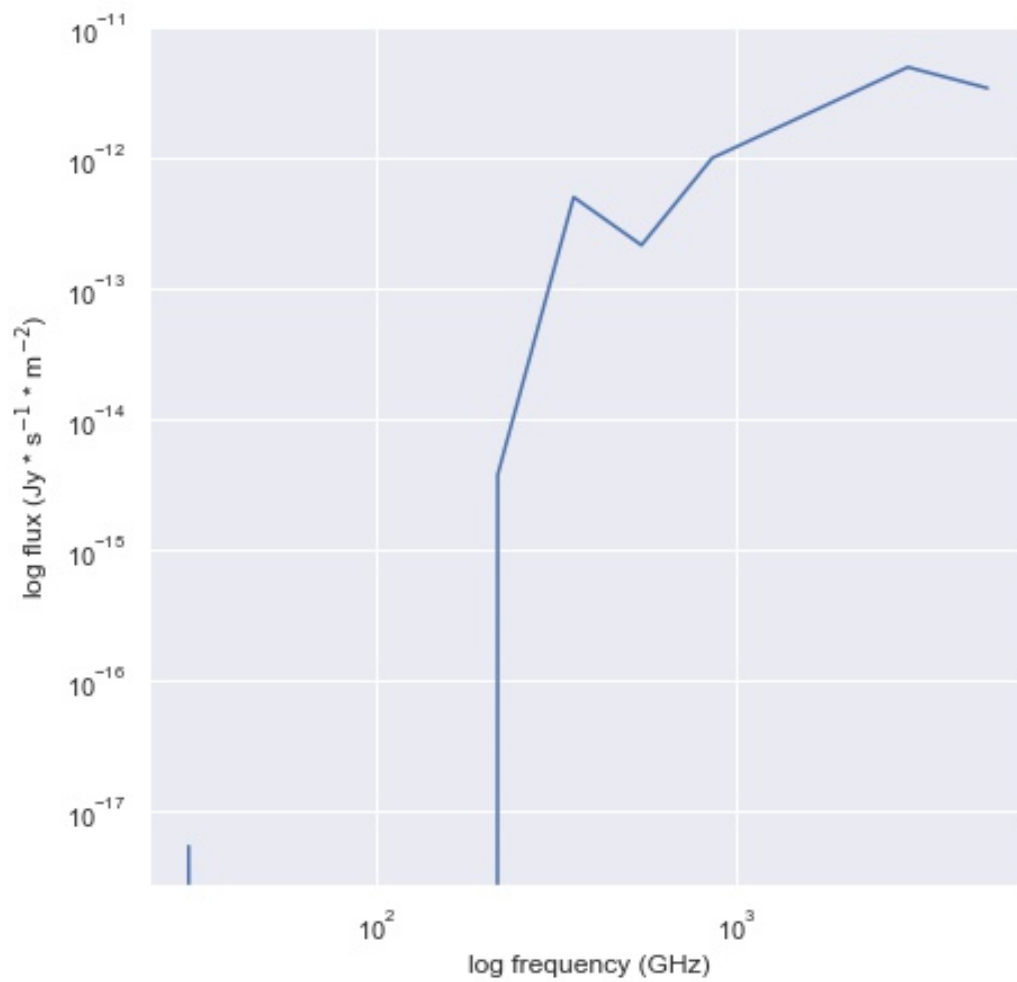


Figure 7.39 Same as figure 7.1 at position $(\ell, b) = (97.9^\circ, -33.0^\circ)$

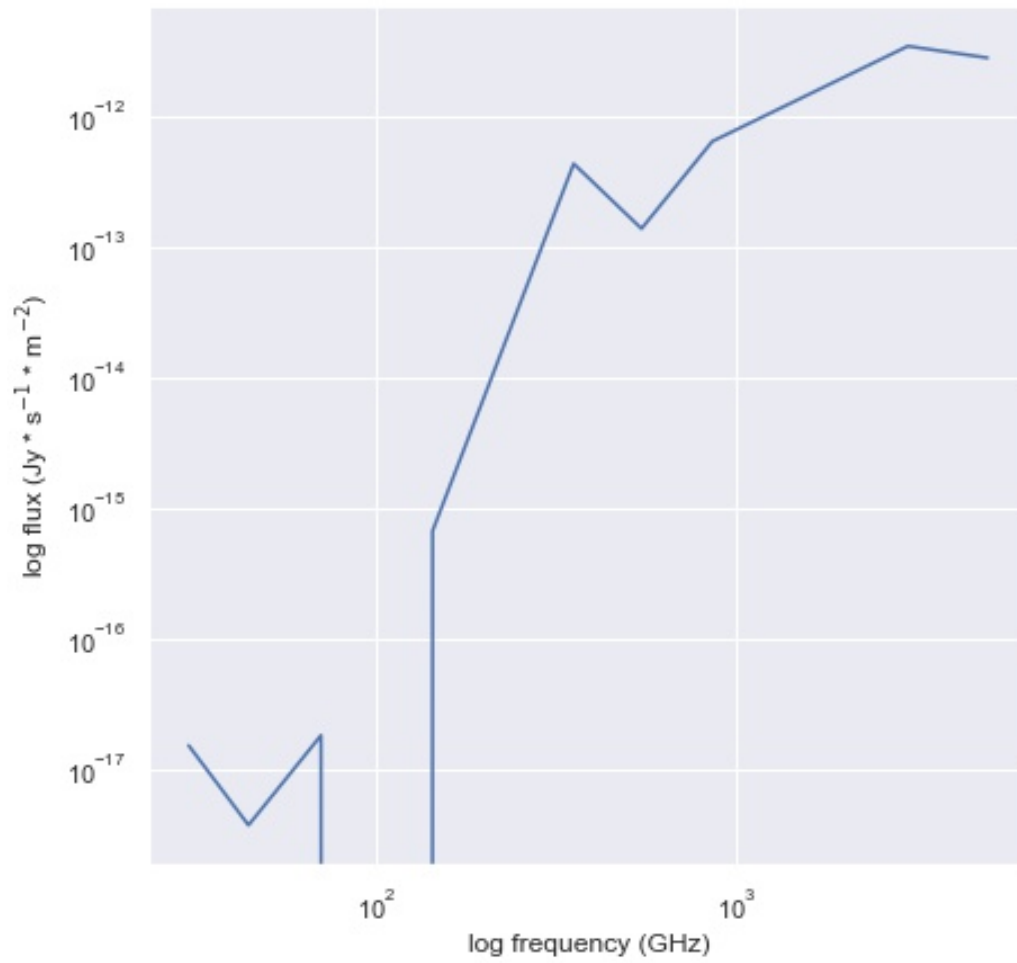


Figure 7.40 Same as figure 7.1 at position $(\ell, b) = (97.9^\circ, -34.0^\circ)$

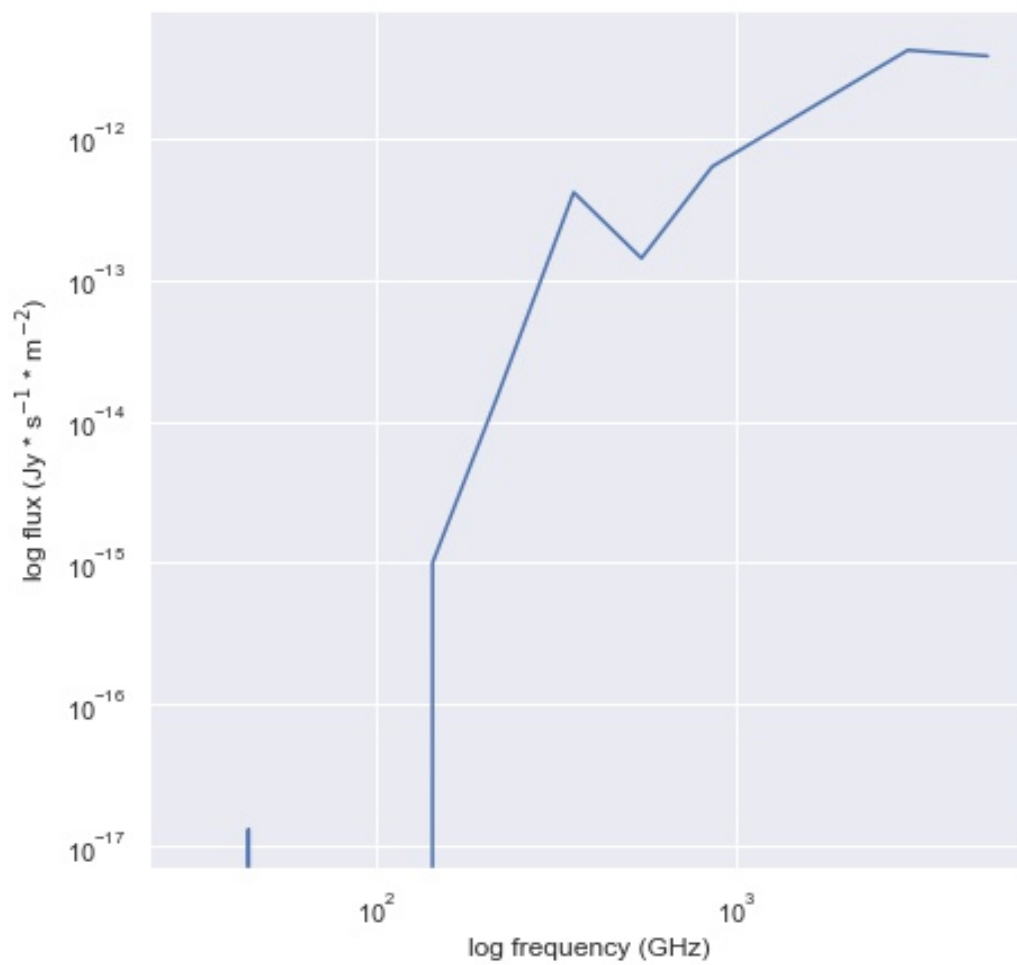


Figure 7.41 Same as figure 7.1 at position $(\ell, b) = (99.0^\circ, -30.0^\circ)$

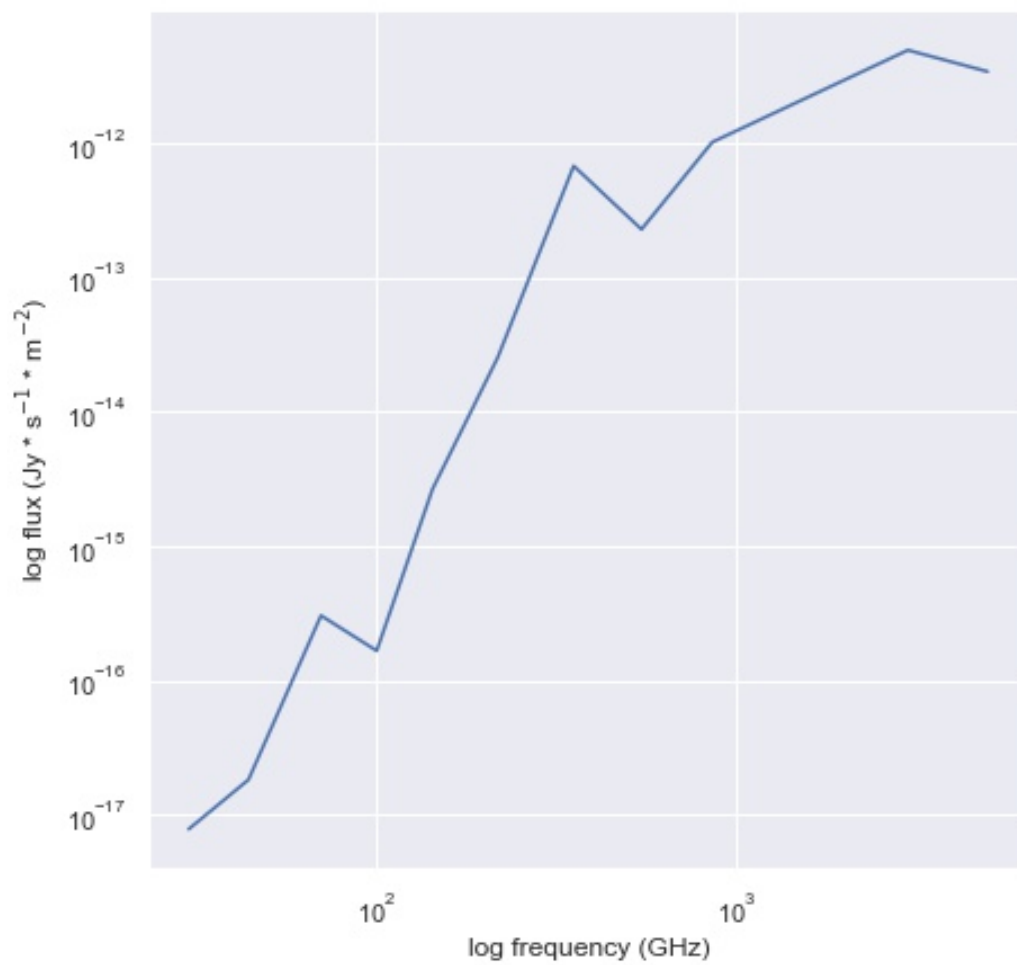


Figure 7.42 Same as figure 7.1 at position $(\ell, b) = (99.0^\circ, -31.0^\circ)$

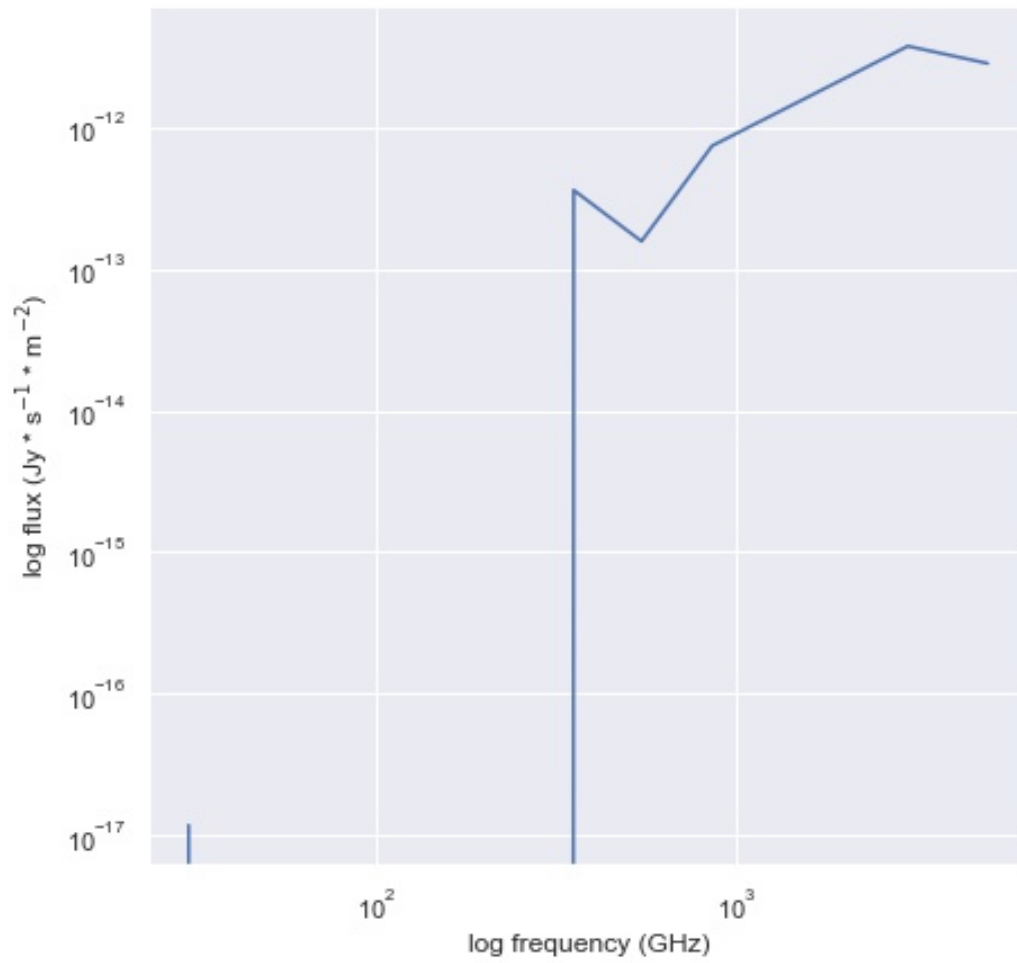


Figure 7.43 Same as figure 7.1 at position $(\ell, b) = (99.0^\circ, -32.0^\circ)$

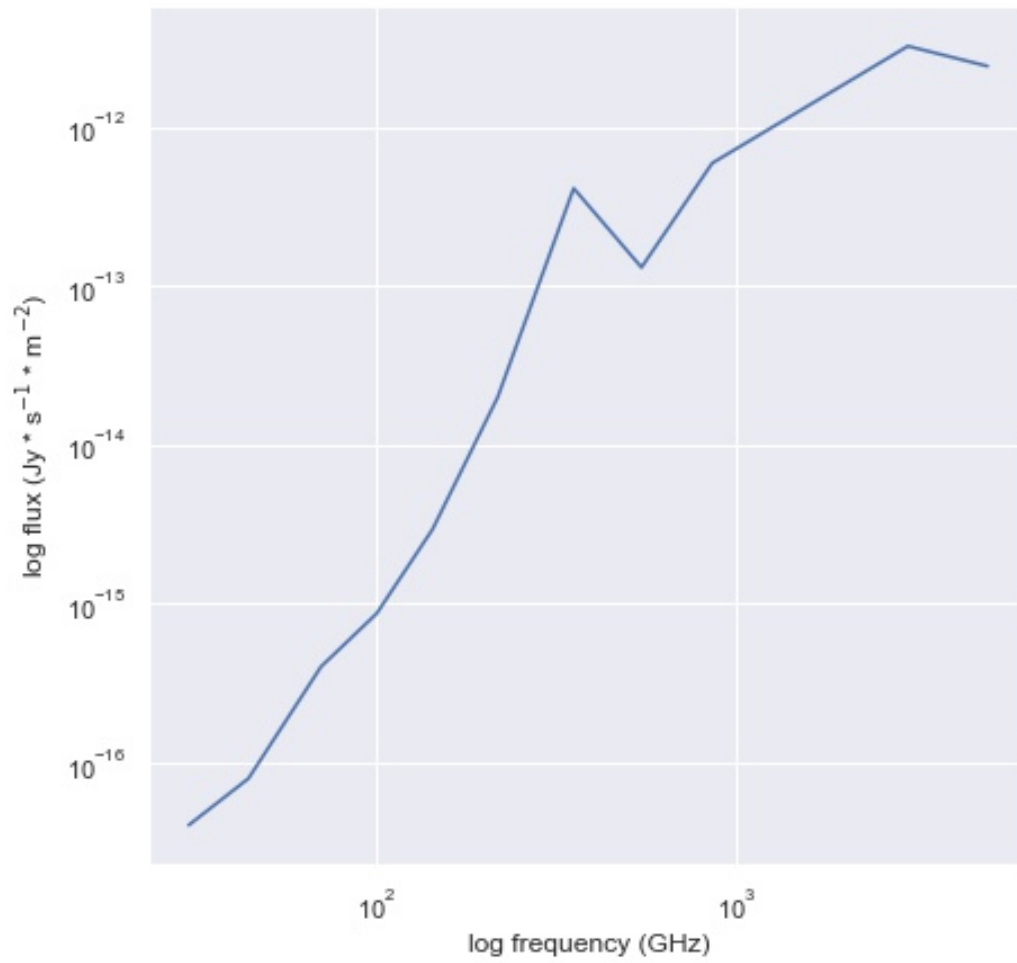


Figure 7.44 Same as figure 7.1 at position $(\ell, b) = (99.0^\circ, -33.0^\circ)$

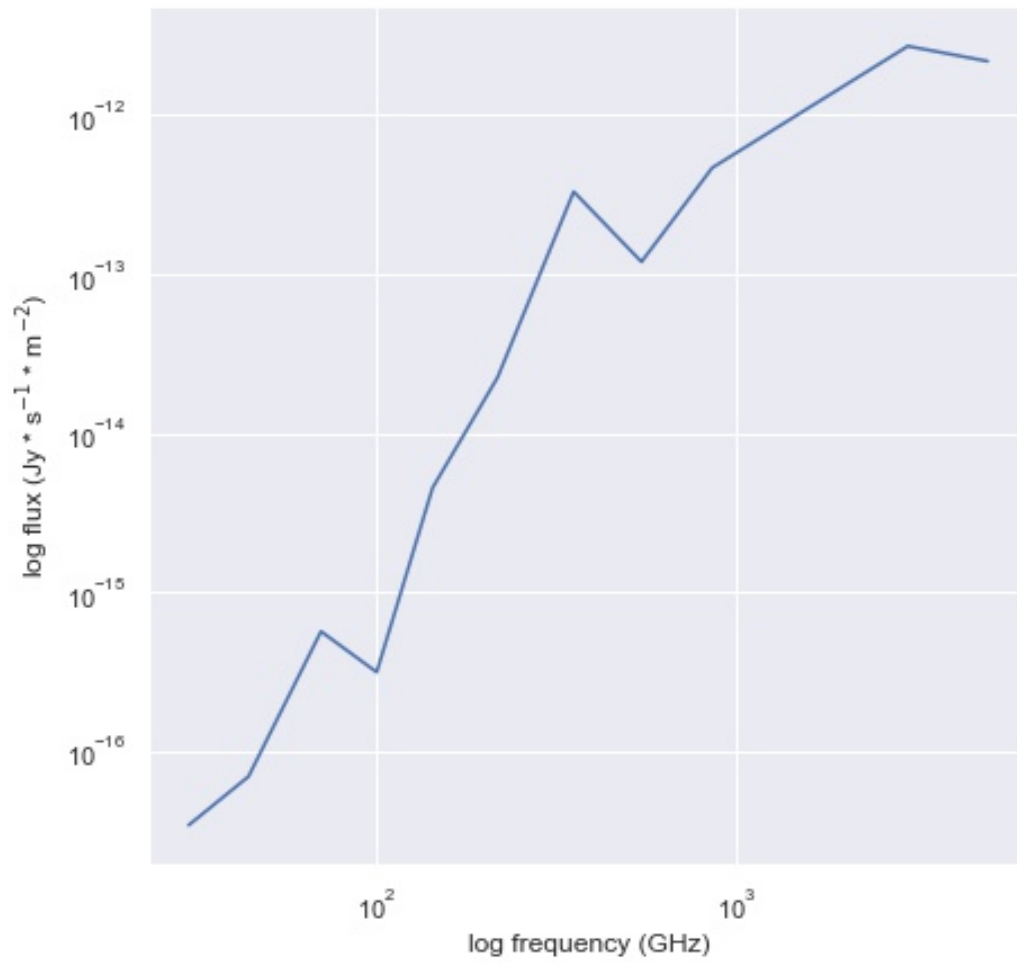


Figure 7.45 Same as figure 7.1 at position $(\ell, b) = (99.0^\circ, -34.0^\circ)$

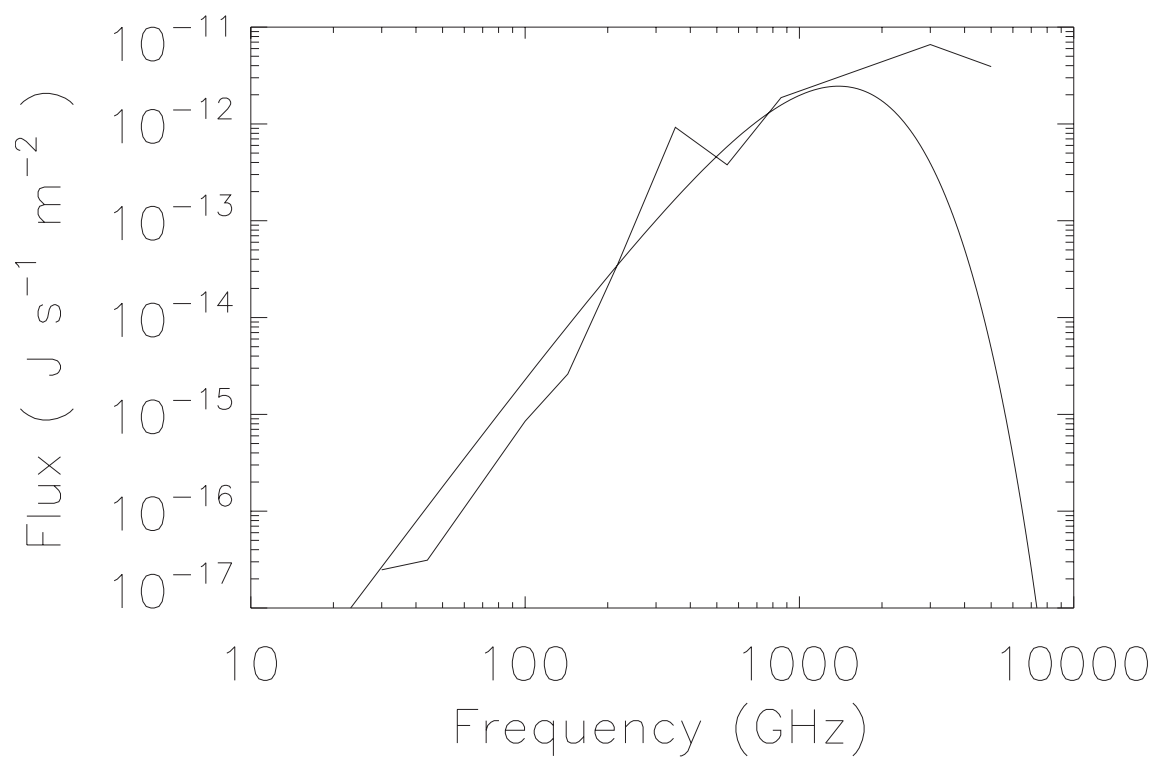


Figure 7.46 The spectrum for position $(\ell, b) = (92.4^\circ, -34.1^\circ)$ shown above with a scaled blackbody spectrum with $T = 14$ K superposed on the data.

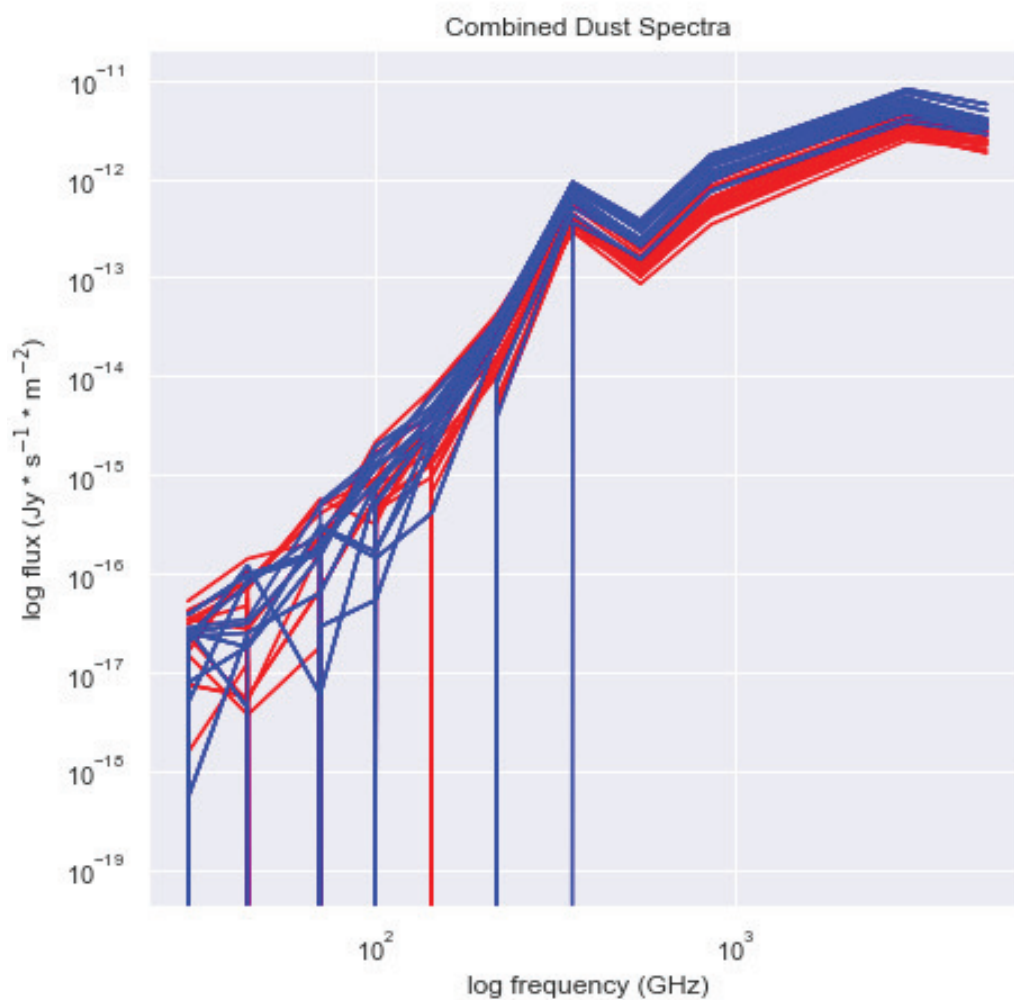


Figure 7.47 Combined dust spectra for all 44 sightlines observed in OH. The blue spectra are for lines of sight with molecular detections of OH and/or CO and the red spectra are for lines of sight with non-detections.

CHAPTER 8

SUMMARY AND FUTURE WORK

8.1 SUMMARY

This project began when we questioned the amount of mass in the dark gas halos discovered by Grenier, Casandijan, and Terrier (2005). They estimated that at least half of the molecular mass of the Galaxy is in a form (dark gas) that was spectroscopically undetectable. This assertion was later modified to mean that the CO(1-0) line was undetectable in emission from these regions, although other tracers could detect this molecular gas. In particular, we chose to investigate a high latitude cloud (MBM 53) for which we could compare a number of different mass estimates from previous molecular surveys. Our results show that Grenier, Casandijan, and Terrier's conclusions that at least half the molecular gas mass is spectroscopically undetectable is overstated. In Chapter 4 we report that sensitive CO(1-0) observations reduce the dark gas mass fraction in a region in MBM 53 by a factor of 2. The sensitive CO(1-0) observations increase the molecular mass of the cloud by a factor of two and this increase has to come at the expense of the dark gas estimate from Grenier, Casandijan, and Terrier (2005).

Other observers, looking to find ways to trace dark gas mass began using OH 18 cm lines (Allen et al. 2012; 2015; Barriault et al 2010a, Cotten et al. 2012). In Chapter 5 we report on our OH observations in MBM 53 and show that although the OH results do indicate a greater dark gas mass than CO observations, the OH does not clearly define the extent of the molecular gas regions as well as the sensitive CO(1-0) observations.

In Chapter 6, we looked at an old data set, the CO(1-0) survey of the Southern Galactic Hemisphere by Magnani et al. (2000), and re-examined the data trading spatial resolution for sensitivity. The original survey was made at $8'$ resolution with one-degree sampling. By adding together the spectra from regions of larger area we increased the sensitivity (at the expense of spatial resolution). In this way, we could estimate how a more sensitive survey would have detected more CO emission. As the sensitivity increased, the detection rate first increased, then decreased as any CO emission in the larger regions was diluted by the increasing number of non-detections. The optimal sensitivity was again, ≈ 0.02 K and the molecular mass in the SGH again increases by a factor of two. The results of this study confirmed our results from Chapter 4 on a larger scale.

Finally, in Chapter 7, we produced continuum spectra in the radio and infrared (from 30 GHz to 5000 GHz) for the same points studied in Chapter 5 (a subset of those studied in Chapter 4). The emission came from a combination of the thermal dust emission from the cloud and a series of thermal and non-thermal backgrounds. We did not remove these backgrounds in the hope that over the relatively small region we studied in MBM 53 the contribution from the backgrounds would be the same. In this way, we hoped to discriminate between lines of sight with CO and OH emission and lines without just by looking at the spectral shape. Although our effort was unsuccessful (i.e., there is no signature spectral shape for lines of sight with detectable CO or OH emission) we did notice that the lines of sight with molecular emission had more radio/infrared flux compared to the lines of sight with non-detections.

The results presented in this thesis apply specifically to the high latitude and or diffuse molecular clouds in the Galaxy. It is unclear how these results would apply to the Giant Molecular Clouds distributed throughout the disk. In summary, at least some of the dark molecular gas is detectable spectroscopically, however, there will always be a regime at the edge of PDRs where H_2 is present, but the usual tracers will be too low in abundance to be detectable in emission by radio spectroscopic techniques. Our results indicate that this

spectroscopically undetectable gas is significantly less than originally stated by GCT and is more commensurate to what is expected from standard PDR models.

8.2 ASSUMPTIONS AND PROBLEMS

To calculate the sensitive CO-dark gas mass we had to make several assumptions about the CO molecule’s abundance in the ISM. In particular we had to guess the value of the X factor, the conversion factor between CO(1-0) observations and $N(\text{H}_2)$. In Chapters 4 and 6 we use the same value as that used by Grenier, Casandjian, and Terrier (2005) because we wanted to compare our results directly to theirs. This was more important than using the “correct” value. Obtaining the correct value for a diffuse or translucent cloud is not trivial, as it has been established that the X factor varies from cloud to cloud and even across a cloud (Magnani and Onello (1995); Magnani et al. (1998)). In contrast, the X-factor seems to be fairly constant for GMCs and dark molecular clouds, (see review by Bolatto, Wolfire, and Leroy 2013). We still do not know when and why it varies in diffuse molecular clouds, thus any mass estimate using a single X factor for a diffuse molecular region is bound to be off the actual mark. There is a way to calibrate the X factor in these clouds, but it requires extensive, sensitive, CH observations to act as calibrators (see below).

When looking at OH we also make a similar assumption: The abundance ratio $N(\text{OH})/N(\text{H}_2)$. We use a constant ratio of 1×10^7 . This is reasonable as studies show that in diffuse clouds this ratio is fairly constant (Liszt and Lucas 1996; Weselak et al. 2010), Moreover, we always used, explicitly or implicitly, a constant gas to dust ratio. While the gas to dust ratio can vary significantly from 10 to 1000 (e.g., Spitzer 1978), most ISM researchers assume this value is ≈ 100 and hope for the best.

Although each of the above assumptions is somewhat problematic, we may be saved by the fact that our principal region of interest (Chapters 4, 5, and 7) is fairly small ($\sim 15^\circ \times 5^\circ$); thus, the X-factor or the OH abundance or the gas to dust ratio may not vary significantly. A

way to check both the value of the X factor and the OH/H₂ ratio is to make CH observations of the 3335 MHz line (see below).

8.3 FUTURE WORK

There are two directions to take this project to check and improve the dark gas mass estimates. We could increase the number of clouds we study or we could increase the number of molecules or tracers of dark gas in places for which we already have sensitive survey data.

A good first move would be to study any of the other MBM clouds in the Pegasus-Pisces region (MBM 1, 2, 3, 4, 51, 52, 54, 55, 56) and, later, any MBM cloud from the Northern and Southern Galactic Hemisphere surveys. Even by studying the edges of one other cloud in OH and CO we could see whether the trends observed in MBM 53 and detailed in Chapters 4 and 5 would hold.

An ideal follow up to the work presented in Chapter 6 would be to take a subset of the Southern Galactic Hemisphere sampled by Magnani et al. (2000) and instead of using the on-off procedure employed by that survey actually use frequency switched spectra for each point. This would eliminate the problem of “negative” CO emission which made interpretation of the results from that chapter difficult.

Perhaps more importantly, we could specifically seek observation time for C⁺ and CH in MBM 53 using SOFIA and Arecibo. It is likely that the C⁺ at 158 μ m is the best way to trace all molecular gas, both dark and non-dark (see Langer et al. 2010; 2014). The problem with this approach is that, currently, the line is observable only with the SOFIA airborne observatory so that observing time is difficult to obtain. More importantly, a substantial fraction of the [CII] line emission arises from the atomic envelope of the molecular cloud (the outermost PDR region). Disentangling the portion of [CII] attributable to the CNM and that to molecular gas will be difficult. The CH approach is easier to pursue, and a proposal to observe the lines of sight studied in this thesis with the 3335 MHz line has been submitted to Arecibo as of March 2019 and will hopefully be scheduled for observations in

2020. These CH observations can lead to robust estimates of $N(\text{H}_2)$ for the lines of sight in question and thus refine our assumptions of the X factor and the OH/ H_2 abundance.

The end goal should be to extend our conclusions based on observations of MBM 53 to other diffuse molecular clouds. Extending our results to other clouds will lead to far better estimates of the dark gas mass and behavior than initial estimates which, after all, are based primarily on a single cloud (though Chapter 6 extended the results to a large region). With observations of other molecular tracers ([CII], CH), the goal is a bit different: The end goal for astronomers here should be to eventually eliminate the dark gas mass, either by using other tracers, by building better telescopes, and/or by using more sophisticated data analysis methods.

We have shown in this thesis that with a little extra effort a lot of what was believed to be dark gas (in its original sense of spectroscopically undetectable molecular gas) can be detected by normal spectroscopic means. With [CII] and perhaps CH, and as telescopes become more sensitive and reduction methods more sophisticated, the gas of the gaps will diminish and maybe even disappear entirely.

BIBLIOGRAPHY

- Abdo, A.A., et al. 2010, ApJ, 710, 133
- Allen, R.J., Ivette Rodríguez, M., Black, J.H., & Booth, R.S. 2012, AJ, 143, 97
- Allen, R.J., Hogg, D.E., & Engelke, P.D. 2015, AJ, 149, 123
- Barriault, L. et al. 2010a, MNRAS, 406, 2713
- Barriault, L., Joncas, G., Lockman, F.J., & Martin, P.G. 2010, MNRAS, 407, 2645
- Barriault, L., Joncas, G., Lockman, F.J., & Martin, P.G. 2010, MNRAS, 407, 2
- Bertojo, M., Cheung, A.C., & Townes, C.H. 1976, ApJ, 208, 914
- Blair, S., et al. 2017, in preparation
- Black, J.H. & Dalgarno, A. 1977, ApJS, 34, 405
- Blitz, L., Magnani, L., & Mundy, L. 1984, ApJL, 282, L9
- Bolatto, A.D., Wolfire, M., & Leroy, A.K. 2013, ARAA, 51, 207
- Burton, W.B. & Gordon, M.A. 1978, A&Ap, 63, 7
- Carpenter, J.M., Snell, R.L., & Schloerb, F.P. 1995, ApJ, 445, 246
- Carrol, B.W. & Ostlie, D.A. 2006, *An Introduction to Modern Astrophysics*, Cambridge U. Press
- Chastain, R.J., 2005, Ph.D. Thesis, University of Georgia
- Chastain, R.J., Shelton, R.L., Raley, E.A., & Magnani, L, 2006, AJ, 132, 1964
- Cheung, A.C., et al. 1968, Phys.Rev.Lett., 21,1701
- Cotten, D.L. 2011, Ph.D. Thesis, University of Georgia
- Cotten, D.L., Magnani, L., Wennerstrom, E.A., Douglas, K.A., & Onello, J.S. 2012, AJ, 144, 163
- Cotten, D.L. & Magnani, L. 2013, MNRAS, 436, 1152
- Cox, D.P. 2006, ARAA, 43, 337

- Crutcher, R.M. 1979, ApJ, 234, 881
- Dame, T.M. 1984, NASA Tech. Pap., NASA TP-2288, 6
- Dame, T.M. & Thaddeus, P. 1994, ApJ, 436, L173
- Dame, T.M., Hartmann, P., & Thaddeus, P. 2001, ApJ, 547, 792
- de Vries, C.P. & van Dishoeck, E. 1988, A&Ap, 203, 23
- de Vries, H.W. 1988, PhD thesis, Columbia University
- de Vries, H.W., Heithausen, A., and Thaddeus, P. 1987, ApJ, 319, 723
- Dickey, J.M., Crovisier, J., and Kázes, I. 1981, A&Ap 98, 271
- Dickey, J.M. & Lockman, F.J. 1990, ARAA, 28, 215
- Dickman, R.L., Comerville, W.B., Whittet, D.C.B., McNally, D., & Blades, J.C. 1983, ApJS, 53, 55
- Digel, S., de Geus, E., & Thaddeus, P. 1994, ApJ, 422, 92
- Donate, E. & Magnani, L. 2017, MNRAS, 472, 3169
- Draine, B.T. 1978, ApJ Suppl, 36, 595
- Dunham, T., Jr. 1937, PASP, 49, 26
- Dunham, T., Jr. & Adams, W.S. 1939, Publ.Am.Astr.Soc., 9, 5
- Federman, S.R. & Wilson, R.F. 1982, ApJ, 260, 124
- Goldsmith, P.F., et al. 2008, ApJ, 680, 428
- Gredel, R., van Dishoeck, E.F., de Vries, C.P., & Black, J.H. 1992, A&Ap, 257, 245
- Grenier, I.A., Cassandjian, J.-M., & Terrier, R. 2005, Science, 307, 1292 (GCT)
- Grossman, V., Heithausen, A., Meyerdiercks, H., & Mebold, U. 1990, A&Ap, 240, 400
- Hartmann, D. & Burton, W.B. 1997, *Atlas of Galactic Neutral Hydrogen*, Cambridge U. Press
- Hartmann, D., Magnani, L., & Thaddeus, P. 1998, ApJ, 492, 205
- Heyer, M. & Dame, T.M. 2015, ARAA, 53, 583
- Hollenbach, D.J. & Tielens, A.G.G.M. 1997, ARAA, 35, 79

- Johansson, L. E. B. 1979, *The Galactic Distribution of CH*, Research Lab. Electronics and Onsala Space Obs. Research Rep. 136 (Onsala: Onsala Space Obs.)
- Keto, E.R. & Meyers, P.C. 1986, *ApJ*, 304, 466
- Kiss, Cs., Moór, A., & Tóth, L.V. 2004, *A&Ap*, 418, 131
- Knapp, G.R. & Jura, M. 1976, *ApJ*, 209, 782
- Kulkarni, S.R. & Heiles, C. 1987, in *Interstellar Processes: Proceedings of the Symposium, Grand Teton National Park, WY, July 1-7, 1986*, Dordrecht: Reidel, 87
- Kutner, M.L. & Ulich, B.L. 1981, *ApJ*, 250, 341
- Langer, W.D., et al. 2010, *A&A*, 521, L17
- Langer, W.D., et al. 2014, *A&A*, 561, 122
- Li, D., et al. 2018, *ApJS*, 235, 1
- Liszt, H. & Lucas, R. 1996, *A&Ap*, 314, 917
- Liszt, H. & Lucas, R. 2002, *A&Ap*, 391, 693
- Liszt, H.S., Pety, J., & Lucas, R. 2010, *A&A*, 518, A45
- Liszt, H.S. & Pety, J. 2012, *A&A*, 541, A58
- Liszt, H. 2014, *ApJ*, 783, 17
- Low, F.J. et al. 1984, *ApJ*, 278, 19
- Lucas, R. & Liszt, H. 1996, *A&Ap*, 518, A45
- Lynds, B.T. 1962, *ApJS*, 7, 1
- Lynds, B.T. 1965, *ApJS*, 12, 163
- Maloney, P. 1990, *ApJ*, 348, L9
- Magnani, L., Blitz, L., & Mundy, L. 1985, *ApJ*, 295, 402
- Magnani, L., Lada, E.A., Blitz, L. 1986, *ApJ*, 301, 395
- Magnani, L., Blitz, L., & Wouterloot, J.G.A. 1988, *ApJ*, 326, 909
- Magnani, L., Lada, E.A., Sandel, G., & Blitz, L. 1989, *ApJ*, 339, 244
- Magnani, L. & Siskind, L. 1990, *ApJ*, 359, 355
- Magnani, L. & Onello, J.S. 1993, *ApJ*, 408, 559

- Magnani, L. & Onello, J.S. 1995, ApJ, 443, 169
- Magnani, L., et al. 2000, ApJ, 535, 167
- Magnani, L. & Shore, S.N. 2017, *A Dirty Window: Diffuse and Translucent Gas in the Interstellar Medium*, Springer
- Magnani, L., et al. 1998, ApJS, 504, 290
- Maloney, P. 1990, ApJ, 348, L9
- Miller, W.M. III & Cox, D.P. 1993, ApJ, 417, 579
- Neugebauer, G. et al. 1984, ApJ, 278, 1
- Nguyen, H., et al. 2018, ApJ, 862, 49
- Pety, J., et al. 2013, ApJ, 779, 43
- The Planck Collaboration; Ade, P.A.R., et al. 2010, A&Ap, 536, A13
- The Planck Collaboration; Ade, P.A.R., et al. 2010, A&Ap, 536, A19
- The Planck Collaboration; Ade, P.A.R., et al. 2011, A&Ap, 536, A21
- The Planck Collaboration; Ade, P.A.R., et al. 2011, A&Ap, 536, A24
- The Planck Collaboration; Ade, P.A.R., et al. 2013, A&Ap, 571, A13
- The Planck Collaboration; Ade, P.A.R., et al. 2016, A&Ap, 594, A10
- The Planck Collaboration; Ade, P.A.R., et al. 2016, A&Ap, 594, A25
- Reach, W.T., Koo, B.-C., & Heiles, C. 1994, ApJ, 429, 672
- Reach, Wall, W.F., & Odegard, N. 1998, ApJ, 507, 507
- Sandell, G., Johansson, L.E.B., Nguyen-Q-Rieu, & Mattila, K. 1981, A&Ap, 97, 317
- Sandell, G., Stevens M.A., & Heiles, C. 1987, A&Ap, 179, 255
- Sanders, D.B., Solomon, P.M. & Scoville, N.Z. 1984, ApJ, 276, 182
- Schlegel, D.J., Finkbeiner, D.P., & Davis, M. 1999, ApJ, 500, 525
- Schlafly, E.F. & Finkbeiner, D.P. 2011, ApJ, 737, 103
- Schlafly, E.F. et al. 2014, ApJ, 786, 29
- Scoville, N.Z. & Sanders, D.B. 1987, in *Interstellar Processes: Proceedings of the Symposium, Grand Teton National Park, WY, July 1-7, 1986*, Dordrecht: Reidel, 21

- Scoville, N.Z., Yun, M.S., Clemens, D.P., Sanders, D.B., & Waller, W.H. 1987, *ApJS*, 63, 821
- Shore, S.N., LaRosa, T.N., Chastain, R.J., & Magnani, L. 2006, *A&Ap*, 457, 197
- Snyder, L.E., Buhl, D., Zuckerman, B., & Palmer, P. 1969, *Phys.Rev.Lett*, 22, 679
- Solomon, P.M., Rivolo, A.R., Barrett, J.W., & Yahil, A.M. 1987, *ApJ*, 319, 730
- Spitzer, L. Jr. 1978, *Physical Processes in the Interstellar Medium*, New York : Wiley
- Stark, A.A. 1979, PhD Thesis, Princeton University
- Stricklan, A. 2019, MS Thesis, University of Georgia
- Strong, A.W. & Mattox, J.R. 1996, *A&Ap*, 308, L21
- Sullivan, W.T. 2009, *Cosmic Noise : A History of Early Radio Astronomy*, Cambridge U. Press
- Tang, N. et al. 2017, *ApJ*, 839, 8
- Tang, N., Li, D., Heiles, C., Wang, S., Pan, Z., & Wang, J.-J. 2018, *A&Ap*, 593, A42
- Tauber, J.A. 2010, *A&Ap*, 520, A1
- Toriseva M. & Mattila, K. 1985, *A&Ap*, 153, 207
- van Dishoeck, E.F. & Black, J.H. 1986, *ApJS*, 62, 109
- van Dishoeck, E.F. & Black, J.H. 1988, *ApJ*, 334, 771
- Verter, F., Magnani, L., Dwek, E. & Rickard, Lee J 2000, *ApJ*, 536, 831
- Wannier, P.G., Andersson, B-G, Federman, S.R., Lewis, B.M., Viala, Y.P., & Shaya, E. 1993, *ApJ*, 407, 163
- Weiland, J.P. et al. 1986, *ApJ*, 306, L101
- Weinreb, S., Barret, A.M., Meeks, M.L., & Henry, J.C. 1963, *Nature*, 200, 829
- Weselak, T., Galazutdinov, G.A., Beletsky, Y., & Krelowski, J. 2010, *MNRAS*, 402, 1991
- Wilson, R.W., Jefferts, K.B., and Penzias, A.A. 1970, *ApJ Let.*, 161, L43
- Wolfire, M.G., Hollenbach, D., & McKee, C.F. 2010, *ApJ*, 716, 1191
- Wouterloot, J.G.A. & Brand 1989, *A&ApS*, 80, 149
- Wouterloot, J.G.A. & Habing, H.J. 1985, *A&ApS*, 60, 43

Xu, D., Li, D., Yue, N., & Goldsmith, P.F. 2016, ApJ, 819, 22

Yamamoto, H., Onishi, T., Mizuno, A., & Fukui, Y. 2003, ApJ, 592, 217 (Y2003)

Yamamoto, H., Kawamura, A., Tachihara, K., Mizuno, N., Onishi, T., & Fukui, Y. 2006, ApJ, 642, 307